

Versatile vaccines against the  
next coronavirus threat p. 227

Recording thousands of  
neurons in the brain p. 258

Three-way quantum  
networking p. 259

# Science

\$15  
16 APRIL 2021  
[sciencemag.org](http://sciencemag.org)

AAAS

## T. REX TALLY

A total of 2.5 billion of the giant  
predators ever lived p. 284





## NOMIS & Science YOUNG EXPLORER AWARD

### Research at the intersection of the social and life sciences

#### Unconventional. Interdisciplinary. Bold.

The newly launched **NOMIS & Science Young Explorer Award** recognizes bold, early-career researchers with an M.D., Ph.D., or M.D./Ph.D. who ask fundamental questions at the intersection of the social and life sciences. It is awarded to scientists who conduct research with an enthusiasm that catalyzes cross-disciplinary collaboration and who take risks to creatively address relevant and exciting questions.

Award winners will receive a cash prize of up to \$15,000, and their essay submissions will be published in *Science*. They will also be invited to share their ideas with leading scientists in their respective fields at an award ceremony and to present their research to the NOMIS Board of Directors for potential future funding.

**Apply by May 15, 2021**  
at [www.sciencemag.org/nomis](http://www.sciencemag.org/nomis)

Science  
AAAS



NOMIS  
FOUNDATION  
Creating the Spark



# CONTENTS

16 APRIL 2021 • VOLUME 372 • ISSUE 6539

## NEWS

### IN BRIEF

**218** News at a glance

### IN DEPTH

#### **220 Vaccine link to serious clotting disorder firms up**

Rare symptoms found in AstraZeneca recipients occur after Johnson & Johnson shot as well *By K. Kupferschmidt and G. Vogel*

#### **221 Biden proposes a funding surge—and new agencies to manage it**

White House floats three new ARPA-like research offices in 2022 spending request to Congress *By J. Mervis*

#### **222 DNA from cave dirt traces Neanderthal upheaval**

First nuclear DNA from sediment shows turnover, migration among ancient cave dwellers in Spain *By A. Gibbons*  
RESEARCH ARTICLE BY B. VERNOT ET AL.  
10.1126/SCIENCE.ABF1667

#### **223 Lab-grown embryos mix human and monkey cells**

Insights from these chimeras could boost efforts to grow replacement human organs in livestock *By M. Leslie*

#### **224 NAS evaluates ejecting Marcy, Ayala for sexual harassment**

First cases slowly proceeding 2 years after change in academy's bylaws allowed members to be ousted *By M. Wadman*

#### **225 Researchers face attacks from Bolsonaro regime**

Harassment, budget cuts leave many fearing for their jobs and safety *By H. Escobar*

#### **226 Calculation could dim hopes for new physics**

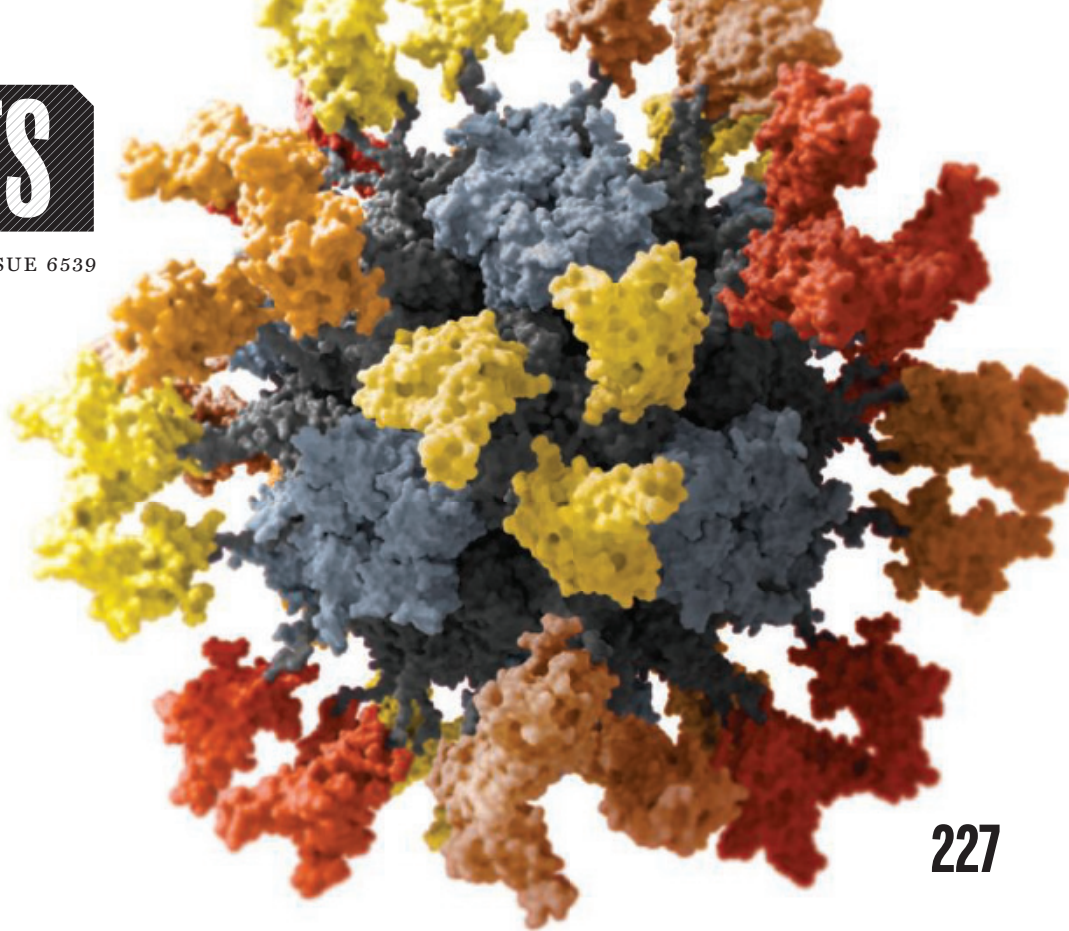
New prediction of muon's magnetism muddies interpretation of tantalizing measurement *By A. Cho*

PODCAST

### FEATURES

#### **227 The dream vaccine**

Why stop at just SARS-CoV-2? Vaccines in development aim to protect against many coronaviruses at once *By J. Cohen*



227

## INSIGHTS

### PERSPECTIVES

#### **232 Preparing for floods on the Third Pole**

Satellite-based real-time monitoring is needed for Himalayan glacial catchments  
*By T. Shukla and I. S. Sen*  
LETTER p. 247

#### **234 The Weyl side of ultracold matter**

Ultracold gases in optical lattices provide control and tunability for the exploration of Weyl semimetal physics  
*By N. Goldman and T. Yefsah*  
RESEARCH ARTICLE p. 271

#### **235 Mosaic synapses in epilepsy**

Mismatch of synaptic cadherins perturbs hippocampal circuitry  
*By B. Shohayeb and H. M. Cooper*  
RESEARCH ARTICLE p. 255

#### **237 Ecological stasis on geological time scales**

Communities and functional structure persist for millions of years in a mammal fauna  
*By P. D. Roopnarine and R. M. W. Banker*  
REPORT p. 300

#### **238 The gut microbiomes of 180 species**

Animal microbiomes are a treasure trove of previously unknown bacteria and genes  
*By A. L. Lind and K. S. Pollard*  
RESEARCH ARTICLE p. 254

#### **239 Diagnosing nutritional stress in the oceans**

Phytoplankton genomes map marine nutrient scarcity *By M. Coleman*  
REPORT p. 287

### POLICY FORUM

#### **241 A water rule that turns a blind eye to transboundary pollution**

We can't presume that states will fill gaps in federal oversight  
*By D. A. Keiser et al.*

### BOOKS ET AL.

#### **245 The cost of scientific patronage**

Military funding encouraged researchers to think of the ocean as a theater of war rather than a dynamic ecosystem  
*By C. Keiner*

#### **246 AI empires**

A Microsoft researcher unpacks the power and perils of today's artificial intelligence *By M. Spezio*

### LETTERS

#### **247 Seismological rockslide warnings in the Himalaya**

*By N. P. Rao et al.*

PERSPECTIVE p. 232

#### **247 Reimagining aquaculture in the Global South**

*By M. S. Bank et al.*

## 248 Weather radars' role in biodiversity monitoring

By J. Shamoun-Baranes et al.

## 249 Technical Comment abstracts

# RESEARCH

## IN BRIEF

250 From *Science* and other journals

## REVIEW

### 253 Quantum computing

Materials challenges and opportunities for quantum computing hardware  
N. P. de Leon et al.

REVIEW SUMMARY; FOR FULL TEXT:  
DOI.ORG/10.1126/SCIENCE.ABB2823

## RESEARCH ARTICLES

### 254 Microbial genomics

Diversity and functional landscapes in the microbiota of animals in the wild  
D. Levin et al.  
RESEARCH ARTICLE SUMMARY; FOR FULL TEXT:  
DOI.ORG/10.1126/SCIENCE.ABB5352  
PERSPECTIVE p. 238

### 255 Neurodevelopment

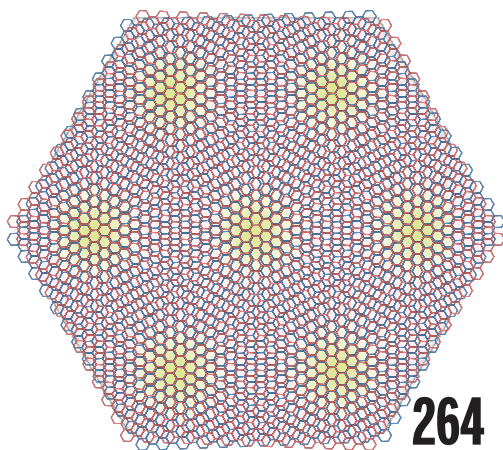
Female-specific synaptic dysfunction and cognitive impairment in a mouse model of *PCDH19* disorder  
N. Hoshina et al.

RESEARCH ARTICLE SUMMARY; FOR FULL TEXT:  
DOI.ORG/10.1126/SCIENCE.AAZ3893  
PERSPECTIVE p. 235

### 256 Coronavirus

SARS-CoV-2 within-host diversity and transmission  
K. A. Lythgoe et al.

RESEARCH ARTICLE SUMMARY; FOR FULL TEXT:  
DOI.ORG/10.1126/SCIENCE.ABG0821



### 257 Gut physiology

An intercrypt subpopulation of goblet cells is essential for colonic mucus barrier function  
E. E. L. Nyström et al.

RESEARCH ARTICLE SUMMARY; FOR FULL TEXT:  
DOI.ORG/10.1126/SCIENCE.ABB1590

### 258 Neuroscience

Neuropixels 2.0: A miniaturized high-density probe for stable, long-term brain recordings  
N. A. Steinmetz et al.

RESEARCH ARTICLE SUMMARY; FOR FULL TEXT:  
DOI.ORG/10.1126/SCIENCE.ABF4588

### 259 Quantum networks

Realization of a multinode quantum network of remote solid-state qubits  
M. Pompili et al.

### 264 2D materials

Nematicity and competing orders in superconducting magic-angle graphene  
Y. Cao et al.

### 271 Quantum simulation

Realization of an ideal Weyl semimetal band in a quantum gas with 3D spin-orbit coupling  
Z.-Y. Wang et al.

PERSPECTIVE p. 234

## REPORTS

### 276 Magnetism

Gapped magnetic ground state in quantum spin liquid candidate  $\kappa$ -(BEDT-TTF)<sub>2</sub>Cu<sub>2</sub>(CN)<sub>3</sub>  
B. Miksch et al.

### 280 Fire ecology

Carbon loss from boreal forest wildfires offset by increased dominance of deciduous trees  
M. C. Mack et al.

VIDEO

### 284 Paleontology

Absolute abundance and preservation rate of *Tyrannosaurus rex*  
C. R. Marshall et al.

PODCAST

### 287 Ocean microbiology

Metagenomic analysis reveals global-scale patterns of ocean nutrient limitation  
L. J. Ustick et al.

PERSPECTIVE p. 239

### 292 Signal transduction

Decoupling transcription factor expression and activity enables dimmer switch gene regulation  
C. Ricci-Tam et al.

### 296 Membranes

Ion-capture electrodialysis using multifunctional adsorptive membranes  
A. A. Uliana et al.

### 300 Paleontology

Punctuated ecological equilibrium in mammal communities over evolutionary time scales  
F. Blanco et al.

PERSPECTIVE p. 237

## DEPARTMENTS

### 217 Editorial

Scientists' lanes and headwinds  
By H. Holden Thorp

### 310 Working Life

Finding my online voice  
By Suhas Eswarappa Prameela



## ON THE COVER

*Tyrannosaurus rex* prowls a Cretaceous coast. By using the rich fossil record of *T. rex*, including its body mass, growth and survivorship curves, geographic range, and geologic longevity, together with the relationship between population density and



body mass among living animals, it is possible to ascertain how many *T. rex* ever roamed the planet and to estimate the fossil recovery rate for this species. See page 284.

Illustration: Julius Csotonyi

New Products..... 304  
Science Careers..... 305

SCIENCE (ISSN 0036-8075) is published weekly on Friday, except last week in December, by the American Association for the Advancement of Science, 1200 New York Avenue, NW, Washington, DC 20005. Periodicals mail postage (publication No. 484460) paid at Washington, DC, and additional mailing offices. Copyright © 2021 by the American Association for the Advancement of Science. The title SCIENCE is a registered trademark of the AAAS. Domestic individual membership, including subscription (12 months): \$165 (\$74 allocated to subscription). Domestic institutional subscription (51 issues): \$2148; Foreign postage extra: Air assist delivery: \$98. First class, airmail, student, and emeritus rates on request. Canadian rates with GST available upon request. GST #125488122. Publications Mail Agreement Number 1069624. Printed in the U.S.A.

Change of address: Allow 4 weeks, giving old and new addresses and 8-digit account number. Postmaster: Send change of address to AAAS, P.O. Box 96178, Washington, DC 20090-6178. Single-copy sales: \$15 each plus shipping and handling available from backissues.science.org; bulk rate on request. Authorization to reproduce material for internal or personal use under circumstances not falling within the fair use provisions of the Copyright Act can be obtained through the Copyright Clearance Center (CCC), www.copyright.com. The identification code for Science is 0036-8075. Science is indexed in the Reader's Guide to Periodical Literature and in several specialized indexes.



# Scientists' lanes and headwinds

**C** OVID-19 will be remembered for many things, including the pandemic that changed science communication. Much of the effect was positive. Outstanding epidemiologists, virologists, and public health experts became household names as they talked about the pandemic through mainstream media and social platforms. In the rapidly evolving situation, hearing directly from the scientific community was more important than ever. But former president Donald Trump and former vice president Mike Pence did enormous damage in the United States by appointing themselves scientists, logisticians, and chief economists and taking control of the information flow. The vaccine arrived, despite all the bungling, but in the meantime, many lives could have been saved had messages about dangers, challenges, and solutions come through more clearly. We still seem to be learning. Although the Biden administration appears to have a firmer grip on the crisis, it now faces a new surge of infections brought on by the variants and an increase in the number of states loosening restrictions. How can science be better communicated in the future, given what we have seen during the pandemic?

Viewers of cable news will easily recognize Juliette Kayyem, a fixture on CNN who also appears occasionally on other networks as a national security analyst. She was assistant secretary of Homeland Security in the Obama administration and is now the Belfer Senior Lecturer in International Security at Harvard's Kennedy School of Government (I was a consultant for a company run by her brother many years ago, but that business relationship has long since ended). Early in the pandemic, Kayyem was one of the first voices assuring the public that the supply chain would hold up and that there was no reason to raid the grocery stores for toilet paper and hand sanitizer. I asked her what scientists could do better in the future. The main message: Stay in their lane.

Kayyem consumes health intelligence the same way she consumes foreign intelligence or climate intelligence and then uses it to create a message for politicians and the public. She thinks scientists did not do enough to acknowledge the economic devastation

that was ushered in by shutting down the economy, which left an opening for the anti-lockdown voices to fight back. She believes scientists could have offered more hope along with the warnings. And she believes that the extreme voices on cable news and social media distracted scientists from seeing that most of the American public could understand the nuances of the situation better than they gave them credit for.

As for the early garbling of the mask message, she feels that some science experts ventured too far into logistics, rather than sticking to what they know. "They all say they didn't want to promote masks initially because there wasn't sufficient supply," she said. "That's not their call." She was also critical of what she saw as a panic over vaccine supply. "Make us the vaccine," she said, "but once you start getting into logistics and supply chain and the use of the Defense Production Act and all that, that's not your lane." As we approach 200 million shots in 100 days, Kayyem's admonition rings true. In other words, just as we were lamenting the rise of armchair epidemiologists, some scientists inadvertently became armchair logisticians.

Though the public discussions on Twitter were sometimes exploited by malicious forces, Kayyem believes that overall, it is good for scientists to join the debate on social media, a point I made in an editorial earlier this year. She was also very complimentary of

the scientists who became household names on social media and cable news, but she cautioned that "rockstar status can make you think that everyone wants your opinion on everything."

One of those scientists who became well known in the pandemic, Georgetown University virologist Angela Rasmussen, agrees that some ventured too far afield. "While I can understand the temptation to be thought of as a leading pandemic Public Thinker," she says, "I remind myself that this isn't the Renaissance and none of us are Leonardo da Vinci."

These are important admonitions, but it is also salient to remember that the headwinds caused by President Trump were intense. We can only hope that in the next pandemic, the messages will have smoother sailing.

—H. Holden Thorp



**H. Holden Thorp**  
Editor-in-Chief,  
*Science* journals.  
hthorp@aaas.org;  
@hholdenthorpe

**"...many lives  
could have  
been saved had  
messages...  
come through  
more clearly."**

## IN BRIEF

Edited by Jeffrey Brainard

The Fukushima plant is running out of space to store tanks of radioactive water.



## NUCLEAR SAFETY

# Japan to release Fukushima water into Pacific despite concerns

**J**apan announced on 13 April it plans to release 1.25 million tons of treated radioactive water from the damaged Fukushima Daiichi Nuclear Power Plant into the Pacific Ocean. The water has been used to cool nuclear fuel debris resulting from meltdowns of three reactors after an earthquake and tsunami hit the plant in March 2011. The government says complex filtration and dilution will reduce

radiation to safe levels, and nuclear plants elsewhere do similar controlled releases. But environmental groups, fisheries organizations, and neighboring countries condemned it, with some saying the release will be vastly larger than at other plants, and scientists worry about the impact of the remaining trace amounts of radiation on marine life. The gradual release will start in 2023 and take 40 years to complete.

## School closures slowed cases

**PUBLIC HEALTH** | School closures in the San Francisco Bay Area in spring 2020 likely prevented more than 13,000 cases of COVID-19 there, scientists estimate this week in the *Journal of the Royal Society Interface*. Researchers surveyed families to determine how much the closures reduced numbers of social contacts; then they modeled the likely number of cases that would have occurred if schools had stayed open without any mitigation measures or with precautions such as masks, smaller class sizes, and keeping groups separate. With masks and

cohorts, elementary schools were less likely to contribute significantly to community spread than middle or high schools, the study's authors concluded.

## Panel cautions on chimeras

**BIOETHICS** | It's extremely unlikely that brain "organoids" or animal brains transplanted with human neural cells will experience humanlike consciousness or pain anytime soon, and current oversight bodies and policies are adequate, a top-level U.S. advisory panel said last week. Eleven scientists, ethicists, and legal experts

convened by the National Academies of Sciences, Engineering, and Medicine reviewed these controversial and fast-moving areas of neuro-science. Organoids are tiny, free-standing, brainlike structures grown from human stem cells. New controls may be needed, the panel's report added, as researchers begin to create chimeras by injecting human stem cells into early animal embryos such as nonhuman primates (p. 223). It said oversight committees might need more expertise if altered animals develop "enhanced capacities." The report was requested by the National Institutes of Health, which in 2015 suspended funding



for chimera research with any species, partly because of potential cognitive changes in the animals.

## COVID-19 publishing gap eases

**DIVERSITY** | The gender gap in authorship of COVID-19 research articles was most pronounced early in the pandemic but has narrowed, a study shows. Women served as first authors of 32% of a subset of COVID-19 papers published from February to May 2020, a drop of 13 percentage points relative to publications in the same journals in the previous year. But the percentage of papers with women in this key authorship role rose to 41% by the period from October 2020 to January. This same pattern of decline and partial rebound was observed across most of the globe, researchers reported last week in *BMJ Open* based on nearly 43,000 COVID-19 papers. Women may have disproportionately increased time spent on child care and other domestic duties, and men's existing professional advantages may have helped them in the rush to publish papers about COVID-19, the authors said. They aren't sure what caused the

rebound, but said institutions and funders should help female scientists cope with the pandemic's continuing impacts.

## New York to end stem cell funds

**BIOMEDICINE** | Scientists are criticizing New York's plan to eliminate one of the United States's few state-level programs to fund stem cell research. Since its creation in 2007, the New York State Stem Cell Science program has awarded \$370 million for research and education, although it has recently appeared dormant. Researchers were surprised in 2020 after they applied for up to 70 projects costing \$50 million over 3 years, but received no official response. In March, 10 Nobel laureates, including Columbia University neuroscientist Eric Kandel, wrote to Governor Andrew Cuomo opposing the proposed cancellation and worrying that "all the momentum gained" would end. But last week, the state Legislature killed the program in its 2022 budget bill, which Cuomo is expected to sign. In contrast, California last year approved a \$5.5 billion increase for its stem cell program.

## THREE QS

## Unraveling Long COVID

After the first surge of COVID-19 cases in spring 2020, a new worry emerged: Some infected people didn't get better. Linger symptoms, often referred to as Long COVID, include brain fog, intense fatigue, and loss of smell and taste. Emilia Liana Falcone of the Montreal Clinical Research Institute and Michael Sneller of the U.S. National Institute of Allergy and Infectious Diseases are each leading a Long COVID study that includes people who never caught the virus for comparison. (A longer version of this interview is at [scim.ag/LongCOVID](https://scim.ag/LongCOVID).)

### Q: How did you get interested in Long COVID?

**Michael Sneller:** About 6 years ago, I was asked to help lead a study of Ebola survivors in West Africa. I knew we needed to have a control group, in order to really determine whether any of the things we were seeing were related to Ebola per se. I learned a lot that I was able to apply to studying post-COVID syndrome.

**Emilia Liana Falcone:** I spent almost 9 years at the National Institutes of Health, where I was looking at long-term inflammatory complications in patients with inborn errors of immunity. It seemed highly plausible that given the intense inflammatory processes in acute COVID-19, there would be long-term effects.

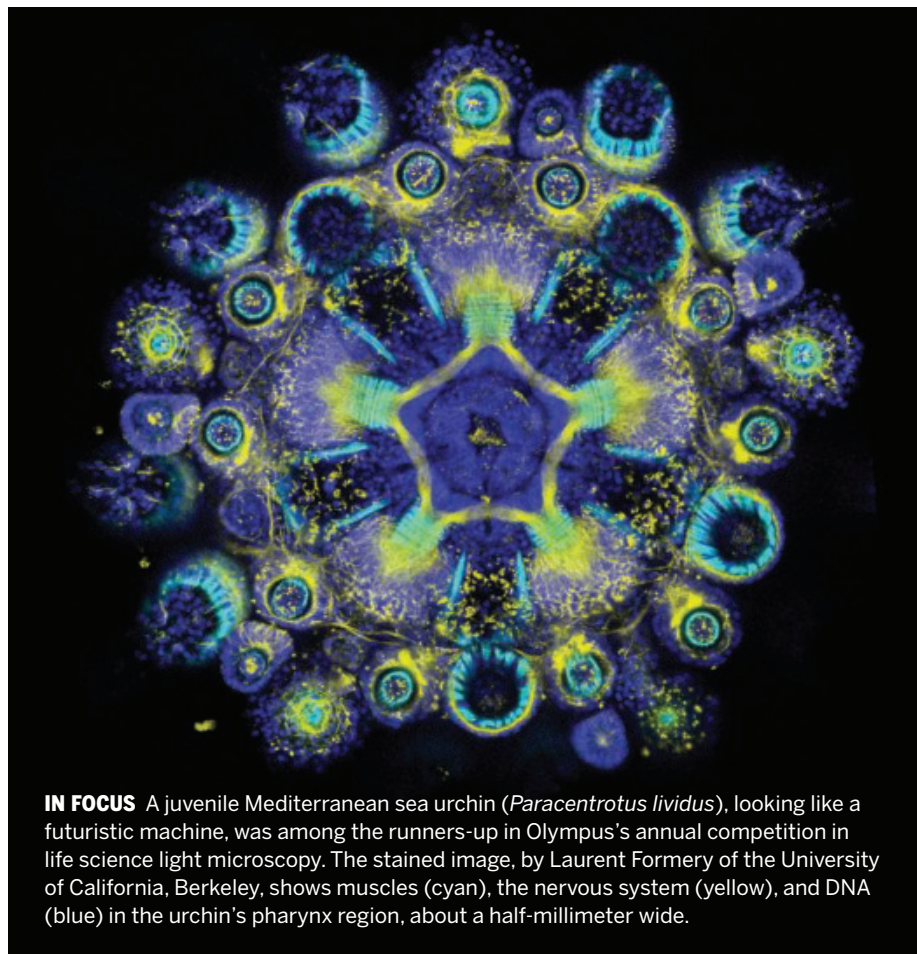
### Q: Why study people who have not had COVID-19?

**E.L.F.:** You need to control for the background noise. A pandemic creates anxiety, stress, insomnia, depression. We have to tease out what is really related to the infection.

**M.S.:** For example, there are published reports about tinnitus being a post-COVID problem. About 12% of our COVID group complains of tinnitus, and about 14% of the control group has tinnitus.

### Q: Some people develop enduring symptoms after infections other than COVID-19. Is Long COVID another example of this?

**E.L.F.:** Some of the neurological complications are common for sure after other infections. Certain features are not quite as common that we're seeing now—the loss of smell and taste. There's also this new onset of some endocrinopathies, such as thyroid problems. It might be more distinctive of COVID.



**IN FOCUS** A juvenile Mediterranean sea urchin (*Paracentrotus lividus*), looking like a futuristic machine, was among the runners-up in Olympus's annual competition in life science light microscopy. The stained image, by Laurent Formery of the University of California, Berkeley, shows muscles (cyan), the nervous system (yellow), and DNA (blue) in the urchin's pharynx region, about a half-millimeter wide.

IMAGE: LAURENT FORMERY/OLYMPUS



People line up to receive AstraZeneca's COVID-19 vaccine in Belfast, Northern Ireland.

## COVID-19

# Vaccine link to serious clotting disorder firms up

Rare symptoms seen in AstraZeneca recipients occur after Johnson & Johnson shot as well

By Kai Kupferschmidt and Gretchen Vogel

A rare but very serious side effect that has complicated Europe's COVID-19 vaccination schedules for the past month has now thrown a wrench into U.S. immunization efforts as well. Researchers believe the problem, characterized by dangerous blood clots and low platelet counts, may be triggered by vaccines produced by AstraZeneca and Johnson & Johnson (J&J), which both contain a modified adenovirus. They have identified an errant immune reaction as the possible cause, but don't yet understand how it arises.

There are 222 suspected cases of the syndrome so far in Europe among 34 million people who have received their first dose of the AstraZeneca vaccine, recently named Vaxzevria; more than 30 have died. The European Medicines Agency (EMA) on 7 April acknowledged "a probable causal association" between the syndrome and the vaccine, and some countries have restricted Vaxzevria to older age groups at higher risks of severe COVID-19.

On 13 April, U.S. authorities said they would pause use of the J&J vaccine, which 6.8 million people have received so far, after six similar cases, including one death.

The move was out of "an abundance of caution," said Peter Marks of the U.S. Food and Drug Administration (FDA), and prompted in part by the similarity to the symptoms observed in Europe. In response, J&J said it would "proactively delay the rollout of our vaccine in Europe," where it was recently authorized for use.

As *Science* went to press, a joint committee of FDA and the Centers for Disease Control and Prevention was expected to meet on 14 April to assess the cases and advise on further use of the J&J vaccine. (FDA has not yet authorized use of the AstraZeneca vaccine.) The similar problems on both sides of the Atlantic Ocean "really increase the concern for a vaccine-related complication,"

says hematologist Gowthami Arepally of Duke University School of Medicine, who is an external consultant with AstraZeneca.

So far, no similar cases have been reported in people who received Russia's Sputnik V or China's CanSino Biologics vaccine, which are both based on an adenovirus as well. But data on those vaccines have been limited, and it isn't clear that regulators in regions where they have been used would either pick up on or report such safety sig-

nals, says Peter Hotez, a virologist and vaccine expert at Baylor College of Medicine. (Hotez is involved in the development of a protein-based COVID-19 vaccine.)

Researchers stress that the troubles by no means spell the end for the two vaccines. In the vast majority of cases, their benefits outweigh the risks, and the cheap and easy to store shots still offer the best hope for vaccinating large numbers of people in low- and middle-income countries.

On 9 April in *The New England Journal of Medicine*, one research team published its observations on 11 Vaxzevria recipients in Germany and Austria and another published data on five patients in Norway. Both found that symptoms resemble a

rare reaction to the drug heparin, called heparin-induced thrombocytopenia (HIT), in which the immune system makes antibodies to a complex of heparin and a protein called platelet factor 4 (PF4), triggering platelets to form dangerous clots throughout the body. Sickened vaccine recipients also had antibodies to PF4, the researchers found. They propose calling the syndrome vaccine-induced immune thrombotic thrombocytopenia.

*Science's* COVID-19 reporting is supported by the Heising-Simons Foundation.



One of the groups, led by clotting expert Andreas Greinacher of the University of Greifswald, also speculates about a mechanism. Vaxzevria, the J&J shot, and similar vaccines consist of an adenovirus engineered to infect cells and prompt them to produce the pandemic coronavirus' spike protein. Among the 50 billion virus particles in each Vaxzevria dose, some may break apart and release their DNA, Greinacher says. Like heparin, DNA is negatively charged, which could cause it to bind to PF4, which has a positive charge. The complex might then trigger the production of antibodies, especially when the immune system is on high alert because of the vaccine.

Alternatively, the antibodies may already be present in the patients and the vaccine may just boost them. Many healthy people harbor antibodies against PF4, but they are kept in check by an immune mechanism called peripheral tolerance, Arepally says. "When you get vaccinated, sometimes the mechanisms of peripheral tolerance get disrupted," she says. "When that happens does that unleash any autoimmune syndromes that you are predisposed to, like HIT?"

Several early ideas about a cause could not be substantiated. A past bout of COVID-19 is not the issue; none of the five patients in Norway had been infected. Others have suggested antibodies against the virus' spike protein—which many vaccines seek to elicit—also recognize PF4, which could spell trouble for many COVID-19 vaccines. But so far, there is no evidence that the messenger RNA-based vaccines made by the Pfizer-BioNTech collaboration and Moderna, which tens of millions of people have received in both the United States and Europe, are causing similar disorders.

For Vaxzevria, Greinacher and his collaborator Rolf Marschalek, a molecular biologist at Frankfurt University, are calling for tests of a simple solution: halving the dose. In AstraZeneca's phase 3 trial in the United Kingdom, a small number of people accidentally received a lower dose and had fewer side effects in general; perhaps a reduced dose is also less likely to trigger the kind of strong inflammation that boosts PF4 antibodies, the researchers say. And unexpectedly, those people were slightly better protected, perhaps because high levels of inflammation can actually block the formation of antibodies. "Part of the problem might be that they just overdose" the vaccine, Greinacher says.

That remains to be seen, Cox cautions. But if the hunch proves correct, what looked like a terrible blow for one of the world's most important weapons against the pandemic might be good news in disguise: Supplies of the vaccine could protect twice as many people—with fewer side effects. ■

## U.S. SCIENCE POLICY

# Biden proposes a funding surge—and new agencies to manage it

White House floats three new ARPA-like research offices in 2022 spending request to Congress

By Jeffrey Mervis

**P**resident Joe Biden wants to go big and bold on science. The research community loves the big, but it has questions about the bold—especially Biden's plan for three new funding entities dedicated to health, technology, and climate.

Last week, in his 2022 budget request, Biden laid out a \$1.5 trillion blueprint that would increase discretionary spending by 8.4%. The \$118 billion bump would fund healthy boosts at many federal research agencies (see table, right), including 20% hikes at the two largest: the National Institutes of Health (NIH), to \$51 billion, and the National Science Foundation (NSF), to \$10.2 billion. Biden is also asking Congress to expand their missions, creating units that would build on their basic research portfolios to address pressing societal problems.

NIH would get \$6.5 billion to stand up an Advanced Research Projects Agency-Health (ARPA-H) initially focused on cancer, diabetes, and Alzheimer's disease. NSF would get a new technology directorate, of an unspecified size, that would lead the nation's efforts to outinnovate China (*Science*, 9 April, p. 112). Biden also wants to create an ARPA-Climate to take more aggressive steps against global warming, although he didn't say where it would be housed.

The model for all three entities is the military's Defense Advanced Research Projects Agency (DARPA). Created during the Cold War, DARPA has both developed high-tech weaponry and funded research on civilian technologies that have spawned trillion-dollar industries. In the past 2 decades, lawmakers have used DARPA's template to create three additional ARPAs tasked with combating bioterrorism, developing new energy technologies, and assisting the intelligence community.

Arati Prabhakar, a former DARPA director, calls the approach "solutions R&D." She's thrilled that the Biden administration wants to expand on it. "The president is asking the R&D community to help with some of the biggest problems facing the country," says Prabhakar, who in 2019

founded Actuate, a California-based non-profit working with private philanthropy to tackle some of those challenges.

Unlike most federal research agencies, which rely on scientists to submit ideas that fit into long-standing program areas and ask outside experts to judge their merit, DARPA gives its program managers the freedom to both solicit proposals and decide which should be funded. They are also quick to end projects that aren't making sufficient progress toward interim milestones. In contrast, other agencies that award basic research grants often give investigators considerable leeway to change course during the lifetime of the award.

Prabhakar says those features have helped DARPA be successful. But she warns against "tarnishing the brand [by] slapping the label on something that isn't

## A rising tide

A White House outline of President Joe Biden's 2022 budget request included these highlights for research.

NIH	\$51 billion (20% increase)
NSF	\$10.2 billion (20% increase)
DOE science	\$7.4 billion (5.5% increase)
NASA earth science	\$2.25 billion (12.5% increase)
NOAA	\$6.9 billion (16% increase)
EPA	\$11 billion (21% increase)
NIST labs	\$916 million (16% increase)
ARPA-Energy and new ARPA-Climate	\$1 billion combined, up from \$427 million for ARPA-E alone

really DARPA." It's important, she says, that any new DARPA clone address a pressing national need that can be met with innovative technology.

The president's 9 April budget outline doesn't give many details about ARPA-H. But the idea has been around for decades, and advocates say it meets Prabhakar's test. They argue that not enough NIH-funded research leads to treatments and cures. "ARPA-H is recognition that funding basic research doesn't necessarily drive commercial innovation and that there are market

failures,” says geneticist Michael Stebbins, a consultant and former White House science office official. The new agency would help promising ideas cross the so-called valley of death that prevents many discoveries from reaching patients. He thinks ARPA-H’s proposed \$6.5 billion budget is warranted “because of the scale of the challenge.”

Breaking the existing NIH mold is important, agrees Robert Cook-Deegan, a research policy professor at Arizona State University, Tempe, and longtime proponent of a DARPA-like agency at NIH. “I’m totally in favor of giving senior NIH people a lot of money and the flexibility to push the boundaries and work outside the existing system of peer review,” he says. But he wonders about the premise that new technologies are the key to improving health outcomes in the United States. “I’m not sure that curing cancer is an engineering problem,” he says.

As vice president, Biden became a champion of cancer research after his son Beau Biden died from brain cancer in 2015, and he led the Obama administration’s Cancer Moonshot that aimed to accelerate cures. He floated the idea of ARPA-H during his presidential campaign and more recently during a visit to a plant making a COVID-19 vaccine.

But Biden’s plan to place ARPA-H within the notoriously cautious NIH surprised some of the idea’s staunchest advocates. “If it’s just another fund within the NIH, we’re not optimistic that it’s going to succeed,” says Liz Feld, president of the Suzanne Wright Foundation, a pancreatic cancer research advocacy group. Instead, Feld and allies want ARPA-H to stand alone within NIH’s parent agency, the Department of Health and Human Services.

Other research advocates worry ARPA-H would divert money from NIH’s existing 27 institutes and centers and say it should start smaller. “We do not believe it is in the nation’s interest to channel funding away from other research priorities,” says Mary Woolley, president of Research!America, which is seeking a 10% boost for NIH’s core programs.

The fate and final form of ARPA-H and the other proposed ARPA-like entities will not be clear for months. Biden’s proposal is the opening move in a budget process for the fiscal year that begins on 1 October and will involve extensive negotiations with Congress. Separately, legislators have already started to debate Biden’s \$2 trillion infrastructure plan, which includes a one-time injection of \$200 billion for a host of research initiatives, including the new tech directorate at NSF. ■

With reporting by Jocelyn Kaiser.



Researchers excavating Estatuas cave in Spain found a long record of Neanderthal DNA in the sediments.

## PALEOANTHROPOLOGY

# DNA from cave dirt traces Neanderthal upheaval

First nuclear DNA from sediment shows turnover, migration among ancient cave dwellers in Spain

By Ann Gibbons

**E**statuas cave in northern Spain was a hive of activity 105,000 years ago. Artifacts show its Neanderthal inhabitants hafted stone tools, butchered red deer, and may have made fires. They also shed, bled, and excreted subtler clues onto the cave floor: their own DNA. “You can imagine them sitting in the cave making tools, butchering animals. Maybe they cut themselves or their babies pooped,” says population geneticist Benjamin Vernot, a postdoc at the Max Planck Institute for Evolutionary Anthropology (MPI-EVA), whose perspective may have been colored by his own baby’s cries during a Zoom call. “All that DNA accumulates in the dirt floors.”

He and MPI-EVA geneticist Matthias Meyer report this week in *Science* that dirt from Estatuas has yielded molecular treasure: the first nuclear DNA from an ancient human to be gleaned from sediments. Earlier studies reported shorter, more abundant human mitochondrial DNA (mtDNA) from cave floors, but nuclear DNA, previously available only from bones and teeth, can be far more informative. “Now, it seems that it is possible to extract nuclear DNA from dirt, and we have a lot of dirt in archaeological sites,” says archaeologist Marie Soressi of Leiden University.

“This is a beautiful paper,” agrees population geneticist Pontus Skoglund of the Francis Crick Institute. The sequences reveal the genetic identity and sex of ancient cave dwellers and show that one group of Neanderthals replaced another in the Spanish cave about 100,000 years ago, perhaps after a climate cooling. “They can see a shift in Neanderthal populations at the very same site, which is quite nice,” Skoglund says.

To date, paleogeneticists have managed to extract ancient DNA from the bones or teeth of just 23 archaic humans, including 18 Neanderthals from 14 sites across Eurasia. In search of more, Vernot and Meyer’s team sampled sediment from well-dated layers in three caves where ancient humans are known to have lived: the Denisova and Chagyrskaya caves in Siberia and Estatuas cave in Atapuerca, Spain.

In what Skoglund calls “an amazing technical demonstration,” they developed new genetic probes to fish out hominin DNA, allowing them to ignore the abundant sequences from plants, animals, and bacteria. Then, they used statistical methods to home in on DNA unique to Neanderthals and compare it with reference genomes from Neanderthals in a phylogenetic tree.

All three sites yielded Neanderthal nuclear and mtDNA, with the biggest surprise coming from the small amount of nuclear



DNA from multiple Neanderthals in Estatuas cave. Nuclear DNA from a Neanderthal male in the deepest layer, dating to about 113,000 years ago, linked him to early Neanderthals who lived about 120,000 years ago in Denisova cave and in caves in Belgium and Germany.

But two female Neanderthals who lived in Estatuas cave later, about 100,000 years ago, had nuclear DNA more closely matching that of later, “classic” Neanderthals, including those who lived less than 70,000 years ago at Vindija cave in Croatia and 60,000 to 80,000 years ago at Chagyrskaya cave, says co-author and paleoanthropologist Juan Luis Arsuaga of the Complutense University of Madrid.

At the same time, the more plentiful mtDNA from Estatuas cave shows declining diversity. Neanderthals in the cave 113,000 years ago had at least three types of mtDNA. But the cave’s Neanderthals 80,000 and 107,000 years ago had only one type. Existing ancient DNA from Neanderthal bones and teeth had also pointed to a falloff in genetic diversity over the same period.

Arsuaga suggests Neanderthals thrived and diversified during the warm, moist interglacial period that started 130,000 years ago. But about 110,000 years ago, temperatures in Europe dipped suddenly as a new glacial period set in. Soon after, all but one lineage of Neanderthals disappeared. Members of the surviving lineage repopulated Europe during later, relatively warm spells, with some taking shelter in Estatuas cave.

Those survivors and their descendants include what Arsuaga calls the “famous” classic Neanderthals, such as skulls from Vindija and La Ferrassie in France. He notes they had bigger brains—up to 1750 cubic centimeters (cm<sup>3</sup>)—than earlier Neanderthals, whose cranial capacities were no larger than 1400 cm<sup>3</sup>. Arsuaga says this mirrors a similar pattern in modern humans in Africa, who also underwent a surge in brain size and multiple population replacements with the onset of the ice age.

“This pattern—dispersal over perhaps long distances and population replacement or admixture—is one that we find almost everywhere we look,” in humans or other mammals, says Beth Shapiro, a molecular biologist at the University of California, Santa Cruz.

Cave dirt DNA is likely to yield more clues. Paleogeneticist Viviane Slon, a co-author of the *Science* paper now at Tel Aviv University, says she and the MPI-EVA team are analyzing ancient DNA from sediments at dozens of sites worldwide. “Hopefully soon, we’ll start to get a very high-resolution, fine-scale view of ancient humans and who was where at what time,” she says. ■

## BIOMEDICINE

# Lab-grown embryos mix human and monkey cells

Insights from these chimeras could boost efforts to grow replacement human organs in livestock

By **Mitch Leslie**

**B**y slipping human stem cells into the embryos of other animals, we might someday grow new organs for people with faltering hearts or kidneys. In a step toward that goal, researchers have created the first embryos with a mixture of human and monkey cells. These chimeras could help scientists hone techniques for growing human tissue in species better suited for transplants, such as pigs.

“The paper is a landmark in the stem cell and interspecies chimera fields,” says stem cell biologist Alejandro De Los Angeles of Yale University. The findings hint at mechanisms by which cells of one species can adjust to survive in the embryo of another, adds Daniel Garry, a stem cell biologist at the University of Minnesota (UM), Twin Cities.

In 2017, researchers reported growing pancreases from mouse stem cells inserted into rat embryos. Transplanting the organs into mice with diabetes eliminated the disease. But cells from more distantly related species, such as pigs and humans, haven’t gotten along as well. That same year, developmental biologist Juan Carlos Izpisua Belmonte of the Salk Institute for Biological Studies and colleagues reported injecting human stem cells into pig embryos. After the embryos had developed in surrogate mother pigs for 3 to 4 weeks, only about one in 100,000 of their cells were human.

The pig study used human skin cells that had been reprogrammed into stem cells. But so-called extended pluripotent stem (EPS) cells, made by exposing stem cells to a certain molecular cocktail, can spawn a greater variety of tissues. In the new study, Izpisua Belmonte, reproductive biologist Weizhi Ji of Kunming University of Science and Technology, and colleagues tested those more capable cells in a closer human relative—cynomolgus monkeys. They inserted 25 human EPS cells into each of 132 monkey embryos and reared the chimeras in culture dishes for up to 20 days.

The team reports this week in *Cell* that

the human cells showed staying power: After 13 days, they were still present in about one-third of the chimeras. The human cells seemed to integrate with the monkey cells and had begun to specialize into cell types that would develop into different organs.

By analyzing gene activity, the researchers identified molecular pathways that were switched on or turned up in the chimeras, possibly promoting integration between human and monkey cells. Izpisua Belmonte says manipulating some of those pathways may help human cells survive in embryos of species “more appropriate for regenerative medicine.”

Still, the human and monkey cells didn’t quite mesh, notes UM stem cell biologist Andrew Crane. The human cells often stuck together, making him wonder whether there’s “another barrier that we aren’t seeing” that could prevent human

cells from thriving if the embryos were to develop further.

In the United States, federal funding cannot be used to create certain types of chimeras, including early nonhuman primate embryos containing human stem cells. The new study was performed in China and funded by Chinese govern-

ment sources, a Spanish university, and a U.S. foundation. Bioethicist Karen Maschke of the Hastings Center in New York says she is satisfied that the work, which passed layers of institutional review and drew on advice from two independent bioethicists, was performed responsibly.

Human-monkey chimeras do raise a worry, addressed in a report released last week by the National Academies of Sciences, Engineering, and Medicine (p. 218): that human nerve cells might enter animals’ brains and alter their mental capabilities. But that concern is moot for the chimeras in this study because they don’t have a nervous system. They “can’t experience pain and aren’t conscious,” says bioethicist Katrien Devolder of the University of Oxford. “If the human-monkey chimeras were allowed to develop further,” she says, “that would be a very different story.” ■

**The chimeras  
“can’t experience  
pain and aren’t  
conscious.”**

**Katrien Devolder,**  
University of Oxford



## SCIENTIFIC COMMUNITY

# NAS evaluates ejecting Marcy, Ayala for sexual harassment

First cases slowly proceeding 2 years after change in academy's bylaws allowed members to be ousted

By **Meredith Wadman**

**T**he U.S. National Academy of Sciences (NAS) is moving for the first time to expel sexual harassers from its membership. *Science* has learned that the institution is adjudicating complaints that could lead to the ejection of astronomer Geoffrey Marcy and evolutionary biologist Francisco Ayala.

The process is unfolding 2 years after the prestigious, 158-year-old academy changed its bylaws to allow expulsion of members. Until then, membership had been for life. Rescinding membership is the most drastic penalty under the new rules, which also allow for lesser sanctions.

With the potential moves against Marcy and Ayala, “We are watching social change happening in front of our eyes,” says Nancy Hopkins, an NAS member and emeritus biologist at the Massachusetts Institute of Technology. “It has been a long time coming.”

Scientists are elected to NAS by existing members and serve as advisers who develop reports for the U.S. government. NAS's 2342 U.S. members are on average 72 years old; 81% are men.

In June 2019, NAS changed its bylaws to allow a member to be ousted if an em-

ployer, funder, or other institution documented violations that breach NAS's Code of Conduct; that code bars “all forms of discrimination, harassment and bullying,” as well as plagiarism and other offenses (*Science*, 7 June 2019, p. 916). But no one came forward to complain about an alleged sexual harasser. In September 2020, François-Xavier Coudert, a computational chemist at CNRS, the French national research agency, read a news article in *Nature* noting that at the time the academy had received no such complaints.

Anyone can file a complaint, but Coudert says the idea of bringing the allegations himself “felt weird because I am not ... based in the U.S. and I know none of these people.” But after he called out NAS on Twitter, President Marcia McNutt responded: “FILE A COMPLAINT already.”

He did so on 21 September, in an email he provided to *Science*, alleging that four NAS members were guilty of sexual harassment: Ayala; Marcy; Sergio Verdú, an information theorist formerly at Princeton University; and Inder Verma, a cancer biologist formerly at the Salk Institute for Biological Studies. (Others later also filed complaints with NAS.)

Marcy was forced out of the University of California (UC), Berkeley, in 2015 after

BuzzFeed published details of the university's Title IX investigation finding him guilty of sexual harassment, including kissing and groping students. (Marcy repeatedly apologized for being a “source of distress” to women, but disagreed with some of their complaints. He did not respond to *Science*'s requests for comment on the NAS proceedings.)

Ayala was terminated from UC Irvine in 2018, after a Title IX investigation found that he had sexually harassed colleagues including making sexually suggestive comments and inviting a junior professor to sit on his lap (*Science*, 27 July 2018, p. 316). Ayala told *Science* last week that he “absolutely” denies the allegations. NAS Executive Director Ken Fulton wrote to Coudert in November that the academy had begun to adjudicate the cases of Ayala and Marcy.

In the case of Verma, *Science* in 2018 published accounts spanning 40 years from eight women who alleged he sexually harassed them; Verma denied the allegations (*Science*, 4 May 2018, p. 480). Salk also investigated, but kept its findings under wraps. That prevented NAS from moving forward, Fulton implied to Coudert. NAS requires official findings of sexual harassment by an organization with jurisdiction over an NAS member. “The NAS cannot act on the basis of media reports,” Fulton wrote.

Princeton dismissed Verdú in 2018 after a Title IX investigation concluded that he sexually harassed one of his graduate students, and a separate probe found he violated a policy prohibiting consensual relationships with students. He has denied both allegations. NAS is deferring action in the case pending the outcome of a lawsuit Verdú filed against Princeton, Fulton told Coudert.

NAS has received a complaint of sexual harassment against a fifth NAS member, which is also being held pending more information, McNutt says. (NAS keeps the names of accused members confidential.) NAS has also received three other complaints, alleging bullying, unspecified “non-scientific misconduct,” and raising an authorship dispute. All were dismissed for want of documentation, McNutt says.

The major impact of the new rules may be preemptive, McNutt thinks. “The biggest change I have witnessed is how much the members are taking into account the conduct of colleagues before putting them forward for membership,” she says.

Hopkins welcomes that information. “That’s very exciting and it’s a reflection of the change we want,” she says. “It used to be ‘Oh well, if someone’s a great scientist we will put up with anything.’” ■



# Researchers face attacks from Bolsonaro regime

Harassment, budget cuts leave many fearing for their jobs and safety

By **Herton Escobar**

**T**his month, scientists at the Chico Mendes Institute for Biodiversity Conservation (ICMBio), Brazil's lead agency for studying and managing the nation's vast protected areas, had to start abiding by an unwelcome new rule. It gives one of ICMBio's top officials the authority to review all "manuscripts, texts and scientific compilations" before they are published.

Researchers fear President Jair Bolsonaro's administration, which has a markedly hostile relationship with Brazil's scientific community, will use the reviews to censor studies that conflict with its ongoing efforts to weaken environmental protections. The administration says that is not the intent. But the move adds to recent developments that have rattled many Brazilian scientists and left some fearing for their jobs and even their physical safety.

"Science is being attacked on several fronts," says ecologist Philip Fearnside of the National Institute of Amazonian Research (INPA). "There is denial of the pandemic, denial of climate change, denial of deforestation; not to mention budget cuts."

Bolsonaro's grievances with scientists date back to the start of his administration in 2019. Then, he accused the National Institute for Space Research of "lying" about satellite data showing increased deforestation in the Amazon and fired its director, physicist Ricardo Galvão, after he defended the numbers. Since then, Bolsonaro has clashed with researchers over issues including his persistent rejection of science-based strategies for combating the COVID-19 pandemic, which has killed at least 355,000 Brazilians. Recently, the relationship has become even tenser.

In February, Brazil's anticorruption agency, the Office of the Comptroller General, informed epidemiologist Pedro Hallal, former rector of the Federal University of Pelotas, that he could be fired because he criticized Bolsonaro during an event in January. Hallal, who coordinates Brazil's largest COVID-19 epidemiology research project, had called Bolsonaro "despicable,"

citing the president's antivaccination rhetoric and his meddling in the selection of university rectors.

Hallal ultimately reached a settlement with the comptroller's office, promising not to "promote expression of appreciation or disapproval in the workplace" for 2 years. But he remains defiant. "If the idea was to silence me, I have to say it backfired," he says. "It's motivating me to be even more critical and say what needs to be said." But the climate is silencing colleagues, he says. "A lot of people are saying less than they would like to, for fear of retaliation."

Scientists are also reconsidering what they study and publish, says Marcus

(including *Science*), his cellphone and social media accounts lit up with threats. Then, in November 2020, he says he was attacked by a man driving what he thought was an Uber vehicle he had hailed; the man told Ferrante he "needed to shut up" and attacked him with a sharp object.

Last week, a group of Brazilian researchers cited safety concerns in explaining why they did not sign their names to a white paper, published by the Climate Social Science Network at Brown University, that outlines Bolsonaro's efforts to dismantle environmental protections. They decided to remain anonymous "for security reasons and considering the current political scenario in Brazil," they wrote.

At ICMBio, the new oversight rule adopted on 1 April gives review authority to the institute's biodiversity research director, one of four ICMBio directors who serve under the institute's president. In a statement, institute officials portrayed the order as simply a bureaucratic shift, noting that ICMBio's president previously had review authority. "There is no censorship," it states. But researchers note that none of the top ICMBio officials is a scientist trained to conduct technical reviews; all are former military police officers or firefighters.

A similar rule was issued last month at Brazil's Institute for Applied Economic Research, a major federal research center.

The political pressure comes on top of a deepening science funding crisis. Government spending on research has shrunk by some 70% from a 2014 peak, and Bolsonaro recently cut this year's overall science ministry budget by 29%.

The constant conflict is wearing down Brazilian researchers, says Mercedes Bustamante, an ecologist at the University of Brasília and co-founder of the Science and Society Coalition, a group created in 2019 to promote science-based policies. "I am so exhausted of having to defend myself all the time," she says. "Meanwhile, all the important issues that we really should be tackling are being left behind." ■

Herton Escobar is a journalist in São Paulo.



President Jair Bolsonaro (center), maskless despite Brazil's COVID-19 crisis, has a frosty relationship with the nation's scientific community.

Lacerda, an infectious disease specialist with the Oswaldo Cruz Foundation in Manaus, Brazil. Last year, he faced intense inquiries from federal prosecutors—and received death threats—after he published work on the health risks of treating COVID-19 patients with the drug chloroquine. (Bolsonaro promoted chloroquine despite evidence it is ineffective against COVID-19.) "A lot of people are afraid to publish after what happened to me," Lacerda says. Colleagues have abandoned COVID-19 studies, he adds, in order to avoid online harassment by what is known as Bolsonaro's "digital militia."

In one case, online harassment appears to have escalated to a physical attack. After biologist Lucas Ferrante, a doctoral candidate at INPA, published articles criticizing Bolsonaro's policies in high-profile journals

## PARTICLE PHYSICS

# Calculation could dim hopes for new physics

New prediction of muon's magnetism muddies interpretation of tantalizing measurement

By **Adrian Cho**

**T**alk about raining on your colleagues' parade. On 7 April, a collaboration of more than 200 experimenters announced to great fanfare that a particle called the muon is slightly more magnetic than predicted by physicists' standard model, a discrepancy that could signal new particles waiting to be discovered (*Science*, 9 April, p. 113). But on the same day, 14 theorists published a paper that suggests the consensus theoretical prediction is wrong. Their value sits closer to the experimental result and makes the tantalizing discrepancy nearly vanish.

"The standard model is just fine, according to our calculation," says Zoltan Fodor, a theorist at Pennsylvania State University, University Park, and the leader of the Budapest-Marseille-Wuppertal (BMW) collaboration, which produced the new theoretical result. However, others say it's too early to throw out the previous calculation, which is the product of decades of painstaking effort. "We can't immediately ignore everything we know and switch over to a single new result of a new method," says Christoph Lehner, a theorist at the University of Regensburg.

A heavier, unstable cousin of the electron, the muon acts like a tiny bar magnet, and its magnetism provides a means to dowse for hints of new particles. Quantum mechanics and relativity demand that the muon have a certain basic magnetism. Thanks to quantum uncertainty, particles and antiparticles also constantly flit in and out of existence around the muon. These "virtual" particles cannot be observed directly, but they can affect the muon's properties, including magnetism. Standard model particles should increase its magnetism by about 0.1%, and as-yet-unknown particles would add their own boost. Such particles might someday be blasted into existence at an atom smasher.

That's why physicists were so excited when the Muon g-2 experiment at Fermi National Accelerator Laboratory confirmed a 20-year-old hint that the muon is about 2.5 parts per billion more magnetic than the standard model predicts, according to the consensus value, hammered out

last year by the 132-member Muon g-2 Theory Initiative.

To make that prediction, the theorists had to account for the thousands of ways standard model particles can flit about the muon and affect its behavior. One family of processes, known as hadronic vacuum polarization, is especially challenging and limits the precision of the entire calculation. In it, the muon emits and reabsorbs particles known as hadrons, which consist of other particles called quarks. The theory of quarks and the strong nuclear force that binds them, quantum chromodynamics (QCD), is so unwieldy that theorists cannot calculate the effects through the usual

netism, albeit with sizable uncertainties.

Now, using hundreds of millions of processor hours at the Jülich Research Center in Germany, Fodor's group has produced a lattice calculation of the hadronic vacuum polarization and a value for the muon's magnetism that rivals the consensus standard model value in precision. And the new result is only one part per billion below the experimental value, the team reported in *Nature*. Given the uncertainties, that's too close to claim a discrepancy, Fodor says.

He also raises questions about the consensus value. For key data, it depends on results mainly from two colliders, and the two data sets disagree to a worrisome extent, Fodor says. His team's result is free of such uncertainties. "This is the only computation on the market, so some people are uncomfortable," he says.

Yet some theorists say it's too early to place so much weight on a single lattice calculation. Aida El-Khadra, a lattice theorist at the University of Illinois, Urbana-Champaign, and a leader of the Muon g-2 Theory Initiative, notes that the uncertainties in the consensus value reflect mainly the limited precision of the input data. In contrast, the uncertainties in the lattice value reflect the reliability of the method itself and are harder to quantify and interpret, El-Khadra says. "The meaning of the errors is very different," she says.

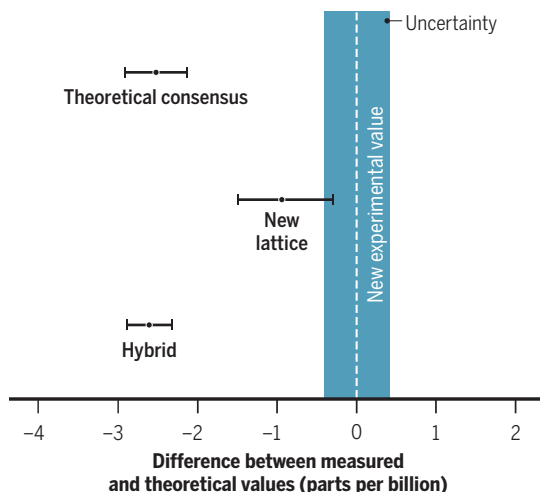
Also, in 2018 Lehner and colleagues performed an analysis combining accelerator data and a lower-precision lattice calculation. Their hybrid estimate of the muon's magnetism agrees well with the consensus prediction, Lehner says.

"The BMW result needs to be confirmed by other independent lattice calculations," says Alexey Petrov, a theorist at Wayne State University. Those high-precision calculations should appear within a year. But if the lattice results agree with one another, but not the data-driven approach, then theorists will still have to figure out why the two methods disagree, Petrov says.

Until then, it would be premature to say the tantalizing mystery raised by the g-2 measurements has been explained away, El-Khadra says. "The standard model calculation is solid," she insists. So, too, is the experimental value. And to the best of physicists' knowledge they're different. ■

## Never mind the gap?

If a new "lattice" value for the magnetism of the muon is correct, a mysterious gap between other predictions and a recent measurement would all but disappear.

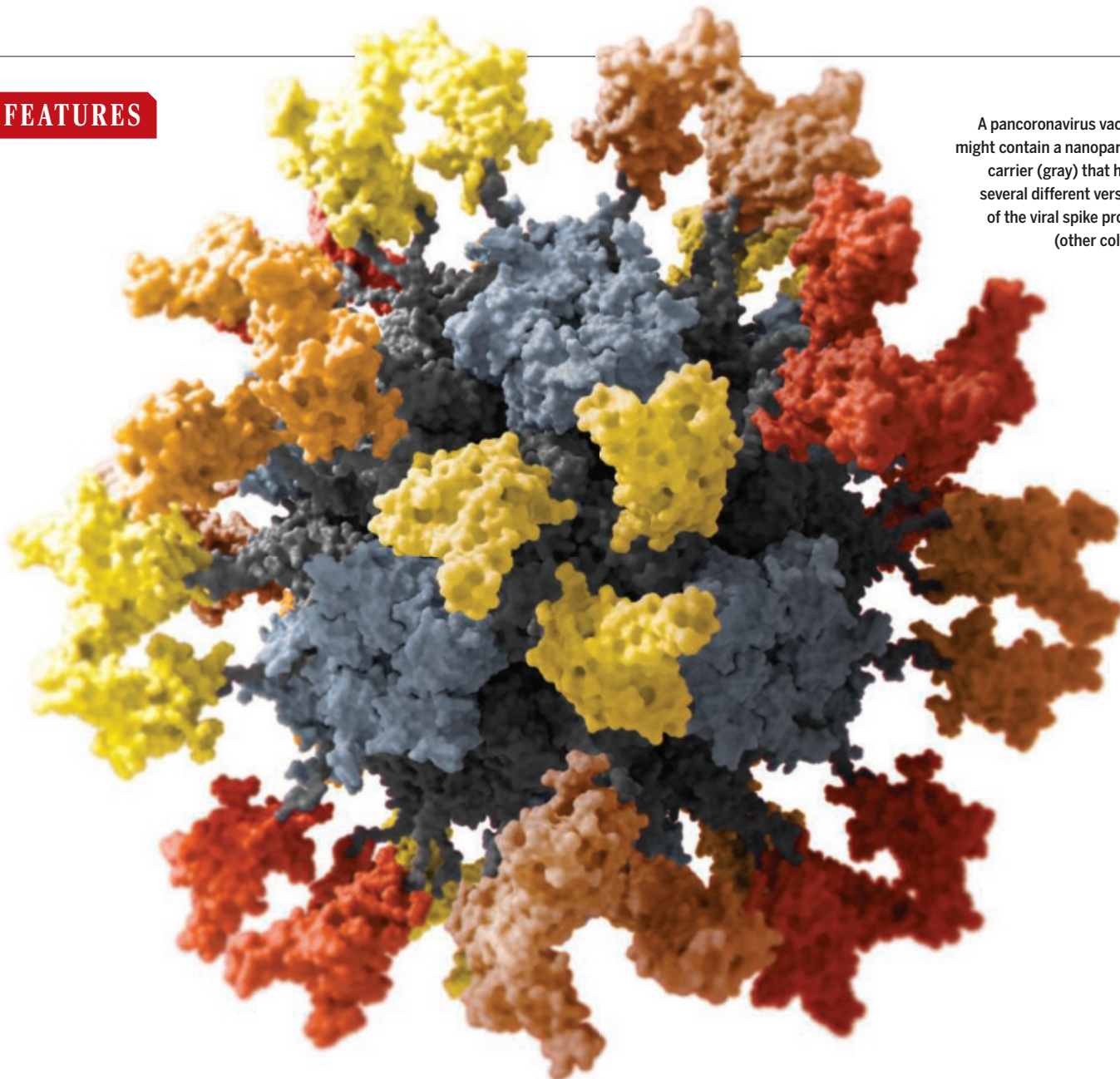


series of ever smaller approximations. Instead, they have to rely on data from accelerators that create hadrons by colliding electrons and positrons.

There is another way, however. Theorists can attempt brute-force QCD calculations on supercomputers, if they model the continuum of space and time as a lattice of discrete points occupied by quarks and particles called gluons, which convey the strong force. Twelve years ago, theorists showed this "lattice QCD" technique could calculate the masses of the proton and the neutron, which are both hadrons. Several groups have also applied the lattice to the muon's mag-



A pancoronavirus vaccine might contain a nanoparticle carrier (gray) that holds several different versions of the viral spike protein (other colors).



# THE DREAM VACCINE

Why stop at just SARS-CoV-2? Vaccines in development aim to protect against many coronaviruses at once

In 2017, three leading vaccine researchers submitted a grant application with an ambitious goal. At the time, no one had proved a vaccine could stop even a single beta coronavirus—the notorious viral group then known to include the lethal agents of severe acute respiratory syndrome (SARS) and Middle East respiratory syn-

By **Jon Cohen**

drome (MERS), as well as several causes of the common cold and many bat viruses. But these researchers wanted to develop a vaccine against them all.

Grant reviewers at the National Institute of Allergy and Infectious Diseases (NIAID) deemed the plan “outstanding.” But they

gave the proposal a low priority score, dooming its bid for funding. “The significance for developing a pan-coronavirus vaccine may not be high,” they wrote, apparently unconvinced that the viruses pose a global threat.

How things have changed.

As the world nears 3 million deaths from the latest coronavirus in the spotlight,

SARS-CoV-2, NIAID and other funders have had a major change of heart. In November 2020, the agency solicited applications for “emergency awards” to pursue pancoronavirus vaccine development. And in March, the Coalition for Epidemic Preparedness Innovations (CEPI), an international nonprofit launched in 2017, announced it would spend up to \$200 million on a new program to accelerate the creation of vac-

cines against beta coronaviruses, a family that now includes SARS-CoV-2.

The threat of another coronavirus pandemic now seems very real. Beyond bats, coronaviruses infect camels, birds, cats, horses, mink, pigs, rabbits, pangolins, and other animals from which they could jump into human populations with little to no immunity, as most researchers suspect SARS-CoV-2 did. “Chances are, in the next

10 to 50 years, we may have another outbreak like SARS-CoV-2,” says structural biologist Andrew Ward of Scripps Research, one of the scientists who submitted the 2017 proposal NIAID rejected.

The agency has not given out any of its new awards yet, but Ward’s lab is already pursuing a vaccine targeting a subset of beta coronaviruses. Some two dozen other research groups around the world have

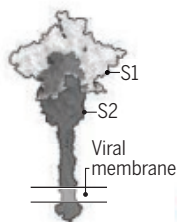
## Finding the best shot

Aiming to prevent a future pandemic like COVID-19, scientists are looking for ways to immunize people against many, if not all, coronaviruses. Several strategies for these pancoronavirus vaccines focus on spike, the surface protein common to all members of the viral family.

### The crown’s jewel

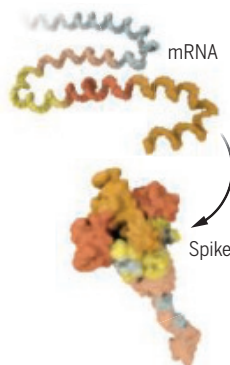
Spike initiates an infection when part of its head (S1) binds to a human cellular receptor and a viral enzyme cleaves spike so its stem (S2) can fuse with the cell. Spike varies between coronaviruses and the most conserved regions of its head or stem may serve as a broadly protective vaccine.

Variable Conserved



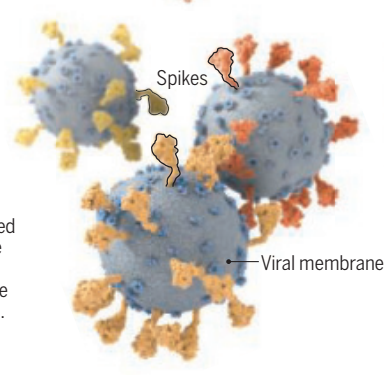
### Chimeric spike

A messenger RNA (mRNA) vaccine that combines spike gene sequences from SARS-CoV, SARS-CoV-2, and other coronaviruses can produce a mix of protein domains that may confer broad immune protection.



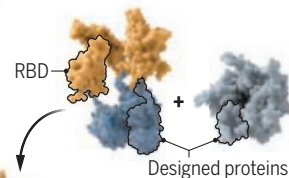
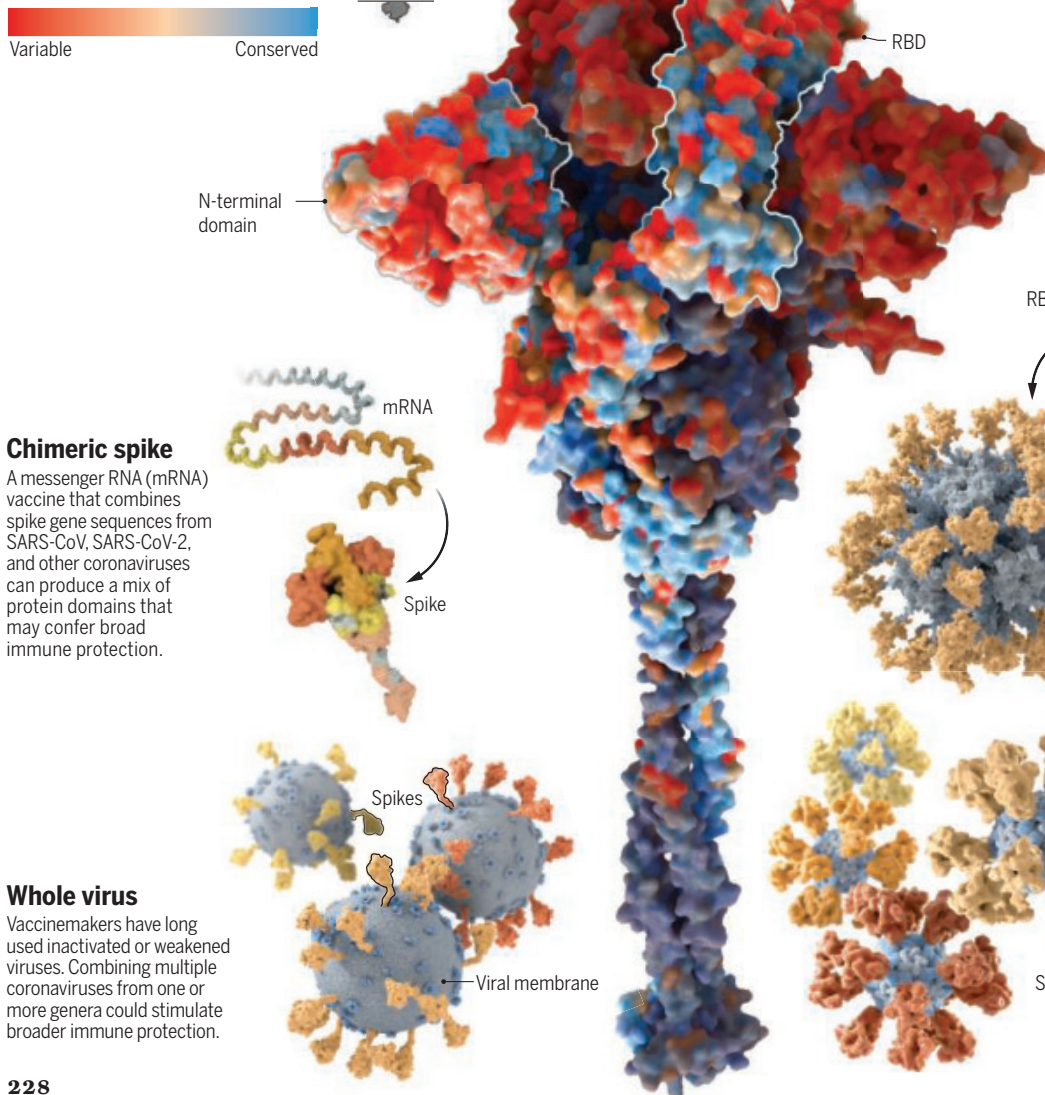
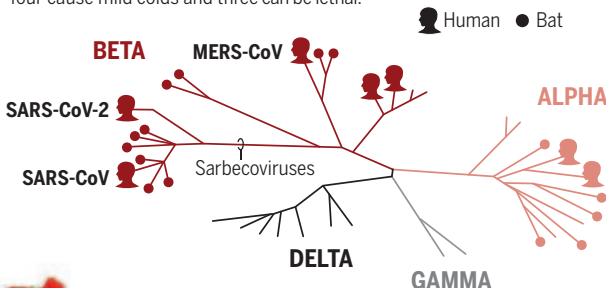
### Whole virus

Vaccinmakers have long used inactivated or weakened viruses. Combining multiple coronaviruses from one or more genera could stimulate broader immune protection.



## Family matters

Coronaviruses are grouped into four genera. They infect many species, although most have been found in bats. Of the seven known to infect people, four cause mild colds and three can be lethal.



### RBD nanoparticles

Because antibodies to spike’s receptor-binding domain (RBD) may be key to vaccine protection, scientists are assembling RBDs from multiple coronaviruses onto nanoparticles or into nanocages.

### Serial vaccines

One pancoronavirus vaccine approach would deliver a series of different spike proteins, each in its natural trimer configuration on a carrier particle.



similar pancoronavirus vaccine projects underway. Their approaches include novel nanocages arrayed with viral particles, the cutting-edge messenger RNA (mRNA) technique at the heart of proven COVID-19 vaccines, and cocktails of inactivated viruses, the mainstay of past vaccines. A few teams have even published promising results from animal tests of early candidates.

No pancoronavirus vaccine has entered human trials, and how to evaluate a candidate's protection against diseases that have not yet emerged remains a challenge. Nor is it clear how such a vaccine might be used. One possibility: keeping it in reserve until a new human threat emerges. "We might be able to prime everybody to get a basic level of immunity" against the emerging virus, buying time to make a more specific vaccine, Ward says.

Despite the many unknowns, the rapid success of vaccines against SARS-CoV-2 has sparked optimism. This coronavirus doesn't seem particularly difficult to foil with a vaccine, which raises hopes that the immune system can be trained to outwit its relatives, too. Survivors of SARS years ago provide more encouragement: Some of their antibodies—an immune memory of that viral encounter—can also stymie the infectivity of SARS-CoV-2 in lab dishes.

NIAID's Barney Graham, who helped develop Moderna's mRNA COVID-19 vaccine, shares the optimism about pancoronavirus vaccines. "Compared to flu and HIV, this is going to be relatively easy to accomplish," he predicts.

**EARLIER THIS YEAR**, Hannah Turner, a technician at Scripps Research who works with Ward, took a cold, hard look at a now infamous protein: SARS-CoV-2's spike, which enables the virus to infect cells and is at the heart of several successful COVID-19 vaccines. All coronaviruses have these spikes, which create the distinctive crown-like appearance that earned them their name, and most pancoronavirus vaccine efforts aim to rouse an immune response to some part of the spike protein.

On this February morning, Turner mixes labmade copies of the SARS-CoV-2 spike with "broadly neutralizing" antibodies harvested from COVID-19 patients. These antibodies powerfully prevent multiple variants of SARS-CoV-2, as well as the original SARS virus, SARS-CoV, from infecting susceptible cells in test tube studies. Turner then freezes the spike-antibody mixtures with liquid nitrogen and places the resulting crystals in a \$4 million microscope the size of three refrigerators. It begins bombarding the samples with up to 200 kilovolts of electrons to map the spike-

antibody complexes at atomic resolution—an increasingly popular technique called cryo-electron microscopy (cryo-EM).

What resembles a telescope view of lunar landscapes unfolds across four monitors. Turner's trained eye spots the crystallized spike proteins, clumped together in groups of three called trimers and studded with antibodies. She points out one of the fan-like structures. "It's pretty cool," she says. "This is what you want to see."

The computers over the next few days will sort through 1100 different angles of her sample, migrating the best views into software that creates a gorgeous "final map" of spike with an attached antibody, at a resolution that approaches 3 angstroms, just a tad thicker than a strand of DNA. By creating similar portraits of spikes from many different coronaviruses with broadly neutralizing antibodies bound to them, Ward hopes to identify short segments of the protein—so-called epitopes—key to that binding for all the pathogens. Those epitopes, Ward believes, are the key to designing a vaccine that can trigger a broad immune attack on coronaviruses.

**"Compared to flu and HIV,  
this is going to be  
relatively easy to accomplish."**

**Barney Graham,**

National Institute of Allergy and Infectious Diseases

An ideal pancoronavirus vaccine would protect us from all four of its genera—alpha, beta, gamma, and delta—but most researchers have more modest goals. "The further you go, the harder it gets" for a vaccine, says immunologist Dennis Burton of Scripps Research, who often collaborates with Ward.

Gamma and delta coronaviruses, mainly found in birds and pigs, are not known to infect humans, so vaccine developers have paid them little attention. There's more interest in alpha coronaviruses because two cause colds in humans. But it's the betas that attract the most effort, and in particular the sarbecoviruses, a subset that includes SARS-CoV-2 and SARS-CoV but not the more genetically distinct MERS and its relatives. Sarbecoviruses are Ward's targets, and Burton is optimistic. "We already know you can get pretty damn good antibodies that work against both SARS-CoV and -2," he says.

Ralph Baric of the University of North Carolina, Chapel Hill, who has studied coronaviruses for 35 years, sees this subgroup as the paramount threat. "That

SARS-CoV-2 is here doesn't mean that that's going to provide any kind of serious protection against another sarbecovirus from coming out of the zoonotic reservoirs," he says. And if a "SARS-CoV-3" jumped into a person infected with the current pandemic virus and created something more lethal by swapping genetic regions—and coronaviruses frequently recombine—that's the making of a Hollywood horror film.

**WARD AND OTHERS IN THIS** nascent field are following the lead of vaccine successes, for diseases from polio to human papillomavirus, that depend on combining components from multiple forms of a pathogen—up to 23 forms of a sugar molecule in a shot against pneumococcal disease, for example—to increase breadth of protection. Although Ward is still at the earliest stages of the design process, trying to identify the conserved viral targets he wants a vaccine to hit, structural biologist Pamela Bjorkman at the California Institute of Technology is a few steps further along. Her team has recently evaluated candidate pancoronavirus vaccines in mice.

Bjorkman and co-workers chose a portion of spike from a range of beta coronaviruses: SARS-CoV and SARS-CoV-2, a virus isolated from a pangolin, and five bat viruses. They used each virus' receptor-binding domain (RBD), the spike region that initiates an infection by docking onto angiotensin-converting enzyme 2 (ACE2), a protein on human cells. The RBD is the apparent target for most antibodies that thwart SARS-CoV-2.

Comparisons of the RNA genes encoding the spikes showed the top section of the RBD varied a great deal, but the lower part was conserved across the different viruses. So the investigators fashioned eight multimers—small proteins—from the conserved RNA sequences. Then, they fastened combinations of them onto the surface of a nanoparticle built from a bacterial protein to create various "mosaic" vaccines. In theory, a mosaic would produce antibodies that protected against the known viruses—and because the sequences are conserved, the vaccine might protect against distant relatives of those viruses as well.

Last year, Bjorkman and colleagues injected mice with some of their mosaic vaccines. They report in the 12 February issue of *Science* that in lab dishes, antibodies harvested from the mice powerfully neutralized the infectivity of a wide array of sarbecoviruses, including ones not used to make the vaccine.

Graham, who worked on pancoronavirus vaccines even before the pandemic, reasons that the whole trimer of spike

might stimulate better or broader immune protection than just the RBDs. His team has taken spike trimers from SARS-CoV-2 and two beta coronaviruses that cause human colds and placed them in malleable nanocages, made from two different proteins developed by computational biologist Neil King of the University of Washington (UW), Seattle. The NIAID group is also using a second scaffolding: nanoparticles created from ferritin, a blood protein that normally sequesters and releases iron.

In a third strategy, Graham envisions giving people a series of vaccines, each one containing trimers from a different member of the beta genus, to create a broad defense against the viruses. “It’s what we do right now for influenza, basically, only it is occurring over a lifetime instead of more deliberately in a shorter period of time,” he says. (The flu shot contains surface proteins from three or four strains of that virus, and as it mutates, vaccinemakers change the ingredients annually.)

By arraying spike proteins on nanoparticles, vaccine developers aim to follow the style of upscale restaurants, where presentation matters nearly as much as the food on the plate. The goal is to cater to the tastes of B cells, the immune cells that pump out antibodies. The cells identify foreigners using Y-shaped proteins called immunoglobulins on their surfaces. (When secreted, the same proteins are antibodies.) B cells respond most strongly when each arm attaches to a different epitope. King says nanocages are ideal for presenting epitopes this way. “We can control spacing and geometry [of the viral pieces] in a much more precise way than anybody could before,” he says.

The resulting B cell cross-linking primes legions of the cells to spit out what researchers have dubbed “superantibodies” for their remarkably high potency. These superantibodies add to a vaccine’s breadth of protection because even when they aren’t a perfect match to a strain, they still retain some neutralizing activity.

Baric’s group is exploring a different way to present diverse antigens. Rather than arranging them on scaffolds, the team uses mRNA coding for a chimeric protein that mixes and matches different parts of spike from distant human and bat sarbecovirus cousins. “Spike is really plastic, so it’s kind of a modular design,” Baric says. “You can move component parts around without any problem.” Four of these mRNA spike chimeras solidly protected mice from a variety of challenges with human and bat sarbecoviruses, Baric, Hayes, and colleagues reported in a bioRxiv preprint posted on 12 March.

Along with calculated strategies, luck can also aid the quest for a pancoronavirus vaccine. Barton Haynes and his team at Duke University, working with Baric’s group, recently designed a vaccine that contains a SARS-CoV-2 RBD in a ferritin nanoparticle. Intended as a booster dose for mRNA COVID-19 vaccines, it turned out to be far more versatile. In monkeys, it worked as intended against SARS-CoV-2. But much to the researchers’ surprise, antibodies taken from the vaccinated monkeys also neutralized SARS-CoV and two related bat coronaviruses in lab studies.

## “Chances are, in the next 10 to 50 years, we may have another outbreak like SARS-CoV-2.”

Andrew Ward, Scripps Research

A clue to this surprisingly broad protection came when the team isolated an antibody from a person who had recovered from SARS many years ago. It, too, could neutralize a wide range of sarbecoviruses—and it turned out to bind tightly to the same RBD used in their COVID-19 vaccine booster. A structural analysis of the antibody bound to the RBD shows it latches onto the domain’s side, not the top region favored by most vaccine-induced neutralizing antibodies.

Because this antibody doesn’t interfere with ones that attach to the top, Haynes thinks a vaccine designed to trigger it and more common neutralizing antibodies could provide a one-two punch to multiple viruses. He expects clinical trials of this idea could begin within 6 months.

**SOME GROUPS HAVE TURNED** their sights far from the RBD, in molecular terms. Spike has both a head, which includes the RBD, and a stem—known as S2—that varies little between coronaviruses. “The S2 subunit is by far the most conserved portion of coronavirus spike,” says Jason McLellan, a structural biologist at the University of Texas, Austin, who co-authored the failed grant proposal with Ward.

After spike lands on a human cellular receptor, a coronavirus enzyme slices off the head, or S1, to expose the stem. That then, yes, spikes the cell and initiates the fusion that allows the virus to unload its genetic cargo. Immune responses against S2 can derail that key process, even though the stem isn’t always visible enough normally to initiate them.

A few years ago, McLellan developed a vaccine from the S2 of the MERS virus that

protects mice from the virus as effectively as vaccines that feature the full spike. The antibodies produced by the vaccine also bind to, but do not neutralize, SARS-CoV, SARS-CoV-2, and a human cold beta coronavirus. McLellan’s lab is now conducting cryo-EM of antibody-stem conjugates, using S2 from SARS-CoV-2, to develop a vaccine for beta coronaviruses. “Our initial immunogens target all of S2, but we might want to refine that and target smaller portions,” McLellan says.

Like most developers of a pancoronavirus vaccine, McLellan is trying to rally antibody-producing B cells. A few groups, however, hope to also rouse the immune system’s other great army: T cells, which protect the body by destroying infected cells. On 18 May 2020 in *Nature*, Vir Biotechnology working with UW structural biologist David Veesler described an antibody, isolated from someone who had SARS in 2003, that neutralized infectivity of both SARS-CoV and SARS-CoV-2—but with help from T cells.

Although the antibody binds to the RBDs of spike of each virus, it does not block them from attaching to ACE2, cryo-EM showed. The groups instead found it may bind to the surface of immune warriors that educate T cells to destroy already infected cells. This “vaccinal effect” was first described more than 15 years ago in cancer research when scientists found that certain monoclonal antibodies can trigger killer T cells to eliminate tumors.

T cells are also central to the vaccine quest of Bette Korber, a computational biologist at Los Alamos National Laboratory. She designs algorithms to scour the genome sequences of beta coronaviruses, looking for regions of viral proteins that can trigger T cell responses, and that vary little among the different coronaviruses. Those conserved T cell epitopes, Korber says, might make a good vaccine.

She hopes to initially combine this T cell approach with a B cell strategy that would protect against all SARS-CoV-2 variants. It draws on an analysis of close to 1 million sequences of the virus now in databases to understand the “evolutionary space” of the pathogen—what changes could help it evade antibody responses and what mutations it cannot afford.

“You need to show the immune system what it needs to recognize to have breadth,” says Korber, who has applied similar techniques to designing vaccines for HIV, flu, and Ebola. Her collaborators plan to convert the sequences she selects into mRNA vaccines.

Finally, there’s an old-school approach to a pancoronavirus vaccine, one that should call into battle both B and T cells.





Structural biologist Andrew Ward studies the nooks and crannies of a coronavirus spike protein for features common to spikes in other members of the virus family.

NIAID's veteran flu researchers Matthew Memoli and Jeffery Taubenberger want to combine inactivated versions of representative coronaviruses from the four known lineages in the beta genus. Vaccines based on the entire virus help the immune system take "multiple shots at the target," Memoli explains, rather than focusing all the responses on spike or bits of it.

"Some antigens give you antibodies, some antigens may give you more T cell responses, some antigens may do both. Some antigens may be better at inducing mucosal immunity than systemic immunity," he says. "The reality is that the best vaccine is going to deliver antigens that induce all of these responses."

**HOW CAN DEVELOPERS** of pancoronavirus vaccines prove their shots protect against a hypothetical SARS-CoV-2? Baric highlights one hurdle: "You have to have a good panel of challenge viruses to actually begin to test these vaccines" in the lab. The U.S. government considers SARS-CoV, MERS, and many coronaviruses to be "select agents," subjecting labs that handle them to greater restrictions. Baric notes that his lab is one of the

few that has the biosecurity needed to grow and experiment with those coronaviruses.

Another regulation could ease the path. Created by the U.S. Food and Drug Administration in the wake of 9/11, when there was increased worry about engineered viruses or other biotreats, the "animal rule" says a therapy or vaccine can receive approval without an efficacy trial if the study cannot ethically or practically be done in humans. A pancoronavirus vaccine might establish its bona fides under that rule if it works in mice or monkey challenge studies against a variety of known coronaviruses, appears safe in humans, and is capable of triggering broadly neutralizing antibodies or other relevant immune responses in people.

If a pancoronavirus vaccine gets authorized, would countries create stockpiles to quickly extinguish an outbreak of a new virus? Or would they instead plan to rapidly start to produce the vaccine from its blueprint once that fresh threat is seen? Those are issues CEPI's initiative will explore, but there's a third, simpler option many in the field propose: using it in the current pandemic, as the ultimate booster shot to prevent potentially waning immunity and

protect against the menacing new variants of SARS-CoV-2 that keep emerging.

Efforts have already begun to develop second generation COVID-19 vaccines that could protect against those variants. But Haynes says this is a game of "whack-a-mole" that has no end in sight. "You're just waiting on the next variant to come up." He and others instead propose that a pancoronavirus vaccine could do double duty. If it can handle other members of the coronavirus family tree, it should have no problem dealing with variations of SARS-CoV-2, which are minor in comparison.


"Over time, it may be that the boosting will be with a vaccine that is more broadly protective," says Luciana Borio, who led a White House unit on medical and bio-defense preparedness and now works for a venture capital firm, In-Q-Tel, whose portfolio includes biotech companies.

That might help end the current pandemic and forestall the next one. "A broadly protective vaccine has the goal of preventing a pandemic from happening," Memoli says. "The issue we have is right now is if a completely new virus appears, we have nothing." ■



# INSIGHTS

## PERSPECTIVES



Gokyo lakes are the world's highest freshwater lake system located in Nepal, Asia. The beautiful, pristine, and sacred lake is vulnerable to climate change-induced natural hazards.

### HYDROLOGY

## Preparing for floods on the Third Pole

Satellite-based real-time monitoring is needed for Himalayan glacial catchments

By **Tanuj Shukla** and **Indra S. Sen**

**T**he mountains that include the Himalayan and adjacent ranges are the highest on Earth and have an average elevation of >4000 m and an area of ~595,000 km<sup>2</sup>. This region is also called the Third Pole or the Asian

water tower because it has the largest ice mass outside the polar regions. Increasing temperatures and human interventions have added stress on the region's hydrological sensitivity and have increased the risks of major flood events.

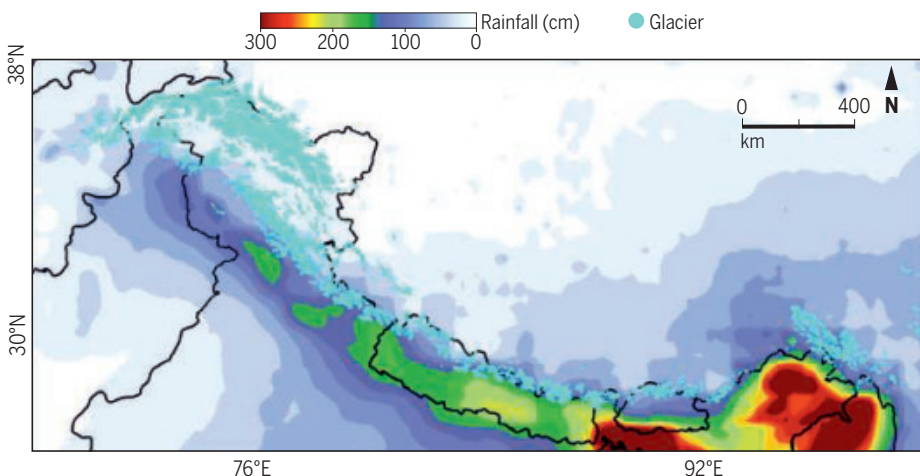
Over the next 100 years, an estimated 1.5°C of warming will likely be enhancing

the melting rates of glaciers, which have already been made fragile by climate change (1). This situation is evident from the accelerating glacier-ice mass loss, permafrost degradation, increasing extreme temperature and precipitation events, landslides, rapid snowmelt, and a substantial shift in seasonal riverine water supply (2, 3). Ad-



## Rainfall in the Himalayas

Glacial lake areas [glacier data from the Randolph Glacier Inventory (6)] are affected by the regional rainfall, which has had local variations from 2000 to 2015 (data source: [https://disc.gsfc.nasa.gov/datasets/TRMM\\_3B42\\_Daily\\_7/summary](https://disc.gsfc.nasa.gov/datasets/TRMM_3B42_Daily_7/summary)) (left). The increasing temperature in the Northern Hemisphere (top right) (data source: <https://data.giss.nasa.gov/gistemp/>) is correlated with an increased number of extreme rainfall events (middle right) (10, 11) and an expansion in the number of glacial lakes, some that are susceptible to glacial lake outburst floods (GLOFs), across the region (bottom right) (12).



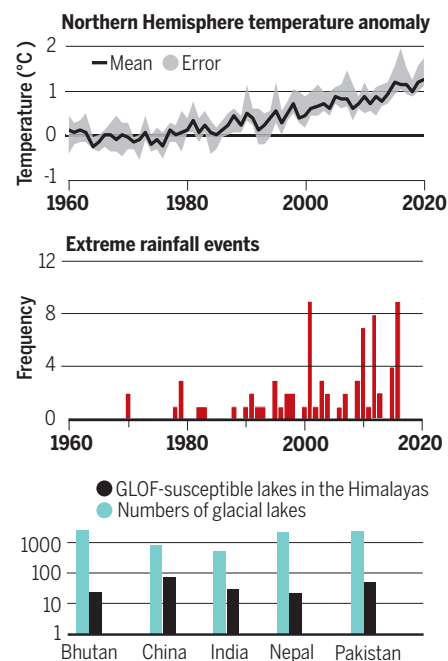
ditionally, the Indian Summer Monsoon is responsible for 300 cm year<sup>-1</sup> of annual rainfall over the south-facing slopes of the Himalayas (see the figure). All of these observations make the region prone to multiple natural hazards, including the increased risks of major flood events (3, 4). Direct human interventions on the rivers, such as the construction of hydroelectric power plants, change the risk profile in other ways (5).

Increasing concern has been centered around glacial lake outburst floods (GLOFs) and cloudburst events. GLOFs occur when either a natural dam bursts or the glacial lake level suddenly increases. These events are usually a result of cloudbursts, where torrential precipitation of >100 mm hour<sup>-1</sup> occurs over a geographical region of ~25 km<sup>2</sup>. These extreme events have increased in recent decades, as have the catastrophes associated with them (6). For example, the GLOF event in the Chorabari glacier valley (30°44'51.26'' N, 79°03'38.79'' E; 3808 m above sea level) in 2013 left behind a death toll of more than 5000 people and a shocking trail of devastation in the Mandakini River Valley. Unfortunately, more lake-breaching events are waiting to unfold because new lakes are continuously forming and the existing ones are expanding in the glaciated Himalayan valleys. Forty-one high-altitude lakes appeared in the Eastern Himalayan region alone during the past 50 years, and the existing lakes in the Third

Pole region have undergone a 50% expansion. The lake area has rapidly expanded, at a rate of 14.44 km<sup>2</sup> year<sup>-1</sup> between 1976 and 2018 (7). As a result, it is likely that the number, extent, and impacts of lake-breaching events in the Himalayas will increase in the near future.

The surge of meltwater in mountain streams is most commonly caused by cloudburst events during the monsoon season (June–July–August) time frame. However, the recent (7 February 2021), sudden surge of meltwater in the river tributary of the Ganga, Dhauli Ganga, during the dry season suggests that this time frame needs to be expanded. The catastrophe in the upper Dhauli Ganga basin is linked to processes other than precipitation events, such as snow avalanches, rock landslides, or other unidentified drivers. We therefore need to rethink the idea that cloudbursts and rainfall are the only drivers of a meltwater surge in the Himalayan region. Determining all of the potential major and minor drivers behind sudden surges of meltwater into headwater streams is vital for understanding the hazard profile of the region.

As we improve our understanding of glacial hydrology, different hypotheses will emerge. However, the most pressing need is to delve deep into mitigation strategies as risks of meltwater surges increase as a result of climate change and human-induced factors. Mitigation strategies should involve engineering solutions, such as the construction of flood-control reservoirs; structures to divert water from high-impact areas to alternative locations; rainwater detention



basins; the construction of dams, dikes, and embankments; the adoption of terraces and other good farming practices to reduce the rates of hillslope runoff; and the building of structures and development of techniques to stabilize mountain slopes to reduce landslides and mudflows. Together with these structural solutions, the community needs to be made aware of the causes and drivers of mountain hydrology through public awareness programs, training, and education. This may allow for a citizen-science approach for some flood risk-management measures to be implemented. Many of these efforts have already been implemented over the past few decades (8), but the magnitude of these flooding events requires a more advanced adaptive measure. In particular, an effective early warning system that would warn local communities of impending flood danger is urgently needed.

As a result, equal emphasis should be given to developing a network of hydro-meteorological, seismic stations and landslide-detection systems with telemetry capability to build a data-driven decision-support system. Particularly, data from the weather stations that record heavy rainfall events, ultrasonic and radar-based sensors that monitor water storage and discharge in lakes and streams, geophones that detect debris flow, and advanced avalanche-mapping technology should be transmitted in real time to support a decision system to warn local communities of the impending danger.

The biggest challenge for this strategy is the lack of cellular connectivity in the

remote Himalayan region that prevents telemetry support, rendering it unavailable. Instead, telemetry-based monitoring of the glacierized Himalayan catchment using satellite systems (e.g., the Narrowband Internet of Things) is needed to take timely actions during the next hydrological disaster. The integration of monitoring devices with satellite networks will not only provide telemetry support in remote locations that lack complete cellular connectivity but will also provide greater connectivity coverage in the cellular dead zones in extreme topographies such as valleys, cliffs, and steep slopes.

Real-time data would help to develop a strong network of early flood warning systems in the glacierized catchment of the Himalayas. Real-time monitoring technologies would not only help to predict and warn of the impending danger and prevent loss of life, but the availability of real-time data would allow scientists to monitor the performance of the installed instruments remotely and take timely actions against any instrument malfunction, preventing the loss of vital data. Therefore, these enriched datasets will help us to better understand the effects of climate change on the Third Pole, which is often regarded as a “white spot” on the global map—indicating the presence of very limited continuous field hydrometeorological data (9). ■

#### REFERENCES AND NOTES

1. P. D. A. Kraaijenbrink, M. F. P. Bierkens, A. F. Lutz, W. W. Immerzeel, *Nature* **549**, 257 (2017).
2. A. F. Lutz, W. W. Immerzeel, A. B. Shrestha, M. F. P. Bierkens, *Nat. Clim. Chang.* **4**, 587 (2014).
3. J. M. Maurer, J. M. Schaefer, S. Ruppert, A. Corley, *Sci. Adv.* **5**, eaav7266 (2019).
4. J. M. Maurer *et al.*, *Sci. Adv.* **6**, eaba3645 (2020).
5. I. Haddeland *et al.*, *Proc. Natl. Acad. Sci. U.S.A.* **111**, 3251 (2014).
6. R. Hock *et al.*, “High Mountain Areas” in *IPCC Special Report on the Ocean and Cryosphere in a Changing Climate* (2019).
7. G. Zhang *et al.*, *Remote Sens. Environ.* **237**, 11154 (2020).
8. A. B. Shrestha, G. C. Eze, R. P. Adhikary, S. K. Rai, *Resource Manual on Flash Flood Risk Management. Module 3: Structural Measures* [International Centre for Integrated Mountain Development (ICIMOD), 2012].
9. The Intergovernmental Panel on Climate Change, *Climate Change 2007: The Physical Science Basis* (Cambridge Univ. Press, 2013).
10. S. Nandargi, O. N. Dhar, *Hydrol. Sci. J.* **56**, 930 (2011).
11. A. P. Dimri *et al.*, *Earth Sci. Rev.* **53**, 225 (2017).
12. J. D. Ives, R. B. Shrestha, P. K. Mool, *Formation of Glacial Lakes in the Hindu Kush-Himalayas and GLOF Risk Assessment* (ICIMOD, 2010).

#### ACKNOWLEDGMENTS

This work was supported by the Department of Science and Technology (grant IUSSTF/WAQM-Water Quality Project-IIT Kanpur/2017) and the Ministry of Earth Sciences (MoES), Government of India (grant MOES/PAMC/H&C/79/2016-PC-II) to I.S.T.S. is thankful for a postdoctoral scholarship from the Indian Institute of Technology Kanpur. We thank V. Vinoj and K. Sri Harsha for their suggestions.

10.1126/science.abh3558

## QUANTUM GASES

# The Weyl side of ultracold matter

Ultracold gases in optical lattices provide control and tunability for the exploration of Weyl semimetal physics

By Nathan Goldman<sup>1</sup> and Tarik Yefsah<sup>2</sup>

**T**he discovery of Weyl semimetals in 2015 was a breakthrough in the modern history of quantum matter, connecting relativistic phenomena predicted in particle physics with unusual topological properties of the solid state (1). This connection originates from the peculiar band structure of Weyl materials. In general, the band structure of a solid governs which energies are accessible to an electron moving with a given momentum. In Weyl semimetals, energy bands touch at singular points (the Weyl nodes), around which energy has a linear dependence on momentum  $k$ , reminiscent of relativistic elementary particles. On page 271 of this issue, Wang *et al.* (2) realized Weyl-type band structures for ultracold atoms with a high degree of control and tunability. This work paves the way for the exploration of the properties of Weyl-type band structures with a bottom-up, tunable approach and incremental complexity.

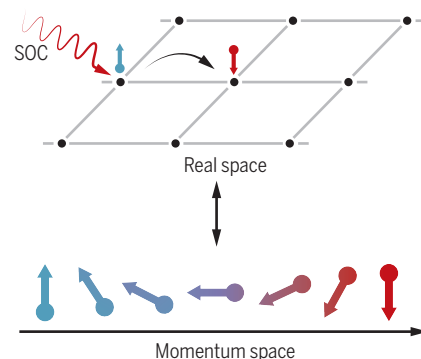
<sup>1</sup>Interdisciplinary Center for Nonlinear Phenomena and Complex Systems, Université Libre de Bruxelles, CP 231, Campus Plaine, B-1050 Brussels, Belgium. <sup>2</sup>Laboratoire Kastler Brossel, ENS-Université PSL, CNRS, Sorbonne Université, Collège de France, 24 rue Lhomond 75005 Paris, France. Email: tarik.yefsah@ikb.ens.fr

Whenever a concept of relativity finds an echo in the realm of quantum materials, it triggers a wave of astonishment and excitement. Indeed, relativistic phenomena are naturally linked to high-energy physics. The excitement comes from the possibility of bringing to reality predictions that otherwise may only be recognized for their mathematical esthetics. Herman Weyl's 1929 prediction of hypothetical massless fermions is a prime example because their existence was never confirmed in particle-physics experiments but was instead observed in solid-state quantum materials (1).

Observing “pseudo-relativistic electrons” in materials is not completely surprising, given the formal equivalence between the Dirac or Weyl equations describing relativistic elementary particles and the effective Schrödinger equation describing electronic excitations in semimetals (1). Beyond this formal analogy, the pseudo-relativistic band structure of Weyl semimetals also hosts a robust mathematical property, a so-called topological defect that cannot be removed under small deformations of the crystal (1). To appreciate this notion, one should first realize that a fictitious “magnetic” field (also called Berry curvature) can be associated with the energy bands of crystalline struc-

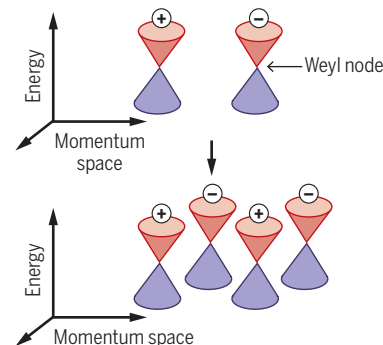
## Tunable Weyl nodes for ultracold atoms

The engineering of Weyl-type band structures in optical lattices relies on correlating the spin and momentum of the atoms along all three spatial directions. By realizing such a spin-orbit coupling (SOC), Wang *et al.* formed and tuned a Weyl-type band structure for ultracold rubidium atoms.



### Tuning spin-orbit coupling

Cold atoms in two internal states (spin-up and spin-down) move on a three-dimensional (3D) optical lattice in the presence of laser-induced SOC. Tomography was used to extract the spin texture in momentum space.



### Varying Weyl points

Tuning 3D SOC modifies the band structure and creates configurations with different numbers of Weyl nodes. Nodes always come in pairs with opposite topological charges (+ and -).



tures (3). In the vicinity of a Weyl node, this fictitious magnetic field emanates radially. This structure implies the existence of a fictitious monopole (a point-like source of fictitious magnetic field) that is located exactly at the Weyl node.

The key ingredient for the emergence of Weyl-type band structures is spin-orbit coupling (SOC) (1), which is an interplay between the intrinsic angular momentum of a particle (spin) and its trajectory. Spin-orbit coupling can create band structures with strong correlations between the momentum and spin of electrons and give rise to a variety of topological quantum states of matter (3). However, not all SOC are equivalent: Emerging topological properties crucially depend on the dimensionality of both the SOC and the material (3). In the case of Weyl semimetals, three-dimensional (3D) SOC is required and, as is often the case in solid-state physics, the path to the 2015 discovery relied on the identification of the “right” materials. Since then, much effort has focused on finding materials displaying only a few Weyl nodes, and ideally only a single pair, the minimum number allowed by the so-called doubling theorem (1).

Synthetic lattices for ultracold atomic gases allow Weyl-type band structures to be built by putting in the right ingredients (4), rather than search for new materials. Wang *et al.* not only created a band structure on-demand with either one or two pairs of Weyl nodes, but they also dynamically turned a trivial band structure into a Weyl-type one. They set ultracold atomic clouds of rubidium-87 in their designed laser landscape that both provides a 3D lattice potential that mimics the crystalline structure of solids and couples the motion of the atoms to their spin in all three spatial directions. Its Weyl-semimetal band structure was revealed by performing tomography of the 3D momentum distribution of the atoms while keeping track of their spin texture (see the figure).

With the spin-momentum distribution at hand, they probed the topological nature of the band structure; namely, the monopole charge associated with each Weyl node. The tunability of the setup allowed the effects of a sudden change in the system's parameters to be studied. Starting from atoms initially placed in a regular lattice configuration without 3D-SOC, they suddenly activated the Weyl semimetal lattice and followed the spin-population dynamics in the band structure. This provided a complementary measure of the Weyl-nodes location. Further studies with ultracold gases could explore special surface modes, previously revealed in the solid state (5) and photonics (6), whose robustness directly follows from the topological nature of the Weyl nodes. The spec-

troscopic detection of these Fermi-arc states could be facilitated by confining the atoms in a box with sharp boundaries (7, 8).

Cold-atom realizations of Weyl semimetals could offer an ideal platform to study their exceptional transport properties. Subjecting them to synthetic electric and magnetic fields should induce a so-called chiral anomaly, a quantized transport of particles from one Weyl node to the other (1). This anomaly is subtle in the context of particle physics, but it could be directly measured in optical lattices through momentum-distribution measurements (9). The chiral anomaly can also be induced by axial gauge fields generated by modulating the optical lattice in space and time (10). Weyl semimetals also exhibit anomalous Hall and circular photogalvanic effects (1) that could both be revealed in optical-lattice setups through circular shaking (11). The tunability of this setting could be exploited to engineer various types of semimetals displaying exotic nodal lines, rings, or spheres in the band structure (12, 13). Synthetic 3D SOC also constitute a central ingredient for the engineering of 3D topological insulators with cold gases (3).

Promoting a 3D optical lattice to a fictitious 4D lattice could also be envisaged through the concept of synthetic dimension (14)—for example, by inducing motion along the space spanned by atomic internal states. Applying this strategy could produce a 4D Weyl semimetal that displays fictitious Kalb-Ramond monopole fields originally introduced in string theory (15). Another exciting possibility would be to engineer 4D topological insulators (14), which have the appealing property of displaying a single isolated Weyl node on their surfaces. ■

#### REFERENCES AND NOTES

1. N. P. Armitage, E. J. Mele, A. Vishwanath, *Rev. Mod. Phys.* **90**, 015001 (2018).
2. Z.-Y. Wang *et al.*, *Science* **372**, 271 (2021).
3. X.-L. Qi, S.-C. Zhang, *Rev. Mod. Phys.* **83**, 1057 (2011).
4. N. R. Cooper, J. Dalibard, B. Spielman, *Rev. Mod. Phys.* **91**, 015005 (2019).
5. S.-Y. Xu *et al.*, *Science* **349**, 613 (2015).
6. B. Yang *et al.*, *Nat. Commun.* **8**, 97 (2017).
7. T. Dubček *et al.*, *Phys. Rev. Lett.* **114**, 225301 (2015).
8. J. Y. Choi *et al.*, *Science* **352**, 1547 (2016).
9. S. Roy *et al.*, *Phys. Rev. B* **94**, 161107(R) (2016).
10. S. Roy *et al.*, *2D Mater.* **5**, 024001 (2018).
11. D. T. Tran, A. Dauphin, A. G. Grushin, P. Zoller, N. Goldman, *Sci. Adv.* **3**, e1701207 (2017).
12. B. Song *et al.*, *Nat. Phys.* **15**, 911 (2019).
13. G. Salerno, N. Goldman, G. Palumbo, *Phys. Rev. Res.* **2**, 013224 (2020).
14. T. Ozawa, H. M. Price, *Nat. Rev. Phys.* **1**, 349 (2019).
15. G. Palumbo, N. Goldman, *Phys. Rev. Lett.* **121**, 170401 (2018).

#### ACKNOWLEDGMENTS

N.G. acknowledges A. Grushin for discussions on the chiral anomaly and the Fund for Scientific Research (FRS-FNRS) (Belgium) and the European Research Council (Starting Grant TopoCold) for financial support.

#### NEUROSCIENCE

## Mosaic synapses in epilepsy

### Mismatch of synaptic cadherins perturbs hippocampal circuitry

By Belal Shohayeb and Helen M. Cooper

**T**he inherited X-linked early-onset childhood epilepsy, called EFMR (epilepsy and mental retardation limited to females), has baffled clinicians and geneticists for more than 50 years. In contrast to other X-linked disorders in which the hemizygous (hemi) male, but not the heterozygous (het) female is affected, it is only the het females that exhibit seizures and intellectual disability (1, 2). Clues to the origin of this enigmatic disorder came when deleterious mutations in the X chromosome gene protocadherin-19 (*PCDH19*), which encodes a cell adhesion molecule, were identified (3). On page 255 of this issue, Hoshina *et al.* (4) provide answers to two pieces of the EFMR puzzle: They reveal that hippocampal synaptic transmission is compromised in *Pcdh19* het female mice but not in hemi males, and they provide a molecular explanation for how the retention of one wild-type (WT) allele, but not the loss of both alleles, disrupts neuronal connectivity.

In general, females with X-linked disorders are asymptomatic because they carry one WT allele. Conversely, hemi males only express the mutated gene and are unable to produce a functional protein. What accounts for the EFMR sex reversal? Important insight came with the identification of idiopathic males with EFMR symptoms (5). Affected males carried postzygotic somatic *PCDH19* mutations, and therefore regions within the developing brain that normally express *PCDH19* comprise a mixture of *PCDH19*-positive and -negative (has a non-functional *PCDH19* allele) neurons. To ensure appropriate levels of gene expression, females undergo X-inactivation in which one X chromosome is silenced. Females heterozygous for *PCDH19* mutations will therefore also exhibit somatic mosaicism due to ran-

dom X-inactivation in individual cells. This raises the question of how the coexistence of PCDH19-positive and -negative neurons might perturb brain development.

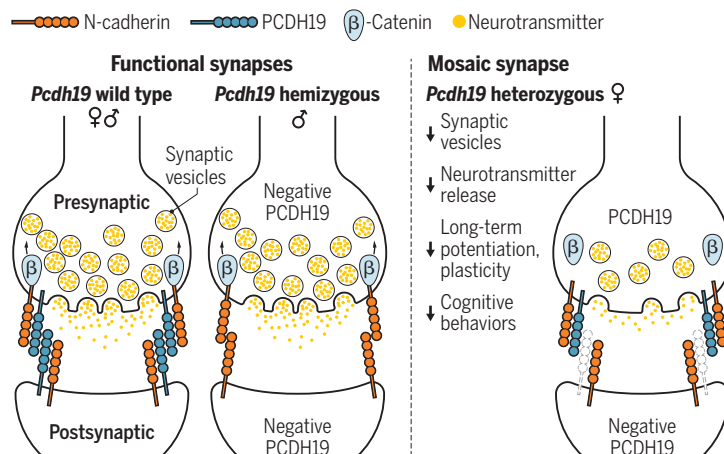
In EFMR, seizures begin at ~10 months of age and dissipate in adolescence (1, 2). *PCDH19* is expressed in the developing hippocampus and neocortex, brain regions associated with higher-order functions such as cognition and memory, and is highly expressed when synapses are forming after birth. However, its role in the establishment of neuronal circuitry remains poorly understood. Hoshina *et al.* focused on the hippocampal mossy-fiber pathway, which plays a central role in memory and mood regulation and has been implicated in some epilepsies (6, 7). In this pathway, the excitatory dentate granule cells receive input from the entorhinal cortex and form mossy-fiber synapses on CA3 pyramidal neurons.

Hoshina *et al.* found a reduction in the size of the presynaptic compartment as well as a depletion in synaptic vesicles in *Pcdh19* het female mice but not hemi males or WT females. The CA3 postsynaptic compartment as well as mossy-fiber axon targeting and synaptic density were not affected in het females. These data suggest that the presence of PCDH19 on only one side of the synaptic cleft may directly affect presynaptic function. Electrophysiological recordings confirmed that the efficiency of neurotransmitter release was compromised in het females. Moreover, the induction of long-term potentiation (LTP), an electrophysiological correlate of presynaptic function and thus memory formation, was completely abolished at the het synapse. The authors also found that het females displayed clear behavioral deficits that were consistent with mossy synapse dysfunction, unlike WT females and hemi males.

These findings strongly suggest that the existence of PCDH19 mosaic synapses has detrimental consequences for presynaptic development and thus hippocampal function. How does this PCDH19 synaptic mismatch perturb mossy-fiber synapses? To explain the unusual mode of inheritance for EFMR, the “cellular interference” hypothesis has been proposed and emerges from the homophilic adhesive binding properties of the protocadherins (1, 5). This model postulates that in mosaic individuals, PCDH19-positive cells are

## Synaptic mosaicism

Deleterious mutations in the X-chromosome gene protocadherin-19 (*PCDH19*) cause epilepsy and mental retardation limited to females (EFMR). In female mice, loss of PCDH19 function (negative PCDH19) in some cells, but not others (mosaicism), leads to mismatched synapses. It is proposed that N-cadherin homophilic adhesion is prohibited between PCDH19-positive and -negative neurons, which prevents presynaptic development.



unable to establish adhesive interactions with PCDH19-negative cells, disrupting tissue cohesion. In hemi males, however, cell-cell adhesion is restored because of the compensatory activity of other protocadherin family members.

Armed with this information, Hoshina *et al.* tested the validity of this hypothesis in the context of the mossy-fiber synapse. Homophilic binding of the classical cadherin N-cadherin promotes adhesion between the pre- and postsynaptic membranes to initiate synapse formation (8). Moreover, N-cadherin forms cis heterodimers with PCDH19 (9). The authors therefore suspected that PCDH19–N-cadherin heterodimer mismatches may underpin synapse dysfunction. They showed that N-cadherin colocalized with PCDH19 in 80% of WT female mossy-fiber synapses but only in 40% of het female synapses and never in hemi males. In parallel, recruitment of  $\beta$ -catenin (a downstream effector of N-cadherin) to the N-cadherin cytoplasm was significantly reduced only in het synapses. N-cadherin– $\beta$ -catenin interactions were therefore retained when PCDH19 was lost from both the pre- and postsynaptic membrane or, conversely, when it was present on both membranes. Further studies showed that increasing the level of N-cadherin expression at mismatched synapses restored presynaptic development and LTP induction.

The authors propose a plausible mismatch model to explain how PCDH19 mosaicism at the mossy-fiber synapse elicits cognitive deficits in EFMR individuals (see the figure). In WT females, trans-synaptic signaling through homophilic adhesion between PCDH19–N-cadherin heterodimers

on opposing membranes promotes  $\beta$ -catenin-mediated presynaptic signaling and development. In hemi males, N-cadherin homophilic adhesion is still permitted when PCDH19 is completely absent, triggering  $\beta$ -catenin signaling. In the mosaic synapse, however, N-cadherin homophilic adhesion is prohibited between PCDH19-positive and -negative compartments, leading to compromised presynaptic development and cognitive impairment. Given that many members of the protocadherin family are involved in cell-cell recognition during brain development (10), this raises the question of whether protocadherin–N-cadherin trans-adhesion is a

general mechanism for ensuring that the correct pre- and postsynaptic partners initiate synapse formation.

One perplexing aspect of this study is that *Pcdh19* het female mice do not exhibit seizures. The dentate granule neurons are excitatory, and their hyperactivity contributes to some epilepsies (6, 11). Paradoxically, the study of Hoshina *et al.* shows that PCDH19 synaptic mismatch leads to reduced synaptic activity. So, does PCDH19 synaptic mismatch initiate or propagate epileptogenic activity? In humans, the mossy-fiber pathway is embedded in complex neuronal circuitry that imposes finely tuned excitatory and inhibitory regulation on granular cell activity and downstream neuronal networks (6, 11). Thus, PCDH19 synaptic mosaicism is likely to have more profound consequences for the hippocampal and cortical circuitry of affected patients. How PCDH19 synaptic mismatch is manifested across complex human neuronal circuitry is an important topic for future studies. ■

## REFERENCES AND NOTES

1. J. Gecz, P. Q. Thomas, *Curr. Opin. Genet. Dev.* **65**, 169 (2020).
2. K. L. Kolc *et al.*, *Mol. Psychiatry* **24**, 241 (2019).
3. L. M. Dibbens *et al.*, *Nat. Genet.* **40**, 776 (2008).
4. N. Hoshina *et al.*, *Science* **372**, eaaz3893 (2021).
5. C. Depienne *et al.*, *PLoS Genet.* **5**, e1000381 (2009).
6. J. J. Botterill *et al.*, *Cell Rep.* **29**, 2875 (2019).
7. Y. Senzai, *Neurosci. Res.* **140**, 43 (2019).
8. E. Seong, L. Yuan, J. Arikath, *Cell Adhes. Migr.* **9**, 202 (2015).
9. M. R. Ermond *et al.*, *J. Cell Biol.* **195**, 1115 (2011).
10. S. E. W. Light, J. D. Jontes, *Semin. Cell Dev. Biol.* **69**, 83 (2017).
11. A. D. Bui *et al.*, *Science* **359**, 787 (2018).

## ACKNOWLEDGMENTS

This work was supported by the National Health and Medical Research Council of Australia (grant 1181459).

10.1126/science.abh3555



# Ecological stasis on geological time scales

Communities and functional structure persist for millions of years in a mammal fauna

By **Peter D. Roopnarine** and  
**Roxanne M. W. Banker**

**T**he rise and decline of organismal lineages dominate our view of life's history. Less appreciated is the persistence of ecological communities for tens of millions of years (1). On p. 300 of this issue, Blanco *et al.* (2), analyzing a series of mammalian faunas spanning the past 21 million years of the Iberian Peninsula, demonstrate increasing persistence of functional systems over time and the decoupling of those systems from species composition and duration. This study adds to a growing body of evidence that community structure is fundamentally important to ecosystem persistence (3).

The Blanco *et al.* study spans a time of dynamic environmental changes. Mild climates of the middle Miocene contributed to the expansion of forest habitats on the peninsula and the immigration of Eurasian faunas (4), followed by a transition to more seasonal climates and the expansion of grasslands (5). The authors defined 169 communities with an average duration of 0.1 million years. Species within each community were aggregated into functional units according to body size, diet, and locomotion. Applying a network-based approach, they identified taxonomic and functional modules shared across communities based on significantly co-occurring species or functional traits, respectively. Durations of taxonomic modules were brief—0.9 million years on average. Functional modules, however, were more persistent, having a mean span of 2.8 million years. Three long-lived communities, identified on the basis of shared faunal modules and called “functional faunas,” subdivide the data temporally.

These successive faunas lasted 2.58 million, 4.66 million, and 9.37 million years,

respectively, representing associations of functional traits that persisted against backdrops of high species turnover. Species turnover occurred only within each fauna's functional structure. The authors interpret this as structure excluding new species on the basis of their functional traits. The transition between functional faunas was in each case associated with major climatic shifts, extinction, and the introduction of new species with functional traits more suited to the new climatic conditions. Extinction rates were not increased during transitions, and species extinctions were more dependent on collapsing functional structures.

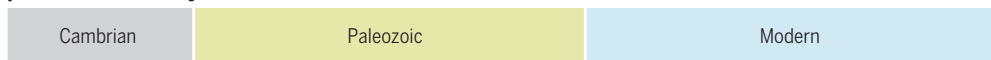
end-Permian and Middle Triassic terrestrial communities in the Karoo Basin of South Africa was marked by several short-lived communities (6). Models of those systems suggest that they would have been unstable and easily replaced by alternatively structured systems, which they were by the Middle Triassic. Their geological transience, however, corresponds to tens of millennia, suggesting that functionally “inferior” systems can persist for considerable intervals on ecological time scales.

Species' functional properties both affect and are affected by the network in which they are embedded. Species' evolution may

## Intervals of static ecological associations at multiple scales

Persistent communities can be seen at multiple taxonomic and temporal scales: Devonian (9), Permian-Triassic (6), and the past 21 million years (Blanco *et al.*). Times for persistent communities are not to scale. Vertical bars show transitions between communities, and patterned intervals are post-mass extinction transitional systems.

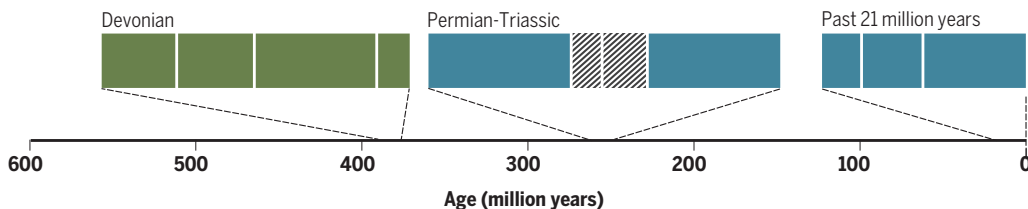
### Sepkoski's evolutionary faunas



### Boucot-Sheehan ecologic evolutionary units



### Persistent communities



Furthermore, the transitions between faunas were abrupt. There were no transient or intermediate faunas to suggest that new faunas were reorganizations of their predecessors rather than replacements.

Blanco *et al.* bolster ideas that the addition of new species to a system, and the extinction of species during crises, are dictated by existing functional structures (6). Indeed, it has been suggested that system dynamics act as agents of selection on species within a system (7). Although transitional faunas were absent in the Iberian series, the transition between persistent

therefore be constrained by the systems to which they belong. System persistence itself is likely the result of diffuse coevolutionary interactions (8) that developed over long, abiotically stable intervals. Differential persistence between systems is based on functional diversity (2), functional redundancy, and the configuration of interactions among functions (6). Features determining the processes and feedbacks of a system may ultimately subject systems to selection (9), from which patterns of persistence emerge.

The shortest-lived types of persistent systems are those based on unchanging

Department of Invertebrate Zoology and Geology,  
California Academy of Sciences, San Francisco, CA 94118,  
USA. Email: proopnarine@calacademy.org

taxonomic composition (10). A hierarchy emerges, however, when definitions are broadened to include ecological traits and processes (see the figure). The largest are Sepkoski's marine evolutionary faunas (11), followed by the ecologic evolutionary units of Boucot and Sheehan (1, 12, 13). Regardless of the hierarchical level at which a system is defined, common features exist across multiple scales when systems are defined functionally and ecologically: Systems last longer than species (12, 13), and species turnover is more rapid and often decoupled from system persistence. The end of a system is marked by species extinction, which is often associated with external abiotic drivers (1). Transitions between systems are abrupt relative to typical system duration, marked either by the absence of structurally intermediate systems, as shown by Blanco *et al.*, or by new systems of short duration (6).

## “Systems last longer than species, and species turnover is more rapid and often decoupled from system persistence.”

Thus, persistent paleoecological systems warrant examination beyond genealogical dynamics, but documentation and analysis using the fossil record are challenging, leaving outstanding questions. How do persistent systems arise, why do they eventually fail (6), and why are some more persistent than others (8)? Addressing these questions from a systems-based perspective is key to understanding processes of community assembly and persistence that exist across hierarchical, temporal, geographical, and spatial scales. ■

### REFERENCES AND NOTES

1. P. M. Sheehan, *Geol. J.* **36**, 231 (2001).
2. F. Blanco *et al.*, *Science* **372**, 300 (2021).
3. M. Loreau, *From Populations to Ecosystems: Theoretical Foundations of New Ecological Synthesis* (Princeton Univ. Press, 2010).
4. J. L. Cantalapiedra, M. S. Domingo, L. Domingo, *Sci. Rep.* **8**, 13413 (2018).
5. J. T. Eronen *et al.*, *Proc. Natl. Acad. Sci. U.S.A.* **106**, 11867 (2009).
6. P. D. Roopnarine, K. D. Angielczyk, A. Weik, A. Dineen, *Earth Sci. Rev.* **189**, 244 (2019).
7. P. D. Roopnarine, K. D. Angielczyk, in *Evolutionary Theory. A Hierarchical Perspective* (Univ. of Chicago Press, 2016), chap. 13.
8. T. M. Lenton *et al.*, *Trends Ecol. Evol.* **36**, 333 (2021).
9. L. R. Fox, *Ecol.* **69**, 906 (1988).
10. C. E. Brett, L. C. Ivany, K. M. Schopf, *Palaeogeogr. Palaeoclimatol. Palaeoecol.* **127**, 1 (1996).
11. J. J. Sepkoski Jr., *Bull. Am. Paleontol.* **363**, 1 (2002).
12. A. J. Boucot, *J. Paleontol.* **51**, 1 (1983).
13. P. M. Sheehan, *Palaeogeogr. Palaeoclimatol. Palaeoecol.* **127**, 21 (1996).

10.1126/science.abh2853

### GENOMICS

# The gut microbiomes of 180 species

Animal microbiomes are a treasure trove of previously unknown bacteria and genes

By Abigail L. Lind and Katherine S. Pollard

**M**icrobial life is ubiquitous in most environments on Earth, including in the gastrointestinal tract of animals. The composition of these collections of microbes, called the microbiota, can differ dramatically between individuals and species. Across the animal tree of life, these microbiotas contain a broad array of microbial diversity. Animal gut microbiota composition is more similar when hosts share diet or genetic ancestry, especially in mammals; the correlation of microbiota composition with genetic ancestry is weaker in fish, reptiles, birds, and invertebrates (1–4). In many cases, gut microbes contribute to key host processes, including metabolizing specialized dietary compounds (5). On page 264 of this issue, Levin *et al.* (6) interrogate the microbes that inhabit the animal gut by sequencing fecal samples from ~180 wild and captive species across the animal tree of life. Most of the bacterial species and genes they found have not been described before.

This massive compendium includes 406 samples from mammals, reptiles, birds, fish, and some invertebrates collected at six different sites globally, with the highest sampling in Israel and Uganda. The animals span a variety of feeding patterns and behavioral traits, although they are predominantly terrestrial vertebrates. The key contribution of Levin *et al.* is the use of whole-metagenome sequencing, as opposed to the single-gene amplicon sequencing that has yielded much of our current understanding of animal gut microbiome (microbial genomes) composition across diverse groups (5). Whole-metagenome sequencing differs from amplicon sequencing in that it involves sequencing all of the DNA present in a sample rather than selecting for a specific piece, as in the case of the 16S ribosomal RNA gene in amplicon sequencing. One major advantage of the whole-metagenome approach is that whole or partial genomes, called metagenome-assembled genomes (MAGs),

can be reconstructed by sorting and piecing together the sequencing reads themselves, a process called binning and assembling. Increasingly large numbers of MAGs are being generated from environmental, human, animal, and plant sources, which has revolutionized our understanding of the function, ecology, and evolution of host-associated and environmental microbiotas (7, 8).

Levin *et al.* find that most of the reads they sequence from animal microbiomes cannot be mapped to existing reference databases, highlighting the unexplored diversity of animal microbiomes. They use their sequencing reads to assemble more than 5000 MAGs from 1209 bacterial species, of which 75% are uncharacterized. This unexplored microbial diversity in animals stands in contrast to the well-studied human microbiome, which is much better represented by reference databases. The animal microbiota species are distributed across the bacterial tree of life, with the highest enrichment in undescribed species coming from Verrucomicrobia, a phylum found in water, soil, and human intestines but with relatively few cultivated species. Aligning the original sequencing reads back to the MAGs increases the amount of the sequencing library that can be assigned to bacterial genomes from 7 to 21% of reads. That most of the sequences remain unassigned is expected because MAGs do not capture all genomes in a sample. Specifically, they often miss lower-abundance taxa, mobile genetic elements, and organisms with large or complex genomes, including most microbial eukaryotes.

Using these assembled genomes, Levin *et al.* recapitulate findings first noted with amplicon sequencing, including that herbivore microbiomes are more diverse than carnivore microbiomes. By examining the gene content of their MAGs, the authors find that the genetic pathways encoded by the microbiomes of different groups of animals differ based on host diet, body size, and other traits. In a compelling proof-of-concept experiment to demonstrate that new bacterial functions can be discovered in animal microbiomes, the authors experimentally validated bacterial toxin-metabolizing proteases found in the MAGs from carrion-eating griffon vul-

Gladstone Institutes, 1650 Owens Street, San Francisco, CA, USA. Email: kpollard@gladstone.ucsf.edu





The newly identified toxin-metabolizing proteases from the gut bacteria of griffon vultures (*Gyps fulvus*), which eat carrion, may have applications in fighting food poisoning.

tures (*Gyps fulvus*). These proteases could be useful as antimicrobial compounds, with potential applications that include fighting human food poisoning.

The greatest contribution of this study is its rich, systematically generated dataset. It is easy to imagine breakthroughs in areas as diverse as microbial conservation and emerging antibiotic resistance being fueled by discoveries made with these metagenomes. The proteases found in griffon vulture microbiomes are a proof of principle for bioprospecting from wild-animal microbiomes, although it is not clear if this case study should be viewed as exceptional or an expected discovery.

This study has just scratched the surface of the hypotheses that can be tested with this dataset. Exciting future directions include questions about how microbiotas help animals degrade toxic plant chemicals, defend from pathogens in food, and extract nutrients from diverse food sources. More broadly, questions remain about what most of the uncharacterized microbes detected by Levin *et al.* are doing in their hosts and whether they are stably colonizing the animals or transiently passing through their gastrointestinal tracts (2). Testing each hypothesis on this massive dataset requires a great deal of computational effort, interpretation, and experimental validation: Each question could be the subject of an entire PhD thesis.

Using MAGs limits progress on one of the study's stated aims, which is to enable conservation of medically and ecologically

important bacterial strains. Characterizing threatened microbial species will require analyzing the unassembled reads, culturing, or enrichment techniques beyond the whole-metagenome sequencing used in this study. Even for bacteria whose genomes are captured by assembling MAGs, these assemblies are prone to exclude the "accessory" genome, the genes that are variably present across strains. Yet these genes often play roles in adaptations to specific hosts and environments (9). For example, antimicrobial resistance, pathogenicity, and energy harvesting are traits frequently encoded by mobile elements or other accessory genes.

Reaping all the potential benefits of wild-animal microbiomes will require studying bacterial isolates in most cases. The study of Levin *et al.* provides a roadmap for where in the world to look for animals that may harbor the strain or gene of interest. How feasible it will be to culture and work with these strains is unknown. ■

#### REFERENCES AND NOTES

1. N. D. Youngblut *et al.*, *Nat. Commun.* **10**, 2200 (2019).
2. T. J. Hammer, J. G. Sanders, N. Fierer, *FEMS Microbiol. Lett.* **366**, fnz117 (2019).
3. D. W. Waite, M. W. Taylor, *Front. Microbiol.* **6**, 673 (2015).
4. K. E. Sullam *et al.*, *Mol. Ecol.* **21**, 3363 (2012).
5. E. C. Lindsay, N. B. Metcalfe, M. S. Llewellyn, *J. Anim. Ecol.* **89**, 2415 (2020).
6. D. Levin *et al.*, *Science* **372**, eabb5352 (2021).
7. L.-X. Chen, K. Anantharaman, A. Shaiber, A. M. Eren, J. F. Banfield, *Genome Res.* **30**, 315 (2020).
8. K. M. Goh *et al.*, *Microorganisms* **7**, 468 (2019).
9. S. M. Soucy, J. Huang, J. P. Gogarten, *Nat. Rev. Genet.* **16**, 472 (2015).

10.1126/science.abg9095

#### OCEANOGRAPHY

## Diagnosing nutritional stress in the oceans

Phytoplankton genomes map marine nutrient scarcity

By Maureen Coleman

**M**arine phytoplankton perform almost half of global photosynthesis, and their capacity for carbon uptake is governed by the availability of scarce nutrients. Climate change and anthropogenic inputs are altering the oceanic distribution of these nutrients (1, 2). How individual phytoplankton groups and ocean productivity are responding to these changes is unknown. On page 287 of this issue, Ustick *et al.* (3) present a global map of nutrient limitation in *Prochlorococcus*, the most abundant photosynthetic organism in the low-latitude oceans, on the basis of a new diagnostic metric that could be widely used to monitor shifts in the nutritional seascape.

The classical test for limitation is a nutrient-amendment experiment: Phytoplankton growth rate and/or biomass increase when the limiting nutrient is added but remain unaffected by other supplements. This approach has long been used in small-scale incubations and whole-ecosystem manipulations, proving that phosphorus controls algal biomass in lakes (4) and that iron limits phytoplankton growth in so-called high-nitrate low-chlorophyll ocean regions (5). Geochemists also infer nutrient deficiency by comparing ratios of dissolved nutrients to the Redfield stoichiometry (the average ratio of carbon, nitrogen, and phosphorus found in marine phytoplankton biomass). Molecular approaches assay the physiological state of cells using RNA or protein expression (6, 7). Yet, all these approaches are low-throughput and laborious, requiring meticulous precautions to prevent trace-metal contamination and exacting analytical methods for low-level detection.

Department of the Geophysical Sciences, University of Chicago, Chicago, IL, USA. Email: mlcoleman@uchicago.edu

By contrast, the metric developed by Ustick *et al.* requires only routine sampling and DNA sequencing of microbial communities, a common approach to survey taxonomic composition and functional potential (8). But the authors extract new information by simplifying complex metagenomes down to a single taxon, *Prochlorococcus*. *Prochlorococcus* genomes continually gain and lose genes, and “use it or lose it” dictates whether a gene persists. Genes that enhance fitness—for instance, by increasing the rate at which a growth-limiting nutrient can be transported into the cell—are selectively retained in ge-

while also revealing the stress “felt” by *Prochlorococcus* in uncharted regions of the Indian Ocean. In the Atlantic, crisscrossing cruise tracks spanning 50°S to 50°N latitude mapped sharp transitions between regions of phosphorus, nitrogen, and iron limitation. Notably, the distributions of marker genes for multiple stressors sometimes overlapped, suggesting the potential for widespread colimitation, or the mixing of populations with distinct nutritional histories.

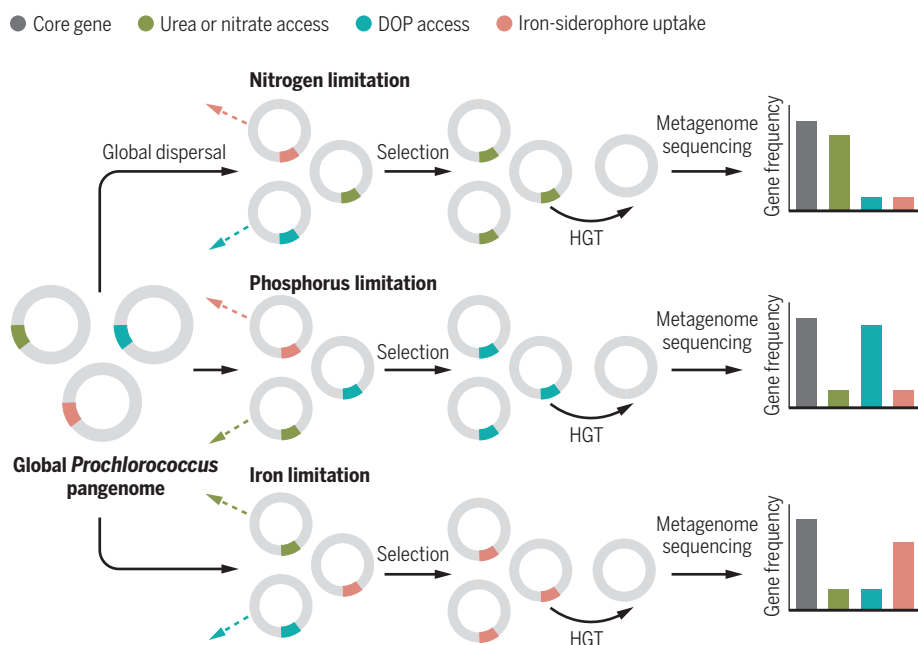
The elegant simplicity of this genetic approach belies many underlying uncertainties. One key mystery is the major mode and

uptake? Ustick *et al.* suggest that their genetic approach is validated by its consistency with classical nutrient amendment experiments. However, there are also discrepancies between the approaches, which is not unexpected and is intriguing. Experiments typically measure the short-term response to nutrient addition in terms of community-level biomass or carbon uptake. The gene metrics used here assess the impact of natural selection, integrated over unspecified time and space, on a single organism. Relating the two measures is not straightforward. Adding back the genome-reported limiting nutrient would not necessarily increase the growth rate or biomass of *Prochlorococcus*, whose growth rate would likely already be near maximal. But it could still increase community-level biomass and carbon uptake by replacing *Prochlorococcus* with faster-growing, larger taxa. These newly abundant taxa would have distinct stoichiometric requirements compared with *Prochlorococcus*, and thus their growth might be limited by different nutrients. Teasing apart the reasons why individual taxa and the community as a whole respond differently to nutrient amendments could provide important new insights into the physiological and ecological controls imposed by nutrient limitation.

The atlas of nutrient limitation presented by Ustick *et al.* leverages routine metagenomic samples collected on a massive scale, providing a baseline assessment of global *Prochlorococcus* nutritional status. Using this approach over time promises to document changing pressures felt by *Prochlorococcus* and potentially other taxa. It will not replace field experiments, physiology, and geochemical tools but rather will complement these approaches with its extremely sensitive and taxon-specific readout. By integrating multiple methods and understanding their (dis)agreements, scientists will be better equipped to monitor, and forecast, changes in ocean biogeochemistry and carbon uptake. ■

## Gene frequencies as a biosensor for ocean nutrient limitation

The phytoplankton *Prochlorococcus* adapts to local environments by gene gain and loss. Dashed arrows show cells that are outcompeted for the limiting nutrient, leading to gene loss from the population. HGT, horizontal gene transfer; DOP, dissolved organic phosphorus.



nomes. Ultimately, every cell in the population may carry the beneficial gene through a combination of vertical inheritance and horizontal gene transfer. Hence, the frequency of the gene, relative to the average core housekeeping gene, serves as a proxy for the physiological limitation that the gene product relieves.

Ustick *et al.* propose a set of diagnostic genes that are linked to phosphorus, nitrogen, or iron stress in *Prochlorococcus* (see the figure). The authors then quantify the frequency of these genes in more than a thousand samples—the vast majority newly collected and sequenced. Their metric confirms results from well-characterized locations (e.g., phosphorus limitation in the North Atlantic gyre) (9)

rates of gene acquisition by *Prochlorococcus* cells. Studies have pointed to viruses (10) and membrane vesicles (11) and potentially to mobile genetic elements (12) as playing roles. To increase the sensitivity of the new metric, Ustick *et al.* categorized each diagnostic gene by the severity of stress (high, medium, or low) it indicates—for example, alkaline phosphatase is presumed to persist only under the most severe phosphorus stress—but the biochemical trade-offs that underpin these categories have not been characterized and likely differ across taxa. How generalizable this approach is to other taxa remains to be seen.

More generally, what does this approach, and the resulting map of global-scale nutrient stress, reveal about ocean biogeochemistry and controls on carbon

## REFERENCES AND NOTES

1. C. M. Moore *et al.*, *Nat. Geosci.* **6**, 701 (2013).
2. A. Krishnamurthy *et al.*, *Global Biogeochem. Cycles* **23**, GB3016 (2009).
3. L. J. Ustick *et al.*, *Science* **372**, 287 (2021).
4. D. W. Schindler, *Science* **184**, 897 (1974).
5. K. H. Coale *et al.*, *Nature* **383**, 495 (1996).
6. A. Marchetti *et al.*, *Proc. Natl. Acad. Sci. U.S.A.* **109**, E317 (2012).
7. M. A. Saito *et al.*, *Science* **345**, 1173 (2014).
8. S. Sunagawa *et al.*, *Science* **348**, 1261359 (2015).
9. M. L. Coleman, S. W. Chisholm, *Proc. Natl. Acad. Sci. U.S.A.* **107**, 18634 (2010).
10. R. Laurenceau *et al.*, *ISME J.* **15**, 129 (2021).
11. S. J. Biller *et al.*, *Science* **343**, 183 (2014).
12. T. Hackl *et al.*, *bioRxiv* 10.1101/2020.12.28.424599 (2020).

10.1126/science.abi4684





## POLICY FORUM

### ENVIRONMENTAL POLICY

# A water rule that turns a blind eye to transboundary pollution

We can't presume that states will fill gaps in federal oversight

By **David A. Keiser**<sup>1,2,3</sup>, **Sheila M. Olmstead**<sup>4,5</sup>, **Kevin J. Boyle**<sup>6</sup>, **Victor B. Flatt**<sup>7</sup>, **Bonnie L. Keeler**<sup>8</sup>, **Catherine L. Kling**<sup>2,3,5</sup>, **Daniel J. Phaneuf**<sup>9</sup>, **Joseph S. Shapiro**<sup>10,11</sup>, **Jay P. Shimshack**<sup>12</sup>

**D**ebates about the decentralization of environmental policy are important and are far from resolved (1, 2). Interregional spillovers provide one key justification for centralized regulation: When regulation is decentralized, individual jurisdictions may not protect downstream or downwind neighbors from their pollution (2, 3). Under the Trump administration, the US Environmental Protection Agency (EPA) and US Army Corps of Engineers (ACE) departed from precedent to support the deregulation of US waterways in the repeal of the 2015 Clean Water Rule (CWR) and its replacement with the 2020 Navigable Waters Protection Rule

(NWPR). In doing so, they assumed (with little evidence) that many states would fill gaps in federal oversight. With the Biden administration having signaled its intent to modernize regulatory review and to review specific deregulatory actions taken by the Trump administration, we describe here how this environmental federalism approach downplays the importance of cross-state pollution and relies on flawed methods of benefit-cost analysis that could be used to weaken other statutes.

Early federal laws that allowed states to lead in setting environmental standards were replaced in the 1970s by a stronger role for federal regulation. Landmarks in this policy shift include the Clean Water Act (CWA) and the Clean Air Act (CAA). But the scope of waters protected under the CWA has been controversial. Unlike many environmental regulations, the CWR promulgated during the Obama administration did not propose new environmental standards. Instead, it sought to define the characteristics of water bodies that are subject to a variety of regulations under the CWA—those that are considered “waters of the United States” (WOTUS)—with a particular focus on those waters in the legal gray areas that have prompted litigation over the past several decades. These include small headwaters, “isolated” wetlands, and ephemeral and intermittent streams. WOTUS jurisdictional definitions determine which water

At Cincinnati, Ohio, the Licking River flows from Kentucky into the Ohio River. One case study considered by the agencies includes the Middle Ohio and Kentucky-Licking watersheds. Together these watersheds cross four state boundaries (Indiana, Kentucky, Ohio, and West Virginia), suggesting that transboundary water pollution is an important concern.

bodies are subject to CWA regulations, affecting agricultural operations, construction and land development projects, and other activities that involve such actions as filling of wetlands or increasing runoff of water pollutants into the bodies of water in contention.

The Trump administration repealed and replaced the CWR with the NWPR, narrowing the CWA's jurisdictional reach. Although exact magnitudes are subject to debate, a 2017 analysis by EPA and ACE suggests that the NWPR excludes 18% of streams (35% in the arid West) and just over one-half of wetlands nationwide (4). This action had a weak scientific basis, as many of the excluded waters are connected biologically, chemically, and hydrologically to protected waters downstream (5).

### DOWNPLAYING THEORY AND EVIDENCE

The economic basis for the NWPR is also flawed. In their analyses, the agencies argued that removing protection from the newly excluded waters would generate net economic benefits because states may be better regulators of “local environmental public goods” (6, 7). The analysis represented a marked shift to decentralized decision-making that downplayed transboundary impacts—the scientific and economic basis on which the federal role is predicated (8).

For the first time since 1975, the NWPR eliminated “interstate waters” as a stand-alone category of federal jurisdictional waters. Interstate waters could still be under federal jurisdiction, but only if they met the requirements of a covered standalone category such as traditional navigable waters, their tributaries, and adjacent water bodies. But, for example, according to the rule, any ephemeral or intermittent stream that crosses state borders or any such stream that feeds into interstate waters would no longer be under federal jurisdiction.

The agencies' analyses implied that the interstate impacts of the NWPR's changes would be minor. In contrast, economic theory and empirical evidence suggest that devolving regulatory authority from the federal government to states can result in weaker-than-optimal regulation when pollution crosses state boundaries (2). Indeed, the agencies noted this finding but downplayed its importance (7). Because affected waters are connected to downstream waters, and because many

<sup>1</sup>University of Massachusetts, Amherst, MA, USA. <sup>2</sup>Cornell University, Ithaca, NY, USA. <sup>3</sup>Center for Agricultural and Rural Development, Iowa State University, Ames, IA, USA. <sup>4</sup>University of Texas, Austin, TX, USA. <sup>5</sup>Resources for the Future, Washington, DC, USA. <sup>6</sup>Virginia Tech, Blacksburg, VA, USA. <sup>7</sup>University of Houston, Houston, TX, USA. <sup>8</sup>University of Minnesota, Minneapolis, MN, USA. <sup>9</sup>University of Wisconsin, Madison, WI, USA. <sup>10</sup>University of California, Berkeley, CA, USA. <sup>11</sup>National Bureau of Economic Research, Cambridge, MA, USA. <sup>12</sup>University of Virginia, Charlottesville, VA, USA. Email: dkeiser@umass.edu; sheila.olmstead@austin.utexas.edu

state boundaries are arbitrary with respect to watershed boundaries, the narrowing of CWA jurisdiction would likely increase interstate water pollution. The magnitude of such impacts is critical to assessing the validity of the agencies' federalism arguments, yet they performed no such analysis. Moreover, the economic analysis was internally inconsistent on this point. The agencies implemented three "case studies" to examine how the NWPR would affect a range of CWA programs (7). Yet all three case-study watersheds cross multiple state boundaries, highlighting that such boundaries do not constrain water pollution.

Following directly from the unsupported conclusion that water quality is a local public good, the agencies implemented a set of "federalism scenarios." The agencies argued that if some states were to decide to regulate the waters over which the federal government abdicates jurisdiction, then estimation of the benefits and costs of rescinding federal protection should not include these states. The agencies suggested that this adjustment by some states "would result in no change in compliance costs... and no change in environmental benefits... suggesting no net impact in the long run" (7). In other words, the agencies assumed that if state regulations filled the gap left by federal regulations, overall costs and benefits would remain unchanged in the long run. But the agencies could only speculate about the future actions of states that are neither legally required nor likely to act—an approach that, to our knowledge, has no precedent in EPA regulatory impact analyses. EPA's own Guidelines for Preparing Economic Analyses say that only related state rules that are legally required but not yet implemented should be included when estimating benefits and costs (9). Public comments on the NWPR raised this very issue (10, 11). This EPA guidance (9) is based on the need for a meaningful counterfactual that is not subject to arbitrary manipulation. In fact, in recent air quality rules under the CAA, EPA noted that "normal practice is to only include changes...from final regulatory actions in its modeling because, until such rules are finalized, any potential changes...are speculative" (12).

### EXCESSIVELY OPTIMISTIC, OR SIMPLY WRONG

If the agencies' basic assumptions about federalism in the NWPR were problematic, how did they apply these assumptions in their economic analysis? To implement the federalism scenarios in the NWPR, the agencies predicted state responses to the narrowing of federal water quality jurisdiction, using three indicators: (i) whether a state currently regu-

lates any intrastate waters beyond federal waters as "waters of the state"; (ii) whether state law restricts regulation of waters outside of federal waters; and (iii) whether a state currently has a dredge-and-fill program under CWA Section 404, commonly known as the wetlands regulatory program. The agencies then removed groups of states deemed "likely to act" from their benefit and cost calculations, excluding 23 states that they predicted would fully subsume the federal role in one scenario, and excluding 31 states in the scenario that was most optimistic about hypothetical future state laws (see the figure).

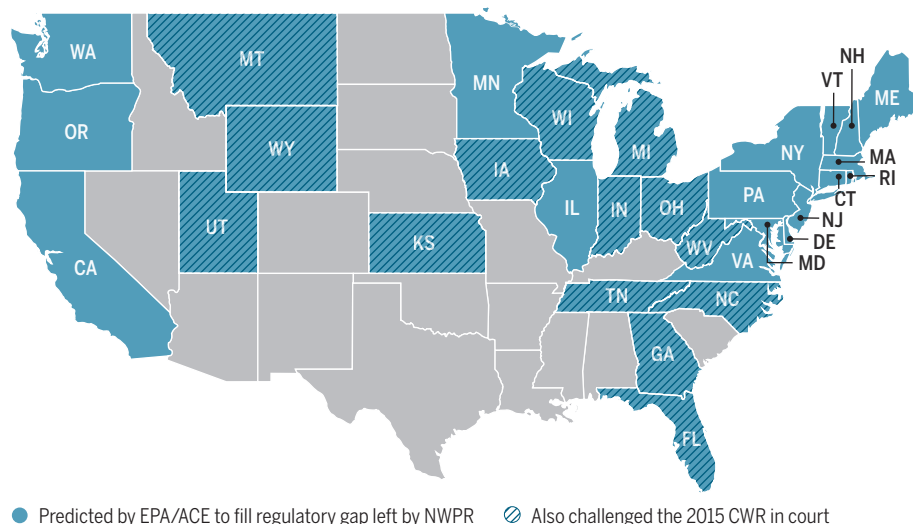
These predictions are inconsistent with states' prior behavior. States have always

dozens of states would enact stricter water quality regulations upon the removal of federal regulation was excessively optimistic, or simply wrong.

A state-by-state review of relevant legislation, executive orders, and other documents provides additional support for our argument that the agencies' predictions of state behavior are unsound. Among 31 states that the agencies deemed likely to regulate newly unprotected wetlands, we identify at least 16 that should not have been included, using the agencies' own classification criteria [see (8) and supplementary materials]. In most of these cases, the agencies asserted that states may easily enact laws that exceed

### Assuming state action, despite evidence to the contrary

This figure shows the 31 states that the agencies assumed will protect some or all of the streams and wetlands newly deregulated under the Navigable Waters Protection Rule (NWPR), despite evidence to the contrary. Best practices in benefit-cost analysis caution against this type of speculation about future state actions. Fourteen of these states, as designated in the figure, challenged the 2015 Clean Water Rule (CWR) in court (13); thus their future support for expanded protections would represent a substantial change in position.



been able to enact water quality protection rules more stringent than those in the CWA; it is unclear why they would do so now when they have not done so already. One prominent example is 32 states' challenge to the 2015 CWR in court, arguing that it would impose excessive costs. Inexplicably, the NWPR's economic analysis projected that 14 of these states would now change their position (13) (see the figure). Another example, from a different context, is states' reaction to a reduction in the CWA's jurisdiction over wetlands as a result of the Supreme Court's 2001 decision regarding the Solid Waste Agency of Northern Cook County. Almost 20 years later, only a few states have moved to expand their own jurisdiction over some of the affected waters (14). These precedents suggest that the agencies' contention that

the minimum federal standard, but our analysis leads to the opposite conclusion. Many states require special legislative and administrative approval to pass environmental rules that are more stringent than corresponding federal law. For example, the agencies identified Indiana as a state that "does not have broad legal limitations" on regulating more stringently than the federal government (6, 7). Since 2016, however, Indiana has mandated that environmental rules more stringent than federal rules cannot go into effect until the legislature has had an opportunity to veto the more stringent state rules.

To describe the impact of this problematic speculation about future state laws on the agencies' economic analysis, we must clarify some terms. Because the NWPR re-



duces the share of US waters under federal protection, the NWPR's benefits are actually avoided costs of regulation that would still be in place but for the rule (e.g., avoided compliance costs for regulated entities). Its costs, in contrast, are actually the forgone benefits from protecting wetlands and streams (e.g., lost wetland acreage) that the CWA no longer covers because of the NWPR. Thus, as a deregulatory action, the NWPR's net benefits are its avoided costs minus forgone benefits. In addition, because the CWR had already been repealed, the baseline for the agencies' economic analysis in the NWPR was the definition of WOTUS that predated the CWR [(7), p. xi].

Using data from the economic analysis for the NWPR (7), we calculate the national net benefits (avoided costs minus forgone benefits) of the rule. When benefits and costs for all states are included, net annual national impacts range from a \$310 million loss to a \$484 million gain (table S1). When the agencies zeroed out 31 states in their economic analysis of the NWPR, assuming that these states would adopt protections equivalent to those being removed, net annual national impacts range from an \$83 million loss to a \$208 million gain. The overall effect of the agencies' federalism analysis is to decrease the extent to which the rule could be costly while maintaining an upside estimate that is favorable to the NWPR.

To further explore the issue, we calculate the net benefits (avoided costs minus forgone benefits) of the NWPR by state (table S2). We find that nearly half of the forgone national benefits from the agencies' narrowing of the CWA's scope are attributable to excluding a single state: Florida. Florida's share of the NWPR's national avoided costs, in contrast, is only about 10%. Florida is one of only two states for which the forgone benefits of the NWPR exceed the avoided costs (for an annual economic loss of more than \$45 million) (table S2). Thus, when the agencies speculated that Florida would step in to regulate where the federal government does not, the result was extremely favorable to the NWPR. Yet our analysis suggests that the agencies miscategorized Florida as a state that is likely to take over the federal role for the newly excluded streams and wetlands (see supplementary materials). This would require a reversal of the state's recent stance on these issues, given that Florida joined 31 other states in litigation against the 2015 CWR.

## PRODUCTIVE POLICY TENSION

The conflicts between EPA's own guidance and its NWPR analysis, between its speculation about state actions under the CWA but

not under the CAA, and between the conclusions of the economic analyses of CWA rules under the Obama and Trump administrations are likely to be legal hurdles for the staying power of the NWPR. In the US, the Administrative Procedures Act requires a "reasoned explanation" for rulemakings like the CWR repeal and replacement and prohibits rules that are "arbitrary and capricious." Failure to meet these requirements has caused federal courts to reject many Trump administration policies since 2017, including the administration's initial suspension of the CWR (15).

Where does this leave important debates about the appropriate locus of environmental regulation? The agencies' flawed estimates do not provide a clear picture. However, the best available scientific and economic evidence suggests that the federalism argument should not be used to support the NWPR's removal of a large share of US waters from CWA protection. The federalism arguments in the NWPR, although unconvincing in that setting, may have implications for other federal environmental statutes in which debates about state versus federal control are germane, such as the CAA's designation of nonattainment areas or the Safe Drinking Water Act's maximum contaminant level standards.

The agencies' economic analysis for the NWPR violated basic tenets of benefit-cost analysis and EPA's peer-reviewed guidelines, with no known precedent in federal rulemaking. The federalism analysis contravened the best available knowledge in the peer-reviewed economics literature to such a degree that the analysis can be considered arbitrary. Because the approach strongly affects the results of the benefit-cost analysis, it also opens the agencies and the process of regulatory impact analysis to concerns about strategic manipulation.

Although it is incorrect to speculate that dozens of states will fully subsume a rescinded federal environmental protection role, it can also be unrealistic to assume that no states will do so. This is why EPA's Guidelines carefully define the thresholds for anticipated new state rules to be incorporated into benefit-cost analysis (9). Given prominent, persistent political debates over environmental federalism, it may be useful to revisit this aspect of the EPA Guidelines. Extensive, peer-reviewed theoretical, experimental, and observational research may yield a better understanding of the conditions that favor federal versus state jurisdiction in environmental policy development. Such policy tension can be productive to the extent that it motivates new research needed to support improved decision-making. ■

## REFERENCES AND NOTES

1. W. E. Oates, R. M. Schwab, *J. Public Econ.* **35**, 333 (1988).
2. B. R. Dijkstra, P. G. Fredriksson, *Annu. Rev. Resour. Econ.* **2**, 319 (2010).
3. H. Sigman, *J. Environ. Econ. Manage.* **50**, 82 (2005).
4. A. Wittenberg, K. Bogardus, "EPA falsely claims 'no data' on waters in WOTUS rule" (E&E News, 2018); [www.eenews.net/stories/1060109323](http://www.eenews.net/stories/1060109323).
5. S. M. P. Sullivan *et al.*, *Science* **369**, 766 (2020).
6. US Environmental Protection Agency and US Department of the Army, "Economic Analysis for the Final Rule: Definition of 'Waters of the United States'—Recodification of Pre-existing Rules" (2019); [www.epa.gov/sites/production/files/2019-09/documents/wotus\\_rin-2040-af74\\_final\\_ea\\_508compliant\\_20190905.pdf](http://www.epa.gov/sites/production/files/2019-09/documents/wotus_rin-2040-af74_final_ea_508compliant_20190905.pdf).
7. US Environmental Protection Agency and US Department of the Army, "Economic Analysis for the Navigable Waters Protection Rule: Definition of 'Waters of the United States'" (2020); [www.epa.gov/sites/production/files/2020-01/documents/econ\\_anal\\_sis\\_-\\_nwpr.pdf](http://www.epa.gov/sites/production/files/2020-01/documents/econ_anal_sis_-_nwpr.pdf).
8. D. A. Keiser *et al.*, "Report on the Repeal of the Clean Water Rule and its Replacement with the Navigable Waters Protection Rule to Define Waters of the United States (WOTUS)" (External Environmental Economics Advisory Committee, 2020); [www.e-eaac.org/wotusreport](http://www.e-eaac.org/wotusreport).
9. US Environmental Protection Agency, "Guidelines for preparing economic analyses" (2010); [www.epa.gov/environmental-economics/guidelines-preparing-economic-analyses#download](http://www.epa.gov/environmental-economics/guidelines-preparing-economic-analyses#download).
10. P. Howard, J. Shrader, "An evaluation of the revised definition of Waters of the United States" (2019); <https://beta.regulations.gov/document/EPA-HQ-OW-2018-0149-5272>.
11. J. C. Whitehead, "Comments on 'Economic Analysis for the Proposed Revised Definition of Waters of the United States'" (2019); <https://beta.regulations.gov/document/EPA-HQ-OW-2018-0149-9717>.
12. US Environmental Protection Agency, "Response to Clean Air Act Section 126(b) Petition from New York" (2019); [www.federalregister.gov/documents/2019/10/18/2019-21207/response-to-clean-air-act-section-126b-petition-from-new-york](http://www.federalregister.gov/documents/2019/10/18/2019-21207/response-to-clean-air-act-section-126b-petition-from-new-york).
13. Institute for Policy Integrity, "Brief of the Institute for Policy Integrity at New York University School of Law as amicus curiae in support of plaintiffs' motion for summary judgment," *US District Court for the District of Massachusetts, Conservation Law Foundation et al. v. US Environmental Protection Agency*, 17 December 2020; [https://policyintegrity.org/documents/Amicus\\_Brief\\_of\\_the\\_Institute\\_for\\_Policy\\_Integrity\\_1.pdf](https://policyintegrity.org/documents/Amicus_Brief_of_the_Institute_for_Policy_Integrity_1.pdf).
14. US Congressional Research Service, "The Wetlands Coverage of the Clean Water Act: Rapanos and Beyond" (2016); [www.everycrsreport.com/files/20160427\\_RL33263\\_e0b1d527d85d13721eb7f29d3e1446c517900c45.pdf](http://www.everycrsreport.com/files/20160427_RL33263_e0b1d527d85d13721eb7f29d3e1446c517900c45.pdf).
15. F. Barbash, D. Paul, "The real reason the Trump administration is constantly losing in court," *The Washington Post*, 19 March 2019; [www.washingtonpost.com/national-security/the-real-reason-president-trump-is-constantly-losing-in-court/2019/03/19/f5ffb056-33a8-11e9-af5b-b51b7ff322e9\\_story.html](http://www.washingtonpost.com/national-security/the-real-reason-president-trump-is-constantly-losing-in-court/2019/03/19/f5ffb056-33a8-11e9-af5b-b51b7ff322e9_story.html).

## ACKNOWLEDGMENTS

We thank anonymous referees whose comments improved the paper, and J. Clement, S. Cullen, A. Gorton, and R. Noe for excellent research assistance. This work is supported by the Alfred P. Sloan Foundation through the External Environmental Economics Advisory Committee (E-EAAC) and the Giannini Foundation (J.S.S.). Our analysis derives from work that D.A.K., S.M.O., K.J.B., V.B.F., B.L.K., D.J.P., J.S.S., and J.P.S. performed as part of an E-EAAC-sponsored review of the CWR and NWPR. Our analysis also derives from work that C.L.K. performed in a similar review of these rules for the New York State Attorney General's Office. D.A.K. is affiliated with the Center for Behavioral and Experimental Agri-Environmental Research.

## SUPPLEMENTARY MATERIALS

[science.sciencemag.org/content/372/6539/241/suppl/DC1](https://science.sciencemag.org/content/372/6539/241/suppl/DC1)

10.1126/science.abf8885

# Bial AWARD

IN BIOMEDICINE 2021

## BIAL Award in Biomedicine 2021 - €300.000

Seeks to recognize a work published in the broad biomedical field after 1 January 2012, the results of which are considered of exceptional quality and scientific relevance.

Only works nominated by the voting members of the Jury, by the members of the Scientific Board of the BIAL Foundation, by previous BIAL award winners or by Scientific Societies may be considered candidates. The Jury may also invite other scientific institutions to submit nominations. Self-nominations are not allowed.

### Jury

#### President

Ralph Adolphs

#### Members

*European Research Council*

Geneviève Almouzni | Paola Bovolenta

*Council of Rectors of Portuguese Universities*

Maria do Carmo Fonseca | Fátima Carneiro

*European Medical Association*

Vincenzo Costigliola | Olga Golubnitschaja

*Scientific Board of the BIAL Foundation*

Hugo Critchley | Menno Witter

*Previous winners of the BIAL Award*

Peter St. George-Hyslop | Daniel Pipeleers

*Scientific Journals*

Howard Bauchner - JAMA | Eric Rubin - NEJM

Nomination form must be sent

by 30 June 2021 to

[fundacao@bial.com](mailto:fundacao@bial.com)

Regulation and nomination  
form available at

[www.fundacaobial.com](http://www.fundacaobial.com)

FUNDAÇÃO  
**Bial**  
Institution of public utility

CONSELHO INTERMUNICIPAL  
DE SAÚDE PÚBLICA  
INSTITUTO DE INVESTIGAÇÃO EM MEDICINA  
E BIOMEDICINA DE LISBOA

  
O Presidente da República

UCRUP  
CONSELHO NACIONAL  
DE INVESTIGAÇÃO  
BIOMÉDICA  



[ScienceTranslationalMedicine.org](http://ScienceTranslationalMedicine.org)


# PUT HUMAN HEALTH AT THE HEART OF YOUR RESEARCH

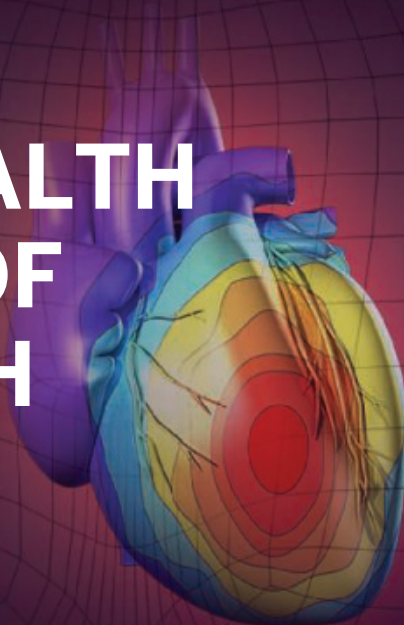
Submit your research at: [cts.Sciencemag.org](https://cts.Sciencemag.org)

Science Translational Medicine

AAAS

 Twitter: @ScienceTM

 Facebook: @ScienceTranslationalMedicine





## HISTORY OF SCIENCE

# The cost of scientific patronage

Military funding encouraged researchers to think of the ocean as a theater of war rather than a dynamic ecosystem

By Christine Keiner



What do Cold War military funding, the golden years of postwar oceanography, the appalling state of our oceans today, and agnotology—the study of the cultural production of ignorance—have to do with each other? Plenty, as historian of science Naomi Oreskes makes clear in her impressive and authoritative new book, *Science on a Mission*.

Over the past two decades, Oreskes has helped transform how scholars understand the history of scientific and political debates over continental drift and anthropogenic climate change. Her latest work weaves together insights from these and other intellectual spheres to deliver a crucial message: Patronage of knowledge production—that is, who pays for science—matters deeply.

Scientific work at sea is expensive, and military financial and logistical support has enabled researchers to elucidate long-standing mysteries of the deep such as abyssal circulation, plate tectonics, and seafloor hydrothermal vents. Yet

Oreskes shows that Cold War navy bureaus paid to solve specific problems, especially concerning submarine warfare. By the middle of the 20th century, navy operational needs shaped the agendas of three major US marine research centers—the Scripps Institution of Oceanography, the Woods Hole Oceanographic Institution (WHOI), and the Lamont Geological Observatory—with considerable consequences.



**Science on a Mission**  
Naomi Oreskes  
University of Chicago  
Press, 2021. 744 pp.

Not all US oceanographers accepted the strings attached to navy largesse. Debates erupted even before the Cold War at Scripps and again in the early 1960s at WHOI over the costs of having to work on classified operational projects. However, trustee budgetary priorities eclipsed faculty concerns about autonomy and military control of “big science” at sea.

Oreskes uses fascinating historical episodes to reveal serious, underappreciated consequences of oceanographers’ prolonged reliance on secret, mission-driven navy projects. Two chapters examine the complex history of the famous *Alvin* submersible, which, contrary to subsequent whitewashing, did not start out as a research vessel. Another chapter tells the disturbing story of a prominent WHOI sedimentologist who spent most

Oceanographers initially minimized concerns that acoustic transmissions might harm marine mammals.

of the 1980s and 1990s trying to convince the US government to bury nuclear waste in the deep sea, despite his earlier codiscovery that the seafloor lacks seismic stability.

The narrative culminates in the 1990s, when Scripps oceanographers pivoted toward climate change research. Blind to their own arrogance and obliviousness about the impact of underwater sound on marine mammals, the scientists provoked public distrust by casting themselves as climate heroes while dismissing concerns about the threats posed to whales by acoustic tomography, which the researchers sought to use to investigate ocean temperatures.

Epistemic effects of “military defense oceanography” continue to ripple outward today. Internalizing the navy’s view of the ocean as a theater of submarine warfare, rather than as a dynamic ecological system, led Scripps, WHOI, and Lamont leaders to brush off ocean biology and ecology. By the time comprehensive marine biological inventories finally started, around the turn of the millennium, it was, Oreskes laments, “much too late” to determine baseline conditions owing to massive changes caused by overfishing and other anthropogenic activities.

Historians of biology and marine environments will likely have other examples of how decision-makers “constructed substantial ignorance about the ocean as an abode of life.” From my own research, I would add that biologists of the late 1960s worked very hard yet failed to convince the US Office of Naval Research and allied agencies to fund studies of how a proposed Central American sea level canal might facilitate disastrous exchanges of invasive species (1).

We need more historical scholarship on how powerful entities produce ignorance as well as knowledge, and Oreskes provides a model for doing so. As an intellectual and institutional history of postwar oceanography, *Science on a Mission* will interest historians and practitioners of the marine sciences, historians of Cold War science, and scholars of epistemology, and it deserves a wide readership. Moreover, as an exposé of how navy-sponsored oceanographers wound up constraining their own research agendas and believing their own myths, the book should give pause to all scientists who consider themselves immune to the potential influence of their funders, or who romanticize the golden age of military scientific patronage. ■

## REFERENCES AND NOTES

1. C. Keiner, *Deep Cut: Science, Power, and the Unbuilt Inter-oceanic Canal* (Univ. of Georgia Press, 2020).

10.1126/science.abf0842

## COMPUTER SCIENCE

# AI empires

A Microsoft researcher unpacks the power and perils of today's artificial intelligence

By Michael Spezio

**K**ate Crawford's new book, *Atlas of AI*, is a sweeping view of artificial intelligence (AI) that frames the technology as a collection of empires, decisions, and actions that together are fast eliminating possibilities of sustainable futures on a global scale. Crawford, a senior principal researcher at Microsoft's FATE (Fairness, Accountability, Transparency, and Ethics in AI) group, conceives of AI as a one-word encapsulation of imperial design, akin to Calder Willingham's invocation of the word "plastics" in his 1967 screenplay for *The Graduate* (1). AI, machine learning, and other concepts are here understood as efforts, practices, and embodied material manipulations of the levers of global power.

By taking power and materiality seriously and leaving aside questions of what intelligence is, Crawford maps answers to how AI is made and how we are trapped by its making. The primary thesis of her book is that AI has nothing to do with understanding or seeking intelligence but is a "registry of power," a metaphor meant to encompass social, political, and economic power as well as the insatiable demands AI places on electric power grids and on nonhuman nature.

Why an "atlas" of AI? Because those in control of AI have a desire for AI "to be the atlas—the dominant way of seeing," to be the single way in which humans understand and run the world. Crawford's anticolonial manual advances an alternative mapping, one that resists AI's extractive, exploitative, and destructive aims. To comprehend Crawford's argument is to understand that AI's danger lies not in a hypothetical future superintelligence but in the reality of its current manifestation.

The book begins with a stark chapter (titled "Earth") on the destructive power of lithium and rare earth element mining

that provides the raw materials that underlie artificial processing power. In "Labor," a visit to an Amazon fulfillment center in New Jersey inspires reflection on the crushing effects of the "logics of production" that undergird just-in-time synchronization of humans by machines and their builder-owners.

In "Data" and "Classification"—two of her most effective chapters—Crawford traces the pragmatics of predictive analytics, which she argues are rooted in promises of

**Atlas of AI: Power, Politics, and the Planetary Costs of Artificial Intelligence**  
Kate Crawford  
Yale University Press, 2021.  
336 pp.



ing them with the opportunity to articulate their own gender and ethnic identities (2).

In "Affect," Crawford applies the lessons of the previous two chapters to highlight the dangers of automating human emotion detection. She effectively strikes down the notion that machine classification of human emotion in policing, security, law, hiring, education, and psychiatric medicine will be bias-free, given its existing track record of othering persons from already marginalized communities.

Crawford's final chapter ("State") describes the US Department of Defense's Project Maven, an initiative in which a weaponized AI would be used to expand the scope of drones. Google, the project's first host, tried to keep its work on the project secret, but when the company's employees found out, more than 3000 signed a letter expressing ethical concerns about the company's involvement in such a program. After Google did not renew the initial contract, Project Maven moved to Palantir, a startup whose funding was partially derived from a CIA-affiliated venture capital group. Crawford shows how Palantir's business model has already made its way into domestic deportation efforts, local policing, and supermarket chains, arguing that the imminent threat of weaponized AI must supersede nagging worries about automated weaponry.

With *Atlas of AI*, Crawford has written a timely and urgent contribution to the interdisciplinary projects seeking to humanize data science practice and policy. One might reasonably object to her view that "we must focus less on ethics and more on power" or push back against her recurrent use of "myth" and "mythologies" to mean "falsehood" and "lies," yet such qualms in no way diminish the value of this book. ■

## REFERENCES AND NOTES

1. C. Willingham, *The Graduate* screenplay, Scripts.com; [www.scripts.com/script-pdf/864](http://www.scripts.com/script-pdf/864).
2. UTKFace, Large-Scale Face Dataset; <https://susanqq.github.io/UTKFace/>.

10.1126/science.abh2250

sciencemag.org **SCIENCE**



A photo series published in 1862 purported to categorize human emotions.

beneficence without attention to nonmaleficence. Here, she describes how AI constructs digital gates that lock us into data cages fixed to a mismeasured atlas over which we have no consent or other control. She offers as an example UTKFace, a database of facial images scraped from the internet that uses restrictive gender binary and ethnic identity classification schemes ("an integer from 0 to 4, denoting White, Black, Asian, Indian, and Others") without attempting to contact the persons in the dataset to ask for their consent or provid-

The reviewer is a faculty member of the Psychology, Neuroscience, and Data Science programs at Scripps College, Claremont, CA 91711, USA. Email: [mspezio@scrippscollege.edu](mailto:mspezio@scrippscollege.edu)





Workers clear debris in the Chamoli district of Uttarakhand, India, after a glaciated ridge failed on Ronti mountain on 7 February, causing massive flooding.

Edited by Jennifer Sills

## Seismological rockslide warnings in the Himalaya

On 7 February, a glaciated ridge of Ronti mountain in the western Himalaya failed at 5600 m above sea level, causing a rockslide that induced a debris flow and flooding in the tributaries of the river Ganga (1). The events destroyed two hydroelectric projects and claimed more than 100 lives. Himalayan countries urgently need a robust early warning mechanism for rockslides and triggered flow cascades such as debris flow and flash floods. These flows move at up to tens of meters per second. In contrast, the elastic waves they generate have speeds of a few kilometers per second [(2), p. 59], arriving quickly at different seismic stations and potentially providing advance notice of disasters. A dense seismological network could be the key to a successful early warning system.

Satellites are conventionally used to detect rockslides and cascading events, but the time gaps between satellite data acquisitions limit their utility for real-time monitoring [e.g., (3)]. Seismic stations can record several data samples per second [(2), p. 385], but the use of seismic data for this purpose strongly depends on the availability and proximity of a dense seismic

network. The network would need several dozen stations within about 100 km of the area prone to hazard (4). The arrival time of various phases of a seismic wave at different stations in such a network could provide a close to real-time alert of a rockslide and could pinpoint when a rockslide transitions to a debris flow and where flood risks might increase (5). If the stations were connected by satellite to a monitoring center, seismic data could support automated detection, location, and early warning of hazardous flash floods.

In the Indian state of Uttarakhand, the Council of Scientific & Industrial Research–National Geophysical Research Institute, Hyderabad, operates a dense network of more than 80 seismic stations (6). The individual phases of the 7 February event are likely identifiable in the records at these stations. Efforts are currently under way to develop a rockslide and flood early warning system for the Himalayan region by using dense networks for seismic monitoring (5, 6), coupled with interpretation of satellite data, numerical modeling, and geomorphic analysis. Such a system could potentially provide crucial warning information shortly after initiation of an event, enabling evacuation at downstream locations. With climate change playing a major role in accelerating ice loss in the mountain glaciers (7), likely leading to increased frequency of flash floods, real-time seismic monitoring may

become the key to minimizing damage and casualties caused by these events.

**N. Purnachandra Rao<sup>1\*</sup>, Rajesh Rekapalli<sup>1</sup>, D. Srinagesh<sup>1</sup>, V. M. Tiwari<sup>1</sup>, Niels Hovius<sup>2</sup>, Kristen L. Cook<sup>2</sup>, Michael Dietze<sup>2</sup>**

<sup>1</sup>Council of Scientific and Industrial Research–National Geophysical Research Institute, Hyderabad, Telangana, India. <sup>2</sup>GFZ German Research Centre for Geosciences, Telegrafenberg, 14473 Potsdam, Germany.

\*Corresponding author.  
Email: pcrao.ngri@gmail.com

### REFERENCES AND NOTES

1. D. Petley, "The catastrophic landslide and flood in Chamoli in Uttarakhand: The sequence of events," *The Landslide Blog* (American Geophysical Union, 2021); <https://blogs.agu.org/landslideblog/2021/02/08/chamoli-2/>.
2. S. Stein, M. Wyss, *An Introduction to Seismology, Earthquakes, and Earth Structure* (Wiley-Blackwell, New York, 2009).
3. N. Casagli, F. Catani, C. Del Ventisette, G. Luzi, *Landslides* **7**, 291 (2010).
4. F. Dammeyer, J. R. Moore, C. Hammer, F. Haslinger, S. Loew, *J. Geophys. Res.* **121**, 351 (2016).
5. K. L. Cook, C. Andermann, F. Gimbert, B. R. Adhikari, N. Hovius, *Science* **362**, 53 (2018).
6. D. Srinagesh et al., *Curr. Sci.* **116**, 518 (2019).
7. J. M. Maurer, J. M. Schaefer, S. Rupper, A. Corley, *Sci. Adv.* **5**, eaav7266 (2019).

10.1126/science.abi4819

## Reimagining aquaculture in the Global South

Aquaculture has existed for millennia, reaching industrial scales in recent decades, and will play an increasingly



important role in feeding the world (1–6). As this industry grows, we must ensure that it is ecologically and socially sustainable. However, the current production process for the food given to farmed fish still threatens coastal ecosystems and the livelihoods of local fishers, especially in the Global South (2–7). Before aquaculture is scaled up further, its global environmental and socioeconomic footprint should be carefully reimagined.

Because small fishes are at the bottom of the trophic pyramid, overharvesting can lead to the collapse of local ecosystems (8, 9). In many places, these small fish also serve as vital, local food sources. Small fish caught in the Global South are increasingly used for fish meal production for livestock and aquaculture rather than for direct human consumption. These practices have disrupted food security in places such as Bangladesh, Gambia, and Ghana (7, 10), as affordable protein has shifted from poorer coastal communities to richer markets. Widespread illegal, unreported, and unregulated fisheries support unsustainable, large-scale fish meal production for regional use or for growing global markets.

To achieve the goals of the United Nations Decade of Ocean Science for Sustainable Development, we must develop strategies to make aquaculture truly sustainable in the Global South and beyond. This will require concerted support for technological advances such as new water recirculation and offshore innovations to efficiently rear species ranging from algae to large predator fish. To meet UN goals within a decade, we also need faster development of environmentally and socially responsible ingredients for fish feed (2–6) and effective policies to support sustainable development production schemes and human nutrition initiatives in affected coastal communities. Fisheries and aquaculture policies should include environmental governance strategies focused on seawater quality and biodiversity protection (such as farm level sustainability certification), comprehensive sustainability assessments, socioeconomic dimensions, capture fisheries, and improved feed ingredient production (1–6, 11, 12).

Michael S. Bank<sup>1,2\*</sup>, Peter W. Swarzenski<sup>3</sup>, Gabriella Bianchi<sup>1</sup>, Marc Metian<sup>3</sup>, Yong Sik Ok<sup>4,5</sup>, Carlos M. Duarte<sup>6</sup>

<sup>1</sup>Institute of Marine Research, Bergen, Norway.

<sup>2</sup>University of Massachusetts Amherst, Amherst, MA 01003, USA.

<sup>3</sup>International Atomic Energy Agency, Principality of Monaco, 98000, Monaco.

<sup>4</sup>Korea University, Seoul, Korea.

<sup>5</sup>Association of Pacific Rim Universities (APRU) Sustainable

Waste Management Program, Korea University, Seoul, Korea. <sup>6</sup>King Abdullah University of Science and Technology, Thuwal 23955, Saudi Arabia.

\*Corresponding author. Email: michael.bank@hi.no

## REFERENCES AND NOTES

1. Food and Agriculture Organization of the United Nations (FAO), "The state of world fisheries and aquaculture" (2020).
2. FAO Technical Guidelines for Responsible Fisheries, No. 5, Suppl. 4 (FAO, Rome, 2010); [www.fao.org/3/i1750e/i1750e00.htm](http://www.fao.org/3/i1750e/i1750e00.htm).
3. R. S. Cottrell *et al.*, *Nat. Food* **1**, 301 (2020).
4. A. G. J. Tacon, M. Metian, *Ambio* **38**, 294 (2009).
5. M. S. Bank *et al.*, *Environ. Sci. Technol.* **54**, 8506 (2020).
6. R. L. Naylor *et al.*, *Nature* **591**, 551 (2021).
7. I. Urbina, "Fish farming is feeding the globe. What's the cost for locals?" *The New Yorker* (2021).
8. E. K. Pikitch *et al.*, *Fish Fish.* **15**, 43 (2014).
9. A. D. M. Smith *et al.*, *Science* **333**, 1147 (2011).
10. V. Lauria *et al.*, *Sci. Tot. Env.* **640**, 1566 (2018).
11. C. C. Hicks *et al.*, *Nature* **574**, 95 (2019).
12. A. K. Farmer *et al.*, *One Earth* **4**, 28 (2020).

10.1126/science.abi5015

## Weather radars' role in biodiversity monitoring

Biodiversity is changing at an unprecedented rate, and long-term monitoring is key to quantifying these changes and identifying their drivers (1, 2). Weather radars are an essential tool for meeting these goals. However, recent policy changes make vital data unavailable. Data policy should be adjusted to take into account the broad role that weather radars play beyond meteorology.

In addition to providing essential meteorological data for weather forecasts, flood risk planning, storm warnings, and atmospheric and climatological research (3, 4), weather radars detect trillions of insects, bats, and birds in the air (5, 6). By collecting such data, they could provide an unrecognized service to society: long-term standardized monitoring of aerial biomass flows (7). In the United States, weather radar data have already been used at a continental scale for these purposes (6, 8). However, similar efforts in Europe (9, 10) are now fundamentally threatened.

The Operational Programme for the Exchange of Weather Radar Information (OPERA) coordinates the exchange of radar data among European national meteorological services (11). It serves as a central hub for accessing weather radar data in Europe, allowing those in search of data to make one request instead of contacting each meteorological service separately. However, because of budget cuts and resulting prioritization of meteorological products, OPERA now requests that national meteorological services submit cleaned rather than uncleaned

polar volume radar data (12). Uncleaned radar data include both meteorological and biological signals, whereas cleaned data exclude biological signals.

OPERA is currently establishing new centers for European weather radar data that could serve as ideal access points for diverse users and stakeholders. Access to uncleaned polar volume data at these data centers would boost their utility for aerial biodiversity monitoring and other multidisciplinary applications. To make this possible, OPERA should revise its data exchange policy to require that all countries submit uncleaned radar data, and Europe must build adequate data infrastructure to transfer and store the full data. National and international funding schemes and policy-makers such as the EU Commission should recognize and stimulate diverse applications of weather radar data, and OPERA should establish an open access data archive, which would facilitate long-term multidisciplinary research and biodiversity monitoring. If all regional associations of the World Meteorological Organization adopted similar policies, weather radars could be used for aerial biodiversity monitoring worldwide.

Judy Shamoun-Baranes<sup>1\*</sup>, Silke Bauer<sup>2\*</sup>, Jason W. Chapman<sup>3</sup>, Peter Desmet<sup>4</sup>, Adriaan M. Dokter<sup>5</sup>, Andrew Farnsworth<sup>5</sup>, Birgen Haest<sup>2</sup>, Jarmo Koistinen<sup>6</sup>, Bart Kranstauber<sup>1</sup>, Felix Liechti<sup>2</sup>, Tom H.E. Mason<sup>2</sup>, Cecilia Nilsson<sup>7</sup>, Raphael Nussbaumer<sup>2</sup>, Baptiste Schmid<sup>2</sup>, Nadja Weisshaupt<sup>6</sup>, Hidde Leijnse<sup>8,9</sup>

<sup>1</sup>Institute for Biodiversity and Ecosystem Dynamics, University of Amsterdam, Amsterdam, Netherlands.

<sup>2</sup>Department of Bird Migration, Swiss Ornithological Institute, Sempach, Switzerland.

<sup>3</sup>Center for Ecology and Conservation, University of Exeter, Penryn, Cornwall, UK.

<sup>4</sup>Research Institute for Nature and Forest (INBO), Brussels, Belgium.

<sup>5</sup>Center for Avian Population Studies, Cornell Lab of Ornithology, Cornell University, Ithaca, NY 14850, USA.

<sup>6</sup>Finnish Meteorological Institute, Helsinki, Finland.

<sup>7</sup>GLOBE Institute, Faculty of Health and Medical Sciences, University of Copenhagen, Copenhagen, Denmark.

<sup>8</sup>Royal Netherlands Meteorological Institute, De Bilt, Netherlands.

<sup>9</sup>Hydrology and Quantitative Water Management, Wageningen University & Research, Wageningen, Netherlands.

\*Corresponding author.

Email: shamoun@uva.nl; silke.s.bauer@gmail.com

## REFERENCES AND NOTES

1. S. Díaz *et al.*, *Science* **370**, 411 (2020).
2. V. Proença *et al.*, *Biol. Conserv.* **213**, 256 (2017).
3. E. Saltikoff *et al.*, *Bull. Am. Meteorol. Soc.* **100**, 1739 (2019).
4. S. Ansari *et al.*, *Bull. Am. Meteorol. Soc.* **99**, 189 (2018).
5. G. Hu *et al.*, *Science* **354**, 1584 (2016).
6. A. M. Dokter *et al.*, *Nat. Ecol. Evol.* **2**, 1603 (2018).
7. S. Bauer *et al.*, *BioScience* **67**, 912 (2017).
8. K. G. Horton *et al.*, *Nat. Clim. Chang.* **10**, 63 (2020).
9. J. Shamoun-Baranes *et al.*, *Movement Ecol.* **2**, 9 (2014).
10. C. Nilsson *et al.*, *Ecography* **42**, 876 (2019).
11. A. Huuskonen, E. Saltikoff, I. Holleman, *Bull. Am. Meteorol. Soc.* **95**, 897 (2014).
12. E. Saltikoff *et al.*, *Atmosphere* **10**, 320 (2019).

10.1126/science.abi4680



## TECHNICAL COMMENT ABSTRACTS

Comment on “Circadian rhythms in the absence of the clock gene *Bmal1*”

Elan Ness-Cohn, Ravi Allada, Rosemary Braun Ray *et al.* (Reports, 14 February 2020, p. 800) report apparent transcriptional circadian rhythms in mouse tissues lacking the core clock component BMAL1. To better understand these surprising results, we reanalyzed the associated data. We were unable to reproduce the original findings, nor could we identify reliably cycling genes. We conclude that there is insufficient evidence to support circadian transcriptional rhythms in the absence of *Bmal1*.

Full text: [dx.doi.org/10.1126/science.abe9230](https://doi.org/10.1126/science.abe9230)

Response to Comment on “Circadian rhythms in the absence of the clock gene *Bmal1*”

Sandipan Ray, Utham K. Valekunja, Alessandra Stangherlin, Steven A. Howell, Ambrosius P. Snijders, Gopinath Damodaran, Akhilesh B. Reddy Ness-Cohn *et al.* claim that our observations of transcriptional circadian rhythms in the absence of the core clock gene *Bmal1* in mouse skin fibroblast cells are supported by inadequate evidence. They claim that they were unable to reproduce some of the original findings with their reanalysis. We disagree with their analyses and outlook.

Full text: [dx.doi.org/10.1126/science.abf1930](https://doi.org/10.1126/science.abf1930)

Comment on “Circadian rhythms in the absence of the clock gene *Bmal1*”

Katharine C. Abruzzi, Cédric Gobet, Felix Naef, Michael Rosbash

Ray *et al.* (Reports, 14 February 2020, p. 800) recently claimed temperature-compensated, free-running mRNA oscillations in *Bmal1*<sup>-/-</sup> liver slices and skin fibroblasts. We reanalyzed these data and found far fewer reproducible mRNA oscillations in this genotype. We also note errors and potentially inappropriate analyses.

Full text: [dx.doi.org/10.1126/science.abf0922](https://doi.org/10.1126/science.abf0922)

Response to Comment on “Circadian rhythms in the absence of the clock gene *Bmal1*”

Sandipan Ray, Utham K. Valekunja, Alessandra Stangherlin, Steven A. Howell, Ambrosius P. Snijders, Gopinath Damodaran, Akhilesh B. Reddy

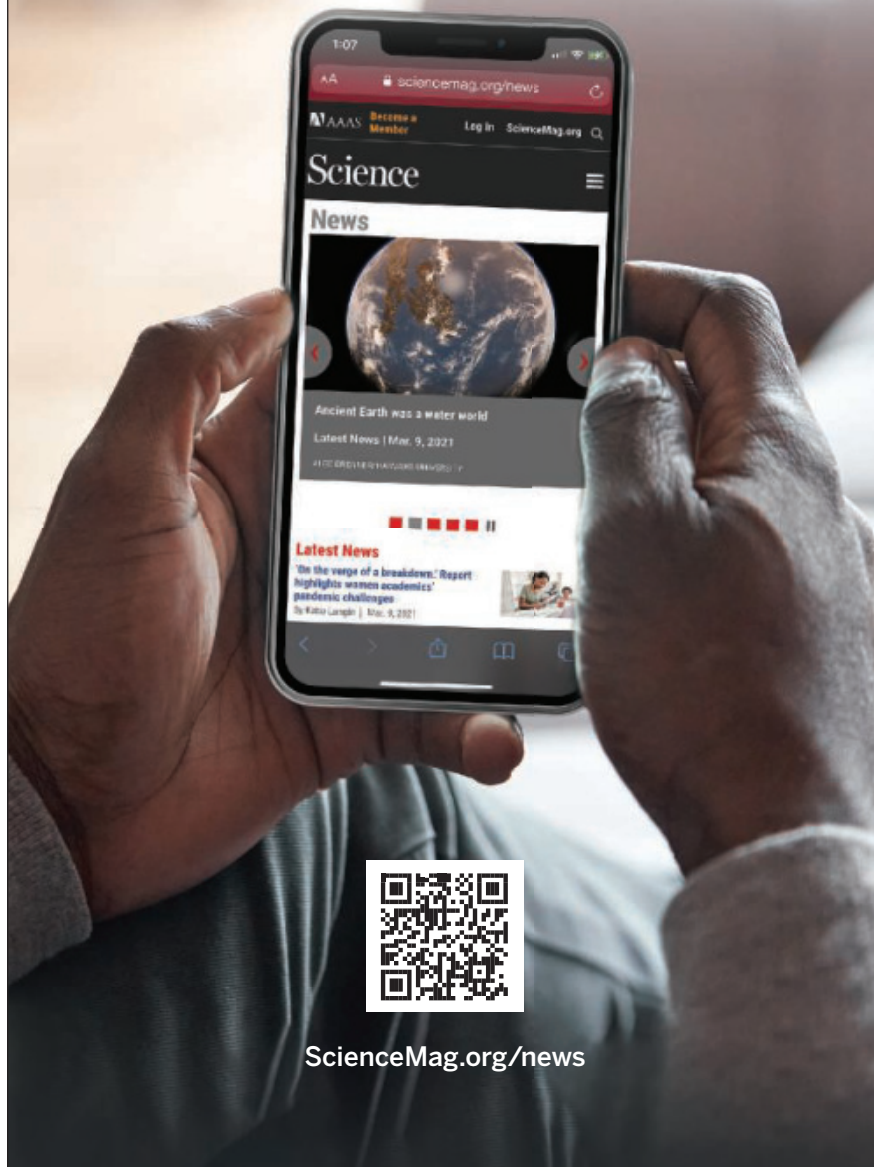
Abruzzi *et al.* argue that transcriptome oscillations found in our study in the absence of *Bmal1* are of low amplitude, statistical significance, and consistency. However, their conclusions rely solely on a different statistical algorithm from what we used. We provide statistical measures and additional analyses showing that our original analyses and observations are accurate. Further, we highlight independent lines of evidence indicating *Bmal1*-independent 24-hour molecular oscillations.

Full text: [dx.doi.org/10.1126/science.abf1941](https://doi.org/10.1126/science.abf1941)

# NEWS FROM Science

**Up-to-the-minute  
research and policy news  
you won't find in print**

Visit us online to read all the news coverage  
that there just wasn't enough room to print  
in this issue.



[ScienceMag.org/news](https://www.sciencemag.org/news)

# RESEARCH

## IN SCIENCE JOURNALS

Edited by Michael Funk

### FIRE ECOLOGY

#### Carbon cycling after boreal forest fire

**W**ildfire activity has been increasing in the boreal forests of the Northern Hemisphere, releasing carbon into the atmosphere from biomass and soil, with potential feedback to climate warming. In a long-term study, Mack *et al.* analyzed wildfire impacts on the carbon balance of boreal forest in Alaska, with particular focus on forest-regeneration patterns. After fire, the species composition in most of the study sites changed

from black spruce to a mixture of conifers and deciduous broadleaf tree species. The stands that had shifted to deciduous dominance stored fivefold more soil carbon than stands that returned to black spruce dominance. Therefore, the functional traits of deciduous trees compensated for the combustion loss of soil carbon, pointing to a potential mitigation of the feedback effect of boreal forest fire to climate warming. —AMS *Science*, this issue p. 280

A burned black spruce forest in Alaska quickly recovers, with deciduous species dominating after fires that burn deep.

### PALEONTOLOGY

#### Estimating dinosaur abundance

Estimating the abundance of a species is a common practice for extant species and can reveal many aspects of its ecology, evolution, and threat level. Estimating abundance for species that are extinct, especially those long extinct, is a much trickier endeavor. Marshall *et al.* used a relationship established between body size and population density in extant species to estimate traits such as density, distribution, total biomass, and species persistence for one

of the best-known dinosaurs, *Tyrannosaurus rex*, revealing previously hidden aspects of its population ecology. —SNV

*Science*, this issue p. 284

### SIGNAL TRANSDUCTION

#### Circuit design for control of metabolism

A transcriptional control mechanism in yeast that allows cells to respond to changes in nutrient concentrations works very much like a household light-dimmer switch. That is, the system separately controls whether gene expression is

“on” or “off” and the extent of gene expression. The galactose-responsive pathway is activated when yeast need to switch from metabolizing glucose to metabolizing galactose. Ricci-Tam *et al.* found that, rather than using two separate elements for the switch and dimmer controls, yeast use a single transcription factor, Gal4p, separately regulating its abundance (through transcriptional regulation) and its catalytic activity (through interaction with a protein-binding partner). Such regulation may be common and can allow responses to the environment on physiological and

evolutionary time scales. —LBR  
*Science*, this issue p. 292

### MEMBRANES

#### One-step purification and desalination

The purification of water for drinking purposes can require multiple filtration steps and technologies to remove contaminants such as salts and heavy metals. Some contaminants could have value if recovered, but these are often discharged in the waste streams. Uliana *et al.* describe a general approach for the fabrication of robust, tunable,



adsorptive membranes through the incorporation of porous aromatic framework (PAF) nanoparticles into ion exchange membranes such as those made from sulfonated polymers. Salts are removed using a series of cation and anion exchange membranes, and the PAF particles can be selected to capture specific target ions, such as those of copper, mercury, or iron. This allows for simultaneous desalination and decontamination of the water. —MSL

*Science*, this issue p. 292

## QUANTUM NETWORKS

### A three-node quantum network

Future quantum networks will provide the means to develop truly secure communication channels and will have applications in many other quantum-based technologies. Pompili *et al.* present a three-node remote quantum network based on solid-state spin qubits (nitrogen-vacancy centers in diamond) coupled by photons. The implementation of two quantum protocols on the network, entanglement distribution and entanglement swapping, illustrates a key platform for exploring, testing, and developing multinode quantum networks and quantum protocols. —ISO

*Science*, this issue p. 259

## 2D MATERIALS

### Twisted and nematic

Electrons in quantum materials can break rotational symmetry even when the underlying crystal lattice does not. This phenomenon, called nematicity, has been observed in many unconventional superconductors. Cao *et al.* found that magic-angle twisted bilayer graphene, in which superconductivity was recently discovered, also exhibits nematicity. The breaking of rotational symmetry was observed through transport measurements, which exhibited characteristic anisotropy. —JS

*Science*, this issue p. 264

## TUMOR IMMUNOLOGY

### Sequence of immunotherapy matters

Immune checkpoint blockade is clinically successful in various cancer types, yet many treated patients relapse. Determining effective combination therapies that induce systemic antitumor immunity is crucial. Immune checkpoint blockade combined with local radiation can improve antitumor responses, but it remains unclear how the sequence of these therapies alters efficacy. Wei *et al.* used mouse tumor models to demonstrate that treatment with anti-PD-1 after stereotactic body radiation therapy (SBRT) elicited superior systemic antitumor immunity, abscopal effects, and protection compared with anti-PD-1 given before SBRT. These data were correlated with improved intratumoral CD8<sup>+</sup> T cell responses and decreased CD8<sup>+</sup> T cell death in local and distant tumors. This work provides preclinical rationale for giving anti-PD-1 after SBRT in patients with cancer. —DAE

*Sci. Immunol.* **6**, eabg0117 (2021).

## IMAGING

### Pathogen-specific PET

*Enterobacterales* infections can affect diverse locations within the body, and multidrug-resistant strains are difficult to diagnose and treat. Ordonez *et al.* used an <sup>18</sup>F-labeled sugar alcohol as a bacteria-specific imaging agent to detect and monitor infections in patients. Positron emission tomography (PET)/computerized tomography imaging showed selective uptake of the tracer in *Enterobacterales* infections as opposed to other types of inflammation or cancer. Signal was reduced in sites of drug-susceptible infections in patients after treatment with antibiotics. The authors also showed that the imaging agent could differentiate bacterial infection from severe acute respiratory syndrome coronavirus 2 in a hamster model, supporting its use for bacteria-specific imaging. —CC

*Sci. Transl. Med.* **13**, eabe9805 (2021).

## IN OTHER JOURNALS

Edited by **Caroline Ash**  
and **Jesse Smith**



## EVOLUTION

### One problem, several solutions

Climate change is increasing desertification and increasing demands on heat and desiccation tolerance. To understand how species adapt to similar challenging environments, Colella *et al.* undertook a comparative genomic study of three species of *Peromyscus* mice that live in overlapping arid North American environments. *Peromyscus maniculatus* and *Peromyscus eremicus* are more closely related to each other than to *Peromyscus crinitus*. However, *P. maniculatus* occupies a broad range of habitats, and *P. eremicus* and *P. crinitus* are restricted to desert environments. The genes under selection for the desert species were found to be functionally similar, but overlapping selection was only observed for a gene involved in ribosomal function. Selective sweeps within the *Peromyscus* genomes have occurred, but each species appears to be under selection for different genes rather than following parallel evolutionary tracks. Therefore, even under similar environmental pressures, species can show different genomic adaptations. —LMZ

*J. Hered.* esab009 (2021).

The deer mouse, *Peromyscus maniculatus*, and its relatives have special genomic signatures for survival under desert conditions.

## EVOLUTIONARY COGNITION

### I know what I saw

Over the past several decades, evidence has accumulated showing that some nonhuman animals have conscious awareness. Some argue that despite high-level cognitive function, this may be occurring without conscious awareness of self. Unfortunately, we cannot ask animals to report

their experiences. Ben-Haim *et al.* exploited the human faculty for crossover double dissociation between nonconscious and conscious processing and applied it to rhesus macaques. People perform in completely opposite ways when they are aware of stimuli compared with when they are not. In the authors' visual tests, the macaques showed nearly identical responses to those of humans,

Bioluminescent bacteria in the Hawaiian bobtail squid, *Euprymna scolopes*, use a small molecule to coordinate light production and symbiosis.



## MICROBIAL SIGNALING Light conversation

In dedicated symbioses, a host organism can communicate with and provide a favorable environment for a single microbial species or even a single strain. The Hawaiian bobtail squid, *Euprymna scolopes*, has such a relationship with the bioluminescent bacterium *Vibrio fischeri*, which colonizes the squid's light organs. Zink *et al.* used imaging mass spectrometry to identify the cyclic dipeptide cyclo(D-histidyl-L-proline) as a contributor to biofilm formation, which is important for successful colonization. This molecule, which is likely produced by the bacteria in response to signals from the squid, was present in the colonized squid light organ and stimulated luminescence by the bacteria *in vitro*. —MAF *mBio* **12**, e03636-20 (2021).

indicating that the monkeys reacted differently when they were consciously aware that they had seen a stimulus compared with when they were not. —SNV

*Proc. Natl. Acad. Sci. U. S. A.* **118**, e2017543118 (2021).

## GEOLOGY

### Clay-driven compaction

Active gas reservoirs often subside during fossil fuel production. The mode of deformation, elastic or inelastic, is critical for assessing the production impact and hazard associated with extraction. Verberne *et al.* compared two drill cores from before and 50 years after gas production began in the Groningen field in the Netherlands. Detailed observations revealed that the permanent deformation was due to the fracture of feldspar grains,

which was driven by deformation of weak clay films. Better understanding this compaction is vital for modeling this site, along with others in various stages of production. —BG

*Geology* **10.1130/G48243.1** (2020).

## SIGNAL TRANSDUCTION

### Taking control of networks

Cell-regulatory signaling pathways can be mapped as binary interaction graphs and Boolean networks. Disruption of such networks might be translatable into cancer therapies, for instance, but it is difficult to predict the best ways to do this. Part of the problem may be the redundancy of causal connections in networks, which likely buffers critical circuits to

unintended perturbations but makes intended adjustments harder to define. Gates *et al.* propose a method to define the “effective graph” for interventions that can switch a system into a more desirable state. The method showed promise in analyzing complex networks controlling flower development and in a breast cancer model. Further testing in other biological systems will determine whether this difficult problem might yield to an effective graph method. —LBR

*Proc. Natl. Acad. Sci. U. S. A.* **118**, e2022598118 (2021).

## VACCINES

### Vaccines, economics, and evolution

Persistent respiratory tract infections caused by *Streptococcus*

*pneumoniae* (pneumococcus) lead to chronic antibiotic misuse. However, the dangers of death from antibiotic resistance, which leads to invasive disease, are growing. Using an agent-based model, Lu *et al.* demonstrate that, to some extent, we can vaccinate our way out of trouble. China accounts for about 12% of global childhood pneumococcal infections. Increasing pneumococcal conjugate vaccine coverage in this country would reduce the use of several common antibiotics. The authors tested various scenarios, including accelerated vaccine coverage, which after 5 years reduces antimicrobial resistance by up to 17% and cumulative costs by up to \$586 million USD. Thus, government investment in pneumococcal vaccination can bring both economic and evolutionary benefits. —CA

*Proc. Natl. Acad. Sci. U. S. A.* **118**, e2004933118 (2021).

## SCIENCE COMMUNICATION

### Creative destruction by review papers

Reviews allow scientists to curate, synthesize, and simplify individual findings into a coherent overview of a specific field. However, once the review is available, what happens to the individual findings themselves? McMahan and McFarland analyzed data from millions of journal articles to determine the consequences of review articles for the publications they cite. In general, the review is cited instead of the specific findings contained within, resulting in a loss of future citations for individual papers. Additionally, reviews lead to focused attention around key findings and the relations between them, resulting in a substantial simplification of a domain of knowledge. The authors describe this as “creative destruction,” in which those who do the science become overshadowed by those who summarize the science. —MMC

*Am. Sociol. Rev.* **10.1177/0003122421996323** (2021).



## REVIEW SUMMARY

## QUANTUM COMPUTING

## Materials challenges and opportunities for quantum computing hardware

Nathalie P. de Leon, Kohei M. Itoh, Dohun Kim, Karan K. Mehta, Tracy E. Northup, Hanhee Paik\*, B. S. Palmer, N. Samarth, Sorawis Sangtawesin, D. W. Steuerman

**BACKGROUND:** The past two decades have seen intense efforts aimed at building quantum computing hardware with the potential to solve problems that are intractable on classical computers. Several hardware platforms for quantum information processing (QIP) are under active development. To realize large-scale systems based on these technologies, we must achieve error rates much lower than have been demonstrated thus far in a scalable platform, or devise a new platform entirely. These activities will require major advances in materials science and engineering, new fabrication and synthesis techniques, and new measurement and materials analysis techniques. We identify key materials challenges that currently limit progress in five quantum computing hardware platforms, propose how to tackle these problems, and discuss some new areas for exploration. Addressing these materials challenges will necessitate interdisciplinary approaches from scientists and engineers beyond the current boundaries of the quantum computing field.

**ADVANCES:** This Review constitutes a roadmap of the current challenges and opportunities for

materials science in quantum information processing. We provide a comprehensive review of materials issues in each physical platform by describing the evidence that has led to the current understanding of each problem. For each platform, we present reasons for particular material choices, survey the current understanding of sources of noise and dissipation, describe materials limitations to scaling, and discuss potential new material platforms. Despite major differences among physical implementations in each hardware technology, there are several common themes: Material selection is driven by heterogeneity, impurities, and defects in available materials. Poorly controlled and characterized surfaces lead to noise and dissipation beyond limits imposed by bulk properties. Scaling to larger systems gives rise to new materials problems that are not evident in single-qubit measurements.

**OUTLOOK:** We identify three principal materials research frontiers of interest in this context. First, understanding the microscopic mechanisms that lead to noise, loss, and decoherence is crucial. This would be accelerated by

developing high-throughput methods for correlating qubit measurement with direct materials spectroscopy and characterization. Second, relatively few material platforms for solid-state QIP have been explored thus far, and the discovery of a new platform is often serendipitous. It is thus important to develop materials discovery pipelines that exploit directed, rational material searches in concert with high-throughput characterization approaches aimed at rapid screening for properties relevant to QIP. Third, there are several materials issues that do not affect single-qubit operations but appear as limitations in scaling to larger systems. Many problems faced by these platforms are reminiscent of some that have been addressed over the past five decades for complementary metal-oxide semiconductor electronics and other areas of the semiconductor industry, and approaches and solutions adopted by that industry may be applicable to QIP platforms. Materials issues will be critical to address in the coming years as we transition from noisy intermediate-scale systems to large-scale, fault-tolerant systems. Quantum computing began as a fundamentally interdisciplinary effort involving computer science, information science, and quantum physics; the time is now ripe for expanding the field by including new collaborations and partnerships with materials science. ■

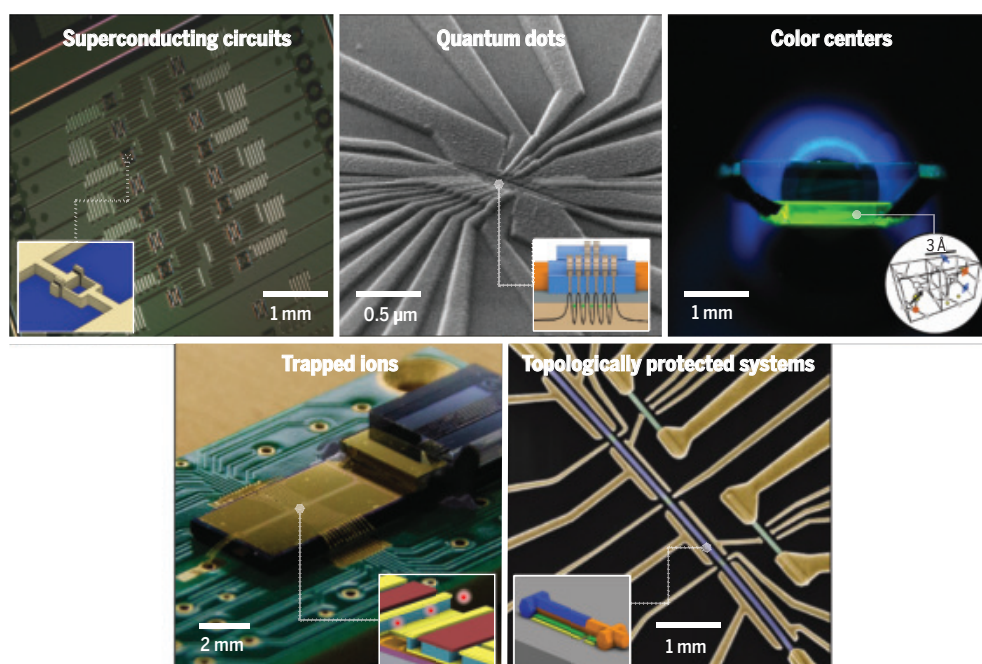
The list of author affiliations is available in the full article online.

\*Corresponding author. Email: hanhee.paik@us.ibm.com

Cite this article as N. P. de Leon *et al.*, *Science* **372**, eabb2823 (2021). DOI: 10.1126/science.abb2823

**READ THE FULL ARTICLE AT**  
<https://doi.org/10.1126/science.abb2823>

**Five quantum computing hardware platforms.** From top left: Optical image of an IBM superconducting qubit processor (inset: cartoon of a Josephson junction); SEM image of gate-defined semiconductor quantum dots (inset: cartoon depicting the confining potential); ultraviolet photoluminescence image showing emission from color centers in diamond (inset: atomistic model of defects); picture of a surface-electrode ion trap (inset: cartoon of ions confined above the surface); false-colored SEM image of a hybrid semiconductor/superconductor [inset: cartoon of an epitaxial superconducting Al shell (blue) on a faceted semiconducting InAs nanowire (orange)].



## RESEARCH ARTICLE SUMMARY

## MICROBIAL GENOMICS

## Diversity and functional landscapes in the microbiota of animals in the wild

Doron Levin<sup>†</sup>, Neta Raab<sup>†</sup>, Yishay Pinto<sup>†</sup>, Daphna Rothschild<sup>†</sup>, Gal Zanir, Anastasia Godneva, Nadav Mellul, David Futorian, Doran Gal, Sigal Leviatan, David Zeevi, Ido Bachelet<sup>‡</sup>, Eran Segal<sup>†,\*</sup>

**INTRODUCTION:** Animals in the wild are able to subsist on pathogen-infected and poisonous food and show immunity to various diseases. These characteristics may be contributed largely by the animals' microbiota. However, compared with the human microbiota, which has been extensively studied, the microbiota of animals in the wild has received less focus. In this study, we aimed to construct and functionally annotate a comprehensive database of microbiota sampled from wild animals in their natural habitats. Several considerations guided our sample collection and analysis strategy. First, we focused on sampling of animals from the wild, despite the many challenges that such sampling poses, because captivity was shown to alter the microbiome of several animal species. Second, to obtain a broad representation of wild ani-

mals, we sampled in four continents and from a diversity of animals with varied traits and feeding patterns. We hand-curated traits for each species, including dietary adaptations, activity hours, and social structures, allowing us to systematically study the relationships between microbiota composition and host phenotype. Finally, we adapted a metagenomic genome assembly pipeline and annotated the assembled genomes taxonomically and functionally, resulting in a broad collection of genomes that represents the microbial landscape of wildlife.

**RATIONALE:** It is becoming evident that animal microbiomes are a rich source of biological functions that may have biotechnological impact, including antibiotics, industrial enzymes,

and immunomodulators. Moreover, animals in the wild exhibit adaptations such as the safe consumption of rotting, pathogen-infected meat and poisonous plants; production of highly potent toxins; bioluminescence; specific immunity to various diseases and microbial pathogens; regenerative capabilities; and, in some species, extreme longevity. Some of these adaptations, such as toxin production and bioluminescence, are conferred, at least in part, by microbial symbionts living in and on the animal. However, despite these examples, a comprehensive view of the association between an animal's traits and its microbiota is still lacking. The microbiota of wild animals is also a natural reservoir for pathogens of both animals and humans, the mapping of which could elucidate the timing and routes of their transmission into the human population, as in the case of the current COVID-19 pandemic. Finally, mapping the microbiota of wild animals could also help in conservation efforts.

**RESULTS:** Our de novo constructed genomes, 75% of which belong to previously undescribed bacterial species, significantly improve the mapping of metagenomic sequencing reads from our animal samples. Notably, the rate at which new genomes are discovered is far from asymptote. We enriched many bacterial phyla with unknown species and found that some bacterial clades have distinctive functional properties relative to other bacteria in the same phylum. We found that the bacterial landscape differs between animal classes and discovered animal class-specific clusters of coexisting bacteria. We identified multiple pathways and orthologs that are significantly enriched in specific animal traits and showed that the functional landscape is associated with these traits. Some of these functions suggest intriguing new roles and properties of wildlife microbiomes. Moreover, we identified previously undescribed proteases in the microbiota of carrion eaters and show experimentally that they are capable of metabolizing bacterial toxins.

**CONCLUSION:** Overall, we present a large-scale annotated bacterial genome database of predominantly unknown species that were extracted from the guts of animals in the wild, identified a multitude of microbial patterns that are associated with the traits and taxonomy of these animals, and highlight its potential as a largely untapped resource for the discovery of new industrial enzymes and therapeutics. ■

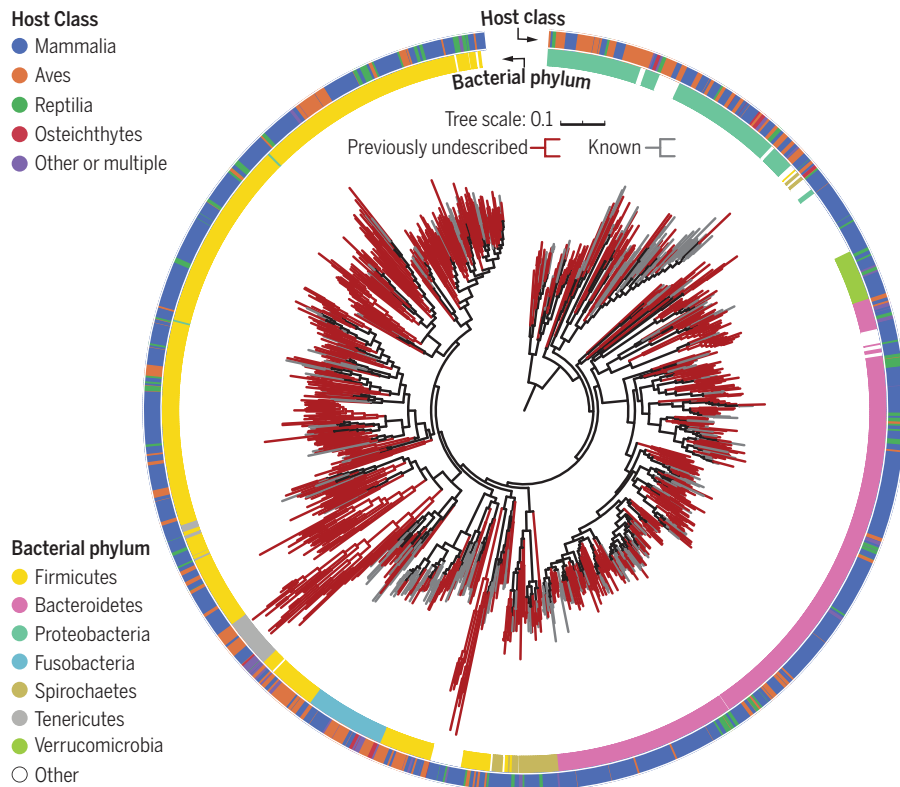
The list of author affiliations is available in the full article online.

<sup>†</sup>These authors contributed equally to this work.

<sup>‡</sup>These authors contributed equally to this work.

\*Corresponding author. Email: [eran.segal@weizmann.ac.il](mailto:eran.segal@weizmann.ac.il)  
Cite this article as D. Levin et al., *Science* 372, eabb5352 (2021). DOI: 10.1126/science.abb5352

**S** READ THE FULL ARTICLE AT  
<https://doi.org/10.1126/science.abb5352>



**A maximum likelihood alignment-based phylogenetic tree of the 1209 genomes assembled in this study.** The inner and outer colored rings denote bacterial phylum and host class, respectively. Clades of previously undescribed genomes are colored dark red.



## RESEARCH ARTICLE SUMMARY

## NEURODEVELOPMENT

Female-specific synaptic dysfunction and cognitive impairment in a mouse model of *PCDH19* disorder

Naosuke Hoshina, Erin M. Johnson-Venkatesh, Miyuki Hoshina, Hisashi Umemori\*

**INTRODUCTION:** Mutations of the X-linked *Protocadherin-19* (*PCDH19*) gene cause *PCDH19* disorder with epilepsy. *PCDH19* disorder is often associated with cognitive impairment and intellectual disabilities. Typically, X-linked disorders exhibit more severe phenotypes in males because of X-linked recessive inheritance. By contrast, symptoms of *PCDH19* disorder manifest in heterozygous females, whereas hemizygous males are largely asymptomatic. Why this unusual presentation occurs is not known. *PCDH19* encodes a single transmembrane protein that mediates cell-cell adhesion by homophilic binding through extracellular cadherin domains. A majority of *PCDH19* mutations found in *PCDH19* disorder alter sites in the extracellular domain of the *PCDH19* protein, suggesting that the mutations may affect *PCDH19* homophilic interactions and, as a result, cell-

cell adhesion. We examined the precise roles of *PCDH19* in the brain and the molecular, synaptic, and circuit bases of female-specific disease phenotypes.

**RATIONALE:** *PCDH19* disorder manifests in heterozygous females but not in hemizygous males. Because heterozygous females have a mixture of cells that express either the wild-type (WT) or mutant form of *PCDH19*, due to random X-inactivation, the mosaic expression of *PCDH19* is proposed to cause pathogenic symptoms. To understand the roles of *PCDH19* in the brain and the basis of female-specific disease phenotypes, we generated an animal model of *PCDH19* disorder (*Pcdh19* mutant mice). Because *PCDH19* protein is highly expressed at hippocampal mossy fiber synapses, we examined the role of *PCDH19* in mossy fiber

synaptic development, function, and relevant cognitive behaviors. We then investigated the molecular bases of the female heterozygote-specific defects in *Pcdh19* mutant mice. For this, we focused on the potential interaction between *PCDH19* and N-cadherin (Ncad), another cell adhesion molecule localized at synapses. *PCDH19* has been proposed to form a cis-complex with Ncad, which may mask the homophilic binding ability of Ncad. If the *PCDH19* expression is mosaic (*Pcdh19*<sup>HET♀</sup>), the *PCDH19*-Ncad cis-complex could not mediate intercellular signals between *PCDH19*-positive and -negative cells. This *PCDH19*-Ncad mismatch would result in reduced downstream intracellular signals and cellular defects. We tested this possibility at mossy fiber synapses.

**RESULTS:** We found that *Pcdh19*<sup>HET♀</sup> but not *Pcdh19*<sup>HEMI♂</sup> mice show defects in mossy fiber presynaptic development, without changes in mossy fiber targeting, dendritic spine development, or postsynaptic development. *Pcdh19*<sup>HET♀</sup> but not *Pcdh19*<sup>HEMI♂</sup> mice show decreased neurotransmitter release probability, impaired mossy fiber long-term potentiation (LTP), and deficits in mossy fiber-dependent cognitive function (pattern completion and separation). Furthermore, we found that *PCDH19* appears to interact with Ncad at mossy fiber synapses. In *Pcdh19*<sup>HET♀</sup> conditions, mismatch between *PCDH19* and Ncad impairs Ncad-dependent  $\beta$ -catenin signaling and mossy fiber presynaptic development. Overexpression of Ncad in *Pcdh19*<sup>HET♀</sup> mice restored not only  $\beta$ -catenin clustering in the mossy fiber synapses but also synaptic function, indicating that impaired Ncad function underlies the phenotype observed in *Pcdh19*<sup>HET♀</sup> mice in vivo.

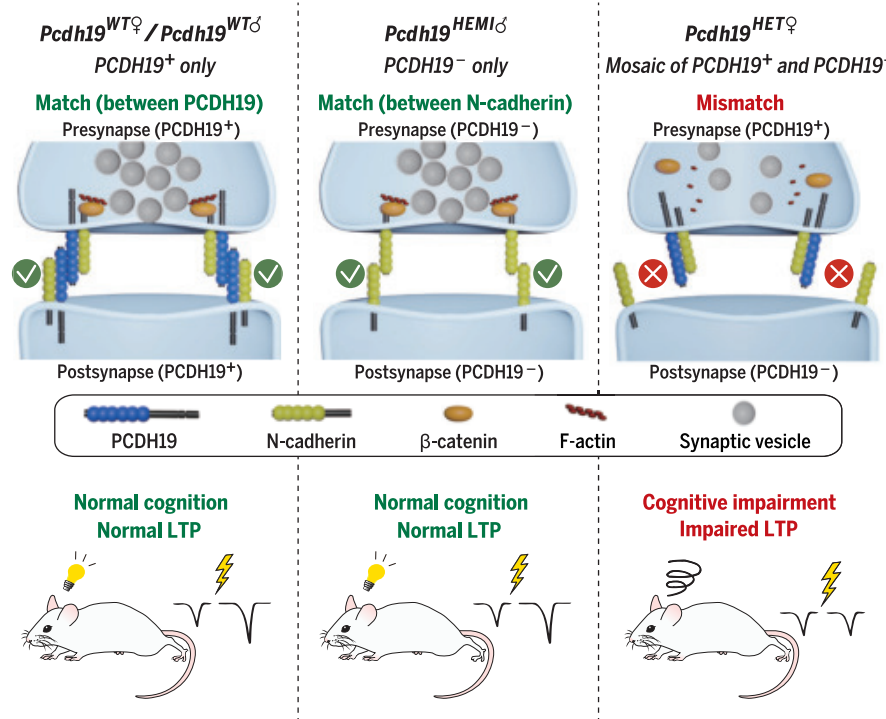
**CONCLUSION:** *Pcdh19*<sup>HET♀</sup> and not *Pcdh19*<sup>HEMI♂</sup> mice show mossy fiber presynaptic dysfunction and cognitive impairments, mimicking the female-specific manifestation of *PCDH19* disorder. In *Pcdh19*<sup>HET♀</sup> mice, mismatched interactions between two cell-adhesion molecules, *PCDH19* and Ncad, impair Ncad-dependent signaling and, subsequently, presynaptic development. *Pcdh19*<sup>WT</sup> and *Pcdh19*<sup>HEMI♂</sup> are spared because they have matched *PCDH19* or Ncad interactions. This study not only uncovers distinctive female-specific disease mechanisms but also suggests possible strategies to treat the disorder on the basis of these molecular interactions. ■

Department of Neurology, F. M. Kirby Neurobiology Center, Boston Children's Hospital, Harvard Medical School, Boston, MA 02115, USA.

\*Corresponding author. Email: hisashi.umemori@childrens.harvard.edu

Cite this article as N. Hoshina et al., *Science* 372, eaaz3893 (2021). DOI: 10.1126/science.aaz3893

**S** READ THE FULL ARTICLE AT  
https://doi.org/10.1126/science.aaz3893



**PCDH19-Ncad mismatch underlies female-specific *PCDH19* disorder.** At *Pcdh19*<sup>WT</sup> synapses, *PCDH19*-Ncad cis-complex mediates trans-synaptic signaling through *PCDH19* homophilic matching and organizes presynaptic terminals. At *Pcdh19*<sup>HEMI♂</sup> synapses, unmasked Ncad can mediate trans-synaptic signaling through Ncad homophilic matching. However, at *Pcdh19*<sup>HET♀</sup> synapses between *PCDH19*-positive and *PCDH19*-negative neurons, *PCDH19*-Ncad cis-complex cannot trans-synaptically bind Ncad because of mismatching, leading to impaired presynaptic development, LTP, and cognition.

## RESEARCH ARTICLE SUMMARY

## CORONAVIRUS

## SARS-CoV-2 within-host diversity and transmission

Katrina A. Lythgoe<sup>†\*</sup>, Matthew Hall<sup>†\*</sup>, Luca Ferretti, Mariateresa de Cesare, George MacIntyre-Cocket, Amy Trebes, Monique Andersson, Newton Otecko, Emma L. Wise, Nathan Moore, Jessica Lynch, Stephen Kidd, Nicholas Cortes, Matilde Mori, Rebecca Williams, Gabrielle Vernet, Anita Justice, Angie Green, Samuel M. Nicholls, M. Azim Ansari, Lucie Abeler-Dörner, Catrin E. Moore, Timothy E. A. Peto, David W. Eyre, Robert Shaw, Peter Simmonds, David Buck, John A. Todd on behalf of the Oxford Virus Sequencing Analysis Group (OVSG)<sup>‡</sup>, Thomas R. Connor, Shirin Ashraf, Ana da Silva Filipe, James Shepherd, Emma C. Thomson, The COVID-19 Genomics UK (COG-UK) Consortium<sup>§</sup>, David Bonsall, Christophe Fraser, Tanya Golubchik\*

**INTRODUCTION:** Genome sequencing at an unprecedented scale during the severe acute respiratory syndrome coronavirus 2 (SARS-CoV-2) pandemic is helping to track spread of the virus and to identify new variants. Most of this work considers a single consensus sequence for each infected person. Here, we looked beneath the consensus to analyze genetic variation within viral populations making up an infection and studied the fate of within-host mutations when an infection is transmitted to a new individual. Within-host diversity offers the means to help confirm direct transmission and identify new variants of concern.

**RATIONALE:** We sequenced 1313 SARS-CoV-2 samples from the first wave of infection in the United Kingdom. We characterized within-host diversity and dynamics in the context of transmission and ongoing viral evolution.

**RESULTS:** Within-host diversity can be described by the number of intrahost single nucleotide variants (iSNVs) occurring above a given minor allele frequency (MAF) threshold. We found that in lower-viral-load samples, stochastic sampling effects resulted in a higher variance in MAFs, leading to more iSNVs being detected at any threshold. Based on a subset of 27 pairs of high-viral-load replicate RNA samples (>50,000 uniquely mapped veSEQ reads, corresponding to a cycle threshold of ~22), iSNVs with a minimum 3% MAF were highly reproducible. Comparing samples from two time points from 41 individuals, taken on average 6 days apart (interquartile ratio 2 to 10), we observed a dynamic process of iSNV generation and loss. Comparing iSNVs among 14 household contact pairs, we estimated transmission bottleneck sizes of one to eight viruses. Consensus differences between

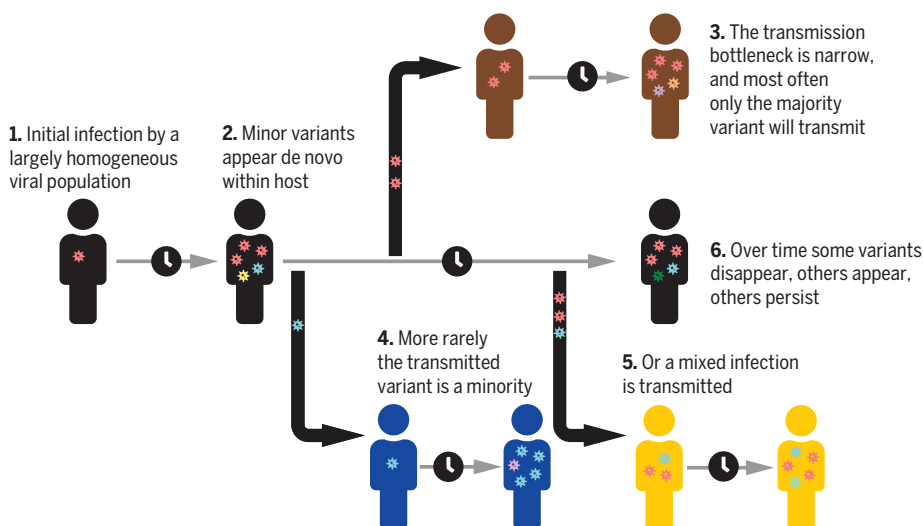


#### Diagram showing low SARS-CoV-2 within-host genetic diversity and narrow transmission bottleneck.

Individuals with high viral load typically have few, if any, within-host variants. Narrow transmission bottlenecks mean that the major variant in the source individual was typically transmitted and the minor variants lost. Occasionally, the minor variant was transmitted, leading to a consensus change, or multiple variants were transmitted, resulting in a mixed infection. Credit: FontAwesome, licensed under CC BY 4.0.

individuals in the same household, where sample depth allowed iSNV detection, were explained by the presence of an iSNV at the same site in the paired individual, consistent with direct transmission leading to fixation. We next focused on a set of 563 high-confidence iSNV sites that were variant in at least one high-viral-load sample (>50,000 uniquely mapped); low-confidence iSNVs unlikely to represent genomic diversity were excluded. Within-host diversity was limited in high-viral-load samples (mean 1.4 iSNVs per sample). Two exceptions, each with >14 iSNVs, showed variant frequencies consistent with coinfection or contamination. Overall, we estimated that 1 to 2% of samples in our dataset were coinfecting and/or contaminated. Additionally, one sample was coinfecting with another coronavirus (OC43), with no detectable impact on diversity. The ratio of nonsynonymous to synonymous ( $dN/dS$ ) iSNVs was consistent with within-host purifying selection when estimated across the whole genome [ $dN/dS = 0.55$ , 95% confidence interval (95% CI) = 0.49 to 0.61] and for the Spike gene ( $dN/dS = 0.60$ , 95% CI = 0.45 to 0.82). Nevertheless, we observed Spike variants in multiple samples that have been shown to increase viral infectivity (L5F) or resistance to antibodies (G446V and A879V). We observed a strong association between high-confidence iSNVs and a consensus change on the phylogeny (153 cases), consistent with fixation after transmission or de novo mutations reaching consensus. Shared variants that never reached consensus (261 cases) were not phylogenetically associated.

**CONCLUSION:** Using robust methods to call within-host variants, we uncovered a consistent pattern of low within-host diversity, purifying selection, and narrow transmission bottlenecks. Within-host emergence of vaccine and therapeutic escape mutations is likely to be relatively rare, at least during early infection, when viral loads are high, but the observation of immune-escape variants in high-viral-load samples underlines the need for continued vigilance. ■

The list of author affiliations is available in the full article online.  
\*Corresponding author. Email: Tanya.Golubchik@bdi.ox.ac.uk (T.G.); Katrina.Lythgoe@bdi.ox.ac.uk (K.A.L.); Matthew.Hall@bdi.ox.ac.uk (M.H.)

†These authors contributed equally to this work.

‡The full list of the OVSG members is provided in the supplementary materials.

§The full list of names and affiliations of COG-UK members is provided in the supplementary materials.

This is an open-access article distributed under the terms of the Creative Commons Attribution license (<https://creativecommons.org/licenses/by/4.0/>), which permits unrestricted use, distribution, and reproduction in any medium, provided the original work is properly cited. Cite this article as K. A. Lythgoe et al., *Science* 372, eabg0821 (2021). DOI: 10.1126/science.abg0821

**READ THE FULL ARTICLE AT**  
<https://doi.org/10.1126/science.abg0821>



## RESEARCH ARTICLE SUMMARY

## GUT PHYSIOLOGY

## An intercrypt subpopulation of goblet cells is essential for colonic mucus barrier function

Elisabeth E. L. Nyström<sup>†</sup>, Beatriz Martinez-Abad<sup>†</sup>, Liisa Arike, George M. H. Birchenough, Eric B. Nonnecke, Patricia A. Castillo, Frida Svensson, Charles L. Bevins, Gunnar C. Hansson, Malin E. V. Johansson\*

**INTRODUCTION:** An intricate balance with our intestinal microbes is pivotal to human health. A key interface of host-microbial interactions occurs in the mucus that covers the intestinal epithelial surface. In the colon, the mucus layer serves as a barrier that inhibits direct epithelial contact with the dense population of microbes. Defects in this system are a hallmark of colitis. The mucus layer is structurally dependent on the polymeric mucin MUC2, which is synthesized by goblet cells (GCs)—specialized secretory cells classically viewed as a homogeneous cell type. Studies identifying divergent functional features in GC subpopulations, including differential mucus biosynthesis rates and responses to bacteria, suggest that GC populations may in fact be heterogeneous.

**RATIONALE:** In the present study, we characterized intestinal GC expression diversity and defined how a specific GC subtype, localized in the intercrypt surface epithelium, functionally contributes to the formation of the mucus barrier.

**RESULTS:** Using mCherry-MUC2 transgenic mice to sort and isolate GCs, we generated transcriptomic and proteomic profiles to characterize the GC expression landscape in

both the small intestine and the colon. Single-cell transcriptomic analysis revealed several distinct GC clusters in each tissue region, which segregated into two separate trajectories. One trajectory had enriched expression of known GC-specific genes (e.g., *Cla1* and *Fcgbp*) and was designated as canonical GCs. Conversely, the other trajectory was enriched for the expression of genes typically associated with enterocytes (e.g., *Dmbt1* and *Gsdmc4*), so we designated this trajectory as noncanonical.

In the colon, the most differentiated GCs are the high-mucus turnover cells localized to the surface epithelium between crypts, which were designated as intercrypt GCs (icGCs). These cells had expression profiles that were distinct from those of crypt-resident GCs, so we investigated their role in forming the mucus barrier. We exploited the lectin-binding features of mucus to resolve the three-dimensional organization of mucus in live tissue explants. Results demonstrated that icGCs secreted distinct mucus that filled the spatial regions between mucus plumes secreted from crypt openings. The intercrypt mucus was impenetrable to bacteria-sized beads; however, it was more penetrable to smaller molecules compared with crypt plume mucus. Penetrable surface mucus may be important for the absorption of ions

and other compounds, whereas denser mucus within the crypt compartment contributes to the shielding of the stem cell niche.

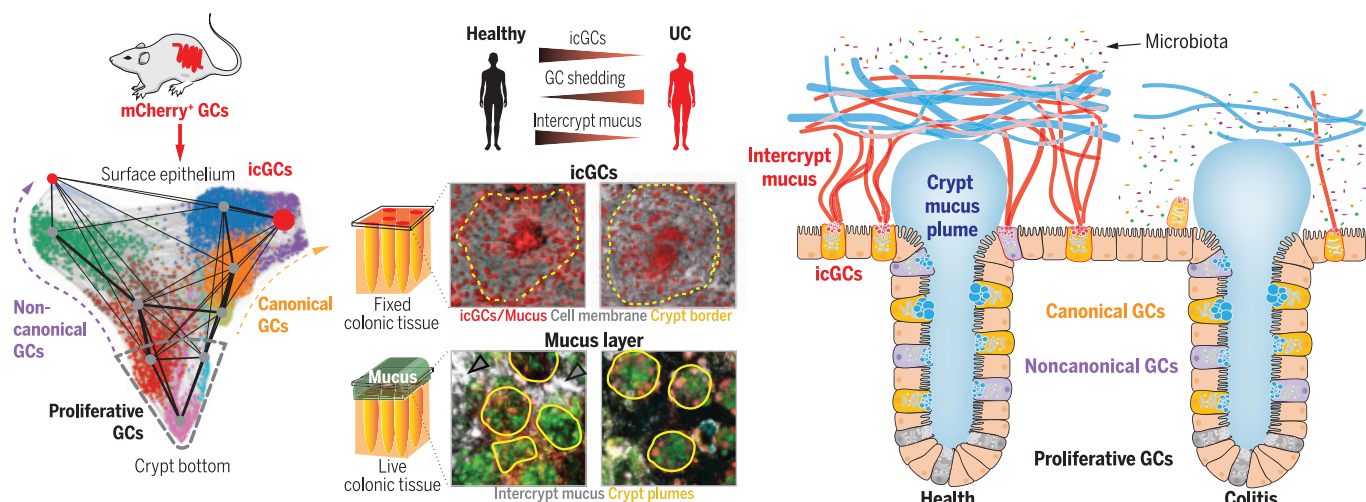
Both mucus subtypes appear to be important for the overall protective function of mucus, because a barrier impenetrable to bacteria was formed by the mixed, net-like organization of intercrypt and crypt plume mucus. A mouse model with dysfunctional icGCs lacking normal intercrypt mucus exhibited an inadequate mucus barrier and was more susceptible to both chemically induced and spontaneous (age-dependent) colitis, which demonstrates the indispensable role of icGCs in maintaining a functional mucus barrier. Furthermore, biopsies from patients with ulcerative colitis—including those in remission—exhibited increased GC shedding and reduced icGC numbers. These characteristics were associated with structural defects in the mucus barrier, including gaps in the intercrypt mucus that exposed areas of the surface epithelium.

**CONCLUSION:** The current study identifies GCs as a heterogeneous population of cells with diverse functional features that indicate a dynamic cellular system. GCs at different locations along the crypt-surface axis contribute to a functional mucus barrier that protects the epithelium from microorganisms. The icGCs possess a specific role in mucus organization, where their malfunction is associated with colitis in both mice and humans. ■

The list of author affiliations is available in the full article online.  
<sup>†</sup>These authors contributed equally to this work.

\*Corresponding author. Email: malin.johansson@medkem.gu.se  
 Cite this article as E. E. L. Nyström et al., *Science* 372, eaabb1590 (2021). DOI: 10.1126/science.aabb1590

**S READ THE FULL ARTICLE AT**  
<https://doi.org/10.1126/science.aabb1590>



**Diversity of GC expression and function.** Intestinal GCs can be divided into several distinct clusters that form canonical and noncanonical trajectories, and gene expression profiles outline their topographical position. The specialized surface GC type—the icGCs—secrete mucus crucial for forming a protective barrier between bacteria and the epithelium. Depletion of icGCs impairs mucus function, a phenomenon observed in ulcerative colitis (UC) patients.

## RESEARCH ARTICLE SUMMARY

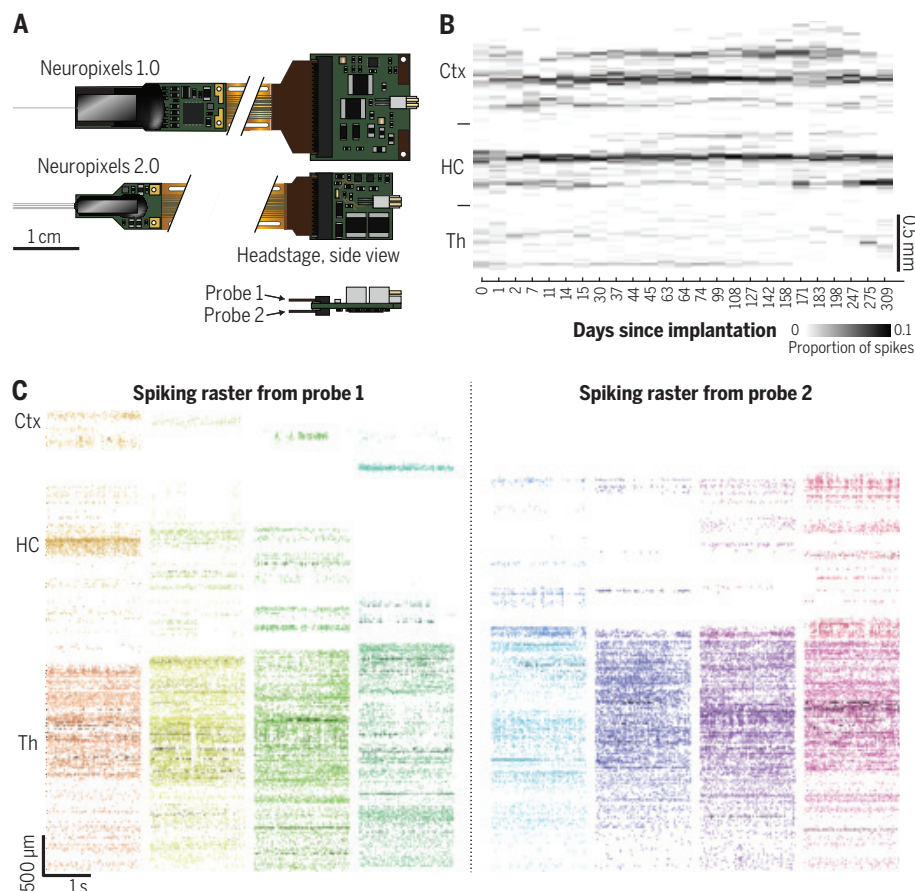
## NEUROSCIENCE

# Neuropixels 2.0: A miniaturized high-density probe for stable, long-term brain recordings

Nicholas A. Steinmetz<sup>\*†</sup>, Cagatay Aydin<sup>†</sup>, Anna Lebedeva<sup>†</sup>, Michael Okun<sup>†</sup>, Marius Pachitariu<sup>†</sup>, Marius Bauza, Maxime Beau, Jai Bhagat, Claudia Böhm, Martijn Broux, Susu Chen, Jennifer Colonell, Richard J. Gardner, Bill Karsh, Fabian Kloosterman, Dimitar Kostadinov, Carolina Mora-Lopez, John O'Callaghan, Junchol Park, Jan Putzeys, Britton Sauerbrei, Rik J. J. van Daal, Abraham Z. Vollan, Shiwei Wang, Marleen Welkenhuysen, Zhiwen Ye, Joshua Dudman, Barundeb Dutta, Adam W. Hantman, Kenneth D. Harris, Albert K. Lee, Edvard I. Moser, John O'Keefe, Alfonso Renart, Karel Svoboda, Michael Häusser, Sebastian Haesler, Matteo Carandini<sup>\*</sup>, Timothy D. Harris<sup>\*</sup>

**INTRODUCTION:** Electrode arrays based on complementary metal-oxide semiconductor silicon fabrication technology, such as Neuropixels probes, have enabled recordings of thousands of individual neurons in the living brain. These tools have led to discoveries about the

brain-wide correlates of perception and action, primarily when used in acute, head-fixed recordings. To study the dynamics of neuronal processing across time scales, however, it is necessary to record from neurons over weeks and months, ideally during un-



**Neuropixels 2.0 probes allow unprecedented recordings.** (A) Comparison of the Neuropixels 1.0 and 2.0 device designs. The Neuropixels 2.0 device is miniaturized and has four shanks. Two probes can be hosted per headstage. (B) Pattern of spiking activity across the cortex (Ctx), hippocampus (HC), and thalamus (Th) recorded over >300 days. (C) Example spiking rasters from two Neuropixels 2.0 probes chronically implanted in a mouse, showing spikes recorded on 6144 of the 10,240 sites available across the two probes. Eight sequential recordings (different colors) were performed from 768 channels each.

restrained behavior and in small animals, such as mice.

**RATIONALE:** To this end, we designed a miniaturized probe, called Neuropixels 2.0, with 5120 recording sites distributed over four shanks. The probe and headstage were miniaturized to about one-third of the original size (i.e., the size of the Neuropixels 1.0 probe), so that two probes and their single headstage weigh only ~1.1 g, without loss of channel count (384 channels per probe). Using two four-shank probes provides 10,240 recording sites in one implant. To achieve stable recordings despite brain movement, we optimized the recording site arrangement. The probe has a denser, linearized geometry that allows for post hoc computational motion correction using a newly designed algorithm. This algorithm, implemented in the Kilosort 2.5 software package, determines the motion over time from the spiking data and corrects it with spatial resampling, as in image registration.

**RESULTS:** To validate these probes for long-term recordings, we implanted them chronically in 21 rats and mice in six laboratories. Twenty of these 21 implants succeeded and yielded neurons over weeks and months while retaining good signal quality. The probes were reliably recoverable using newly engineered implant fixture designs.

To test the performance of the motion correction algorithm, we performed recordings with known imposed motion of the probe relative to the brain. The algorithm improved the yield of stable neurons and largely eliminated the impact of motion on the recording.

A version of this algorithm allowed the recording of neurons stably across days. We assessed this by “fingerprinting” individual chronically recorded neurons in the primary visual cortex using their distinctive visual responses to a battery of images. Neuron tracking was >90% successful for up to 2 weeks and >80% successful for up to 2 months.

**CONCLUSION:** This work demonstrates a suite of electrophysiological tools comprising a miniaturized high-density probe, recoverable chronic implant fixtures, and algorithms for automatic post hoc motion correction. These tools enable an order-of-magnitude increase in the number of sites that can be recorded in small animals, such as mice, and the ability to record from them stably over long time scales. ■

The list of author affiliations is available in the full article online.

<sup>\*</sup>Corresponding author. Email: nick.steinmetz@gmail.com (N.A.S.); m.carandini@ucl.ac.uk (M.C.); harrist@janelia.hhmi.org (T.D.H.)

<sup>†</sup>These authors contributed equally to this work.

Cite this article as N. A. Steinmetz *et al.*, *Science* 372, eabf4588 (2021). DOI: 10.1126/science.abf4588

**READ THE FULL ARTICLE AT**  
<https://doi.org/10.1126/science.abf4588>



## RESEARCH ARTICLES

## QUANTUM NETWORKS

## Realization of a multinode quantum network of remote solid-state qubits

M. Pompili<sup>1,2,†</sup>, S. L. N. Hermans<sup>1,2,†</sup>, S. Baier<sup>1,2,†,‡</sup>, H. K. C. Beukers<sup>1,2</sup>, P. C. Humphreys<sup>1,2,§</sup>, R. N. Schouten<sup>1,2</sup>, R. F. L. Vermeulen<sup>1,2</sup>, M. J. Tiggeleman<sup>1,2,¶</sup>, L. dos Santos Martins<sup>1,2</sup>, B. Dirkse<sup>1,2</sup>, S. Wehner<sup>1,2</sup>, R. Hanson<sup>1,2,\*</sup>

The distribution of entangled states across the nodes of a future quantum internet will unlock fundamentally new technologies. Here, we report on the realization of a three-node entanglement-based quantum network. We combine remote quantum nodes based on diamond communication qubits into a scalable phase-stabilized architecture, supplemented with a robust memory qubit and local quantum logic. In addition, we achieve real-time communication and feed-forward gate operations across the network. We demonstrate two quantum network protocols without postselection: the distribution of genuine multipartite entangled states across the three nodes and entanglement swapping through an intermediary node. Our work establishes a key platform for exploring, testing, and developing multinode quantum network protocols and a quantum network control stack.

Future quantum networks sharing entanglement across multiple nodes (1, 2) will enable a range of applications such as secure communication, distributed quantum computing, enhanced sensing, and fundamental tests of quantum mechanics (3–8). Efforts in the past decade have focused on realizing the building blocks of such a network: quantum nodes capable of establishing remote entangled links as well as locally storing, processing, and reading out quantum information.

Entanglement generation through optical channels between a pair of individually controlled qubits has been demonstrated with trapped ions and atoms (9–12), diamond nitrogen-vacancy (NV) centers (13, 14), and quantum dots (15, 16). In addition, a number of quantum network primitives have been explored on these elementary two-node links, including nonlocal quantum gates (17, 18) and entanglement distillation (19). Moving these qubit platforms beyond two-node experiments has so far remained an outstanding challenge owing to the combination of several demanding requirements. Multiple high-performance quantum nodes are needed that include a communication qubit with an optical interface as well as an efficient memory qubit for storage and processing. Additionally, the individual entanglement links need to be embedded into a multinode quantum network, requiring a

scalable architecture and multinode control protocols.

Here, we report on the realization and integration of all elements of a multinode quantum network: optically mediated entanglement links connected through an extensible architecture, local memory qubit and quantum logic, and real-time heralding and feed-forward operations. We demonstrate the full operation of

the multinode network by running two key quantum network protocols. First, we establish Greenberger-Horne-Zeilinger (GHZ) entangled states across the three nodes. Such distributed genuine multipartite entangled states are a key ingredient for many network applications (2) such as anonymous transmission (20), secret sharing (21), leader election (22), and clock stabilization (8). Second, we perform entanglement swapping through an intermediary node, which is the central protocol for entanglement routing on a quantum network enabling any-to-any connectivity (23, 24). Owing to efficient coherence protection on all qubits, combined with real-time feed-forward operations, these protocols are realized in a heralded fashion, delivering the final states ready for further use. This capability of heralding successful completion of quantum protocols is critical for scalability; its demonstration here presents a key advance from earlier experiments using photons (25) and quantum memories (26).

Our network is composed of three spatially separated quantum nodes (Fig. 1, A and B), labeled Alice, Bob, and Charlie. Each node consists of an NV center electronic spin as a communication qubit. In addition, the middle node Bob uses a carbon-13 nuclear spin as a memory qubit. Initialization and single-shot readout of the communication qubits are performed through resonant optical excitation and measurement of state-dependent

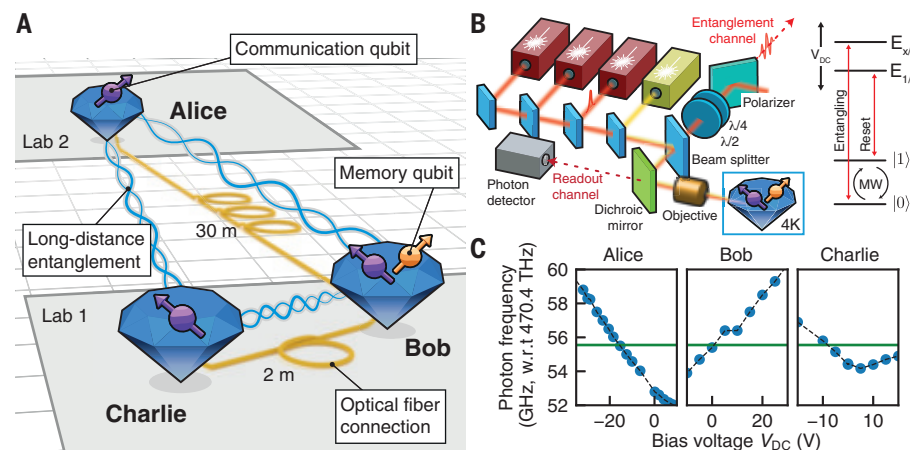


**Fig. 1. The three-node quantum network.** (A) Layout of the network. Three nodes, labeled Alice, Bob, and Charlie, are located in two separate labs. Each node contains an NV center communication qubit (purple). At Bob, an additional nuclear spin qubit (orange) is used in the presented experiments. Fiber connections between the nodes (lengths indicated) enable remote entanglement generation on the links Alice-Bob and Bob-Charlie, which, combined with local quantum logic, allow for entanglement to be shared between all nodes (wiggly lines). (B) On the left is a simplified schematic of the optical setup at each node [see fig. S1, table S1, and (27) for additional details]. On the right is a diagram of the relevant levels of the electronic spin qubit, showing optical transitions for remote entanglement generation and readout ("entangling"), qubit reset ("reset"), and resonant microwaves ("MW") for qubit control (see figs. S2 and S3 for additional details). The memory qubit at Bob is initialized, controlled, and read out via the electronic qubit (fig. S4). Optical transition frequencies are tuned via the dc bias voltages ( $V_{DC}$ ).  $\lambda/2$  ( $\lambda/4$ ) is a half-waveplate (quarter-waveplate);  $E_{xy}$  and  $E_{1/2}$  are electronic excited states. (C) Tuning of the optical "entangling" transition at each of the three nodes. The solid line is the working point, 470.45555 THz; the dashed line is a guide to the eye. w.r.t., with respect to.

<sup>1</sup>QuTech, Delft University of Technology, 2628 CJ Delft, Netherlands. <sup>2</sup>Kavli Institute of Nanoscience, Delft University of Technology, 2628 CJ Delft, Netherlands.

\*Corresponding author. Email: r.hanson@tudelft.nl

†These authors contributed equally to this work.

‡Present address: Institut für Experimentalphysik, Universität Innsbruck, Technikerstraße 25, 6020 Innsbruck, Austria.

§Present address: DeepMind, London, UK.

¶Present address: QBlox, 2628 CJ Delft, Netherlands.

fluorescence (14). Universal quantum logic on the electronic-nuclear register is achieved through tailored microwave pulses delivered on chip (27). The nodes are connected through an optical fiber network for the quantum signals, as well as classical communication channels for synchronizing the control operations and relaying heralding signals (see below).

Remote entanglement generation hinges on indistinguishability between emitted photons. For NV centers in high-purity low-strain diamond devices, the optical transition frequencies show relatively minor variations (few GHz). We remove the remaining offsets by using dc Stark tuning at each node with bias fields generated on chip (Fig. 1C). We are thus able to bring the relevant optical transitions of all three nodes to the same frequency, which we choose to be the zero-bias frequency of Bob.

### Establishing remote entanglement in a network architecture

To generate remote entanglement between a pair of nodes (i.e., one elementary link), a single-photon protocol is used (28, 29) (Fig. 2A). The communication qubits of the nodes are each prepared in a superposition state  $|\alpha\rangle = \sqrt{\alpha}|0\rangle + \sqrt{1-\alpha}|1\rangle$ . At each node, pulsed optical excitation, which is resonant only for the  $|0\rangle$  state, and subsequent photon emission deterministically create an entangled state between the communication qubit and the presence-absence of a photon (the flying qubit). The photonic modes from the two nodes are then interfered on a beam splitter, removing the which-path information. The beam splitter closes an effective interferometer formed by the optical excitation and collection paths. Detection of a single photon after the beam splitter heralds the state  $|\psi^\pm\rangle \approx (|01\rangle \pm e^{i\Delta\theta}|10\rangle)/\sqrt{2}$  between the two communication qubits, where the  $\pm$  sign depends on which of the two detectors clicked and  $\Delta\theta$  is the optical phase difference between the two arms of the effective interferometer (27). Experimentally, this phase difference is set to a known value by stabilizing the full optical path using a feedback loop (14, 16). This scheme yields states at maximum fidelity  $1 - \alpha$  at a rate  $\approx 2\alpha p_{\text{det}}$ , with  $p_{\text{det}}$  the probability that an emitted photon is detected.

Scaling this entangling scheme to multiple nodes requires each elementary link to be phase-stabilized independently (Fig. 2B), posing a number of new challenges. The different links, and even different segments of the same link, will generally be subject to diverse noise levels and spectra. Additionally, the optical power levels used are vastly different, from microwatts for the excitation path to attowatts for the single-photon heralding station, requiring different detector technologies for optimal signal detection. We solve these challenges with a hybrid phase-stabilization scheme that

is scalable to an arbitrary number of nodes. We decompose the effective interferometer for each link into three independently addressable interferometers and stabilize each separately (see Fig. 2C for the Alice-Bob link; the link Bob-Charlie is phase-stabilized in an analogous and symmetric way; see figs. S5 to S8).

First, each node has its own local stabilization that uses unbalanced heterodyne phase detection (Fig. 2C, left). In comparison to the previous homodyne stabilization method (14), this enables us to obtain a higher bandwidth phase signal from the small part of the excitation light that is reflected from the diamond surface ( $\approx 1\%$ ) by boosting it with a strong

reference-light beam at a known frequency offset. Moreover, this scheme allows for optimal rejection of the reflected excitation light by polarization selection, thus preventing excitation light from entering the single-photon path toward the heralding detectors and creating false entanglement heralding events. The measured phase signals are fed back on piezoelectric-mounted mirrors to stabilize the local interferometers.

Second, the global part of the effective interferometer (Fig. 2C, right) is stabilized by single-photon-level homodyne phase detection with feedback on a fiber stretcher: A small fraction of the strong reference-light beam is

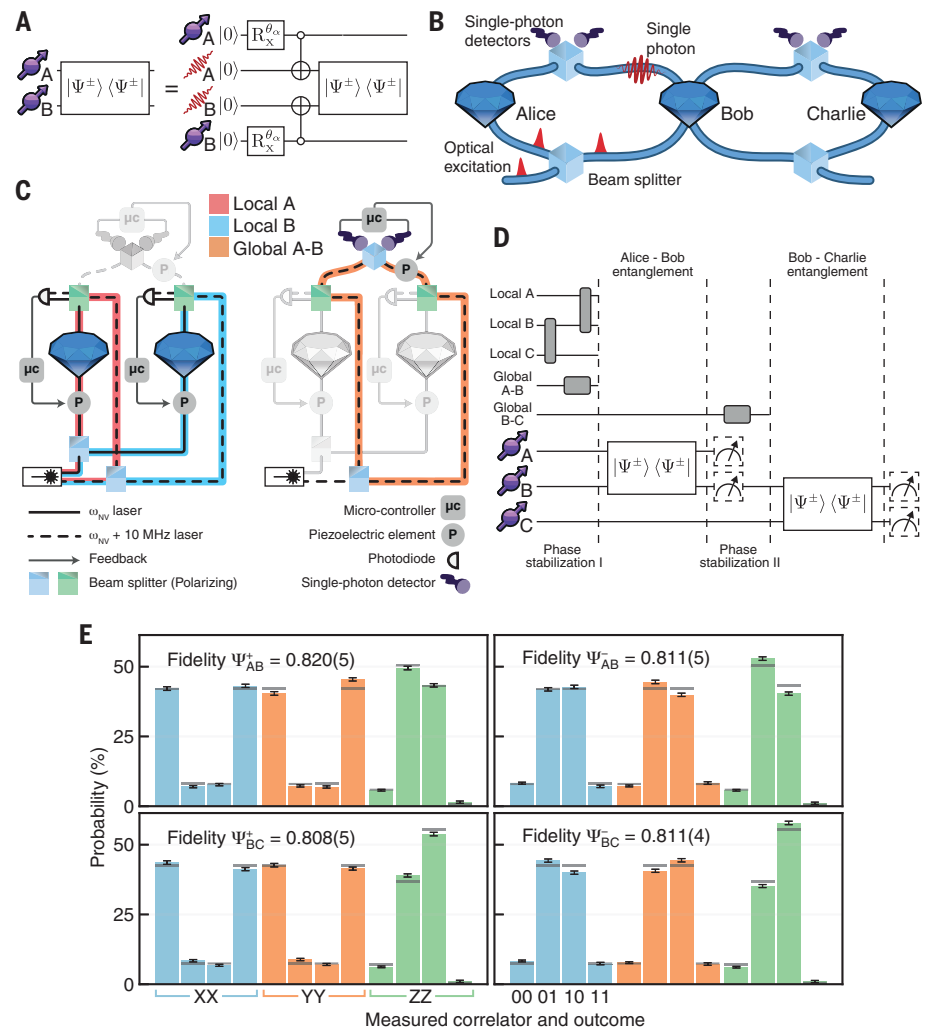


**Fig. 2. Establishing remote entanglement in a network architecture.** (A) Circuit diagram of the single-photon entanglement protocol, where  $R_{\theta_x}^{\theta_x}$  is a rotation around the  $x$  axis with angle  $\theta_x$ ,  $\theta_x = 2\cos^{-1}(\sqrt{\alpha})$ . (B) Sketch of three quantum network nodes in line configuration, showing the two effective interferometers. (C) Phase stabilization diagram of the Alice-Bob link, highlighting the local interferometers (left) and the global interferometer (right). See (27) for further details. (D) Experimental sequence to generate Bell pairs on both Alice-Bob (A-B) and Bob-Charlie (B-C) links. Dashed boxes display measurements used in (E). (E) Correlation measurements on entangled states on A-B (top) and B-C (bottom) links. The left plots correspond to  $|\Psi^+\rangle$  states; the right plots correspond to  $|\Psi^-\rangle$  states. Shown are observed probabilities for outcomes (from left to right) 00, 01, 10, and 11 for correlation measurements in the bases XX (blue), YY (orange), and ZZ (green). Gray bars depict values from the theoretical model. Error bars indicate one standard deviation.



directed into the single-photon path, and the interference is measured using the same detectors used for entanglement generation.

This architecture provides scalability in the number of nodes and a higher feedback bandwidth compared with our previous implementation on a single link [fig. S9; see (27) for details]. In our current implementation, the central node—Bob—has combining optics to merge the signals coming from Alice and Charlie, so that the single-photon detectors can be shared by the two links.

Crucially, this architecture enables the successive generation of entanglement on the two elementary links as required for network protocols exploiting multinode entanglement. We benchmark its performance by running entanglement generation on both elementary links within a single experimental sequence (Fig. 2D). We achieve fidelities of the entangled Bell states exceeding 0.8 for both links (Fig. 2E), on par with the highest fidelity reported for this protocol for a single link (14). For the same fidelity, the entangling rates are slightly higher than in (14) (9 and 7 Hz for links Alice-Bob and Bob-Charlie, respectively), despite the additional channel loss from connecting the two links. The main sources of infidelity are the probability  $\alpha$  that both nodes emit a photon, remaining optical phase uncertainty, and double excitation during the optical pulse [see table S2 and (27)]. A detailed physical model that includes known error sources is used here and below for comparison to the experimental data (27); predictions by the model are indicated by the gray bars in the correlation and fidelity plots.

### Memory qubit performance and real-time feed-forward operations

To distribute entangled states across multiple nodes, generated entangled states must be stored in additional qubits while new entanglement links are created. Carbon-13 nuclear spins are excellent candidates for such memory qubits, thanks to their long coherence times, controllability, and isolation from the control drives on the electronic qubit (30). Recent work (31) indicated that their storage fidelity under network activity is mainly limited by dephasing errors resulting from the coupling to the electronic spin that is randomized on failed entanglement generation. It was suggested that the memory robustness to such errors may be further improved by operating under an increased applied magnetic field. Here, we use a magnetic field of 189 mT for our central node, as opposed to ~40 mT used in past experiments (19, 31).

This higher field puts much stricter demands on the relative field stability in order to not affect the qubit frequencies; we achieve an order of magnitude reduction in field fluctuations by actively stabilizing the temperature of

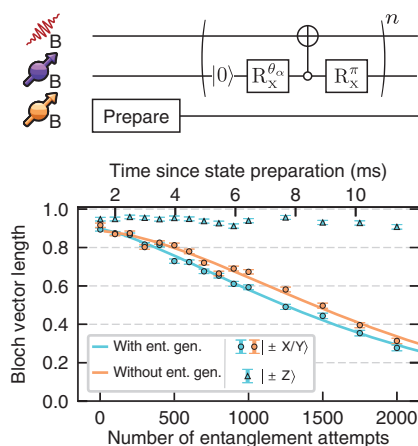


**Fig. 3. Memory qubit coherence under network activity.** (Top) Circuit diagram displaying the experimental sequence, where  $n$  is the number of entanglement attempts. (Bottom) Blue represents the measured Bloch vector length of memory qubit eigenstates (triangles) and superposition states (circles) versus entanglement attempts, for  $\alpha = 0.05$ . Orange represents measured superposition decay versus time in the absence of entanglement attempts. Solid lines are fits, yielding decay constants of  $N_{1/e} = 1843 \pm 32$  ( $2042 \pm 36$ ) with (without) entanglement generation attempts [see table S3 and (27) for additional details].

the sample holder, which in turn stabilizes the permanent magnet inside the cryostat (27). Additionally, the higher magnetic field splits the two optical transitions used for electronic spin initialization, hindering fast qubit resets; the addition of a second initialization laser, frequency locked to the first one with an offset of 480 MHz, enables us to maintain high-fidelity ( $>0.99$ ) and fast (few microsecond) resets (27).

We measure the fidelity of stored states on Bob's memory qubit for a varying number of entanglement generation attempts (Fig. 3). The two eigenstates ( $\pm Z$ ) do not show appreciable decay as we increase the number of entanglement generation attempts, as expected from the pure dephasing nature of the process (31). The superposition states degrade with an average decay constant of  $N_{1/e} \approx 1800$  attempts. To gain insight into the contribution of network activity to this decay, we repeat these measurements in the absence of entanglement attempts, in which case dephasing of the memory qubit is mainly due to uncontrolled interactions with nearby nuclear spins. We find this intrinsic dephasing time to be  $T_2^* = 11.6(2)$  ms, equivalent to the duration of  $\approx 2000$  entanglement generation attempts. We conclude that the intrinsic dephasing accounts for most of the decay observed under network activity, indicating the desired robustness. For the experiments discussed below, we

use a timeout of 450 attempts before the sequence is restarted, as a balance between optimizing entanglement generation rate and fidelity of the stored state.

Executing protocols over quantum networks requires real-time feed-forward operations among the various nodes: Measurement outcomes at the heralding station or at nodes need to be translated into quantum gates on other nodes. We implement an asynchronous bidirectional serial communication scheme between microcontrollers at the nodes, enabling both the required timing synchronization of the nodes and the exchange of feed-forward information for the quantum network protocols (27). Furthermore, we integrate the feed-forward operations with local dynamical decoupling protocols that actively protect the communication qubits from decoherence. The resulting methods enable us to run multinode protocols in a heralded fashion: “Flag” signals indicate in real time the successful execution of (sub) protocols and generation of desired states that are then available for further use, thus critically enhancing the efficiency and removing the need for any postselection.

### Demonstration of multinode network protocols

We now turn to the full operation of the three-node network that combines the different elements discussed above. We perform two canonical network protocols: the distribution of genuine multipartite entanglement and entanglement swapping to two non-nearest-neighbor nodes.

In both protocols, the sequence depicted in Fig. 4A is used to establish a remote entangled state on each of the two links. This sequence starts with a preparation step (depicted only in fig. S10) that synchronizes the microcontrollers of the nodes and makes sure that the NV centers in each node are in the desired charge state and in resonance with all the relevant lasers. After initialization of the memory qubit, the first entangled state is prepared on the link Alice-Bob. We interleave blocks of entanglement generation attempts with phase-stabilization cycles. Once Alice-Bob entanglement is heralded, Alice's entangled qubit is subject to a dynamical decoupling sequence while awaiting further communication from the other nodes. At Bob, deterministic quantum logic is used to swap the other half of the entangled state to the memory qubit.

The second part of the phase stabilization is then executed, followed by the generation of remote entanglement between the communication qubits of Bob and Charlie. In case of a timeout (no success within the preset number of attempts), the full protocol is restarted. In case of success, a dynamical decoupling sequence is started on Charlie's communication qubit analogous to the protocol on Alice. At Bob, a Z-rotation is applied to the memory

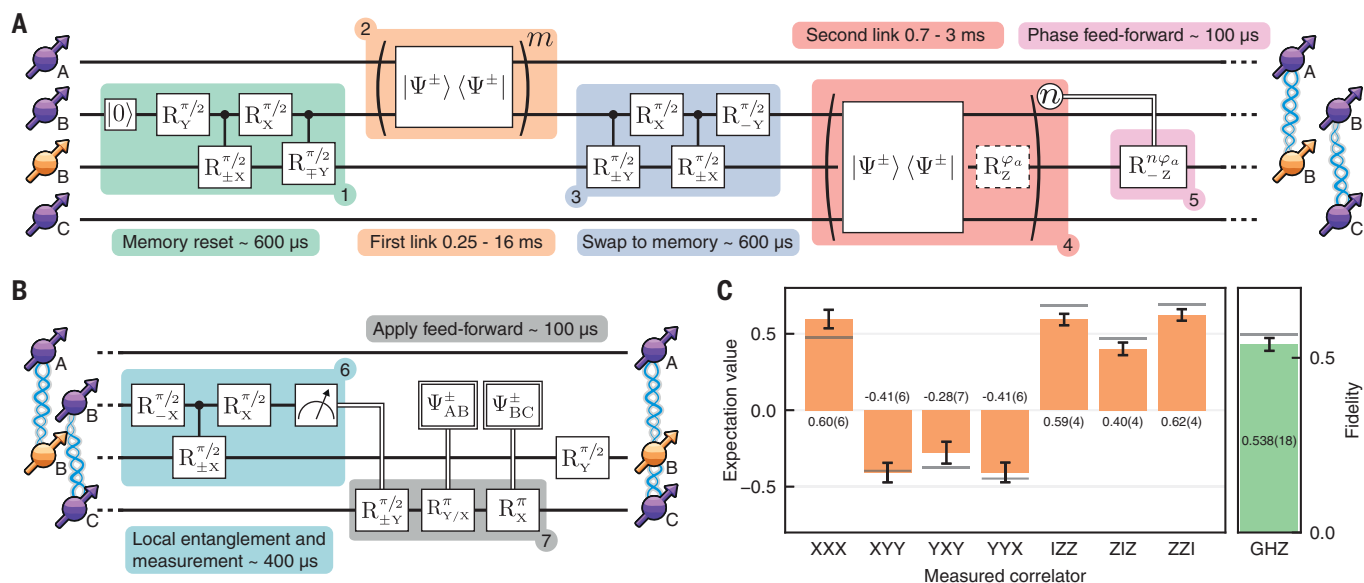


**Fig. 4. Distribution of genuine multipartite entanglement across the quantum network.** (A) Circuit diagram displaying the experimental sequence used to establish entanglement on both elementary links. (B) Circuit diagram displaying the experimental sequence for distributing a three-partite GHZ state across the three nodes. (C) Outcomes of correlation measurements and the resulting fidelity of the heralded GHZ state, demonstrating genuine multipartite entanglement. Gray bars depict values from the theoretical model. Error bars indicate one standard deviation.

qubit to compensate for the acquired phase that depends linearly on the (a priori unknown) number of entanglement attempts. This gate is implemented through an XY4 decoupling sequence on the communication qubit, with a length set in real time by the microcontroller based on which entanglement attempt was successful (27). After this step, the two links each share an entangled state ready for further processing: one between the communication qubit at Alice and the memory qubit at Bob and one between the communication qubits of Bob and Charlie.

The first protocol we perform is the generation of a multipartite entangled GHZ state across the three nodes. The circuit diagram describing our protocol is depicted in Fig. 4B. We first entangle the two qubits at Bob, followed by measurement of the communication qubit in a suitably chosen basis. The remaining three qubits are thereby projected into one of four possible GHZ-like states, which are all equivalent up to a basis rotation. The specific basis rotation depends both on the measurement outcome at Bob and on which Bell states ( $|\Psi^+\rangle$  or  $|\Psi^-\rangle$ ) were generated in the first part of the sequence, which in turn depends on which two photon detectors heralded the remote entangled states. These outcomes are communicated and processed in real time and the corresponding feed-forward operations are applied at Charlie. As a result, the protocol is able to achieve delivery of the same GHZ state  $|\text{GHZ}\rangle_{\text{ABC}} = (|000\rangle + |111\rangle)/\sqrt{2}$ , irrespective of the intermediate outcomes. Here, we choose to herald only on Bob reporting the  $|0\rangle$  readout

outcome, because the asymmetry in the communication qubit readout fidelities renders this outcome more faithful (27). Additionally, this choice automatically filters out events in which the NV center of Bob was in the incorrect charge state or off resonance [occurrence  $\approx 10\%$  in this experiment; see (27)]. With this heralding choice, the protocol delivers GHZ states at a rate of about  $1/(90\text{ s})$ .

We extract the fidelity to the ideal GHZ state from correlation measurements by using  $F = (1 + \langle \text{IZZ} \rangle + \langle \text{ZIZ} \rangle + \langle \text{ZZI} \rangle + \langle \text{XXX} \rangle - \langle \text{XYY} \rangle - \langle \text{YXY} \rangle - \langle \text{YYX} \rangle)/8$  and find  $F = 0.538(18)$  (Fig. 4C). The state fidelity above 0.5 certifies the presence of genuine multipartite entanglement distributed across the three nodes (32).

In this experiment, the fidelities of the entangled states on the elementary links bound the fidelity of the heralded GHZ state to about 0.66. Other relevant error sources are the dephasing of the memory qubit and accumulation of small quantum gate errors (see table S4). We emphasize that, contrary to earlier demonstrations of distributed GHZ states with photonic qubits (25) and ensemble-based memories (26) that relied on postselection, we achieve heralded GHZ state generation: A real-time heralding signal indicates the reliable delivery of the states.

The second protocol, illustrated in Fig. 5A, demonstrates entanglement swapping of the two direct links into an entangled state of the outer two nodes. Once entanglement is established on the two links as described above, the central part of the entanglement swapping is

executed: Bob, the central node, performs a Bell state measurement (BSM) on its two qubits. One way to read this protocol is that the BSM induces teleportation of the state stored on Bob's memory qubit to Charlie, by consuming the entangled state shared by Bob's communication qubit and Charlie. Because the state teleported to Charlie was Bob's share of an entangled state with Alice, the teleportation establishes direct entanglement between Alice and Charlie.

After the BSM is completed, we perform a charge and resonance (CR) check on Bob to prevent heralding on events in which the NV center of Bob was in the incorrect charge state or off resonance. We note that this CR check was not used in the heralding procedure of the GHZ generation protocol because its current implementation induces decoherence on Bob's memory qubit, which is part of the final GHZ state to be delivered. To complete the entanglement swapping, feed-forward operations are performed at Charlie to account in real time for the different measurement outcomes, analogous to the previous protocol, resulting in the delivery of the Bell state  $|\Phi^+\rangle_{\text{AC}} = (|00\rangle + |11\rangle)/\sqrt{2}$ .

We assess the performance of the entanglement swapping by measuring three two-node correlators on the generated Bell state shared by Alice and Charlie. Because the BSM is performed with local quantum logic and single-shot readout, it is (except for the CR check step) a deterministic operation. However, given the asymmetry in the readout errors as discussed above, the fidelity of the final state will



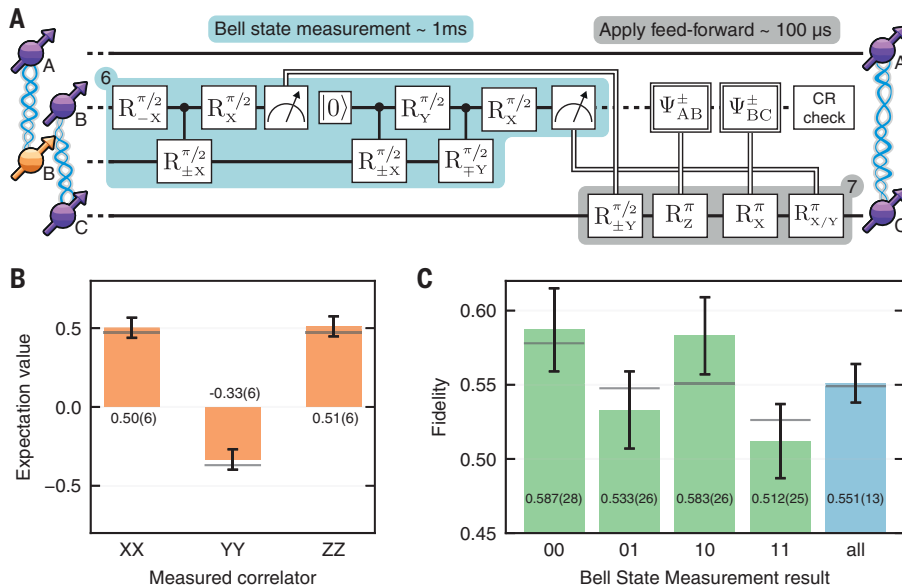


**Fig. 5. Entanglement swapping on a multinode quantum network.** (A) Circuit diagram displaying the experimental sequence for entanglement swapping, yielding an entangled state shared between the two nonconnected nodes. (B) Outcomes of correlation measurements on the heralded entangled state shared between Alice and Charlie for the selected Bell-state measurement outcome (see main text). (C) State fidelities for different outcomes of Bob's Bell-state measurement (green) and the state fidelity averaged over all outcomes (blue). In (B) and (C), gray bars depict values from the theoretical model, and error bars indicate one standard deviation.

depend on the readout outcomes. Figure 5B shows the results of the correlation measurements on the delivered state for heralding on Bob obtaining twice the outcome  $|0\rangle$ , yielding a state fidelity of  $F = 0.587(28)$ . Figure 5C compares the state fidelities across the different BSM outcomes, displaying the expected lower fidelities for outcomes of  $|1\rangle$  and an average fidelity over all outcomes of  $F = 0.551(13)$ . The combined heralding rate is  $1/(40\text{ s})$ . The sources of infidelity are similar to the ones discussed above (see table S5). This experiment constitutes the first demonstration of entanglement swapping from previously stored remote entangled states, enabled by the network's ability to asynchronously establish heralded elementary entanglement links, to store these entangled states, and then to efficiently consume them to teleport entanglement to distant nodes.

### Conclusion and outlook

We have demonstrated the realization of a multinode quantum network. We achieved multipartite entanglement distribution across the three nodes and any-to-any connectivity through entanglement swapping. It is noteworthy that the data acquisition for the network protocols has been performed fully remotely because of the COVID-19 pandemic, highlighting the versatility and stability of our architecture. Near-term advances in the capabilities and performance of the network will

be driven by further reducing the infidelities of the elementary links (27), by adding new subprotocols such as control methods (30), decoupling sequences (31), and repetitive readout (33) for the nuclear spin qubits; by improved photonic interfaces to enhance the entangling rates (34–36); and by improved control over the charge state of the NV center (37).

Our results open the door to exploring advanced multinode protocols and larger entangled states, for instance, by extending the local registers at the nodes. We note that a fully controlled 10-qubit register has recently been demonstrated on a similar device (30). Furthermore, the network provides a powerful platform for developing and testing higher-level quantum network control layers (38–40), such as the recently proposed link layer protocol for quantum networks (41). Quantum frequency conversion of the NV photons (42) can be used to interface the network nodes with deployed telecom fiber, paving the way to near-term quantum network tests over metropolitan distances. Finally, we expect the methods developed here to provide guidance for similar platforms reaching the same level of maturity in the future (43–46).

### REFERENCES AND NOTES

1. H. J. Kimble, *Nature* **453**, 1023–1030 (2008).
2. S. Wehner, D. Elkouss, R. Hanson, *Science* **362**, eaam9288 (2018).

3. L. Jiang, J. M. Taylor, A. S. Sørensen, M. D. Lukin, *Phys. Rev. A* **76**, 062323 (2007).
4. A. Broadbent, J. Fitzsimons, E. Kashefi, in *Proceedings of the 2009 50th Annual IEEE Symposium on Foundations of Computer Science* (IEEE Computer Society, 2009), pp. 517–526.
5. D. Gottesman, T. Jennewein, S. Croke, *Phys. Rev. Lett.* **109**, 070503 (2012).
6. A. Ekert, R. Renner, *Nature* **507**, 443–447 (2014).
7. N. H. Nickerson, J. F. Fitzsimons, S. C. Benjamin, *Phys. Rev. X* **4**, 041041 (2014).
8. P. Kómár et al., *Nat. Phys.* **10**, 582–587 (2014).
9. D. L. Moehring et al., *Nature* **449**, 68–71 (2007).
10. S. Ritter et al., *Nature* **484**, 195–200 (2012).
11. J. Hofmann et al., *Science* **337**, 72–75 (2012).
12. L. J. Stephenson et al., *Phys. Rev. Lett.* **124**, 110501 (2020).
13. H. Bernien et al., *Nature* **497**, 86–90 (2013).
14. P. C. Humphreys et al., *Nature* **558**, 268–273 (2018).
15. A. Delteil et al., *Nat. Phys.* **12**, 218–223 (2016).
16. R. Stockill et al., *Phys. Rev. Lett.* **119**, 010503 (2017).
17. P. Maunz et al., *Phys. Rev. Lett.* **102**, 250502 (2009).
18. S. Daiss et al., *Science* **371**, 614–617 (2021).
19. N. Kalb et al., *Science* **356**, 928–932 (2017).
20. M. Christandl, S. Wehner, in *Advances in Cryptology - ASIACRYPT 2005*, B. Roy, Ed. (Lecture Notes in Computer Science Series, Springer, 2005), pp. 217–235.
21. M. Hillery, V. Bužek, A. Berthiaume, *Phys. Rev. A* **59**, 1829–1834 (1999).
22. A. Ambainis, H. Buhrman, Y. Dodis, H. Rohrig, in *Proceedings. 19th IEEE Annual Conference on Computational Complexity* (IEEE Computer Society, 2004), pp. 250–259.
23. H.-J. Briegel, W. Dür, J. I. Cirac, P. Zoller, *Phys. Rev. Lett.* **81**, 5932–5935 (1998).
24. M. Pant et al., *npj Quantum Inf.* **5**, 25 (2019).
25. D. Bouwmeester, J.-W. Pan, M. Daniell, H. Weinfurter, A. Zeilinger, *Phys. Rev. Lett.* **82**, 1345–1349 (1999).
26. B. Jing et al., *Nat. Photonics* **13**, 210–213 (2019).
27. Materials and methods are available as supplementary materials.
28. C. Cabrillo, J. I. Cirac, P. García-Fernández, P. Zoller, *Phys. Rev. A* **59**, 1025–1033 (1999).
29. S. Bose, P. L. Knight, M. B. Plenio, V. Vedral, *Phys. Rev. Lett.* **83**, 5158–5161 (1999).
30. C. E. Bradley et al., *Phys. Rev. X* **9**, 031045 (2019).
31. N. Kalb, P. C. Humphreys, J. J. Slim, R. Hanson, *Phys. Rev. A* **97**, 062330 (2018).
32. O. Gühne, G. Tóth, *Phys. Rep.* **474**, 1–75 (2009).
33. L. Jiang et al., *Science* **326**, 267–272 (2009).
34. D. Riedel et al., *Phys. Rev. X* **7**, 031040 (2017).
35. E. Janitz, M. K. Bhaskar, L. Childress, *Optica* **7**, 1232–1252 (2020).
36. M. Ruf, M. J. Weaver, S. B. van Dam, R. Hanson, *Phys. Rev. Appl.* **15**, 024049 (2021).
37. S. Baier et al., *Phys. Rev. Lett.* **125**, 193601 (2020).
38. R. Van Meter, *Quantum Networking* (Networks and Telecommunications Series, Wiley, 2014).
39. A. Pirker, W. Dür, *New J. Phys.* **21**, 033003 (2019).
40. W. Kozłowski, S. Wehner, in *NANOCOM '19: Proceedings of the Sixth Annual ACM International Conference on Nanoscale Computing and Communication* (Association for Computing Machinery, 2019), pp. 1–7.
41. A. Dahlberg et al., in *SIGCOMM '19: Proceedings of the ACM Special Interest Group on Data Communication* (Association for Computing Machinery, 2019), pp. 159–173.
42. A. Tchebotareva et al., *Phys. Rev. Lett.* **123**, 063601 (2019).
43. B. C. Rose et al., *Science* **361**, 60–63 (2018).
44. C. T. Nguyen et al., *Phys. Rev. Lett.* **123**, 183602 (2019).
45. M. E. Trusheim et al., *Phys. Rev. Lett.* **124**, 023602 (2020).
46. N. T. Son et al., *Appl. Phys. Lett.* **116**, 190501 (2020).
47. M. Pompili et al., Data and software supporting “Realization of a multinode quantum network of remote solid-state qubits.” 4TU.ResearchData (2021); <https://doi.org/10.4121/13600589>.

### ACKNOWLEDGMENTS

We thank C. E. Bradley, S. Cadot, and J. van Rantwijk for experimental support and A. S. Sørensen, T. E. Northup, J. Borregaard, and T. H. Taminiau for critically reviewing the manuscript. **Funding:** We acknowledge financial support from the EU Flagship on Quantum Technologies through the project

Quantum Internet Alliance (EU Horizon 2020, grant agreement no. 820445); from the Netherlands Organisation for Scientific Research (NWO) through a VICI grant (project no. 680-47-624) and the Zwaartekracht program Quantum Software Consortium (project no. 024.003.037/3368); from the European Research Council (ERC) through an ERC Starting Grant (S.W.); and from a Consolidator Grant (grant agreement no. 772627 to R.H.) under the European Union's Horizon 2020 Research and Innovation Programme. M.P. acknowledges support from the Marie Skłodowska-Curie Actions - Nanoscale solid-state spin systems in emerging quantum technologies - Spin-NANO, grant agreement no. 676108. S.B. acknowledges support from an Erwin-Schrödinger

fellowship (QuantNet, no. J 4229-N27) of the Austrian National Science Foundation (FWF). **Author contributions:** M.P., S.L.N.H., S.B., and R.H. devised the experiment. M.P., S.L.N.H., S.B., and H.K.C.B. carried out the experiments and collected the data. M.P., S.L.N.H., S.B., H.K.C.B., P.C.H., R.N.S., R.F.L.V., M.J.T., and L.d.S.M. prepared the experimental apparatus. M.P. and R.H. wrote the main manuscript with input from all authors. M.P., S.L.N.H., S.B., H.K.C.B., and R.H. wrote the supplementary materials. M.P., S.L.N.H., and S.B. analyzed the data and discussed with all authors. R.H. supervised the research.

**Competing interests:** The authors declare no competing interests. **Data and materials availability:** The datasets that

support this manuscript and the software to analyze them are available at 4TU.ResearchData (47).

## SUPPLEMENTARY MATERIALS

science.sciencemag.org/content/372/6539/259/suppl/DC1  
Materials and Methods  
Figs. S1 to S10  
Tables S1 to S5  
Reference (48)

26 January 2021; accepted 19 March 2021  
10.1126/science.abg1919

## 2D MATERIALS

# Nematicity and competing orders in superconducting magic-angle graphene

Yuan Cao<sup>1\*</sup>, Daniel Rodan-Legrain<sup>1</sup>, Jeong Min Park<sup>1</sup>, Noah F. Q. Yuan<sup>1</sup>, Kenji Watanabe<sup>2</sup>, Takashi Taniguchi<sup>3</sup>, Rafael M. Fernandes<sup>4</sup>, Liang Fu<sup>1</sup>, Pablo Jarillo-Herrero<sup>1\*</sup>

Strongly interacting electrons in solid-state systems often display multiple broken symmetries in the ground state. The interplay between different order parameters can give rise to a rich phase diagram. We report on the identification of intertwined phases with broken rotational symmetry in magic-angle twisted bilayer graphene (TBG). Using transverse resistance measurements, we find a strongly anisotropic phase located in a “wedge” above the underdoped region of the superconducting dome. Upon its crossing with the superconducting dome, a reduction of the critical temperature is observed. Furthermore, the superconducting state exhibits an anisotropic response to a direction-dependent in-plane magnetic field, revealing nematic ordering across the entire superconducting dome. These results indicate that nematic fluctuations might play an important role in the low-temperature phases of magic-angle TBG.

Spontaneous symmetry breaking is a ubiquitous process that occurs at all length scales in nature (1). In a solid-state system, besides time-reversal and gauge symmetries, there are certain discrete symmetries imposed by the underlying crystal lattice. However, these symmetries can be spontaneously broken when many-body electron-electron interactions in the system are appreciable. Understanding these broken-symmetry states is fundamental to elucidating the various phases in these many-body systems (2, 3). One example is the electronic nematic phase, in which the discrete rotational symmetry of the lattice is spontaneously broken owing to electron correlations, although lattice translational and time-reversal symmetries are preserved (4, 5). The resulting anisotropy of the system is in turn manifested in the properties involving spin, charge, and lattice degrees of freedom, which can be measured

by scattering, transport, and scanning probe experiments (6–11).

When a correlated system has multiple broken-symmetry phases, their relationship often goes beyond mere competition, giving rise to a complex phase diagram of intertwined phases (3, 12–17). An example of intertwined order is a nematic superconducting state, which simultaneously breaks lattice rotational and gauge symmetries. Nematic superconducting states have been reported in certain iron pnictides and in doped Bi<sub>2</sub>Se<sub>3</sub>, as revealed by thermal, magnetic, and transport measurements (18–24), although their microscopic origin is still unclear.

The recent discovery of correlated insulator and superconducting behaviors (25, 26) in two-dimensional (2D) graphene superlattices brings the possibility of studying correlated superconducting materials with unmatched tunability and richness. Twisted 2D materials exhibit long-range moiré patterns in real space that can be tuned by the twist angle (Fig. 1A). In twisted bilayer graphene (TBG) near the first magic-angle  $\theta \approx 1.1^\circ$ , the interlayer hybridization results in nearly flat bands at low energies, in which the electrons are localized in real space (Fig. 1A) (27–29). Near half-filling of the nearly flat bands, emergent correlated insulator behavior, and superconductivity have been demonstrated (25, 26, 30). In this work, we study the interplay between the supercon-

ducting phase and other many-body phases in magic-angle TBG. Compared to conventional materials, a major advantage of magic-angle TBG is that the band filling can be continuously tuned by electrostatic gating instead of chemical doping, so that different phases can be accessed in a single device.

## Characterization of magic-angle graphene

Using the previously developed “tear and stack” dry-transfer technique (31, 32), we fabricate high-quality encapsulated TBG devices with twist angles around the first magic angle  $\theta \approx 1.1^\circ$  [see (33) Landau fan diagram]. The main two devices we report about are devices A and B, with twist angles of  $\theta = 1.09^\circ$  and  $\theta = 1.08^\circ$ , respectively. We also studied a third device C with  $\theta = 1.07^\circ$  [shown in (33)], which exhibits very similar behaviors. The low-energy bands in TBG are fourfold degenerate (owing to spin and valley degrees of freedom) and can support an electron density of  $n_s = 4/A$ , where  $A$  is the area of a moiré unit cell. This density corresponds to filling four electrons or holes per moiré unit cell. Near the first magic angle, correlated states can form at integer electron fillings of the moiré superlattice—i.e. when  $n = \pm n_s/4$ ,  $\pm n_s/2$ ,  $\pm 3n_s/4$ —where electronic interactions are believed to become comparable to the bandwidth of the nearly flat bands. In the resistivity measurements of device A [shown in Fig. 1B], we indeed find an enhancement of the resistivity  $\rho_{xx}$  at all these integer fillings. A superconducting dome is recognizable upon hole-doping of the  $-n_s/2$  insulating state, at temperatures below 2.5 K. Figure 1C shows the  $\rho_{xx}(T)$  curves of device A and device B at their optimal doping levels (highest  $T_c$ ), where  $T$  is the sample temperature. Both devices exhibit a  $T_c$  in the range of 2.5 to 3 K (at 50% normal resistance), which is among the highest in our MATBG devices (Fig. 1E). Figure 1D shows the evolution of the  $V_{xx}$ - $I_{\text{bias}}$  curves with temperature. From the log-log plot shown in the inset, we can extract the Berezinskii-Kosterlitz-Thouless (BKT) transition temperature to be  $T_{\text{BKT}} \approx 2.2$  K. Devices A and B have some of the highest transition temperatures among all reported magic-angle TBG devices so far (table S1 and fig. S4), as evident from the  $T_c$  statistics shown in Fig. 1E, as well as devices reported in the literature (26, 30, 34).

<sup>1</sup>Department of Physics, Massachusetts Institute of Technology, Cambridge, MA 02139, USA. <sup>2</sup>Research Center for Functional Materials, National Institute for Materials Science, Namiki 1-1, Tsukuba, Ibaraki 305-0044, Japan.

<sup>3</sup>International Center for Materials Nanoarchitectonics, National Institute for Materials Science, Namiki 1-1, Tsukuba, Ibaraki 305-0044, Japan. <sup>4</sup>School of Physics and Astronomy, University of Minnesota, Minneapolis, MN 55455, USA.

\*Corresponding author. Email: caoyuan@mit.edu (Y.C.); pjarillo@mit.edu (P.J.H.)



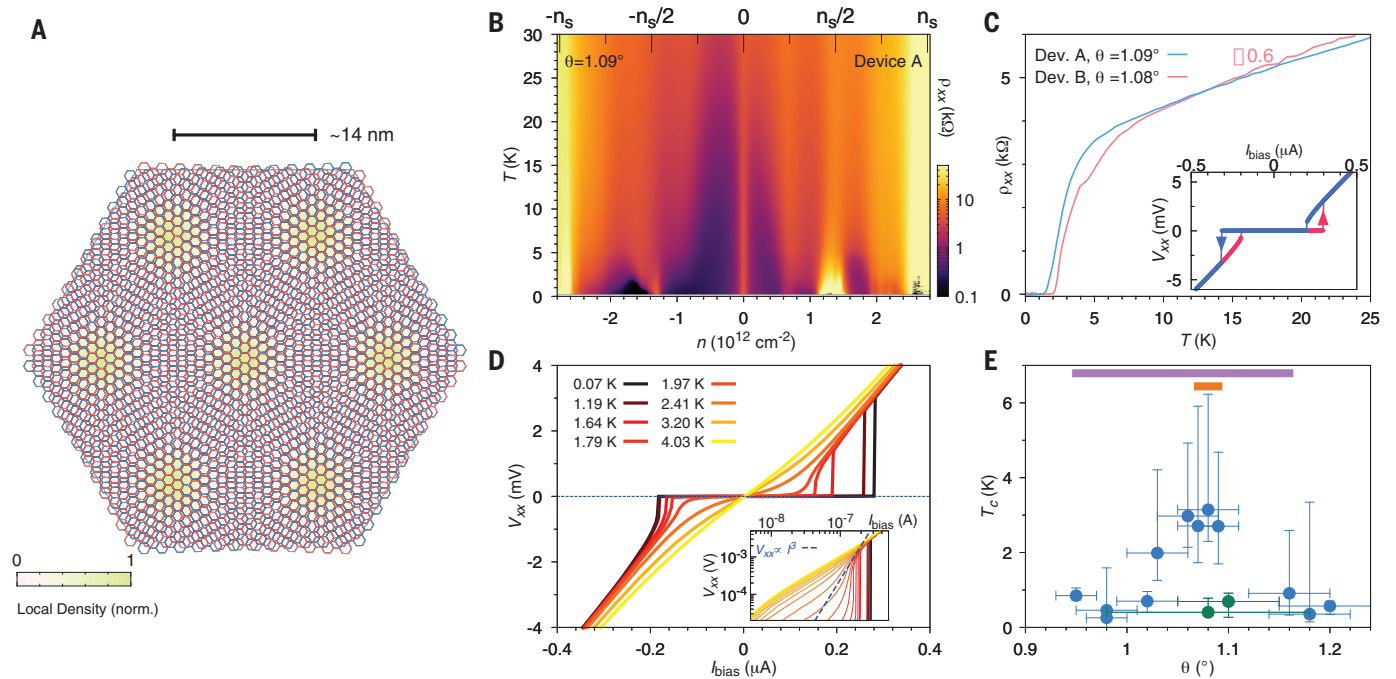


**Fig. 1. Characterization and statistics of magic-angle twisted bilayer graphene (TBG) devices.** (A) Illustration of the moiré pattern in magic-angle TBG. The color scale shows the normalized local density in the flat bands when the twist angle is close to the magic angle. The twist angle of the displayed pattern is exaggerated for clarity. (B) Resistivity of device A (twist angle  $\theta = 1.09^\circ$ ) versus gate-induced carrier density and temperature, showing correlated features at all integer electron fillings of the superlattice. Superconductivity is found at hole doping of the  $-n_s/2$  insulator with critical temperature  $\sim 2.5$  K. (C) Resistivity versus temperature for devices A and B, with twist angles  $\theta = 1.09^\circ$  and  $\theta = 1.08^\circ$ , respectively, at their optimal doping concentrations. Inset: Forward and backward sweeps of the  $V_{xx}$ - $I_{bias}$  curves in device B, which exhibit a considerable hysteresis. (D) Temperature dependence of the  $V_{xx}$ - $I_{bias}$  curves measured in device B. Inset: Log-log plot of the  $I > 0$

part of the data. The Berezinskii-Kosterlitz-Thouless transition temperature  $T_{BKT} \approx 2.2$  K is identified where the slope of the curve crosses  $d(\log V_{xx})/d(\log I_{bias}) = 3$  (equivalent to  $V_{xx} \propto I_{bias}^3$ ). (E) Statistics of optimal doping  $T_c$  in 14 of the magic-angle TBG devices that we have measured. We find that  $T_c$  peaks around  $1.1^\circ$ , the theoretically predicted first magic-angle in TBG. The green data points are from devices exhibiting substantial disorder, hence the large error bars in the twist angle determination. This disorder may be responsible for the relatively low  $T_c$ . The orange and purple bars denote the range of twist angles where we have observed anisotropic normal-state and nematic superconductivity, respectively. The latter has been seen in all the devices where it was investigated (see table S1), spanning from  $\theta = 0.95^\circ$  to  $\theta = 1.16^\circ$ . The error bar in temperature represents  $T_c$  determined from 10 and 90% of normal resistance, respectively (33).

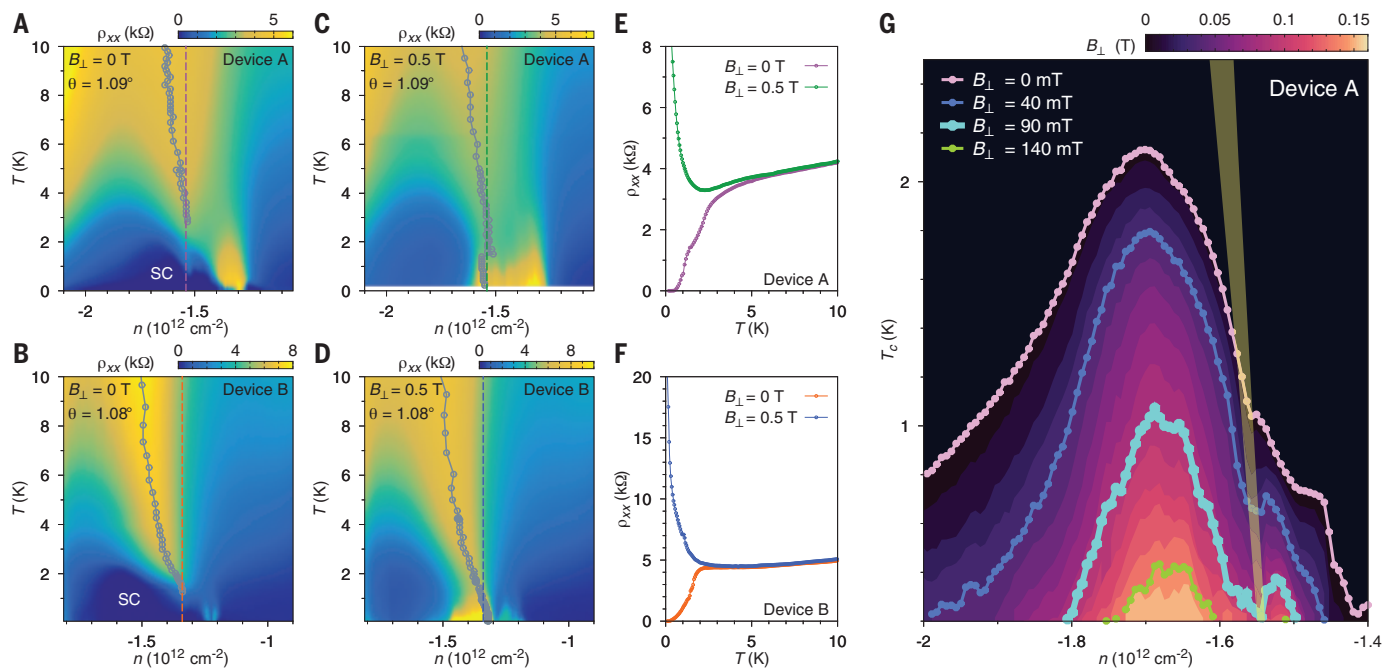
### Anisotropic behavior in the normal phase

Figure 2, A and B, show the resistivity versus gate-induced density,  $n$ , and temperature,  $T$ , maps of devices A and B, respectively, in the vicinity of  $-n_s/2$ . In both devices, the  $-n_s/2$  region of the phase diagram has a rather complicated structure. There are two resistive features in the normal state: one “wedge”-like feature above the superconducting dome (near  $-1.5 \times 10^{12}$  cm $^{-2}$  for device A and  $-1.4 \times 10^{12}$  cm $^{-2}$  for device B) that bends at increased temperatures, and one resistive feature on the right-hand side of the dome (near  $-1.3 \times 10^{12}$  cm $^{-2}$  for both devices). Whereas the latter feature corresponds to the  $-n_s/2$  state, similar to the correlated states previously reported in magic-angle TBG (25, 26, 30, 34), the wedge-like feature creates a noticeable “kink” (i.e., decrease in  $T_c$ ) where it approaches the superconducting dome. To further probe the resistive wedge-like feature, we apply a small perpendicular magnetic field to fully suppress superconductivity (Fig. 2, C and D). Line cuts of the resistivity versus temperature at the densities

corresponding to the “kinks” of  $T_c$  are compared in Fig. 2, E and F for the two devices. When superconductivity is suppressed, the resistive wedge-like feature turns insulating upon approaching zero temperature. A small magnetic field thus results in a superconductor-to-insulator transition at this density. In Fig. 2G, we show the gradual suppression of  $T_c$  by the perpendicular magnetic field from zero to 150 mT in device A. Above about 90 mT, the superconducting dome splits at  $n \approx -1.54 \times 10^{12}$  cm $^{-2}$  into two domes. This density approximately coincides with the density at which the wedge-like feature extrapolates to zero temperature. The separated domes are centered at around  $-1.52 \times 10^{12}$  cm $^{-2}$  and  $-1.67 \times 10^{12}$  cm $^{-2}$ , respectively. The position of the splitting point corresponds to  $15 \pm 5\%$  hole doping with respect to the correlated insulator state. These findings are reminiscent of the behavior in certain underdoped cuprates near  $1/8$  doping (3, 15, 16, 35).

To gain more insight into the possible origin of the resistive wedge-like feature, we measure the transverse voltage across the sample at

zero magnetic field, which gives the transverse resistance  $R_{xy} = V_y/I_x$  (36, 37). In an anisotropic conductor in two dimensions, the 2-by-2 resistivity tensor has two diagonal components  $\rho = \text{diag}\{\rho_1, \rho_2\}$ . If the major axis of the anisotropy (usually one of the crystal axis) is not aligned with the reference frame of the tensor, the off-diagonal terms of the resistivity tensor are proportional to  $(\rho_1 - \rho_2)\sin(2\theta)$ , where  $\theta$  is the angle between the anisotropy axis and the reference  $x$  axis [see (33) for derivation]. As a result, when an electrical current  $I_x$  flows in the  $x$  direction, a transverse voltage  $V_y$  appears across the edges perpendicular to the  $y$  axis, giving a nonvanishing  $R_{xy} = V_y/I_x \propto (\rho_1 - \rho_2)\sin(2\theta)$ , as long as  $\sin(2\theta) \neq 0$  and  $\rho_1 \neq \rho_2$ . The first condition is assumed to be true in our experiment because the lattice orientation is random with respect to the sample edge. Consequently, a nonvanishing transverse resistance in our experiment implies anisotropic resistivity,  $\rho_1 \neq \rho_2$ , and therefore the breaking of the sixfold rotational symmetry of TBG. This transverse voltage is fundamentally different



**Fig. 2. Competing phases near the superconducting domes of magic-angle TBG.** (A and B) Resistivity versus gate-induced carrier density and temperature for device A and device B, respectively. (C and D) Same measurement but in a perpendicular magnetic field of 0.5 T. (E and F) Line cuts of resistivity versus temperature for devices A and B at 0 and 0.5 T at the densities indicated by the dashed lines in (A) to (D), showing a superconductor-to-insulator transition induced by the magnetic field. In both devices, we find a wedge-like feature above the superconducting dome in addition to the  $-n_s/2$  correlated state. The gray circles in (A) to (D) indicate the resistivity maxima associated with the

wedge-like feature at different temperatures. (G) Evolution of  $T_c$  of device A in a perpendicular magnetic field up to 0.15 T. Each contour line is  $T_c$  (10% normal resistance) versus carrier density at the magnetic field indicated by the color shading. Contour lines for four values of the magnetic field are highlighted in contrasting colors. The yellow band represents the approximate position of the wedge-like feature. At  $B_{\perp} = 0.09$  T (light blue curve), the  $T_c$  kink touches zero at the same density where the wedge-like feature extrapolates to zero temperature. Above this field, the superconducting dome splits into two domes roughly centered at  $-1.52 \times 10^{12} \text{ cm}^{-2}$  and  $-1.67 \times 10^{12} \text{ cm}^{-2}$ , respectively.

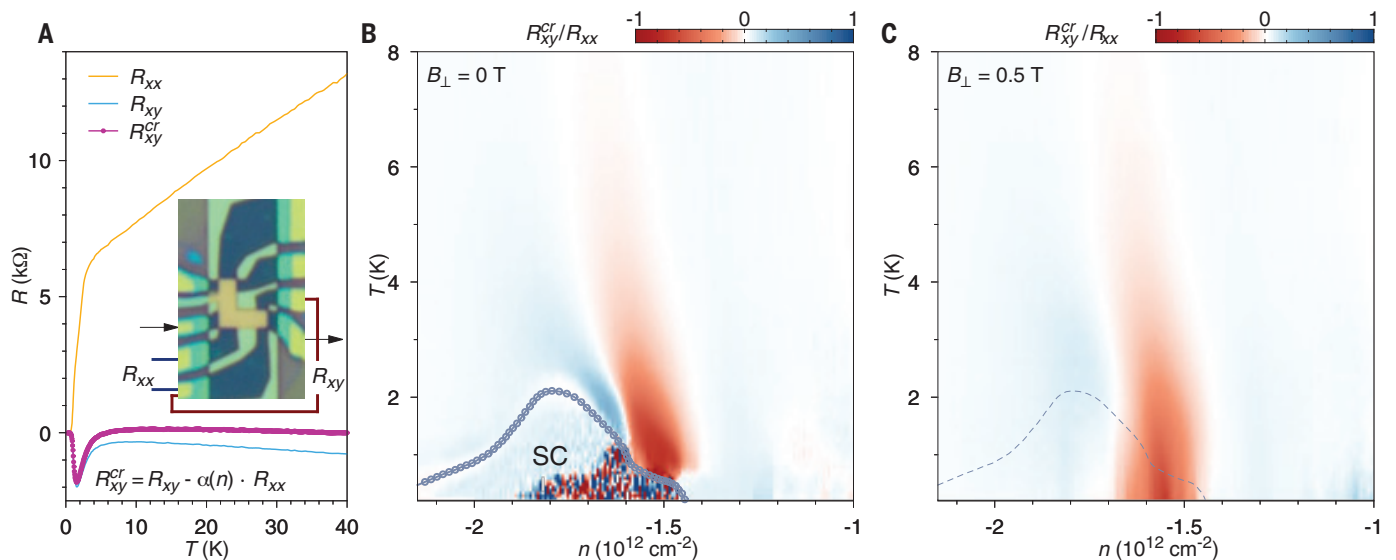


**Fig. 3. Normal-state anisotropy in magic-angle TBG device A.** (A) Inset shows the device configuration that we used to measure the transverse resistance, with black arrows indicating current source and drain.  $R_{xx}$ ,  $R_{xy}$  label the leads on which longitudinal and transverse resistances are measured, respectively. The purple trace,  $R_{xy}^{cr}$ , is the transverse resistance corrected for leads misalignment (33).  $n = -1.53 \times 10^{12} \text{ cm}^{-2}$  in this measurement.

(B and C) Anisotropy ratio versus carrier density and temperature at zero magnetic field and  $B_{\perp} = 0.5$  T, respectively (33). The circles in (B) and the dashed line in (C) outline the approximate shape of the superconducting dome (at zero field). We find the strongest anisotropy near the kink in  $T_c$  at  $n = -1.54 \times 10^{12} \text{ cm}^{-2}$ , coinciding with the resistive wedge-like feature we identified in Fig. 2, A and G.



from the Hall effect considering that time-reversal symmetry is not broken. To quantitatively analyze the transverse voltage, it is necessary to remove any residual longitudinal component that might appear in the transverse voltage owing to imperfect alignment of the four-probe voltage contacts and/or sample inhomogeneity (33, 36). Figure 3A shows the raw  $R_{xx}$  and  $R_{xy}$  measured for device A near the wedge-like feature, as shown in Fig. 2A. At high temperatures (40 K), where the anisotropies associated with electron correlation effects are presumably overwhelmed by thermal fluctuations, both  $R_{xx}$  and  $R_{xy}$  are linear in  $T$  and proportional to each other:  $R_{xy} \approx -0.05R_{xx}$  (36). To correct for this background signal that is likely a result of the imperfect voltage probe alignment, we subtract this  $R_{xx}$  component from  $R_{xy}$  so that at the highest temperature of 40 K, the net signal

is zero. This corrected transverse voltage  $R_{xy}^{\text{cr}} = R_{xy} - \alpha(n)R_{xx}$  where  $\alpha(n)$  is a density-dependent numerical factor typically within  $\pm 0.1$ , constitutes an accurate measure of the resistivity anisotropy (purple curve in Fig. 3A). Whereas no signal is present at higher temperatures, below 6 K there is a pronounced negative peak in  $R_{xy}^{\text{cr}}$ , which indicates the onset of anisotropy at this temperature.

The gate and temperature dependence of the anisotropy, shown in Fig. 3, B and C, for zero magnetic field and  $B_{\perp} = 0.5$  T (33), clearly reveals a prominent anisotropy wedge as well. The transverse voltage measured at  $B_{\perp} = 0.5$  T is symmetrized with data measured at  $B_{\perp} = -0.5$  T to remove the contribution from the Hall voltage. Here we plot the normalized quantity  $R_{xy}^{\text{cr}}/R_{xx}$ , which is approximately proportional to the anisotropy ratio  $(\rho_1 - \rho_2)/(\rho_1 + \rho_2)$  (33). We also mark out the superconducting

dome in Fig. 3, B and C. Immediately above the superconducting dome on the “underdoped” side (lower  $|n|$ ), we find a strong transverse voltage signal with a sign change at around  $-1.59 \times 10^{12} \text{ cm}^{-2}$  (see fig. S2 for the entire range of density). The position of the anisotropy wedge matches well that of the resistive wedge-like feature that we observed in Fig. 2A. The sign change indicates that the anisotropy changes from  $\rho_1 > \rho_2$  to  $\rho_1 < \rho_2$  (or vice versa). In  $B_{\perp} = 0.5$  T (Fig. 3C), the anisotropy wedge with negative values of  $R_{xy}^{\text{cr}}$  persists to zero temperature, consistent with the behavior of the resistive wedge-like feature in Fig. 2B. However, we notice that the anisotropy with positive  $R_{xy}^{\text{cr}}$  near  $-1.65 \times 10^{12} \text{ cm}^{-2}$  disappears as superconductivity is suppressed by the magnetic field, which might be explained by the vestigial order from the nematic superconductivity that will be discussed in the next section.

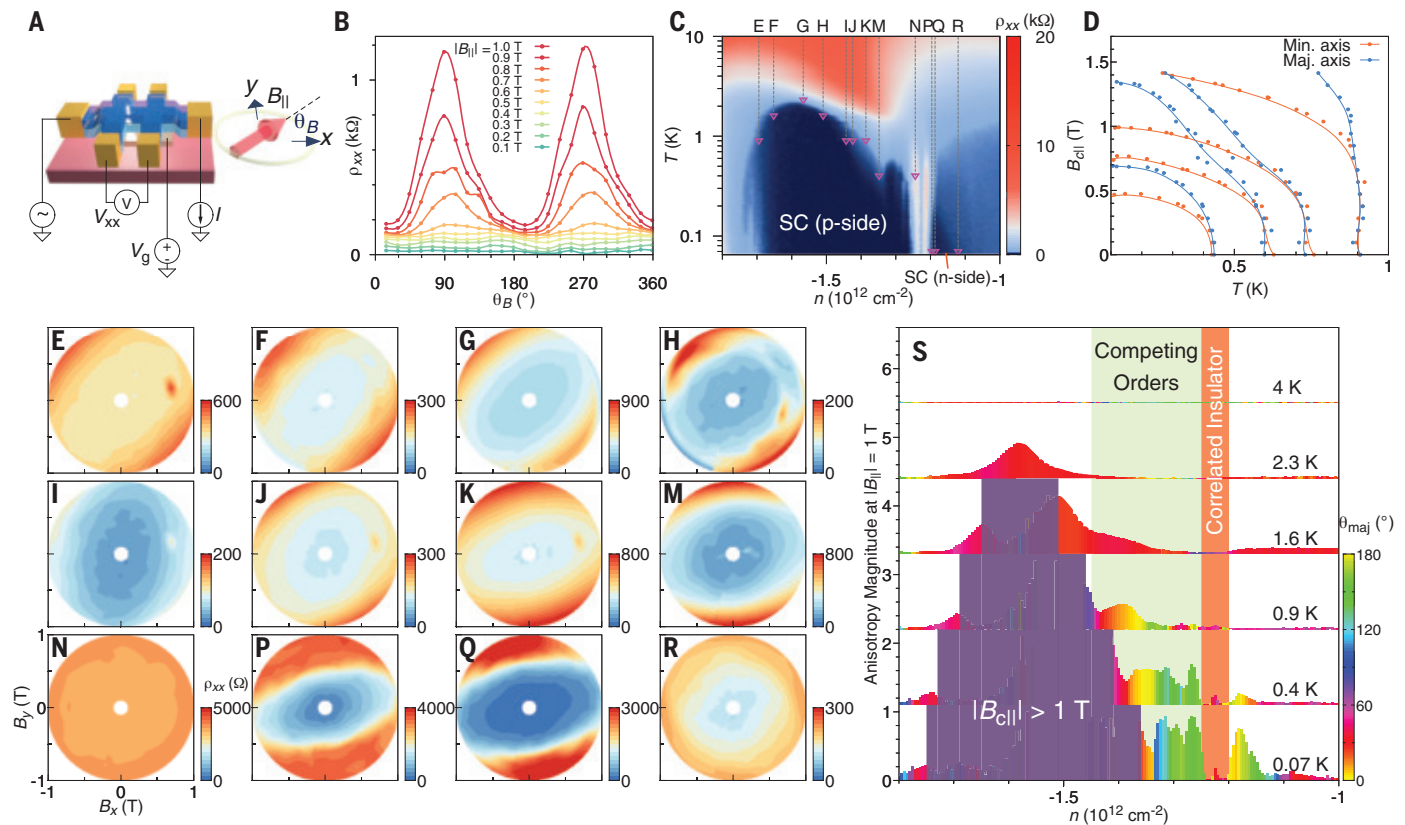


**Fig. 4. Evidence for nematic superconductivity in magic-angle TBG.**

(A) Schematic of the Hall bar device. The in-plane field angle  $\theta_B$  is defined with respect to the source-drain direction ( $x$  axis). (B) Resistivity as a function of  $\theta_B$  for different magnitudes of the in-plane magnetic field, showing a clear two-fold anisotropy. Measurement is taken at  $n = -1.18 \times 10^{12} \text{ cm}^{-2}$  and  $T = 70$  mK in device B. (C) Detailed view of the superconducting domes in device B, showing a large and a small superconducting dome on the p-side and n-side of the insulating state. (D) Critical in-plane magnetic field  $B_{c||}$  versus temperature along the major and minor axis of the twofold anisotropy, measured in device A at carrier densities of  $-1.44 \times 10^{12}$ ,  $-1.42 \times 10^{12}$ ,  $-1.40 \times 10^{12}$ , and  $-1.23 \times 10^{12} \text{ cm}^{-2}$  (from right to left). (E to R) Polar maps of the anisotropic response of

the resistivity across the superconducting domes in device B. The carrier densities and temperatures at which (E) to (R) are measured correlate with the labels in (C). (S) For device B, we extracted the magnitude (represented by height) and the polar angle of the major axis  $\theta_{maj}$  [represented by the color; see (33) for details] of the nematicity at different densities and temperatures, with  $|B_{||}| = 1$  T. The data for different temperatures are shifted vertically for clarity. Inside the region shaded in purple, the critical in-plane magnetic field is larger than 1 T and cannot be measured in our setup. In the density range of  $-1.45 \times 10^{12}$  to  $-1.2 \times 10^{12} \text{ cm}^{-2}$ , the anisotropy polar angle  $\theta_{maj}$  rotates rapidly with the carrier density, possibly owing to the competition with the wedge-like feature that we identified in Figs. 2 and 3.

### Nematic superconducting state

A natural question to ask is whether the superconducting phase exhibits any anisotropic properties as well. To investigate this, we measure the angle-dependent in-plane magnetic

field response of the superconducting phase. In magic-angle TBG, the superconductivity is suppressed by an in-plane magnetic field of the same order of magnitude as the Pauli paramagnetic limit (26). Using a vector magnet in

a dilution refrigerator, we apply a magnetic field  $B_{||}$  up to 1 T in an arbitrary direction within the sample plane (Fig. 4A). We compensate for possible sample tilt by applying a small out-of-plane magnetic field, so that the magnetic field is parallel to the sample to within  $|B_{\perp}| < 2$  mT at  $|B_{||}| = 1$  T, which is much less than the perpendicular critical magnetic field of our devices [see (33) and fig. S3 for detailed calibration procedure, and see fig. S5 for the perpendicular critical magnetic field of devices A and B]. Figure 4B shows an example of the resistivity versus in-plane magnetic field magnitude  $|B_{||}|$  and angle  $\theta_B$  (with respect to the length of the Hall bar; Fig. 4A). A twofold anisotropic suppression of the superconductivity (emergence of a finite dissipation) can be clearly seen. We have checked that the direction of the current flow is not correlated with the anisotropy direction, and therefore the anisotropic Lorentz force contribution can be excluded (fig. S6). The anisotropy is not aligned with the length or width of the Hall bar either (fig. S6).

The twofold anisotropy of the in-plane magnetotransport response points toward nematicity that is intrinsic to the superconducting phase, as it breaks the sixfold rotational symmetry of the moiré superlattice. We have systematically studied this nematic behavior across the entire superconducting dome of device B. In Fig. 4, E to R, we show polar maps of the magnetoresistivity at different carrier densities and temperatures in the hole-doping and electron-doping superconducting domes as labeled in Fig. 4C. At all densities except those in Fig. 4, N and R, we find elliptic contours that have major/minor axis ratios up to  $\sim 3$ . We chose to always measure near  $T_c$ , because deep inside the superconducting dome, the in-plane critical field is usually larger than 1 T and cannot be measured in our setup. However, we have confirmed the nematicity in the  $T \ll T_c$  region by simultaneously applying a small perpendicular field to partially suppress the superconducting state (fig. S7). At the densities corresponding to Fig. 4, N and R, which are outside the superconducting regions, the anisotropy is essentially nonexistent. In general, the twofold anisotropy occurs inside the broad transition from superconducting to normal state as a function of  $B_{||}$ , suggesting that it is a property intrinsic to the superconducting fluctuations (38); the normal state does not show any anisotropy in the in-plane magnetoresistance (fig. S9). In device A, we have observed a similar twofold anisotropic in-plane critical field (Fig. 4D). The critical magnetic field  $B_{c||}$  along the major axis extrapolated to zero temperature exceeds that along the minor axis by 40 to 80% in this device.

Figure 4S shows the evolution of the magnitude and of the director of the nematic

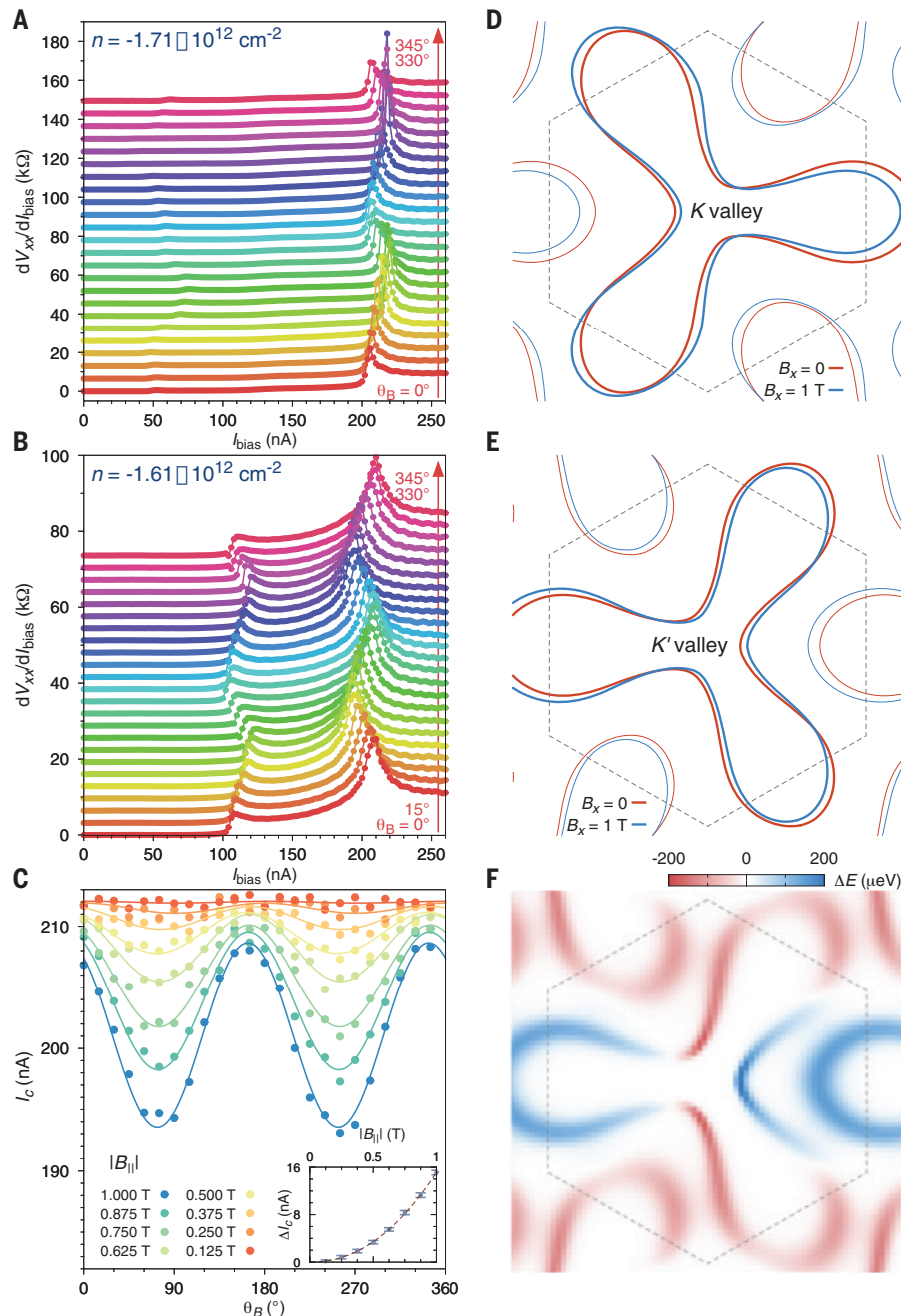


**Fig. 5. Anisotropic response of the superconducting critical current.** (A and B) Differential resistance  $dV_{xx}/dI_{bias}$  versus bias current  $I_{bias}$  as a function of the orientation of the in-plane magnetic field at two carrier densities. The orientation is indicated by the color, differing by 15° between adjacent curves, which are vertically shifted for clarity. (C) Modulation of the larger critical current in (B) by in-plane magnetic fields with different orientations and magnitudes. A sinusoidal function is used to fit the data (see main text). Inset: The modulation amplitude (peak-peak) as a function of the field magnitude, which can be fit by a power law  $\Delta I_c \propto |B_{||}|^\alpha$  with  $\alpha \approx 2.1$ . (D and E) Calculated Fermi contour of  $\theta = 1.09^\circ$  TBG at  $B_x = 0$  and  $B_x = 1$  T around K and K' valleys, respectively (33). (F) Energy splitting between states at opposite momentum and opposite valleys along the Fermi surface  $\Delta E(\mathbf{k}) = E_K(\mathbf{k}) - E_{K'}(-\mathbf{k})$  at  $B_x = 1$  T. For comparison, the Zeeman splitting  $g\mu_B B$  at  $B = 1$  T for  $g = 2$  is 115  $\mu\text{eV}$ . The gray hexagons in (D) to (F) denote the moiré Brillouin zone.

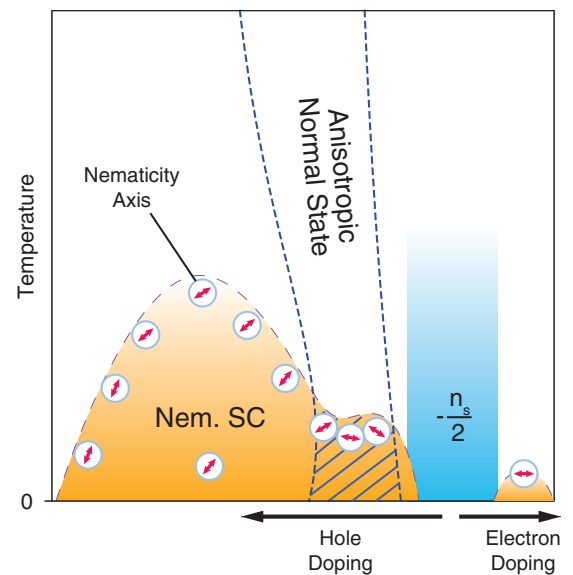


component of the superconducting state in device B as a function of carrier density and temperature. Our data show that the nematic director, as measured by the angle of rotation of the ellipse's major axis, does not appear to be exactly locked to any particular spatial axis, but instead evolves continuously with carrier density and temperature. In particular, in the superconducting dome on the hole-doping side of  $-n_s/2$ , the direction of the major axis varies slowly within  $+20$  to  $+50^\circ$  in the density range of  $-1.70 \times 10^{12}$  to  $-1.45 \times 10^{12} \text{ cm}^{-2}$  (corresponding to the ellipses from Fig. 4, E to H), whereas in the range of  $-1.45 \times 10^{12}$  to  $-1.25 \times 10^{12} \text{ cm}^{-2}$  (from Fig. 4, I to M), the major axis rotates quickly with the carrier density. From Fig. 4, I to M, the major axis rotates by  $\sim 90^\circ$ . The latter range of density again coincides with the resistive wedge-like feature for device B, as shown from Fig. 2, B and D. The smaller superconducting dome on the electron-doping side near  $-1.20 \times 10^{12} \text{ cm}^{-2}$  exhibits appreciable nematicity as well (Fig. 4, P and Q), with a director pointing from  $150^\circ$  to  $190^\circ$  ( $10^\circ$ ). As we explain below, that the nematic director changes direction as a function of doping and temperature makes it unlikely that the superconducting anisotropy is simply a response to strain present in the sample. On the contrary, this observation is consistent with spontaneous rotational symmetry-breaking characteristic of an intrinsic nematic superconductor.

### Anisotropic response of the superconducting gap

The observation of nematicity puts certain constraints on possible pairing symmetries of the superconducting order parameter (14, 39, 40). One can obtain information about the superconducting gap by measuring the critical current  $I_c$ . Here, by measuring  $I_c$  of device B in the presence of in-plane magnetic fields, we demonstrate that the nematicity not only is manifested in the resistivity measurements but also creates an anisotropic modulation of the superconducting gap. Figure 5, A and B, show the waterfall plots of differential resistance  $dV_{xx}/dI_{\text{bias}}$  versus dc bias current  $I_{\text{bias}}$  at two carrier densities, in an in-plane magnetic field  $|B_{\parallel}| = 1 \text{ T}$  along different directions indicated by the colors. At the carrier density in Fig. 5B, the plot shows two critical currents at 110 and 210 nA, respectively, which might be a consequence of domains in the device with different twist angles or nematic directors. At both carrier densities, the critical current shows notable twofold modulation by the in-plane magnetic field direction  $\theta_B$ . The  $\theta_B$  dependence can be fit by a sinusoidal function  $\cos(2(\theta_B - \theta_{B0}))$  (Fig. 5C), where  $\theta_{B0}$  is the direction of the major axis. The modulation amplitude as a function of the in-plane field magnitude is shown in the inset of Fig. 5C and

**Fig. 6. Summary of various competing phases.** On the underdoped side of the superconducting dome, we find a normal-state anisotropic phase that, at low temperatures, competes with superconductivity, creating a depression in the  $T_c$  curve. In the superconducting state, we find nematicity, manifested in its response to in-plane magnetic fields. By comparing the extracted nematicity temperature  $T_{\text{nem}}$  to  $T_c$ , we find that the entire superconducting dome exhibits nematicity, which suggests that the nematicity is intrinsic to the superconductivity and points toward a possible unconventional pairing symmetry. The dashed area denotes the competing region between the two states, where a reduction in  $T_c$ , as well as a strong rotation of the nematicity axis, is seen.



follows an approximately quadratic power-law dependence.

An anisotropic response in the critical current may originate from (i) an anisotropic angular dependence of the superconducting gap  $\Delta$  and/or (ii) anisotropic properties of the underlying normal-state resistance ( $R_n$ ). Although we have shown that the normal state exhibits considerable resistivity anisotropy at densities near the wedge-like feature in Fig. 3, we argue here that the anisotropic response of the critical current is not a result of the anisotropy of  $R_n$ . First, Fig. 5A is measured at a density for which there is essentially no resistivity anisotropy in the normal state ( $R_{xy}^{cr}/R_{xx} = -0.007$  at the lowest  $T$  in Fig. 3C), whereas Fig. 5B is measured at a density with considerable anisotropy in the normal state ( $R_{xy}^{cr}/R_{xx} = -0.325$  at the lowest  $T$  in Fig. 3C). However, the modulation of the critical current at these two densities shows similar magnitudes. Second, an anisotropy in the resistivity tensor may not necessarily imply a large anisotropic response of the resistivity versus in-plane magnetic field. Indeed, inside the wedge-like feature in the normal state in device A, we could not measure any substantial anisotropic response to the in-plane field (fig. S9). Thus, these results suggest that the anisotropic response of the critical current might not be directly related to the resistivity anisotropy of the normal state and hence may originate from an anisotropic superconducting gap.

To discuss the mechanism by which the in-plane field couples to the superconducting gap, we note that if the former couples solely to the spin degree of freedom (and thus the gap is only suppressed by the Zeeman coupling), spin-orbit interaction must be introduced to explain the dependence of  $I_c$  on the direction of  $B_{\parallel}$ . However, the intrinsic spin-orbit coupling in graphene-based systems is known to

be very weak. We might consider the following mechanism to reconcile these findings. As illustrated in Fig. 1A, the unit cell of magic-angle TBG has a length scale of  $a \sim 14 \text{ nm}$ . Despite the separation between the graphene sheets in TBG being merely  $\delta \sim 0.3 \text{ nm}$ , an in-plane magnetic field that threads through the space between them induces a small but non-negligible magnetic flux in the cross-section of the unit cell with an area  $S \sim a\delta$ , which modifies the Fermi contours. To demonstrate this effect, we numerically calculated the Fermi contours at  $-n_s/2$  for  $B_{\parallel} = 0$  and  $B_{\parallel} = 1 \text{ T}$  along the  $x$  direction using the Bistritzer-MacDonald continuum model (28). Figure 5, D and E, show the original and modified Fermi contours for the  $K$  and  $K'$  valleys, respectively; a noticeable shift is induced by the in-plane magnetic field. The  $K/K'$  valley degeneracy is lifted by the momentum shift between the two layers introduced by the in-plane field, which is proportional to  $e\delta B_{\parallel}$ , a substantial shift given the small size of the Brillouin zone. If one assumes that only electrons with opposite momentum and valley are allowed to form Cooper pairs in the superconducting phase, the two states from opposite valleys would be at slightly different energies when an in-plane field is applied, which serves to suppress the superconductivity in a manner similar to that of the paramagnetic (Zeeman) effect in the case of spins. To more intuitively demonstrate this, Fig. 5F shows the depairing energy along the Fermi contour  $\Delta E(\mathbf{k}) = E_K(\mathbf{k}) - E_{K'}(-\mathbf{k})$ . It is strongly direction dependent and has an order of magnitude similar to that of the Zeeman energy at  $B_{\parallel} = 1 \text{ T}$  ( $g\mu_B B_{\parallel} \approx 115 \mu\text{eV}$ , where  $g = 2$  and  $\mu_B$  is the Bohr magneton). The depairing energy exhibits a six-fold variation with respect to the direction of the in-plane magnetic field, whereas the nematic component of the superconducting order can further spontaneously

break this symmetry down to the observed twofold symmetry (38, 39, 41). A small strain can further assist to pin down the nematic domain along a given direction.

## Discussion

Our measurements reveal two distinct anisotropic states in the phase diagram of magic-angle TBG: a normal-state wedge-like feature above the superconducting dome and a nematic superconducting state. The wedge-like feature is associated with a zero-temperature insulating phase that shows appreciable resistivity anisotropy, indicative of broken sixfold lattice rotational symmetry. Thus, this normal-state phase might be either an electronic nematic state or an electronic smectic state—i.e., a charge or spin-density wave that, in addition to rotational symmetry, also breaks translational lattice symmetry. In either case, the rotational symmetry breaking can be described by a two-component three-state Potts nematic order parameter (41, 42). Electronic correlations might be important for the formation of such a state. Twisted bilayer graphene is well-known to exhibit van Hove singularities (vHs), which in general do not occur exactly at half-filling (43, 44). Near the vHs, it has been theoretically shown that the considerable nesting between the  $K$ - and  $K'$ -valley Fermi contours might induce density wave ordering (40). Notably, recent scanning tunneling experiments have identified prominent rotational-symmetry-broken features in the normal-state local density of states (45–47). Alternatively, strong-coupling models can also yield nematic and density-wave states (48, 49). For the superconducting phase, it remains to be seen whether its nematic character, as revealed by the measured in-plane anisotropy of the critical field, can be reconciled with  $s$ -wave pairing. This behavior could be explained in terms of a two-component  $p$ -wave/ $d$ -wave gap, indicative of an unconventional pairing mechanism (50).

A crucial question is whether the anisotropies observed here have intrinsic or extrinsic origins. The observation that we do not observe multiple nematic domains within the same device implies that some degree of residual strain is present. The issue is whether this strain is the sole cause of the anisotropy (extrinsic origin) or is mainly pinning one of the three underlying nematic domains (intrinsic origin). To address this, we note that such a residual strain should be a property of the device and thus should be present at all temperatures and doping. By contrast, as shown in Fig. 3, the onset of the normal-state anisotropy is restricted to a narrow doping range and to temperatures below 10 K. Furthermore, the resistance anisotropy is on the order of one in the wedge-like feature (see Fig. 3B). Such a large effect would be difficult to attribute to a reasonably sized residual strain.

These quantitative arguments rely on the amplitude of the anisotropy, but a more direct argument against an extrinsic origin can be made from the direction of the anisotropy. Our measurements in the superconducting state clearly show a rotation of the nematic director (Fig. 4, E to S). In the three-state Potts model, the three states correspond to the three nearest-neighbor directions in the moiré superlattice (41). Here, strain acts as a conjugate field to the nematic order parameter, similarly to how a magnetic field acts on a ferromagnet. If the strain is “parallel” to one of the three anisotropy directions, the corresponding nematic director is favored over the other two. As a result, the nematic director is fixed at all temperatures. If the strain is “antiparallel” to a direction, the other two directions become favored. Consequently, as the temperature is lowered toward the nematic state, the nematic director continuously rotates from the disfavored direction to one of the two favored directions (41). Notably, this can only happen if nematic order is spontaneous; i.e., if it is an intrinsic instability of the system (33). Therefore, the continuous rotation of the nematic director in our observation indicates that the anisotropy of the superconducting state is more likely to be intrinsic, as an extrinsic origin would result in a fixed orientation.

Another possible source of anisotropy is twist angle variations across the device, which could create an inhomogeneous distribution of strain (51). Although further studies are needed, we note that such an inhomogeneous strain would act as a random field to the Potts-nematic order parameter, which might affect the nematic properties in 2D (52). However, that we do not see different nematic domains across our device suggests that the global residual strain is probably dominating over the local strain caused by twist angle fluctuations.

The various phases discussed throughout this article are summarized in Fig. 6 [see (33) and fig. S8 for the extracted nematicity temperature  $T_{\text{nem}}$ ]. An anisotropic response to an in-plane magnetic field is seen only in the superconducting state, but not in the wedge-like feature, suggesting that the origins of nematicity in the normal and superconducting states are likely different. This is also consistent with the observation that these two orders compete, as evident from the suppression of  $T_c$  when the wedge-like feature meets the superconducting dome. However, because both phases break the same sixfold lattice rotational symmetry, the order parameters of these two phases can interact beyond mere competition, which may be responsible for the rapid change of the ellipse direction in the part of the phase diagram below the wedge (33). Moreover, normal-state nematic fluctuations may play an important role in favoring a superconducting ground state that is also nematic. Although the

onsets of nematicity and of superconductivity seem very close in our experiment (33), it is possible that the nematic order in magic-angle TBG persists even above  $T_c$ , a phenomenon known as vestigial nematic order (12, 14, 42). In Fig. 3B, there is a region just above the superconducting dome with positive transverse voltage signal at  $n \approx -1.65 \times 10^{12} \text{ cm}^{-2}$  and  $T \approx 2 \text{ K}$ . This signal not only has the opposite sign of the anisotropy of the wedge-like state, but it also disappears when superconductivity is suppressed (Fig. 3C). Thus, this feature might be explained by a vestigial nematic order that forms before the condensation of Cooper pairs (12, 14, 42). Scanning probe experiments are needed to confirm this nematic phase above the superconducting transition.

## REFERENCES AND NOTES

1. P. W. Anderson, *Science* **177**, 393–396 (1972).
2. S. Sachdev, *Rev. Mod. Phys.* **75**, 913–932 (2003).
3. B. Keimer, S. A. Kivelson, M. R. Norman, S. Uchida, J. Zaanen, *Nature* **518**, 179–186 (2015).
4. E. Fradkin, S. A. Kivelson, M. J. Lawler, J. P. Eisenstein, A. P. Mackenzie, *Annu. Rev. Condens. Matter Phys.* **1**, 153–178 (2010).
5. R. M. Fernandes, A. V. Chubukov, J. Schmalian, *Nat. Phys.* **10**, 97–104 (2014).
6. V. Hinkov et al., *Science* **319**, 597–600 (2008).
7. J.-H. Chu, H.-H. Kuo, J. G. Analytis, I. R. Fisher, *Science* **337**, 710–712 (2012).
8. T.-M. Chuang et al., *Science* **327**, 181–184 (2010).
9. E. P. Rosenthal et al., *Nat. Phys.* **10**, 225–232 (2014).
10. B. E. Feldman et al., *Science* **354**, 316–321 (2016).
11. Y. Sato et al., *Nat. Phys.* **13**, 1074–1078 (2017).
12. L. Nie, G. Tarjus, S. A. Kivelson, *Proc. Natl. Acad. Sci. U.S.A.* **111**, 7980–7985 (2014).
13. E. Fradkin, S. A. Kivelson, J. M. Tranquada, *Rev. Mod. Phys.* **87**, 457–482 (2015).
14. R. M. Fernandes, P. P. Orth, J. Schmalian, *Annu. Rev. Condens. Matter Phys.* **10**, 133–154 (2019).
15. C. Proust, L. Taillefer, *Annu. Rev. Condens. Matter Phys.* **10**, 409–429 (2019).
16. J. Chang et al., *Nat. Phys.* **8**, 871–876 (2012).
17. S. D. Edkins et al., *Science* **364**, 976–980 (2019).
18. J. Li et al., *Nat. Commun.* **8**, 1880 (2017).
19. J. Shen et al., *npj Quantum Mater.* **2**, 59 (2017).
20. A. Y. Kuntsevich et al., *New J. Phys.* **20**, 103022 (2018).
21. K. Matano, M. Kriener, K. Segawa, Y. Ando, G. Zheng, *Nat. Phys.* **12**, 852–854 (2016).
22. T. Asaba et al., *Phys. Rev. X* **7**, 011009 (2017).
23. Y. Pan et al., *Sci. Rep.* **6**, 28632 (2016).
24. M. P. Smylie et al., *Sci. Rep.* **8**, 7666 (2018).
25. Y. Cao et al., *Nature* **556**, 80–84 (2018).
26. Y. Cao et al., *Nature* **556**, 43–50 (2018).
27. E. Suárez Morell, J. D. Correa, P. Vargas, M. Pacheco, Z. Barticevic, *Phys. Rev. B Condens. Matter Mater. Phys.* **82**, 121407 (2010).
28. R. Bistritzer, A. H. MacDonald, *Proc. Natl. Acad. Sci. U.S.A.* **108**, 12233–12237 (2011).
29. J. M. B. Lopes dos Santos, N. M. R. Peres, A. H. Castro Neto, *Phys. Rev. B Condens. Matter Mater. Phys.* **86**, 155449 (2012).
30. M. Yankowitz et al., *Science* **363**, 1059–1064 (2019).
31. Y. Cao et al., *Phys. Rev. Lett.* **117**, 116804 (2016).
32. K. Kim et al., *Nano Lett.* **16**, 1989–1995 (2016).
33. See supplementary materials.
34. X. Lu et al., *Nature* **574**, 653–657 (2019).
35. B. J. Ramshaw et al., *Science* **348**, 317–320 (2015).
36. P. Walmsley, I. R. Fisher, *Rev. Sci. Instrum.* **88**, 043901 (2017).
37. J. Wu, A. T. Bollinger, X. He, I. Božović, *Nature* **547**, 432–435 (2017).
38. J. W. F. Venderbos, V. Kozii, L. Fu, *Phys. Rev. B* **94**, 094522 (2016).
39. V. Kozii, H. Isobe, J. W. F. Venderbos, L. Fu, *Phys. Rev. B* **99**, 144507 (2019).
40. H. Isobe, N. F. Q. Yuan, L. Fu, *Phys. Rev. X* **8**, 041041 (2018).
41. R. M. Fernandes, J. W. F. Venderbos, *Sci. Adv.* **6**, eaba8834 (2020).



42. M. Hecker, J. Schmalian, *npj Quantum Mater.* **3**, 26 (2018).
43. G. Li et al., *Nat. Phys.* **6**, 109–113 (2010).
44. A. Luican et al., *Phys. Rev. Lett.* **106**, 126802 (2011).
45. A. Kerelsky et al., *Nature* **572**, 95–100 (2019).
46. Y. Jiang et al., *Nature* **573**, 91–95 (2019).
47. S.-Y. Li et al., *Phys. Rev. B* **96**, 155416 (2017).
48. J. Kang, O. Vafeek, *Phys. Rev. Lett.* **122**, 246401 (2019).
49. J. F. Dodaro, S. A. Kivelson, Y. Schattner, X. Q. Sun, C. Wang, *Phys. Rev. B* **98**, 075154 (2018).
50. D. V. Chichinadze, L. Classen, A. V. Chubukov, *Phys. Rev. B* **102**, 125120 (2020).
51. A. Uri et al., *Nature* **581**, 47–52 (2020).
52. D. Blankschtein, Y. Shapir, A. Aharony, *Phys. Rev. B Condens. Matter* **29**, 1263–1267 (1984).
53. Y. Cao et al., Replication Data for: Nematicity and Competing Orders in Superconducting Magic-Angle Graphene, Version 1.0, Harvard Dataverse (2021).

## ACKNOWLEDGMENTS

We acknowledge helpful discussions with P. A. Lee, S. Todadri, A. Vishwanath, A. Hristov, I. Fisher, J. Venderbos, and S. A. Kivelson. **Funding:** This work was supported by the STC Center for Integrated Quantum Materials (NSF grant no. DMR-1231319) for

most devices' fabrication, transport measurements, and data analysis (Y.C., D.R.-L.). J.M.P. acknowledges the US Department of Energy (DOE), Office of Basic Energy Sciences (BES), Division of Materials Sciences and Engineering under Award DE-SC0001819 for additional device fabrication. D.R.-L. acknowledges partial support from Fundación Bancaria "la Caixa" (LCF/BQ/AN15/10380011) and from the US Army Research Office (grant no. W911NF-17-S-0001). P.J.-H. acknowledges support from the Gordon and Betty Moore Foundation's EPIQS Initiative through grant GBMF9643 and the National Science Foundation (DMR-1809802). The development of new nanofabrication and characterization techniques enabling this work has been supported by the US DOE Office of Science, BES, under award DE-SC0019300. K.W. and T.T. acknowledge support from the Elemental Strategy Initiative conducted by MEXT, Japan (grant no. JPMXP0112101001), JSPS KAKENHI (grant no. JP20H00354), and CREST (JPMJCR15F3). JST. This work made use of the Materials Research Science and Engineering Center Shared Experimental Facilities supported by the National Science Foundation (DMR-0819762) and of Harvard's Center for Nanoscale Systems, supported by the NSF (ECS-0335765). R.M.F. (phenomenological modeling) acknowledges support by the U.S. Department of Energy, Office of Science, Basic Energy Sciences, Materials Sciences and Engineering Division,

under Award no. DE-SC0020045. N.F.Q.Y. and L.F. (in-plane field modeling) were supported by the US DOE, Office of Science, Office of Basic Energy Sciences (BES), Division of Materials Sciences and Engineering under Award DE-SC0018945; **Author contributions:** Y.C., D.R.-L., and J.M.P. fabricated samples and performed transport measurements. Y.C., D.R.-L., and P.J.-H. performed data analysis and discussed the results. P.J.-H. supervised the project. N.F.Q.Y., L.F., and R.M.F. provided theoretical support. K.W. and T.T. provided h-BN samples. Y.C., D.R.-L., and P.J.-H. co-wrote the manuscript with input from all coauthors. **Competing interests:** The authors declare no competing financial interest. **Data and materials availability:** The data from this study are available at the Harvard Dataverse (53).

## SUPPLEMENTARY MATERIALS

science.sciencemag.org/content/372/6539/264/suppl/DC1  
Materials and Methods  
Figs. S1 to S12  
Table S1  
References (54–61)

16 April 2020; accepted 12 March 2021  
10.1126/science.abc2836

## QUANTUM SIMULATION

# Realization of an ideal Weyl semimetal band in a quantum gas with 3D spin-orbit coupling

Zong-Yao Wang<sup>1,2,3,†</sup>, Xiang-Can Cheng<sup>1,2,3,†</sup>, Bao-Zong Wang<sup>1,4,†</sup>, Jin-Yi Zhang<sup>1,2,3,†</sup>, Yue-Hui Lu<sup>4,5</sup>, Chang-Rui Yi<sup>1,2,3</sup>, Sen Niu<sup>4,5</sup>, Youjin Deng<sup>1,2,3</sup>, Xiong-Jun Liu<sup>4,5\*</sup>, Shuai Chen<sup>1,2,3\*</sup>, Jian-Wei Pan<sup>1,2,3\*</sup>

Weyl semimetals are three-dimensional (3D) gapless topological phases with Weyl cones in the bulk band. According to lattice theory, Weyl cones must come in pairs, with the minimum number of cones being two. A semimetal with only two Weyl cones is an ideal Weyl semimetal (IWSM). Here we report the experimental realization of an IWSM band by engineering 3D spin-orbit coupling for ultracold atoms. The topological Weyl points are clearly measured via the virtual slicing imaging technique in equilibrium and are further resolved in the quench dynamics. The realization of an IWSM band opens an avenue to investigate various exotic phenomena that are difficult to access in solids.

In a Weyl semimetal, the valence and conduction bands meet at nodal points, where the quasiparticles are characterized by the Weyl Hamiltonian and have linear dispersions (1–7). A Weyl node corresponds to a topological monopole whose charge equals the Chern number of the metallic Fermi surface enclosing the nodal point; this charge defines the chirality of the Weyl fermions at the node. According to the Nielsen-Ninomiya no-go theorem (8), Weyl nodes emerge in pairs, with the two nodes in each pair having opposite

chiralities—hence, the minimum number of Weyl nodes in a semimetal is two. A semimetal with only two Weyl nodes is an ideal Weyl semimetal (IWSM) (9), the most fundamental phase in the Weyl semimetal family. Because the two nodes in an IWSM cannot be trivially gapped out, any interacting phase born of an IWSM is nontrivial. Thus, IWSMs can host noninteracting Weyl physics such as the chiral anomaly (10, 11), as well as many-body phenomena such as space-time supersymmetry (12) and non-Abelian chiral Majorana modes (13), which may not be favored in the interacting Weyl semimetals with more Weyl points. Although various Weyl and Weyl-like phases have been widely reported, including type II Weyl semimetals (14, 15), triply degenerate semimetals (16, 17), and magnetic Weyl semimetals (18–20), a direct observation of IWSMs remains elusive (21, 22).

Meanwhile, the realization of various topological models has been an active pursuit in quantum simulation with ultracold atoms (23–29). In particular, ultracold quantum gases with synthetic spin-orbit (SO) inter-

actions provide pristine platforms to investigate exotic topological phenomena. SO interactions synthesized in different dimensions have distinct features. One-dimensional (1D) SO couplings correspond to Abelian gauge potentials (30–32), whereas 2D SO couplings correspond to non-Abelian gauge potentials (33, 34), including 2D Dirac (35) and Rashba (36) types; the Dirac type has been actively studied for realizing 2D quantum anomalous Hall (QAH) models in optical Raman lattices (27, 37). The 3D SO interactions, characterized by 3D non-Abelian gauge potentials, are an essential ingredient for achieving high-dimensional topological matter. In particular, the emergent Weyl Hamiltonian in the Weyl semimetal (38–41) describes a 3D Weyl-type SO coupling, the realization of which has been a long-standing challenge in the field of quantum simulation.

In this study, we realize and detect a 3D SO coupling and IWSM band for ultracold <sup>87</sup>Rb atoms following the recent proposal in (42), with the Hamiltonian in the 3D Bloch momentum **q**-space

$$H_{\text{Weyl}} = \hbar(\mathbf{q}) \cdot \sigma \quad (1)$$

where  $\sigma = (\sigma_x, \sigma_y, \sigma_z)$  are the Pauli matrices and  $\hbar(\mathbf{q})$  characterizes the **q**-dependent SO-coupling axis. The Hamiltonian  $H_{\text{Weyl}}$  at a fixed  $q_x$  reduces to a 2D QAH model, the topology of which is modulated by  $q_x$ . In our experiment, the number of Weyl points is tuned by adjusting the frequencies of optical transitions that generate 3D SO coupling. We use a virtual slicing reconstruction imaging technique (42, 43) and measure the quench dynamics of the system to clearly resolve the Weyl points.

## Construction of 3D spin-orbit coupling

The 3D SO coupling is constructed using 3D optical Raman lattices (Fig. 1A). Spin is defined

<sup>1</sup>Hefei National Laboratory for Physical Sciences at the Microscale and Department of Modern Physics, University of Science and Technology of China, Hefei, Anhui 230026, China.

<sup>2</sup>Shanghai Branch, CAS Center for Excellence in Quantum Information and Quantum Physics, University of Science and Technology of China, Shanghai 201315, China. <sup>3</sup>Shanghai Research Center for Quantum Science, Shanghai 201315, China.

<sup>4</sup>International Center for Quantum Materials, School of Physics, Peking University, Beijing 100871, China. <sup>5</sup>CAS Center for Excellence in Topological Quantum Computation, University of Chinese Academy of Sciences, Beijing 100190, China.

\*Corresponding author. Email: xiongjunliu@pku.edu.cn (X.-J.L.); shuai@ustc.edu.cn (S.C.); pan@ustc.edu.cn (J.-W.P.)

†These authors contributed equally to this work.

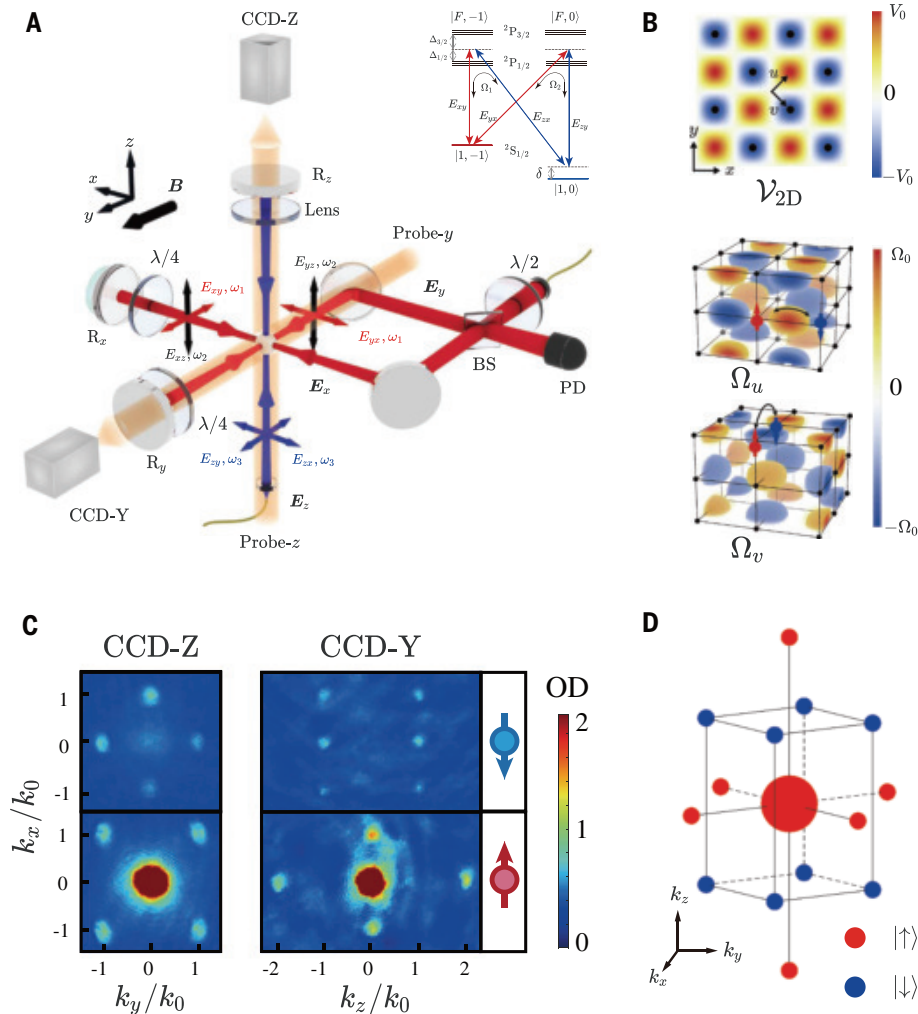


**Fig. 1. Experimental apparatus and 3D SOC.** (A) Experimental setup. Laser beams  $E_x$ ,  $E_y$ , and  $E_z$  with a wavelength of 787 nm produce 3D optical lattices with Raman couplings. Polarization components with frequency  $\omega_1$ , ( $\omega_2, \omega_3$ ) are marked by red (black, blue). Raman couplings are generated by beam pairs ( $E_{zx}, E_{xy}$ ) and ( $E_{zy}, E_{yx}$ ), composing the double- $\Lambda$  configuration shown in the inset. BS, beam splitter; PD, photodiode. (B) Density plot of checkerboard lattice potential in real space (top). The 3D antisymmetric structures of the two Raman couplings  $\Omega_u$  (middle) and  $\Omega_v$  (bottom) are also shown. The grids represent lattice sites of  $\mathcal{V}_{\text{Latt}}$ . (C) Spin-resolved TOF images of the ground state of a 3D SO-coupled BEC along  $\hat{z}$  and  $\hat{y}$ , where  $V_{2D} = 1.77E_r$ ,  $V_z = 3.54E_r$ ,  $\Omega_0 = 1.02E_r$  and  $\delta = -0.1E_r$ . OD, optical density. (D) Illustration of the reconstruction of the momentum distribution.

as the magnetic sublevels of  $^{87}\text{Rb}$  atoms in the  $|\uparrow\rangle = |1, -1\rangle$  and  $|\downarrow\rangle = |1, 0\rangle$  states. A bias magnetic field  $\mathbf{B} = 14.5$  G applied along the  $y$  axis provides quantization of the  $y$  axis and Zeeman splitting of 10.2 MHz. The  $|1, +1\rangle$  state is 30.2 kHz off resonance, owing to the quadratic Zeeman shift—hence, it is effectively excluded (27, 31, 32, 37). Three retroreflective laser beams with a wavelength  $\lambda = 787$  nm [wave vector  $\mathbf{k}_0 = 2\pi/\lambda$  and recoil energy  $E_r = \hbar^2 k_0^2 / 2m$  ( $\hbar$ , Planck's constant divided by  $2\pi$ ;  $m$ , mass of an atom)] shine on the atoms along the  $x$ ,  $y$ , and  $z$  directions, marked as  $E_i$  ( $i = x, y, z$ ), respectively, in Fig. 1A. Each laser has orthogonal polarization components  $E_{ij}$  ( $j = x, y, z$ ).  $E_{xy}$  and  $E_{yx}$  have frequency

$\omega_1$ ,  $E_{xz}$  and  $E_{yz}$  have frequency  $\omega_2$ , and  $E_{zx}$  and  $E_{zy}$  have frequency  $\omega_3$ . We set  $\omega_3 - \omega_1 \approx 2\pi \times 10.2$  MHz, matching the Zeeman splitting of  $|\uparrow\rangle$  and  $|\downarrow\rangle$ , and set  $\omega_1 - \omega_2 = 2\pi \times 200$  kHz. Two  $\lambda/4$  waveplates with optical axis aligned along  $\hat{z}$  are placed in front of the retroreflectors, producing a  $\pi$  phase shift between  $E_{xz(yz)}$  and  $E_{xy(yx)}$ .

In the experiment,  $E_x$  and  $E_y$  form checkerboard lattices in the  $xy$  plane when their relative phase is adjusted to  $\varphi = 0$ . Using a coordinate frame  $(u, v)$  rotated from  $(x, y)$  as  $u = (x + y)/\sqrt{2}$  and  $v = (x - y)/\sqrt{2}$ , one can write down the lattice potential as  $\mathcal{V}_{2D}(u, v) = V_{2D}(\cos^2 k_1 u + \cos^2 k_1 v)$ , with  $k_1 = k_0/\sqrt{2}$  (44). The density profile of  $\mathcal{V}_{2D}$  is shown in Fig. 1B.

The total 3D lattice potential is  $\mathcal{V}_{\text{Latt}}(u, v, z) = \mathcal{V}_{2D}(u, v) + \mathcal{V}_z(z)$ , where  $\mathcal{V}_z(z) = V_z \cos^2 k_0 z$  is the lattice potential along the  $z$  direction.

Raman couplings are generated by beam pairs ( $E_{zx}, E_{xy}$ ) and ( $E_{zy}, E_{yx}$ ). The frequency difference  $\omega_2 - \omega_1$  prevents the couplings between ( $E_{zy}, E_{xz}$ ) and ( $E_{zy}, E_{yz}$ ). The Raman couplings have 3D structures and, in the  $u$ - $v$ - $z$  coordinates, are  $\Omega_R(u, v, z) = \Omega_u(u, v, z)\sigma_x + \Omega_v(u, v, z)\sigma_y$ , where  $\Omega_u(u, v, z) = \Omega_0 \cos k_0 z \sin k_1 u \cos k_1 v$  and  $\Omega_v = \Omega_u(u \leftrightarrow v, z)$ . As shown in Fig. 1B,  $\Omega_u$  ( $\Omega_v$ ) is antisymmetric along  $\hat{u}$  ( $\hat{v}$ ) and symmetric along  $\hat{z}$ , leading to spin-flipped hopping in the  $\hat{u}$  ( $\hat{v}$ ) direction. We finally reach the following Hamiltonian (44)

$$H = \frac{\hbar^2 \mathbf{k}^2}{2m} + \mathcal{V}_{\text{Latt}}(u, v, z) + \Omega_u(u, v, z)\sigma_x + \Omega_v(u, v, z)\sigma_y + \frac{\delta}{2}\sigma_z \quad (2)$$

where  $\hbar \mathbf{k}$  is momentum and  $\delta$  is the two-photon Raman detuning.

Within the tight-binding approximation, Eq. 2 in Bloch momentum space reads (41, 42, 44)

$$H_{\text{TB}}(\mathbf{q}) = \hbar(\mathbf{q}) \cdot \boldsymbol{\sigma} = 2t_{\text{SO}}(\sin q_u \sigma_x + \sin q_v \sigma_y) + [m_z - 2t_z \cos q_z - 2t_1(\cos q_u + \cos q_v)]\sigma_z \quad (3)$$

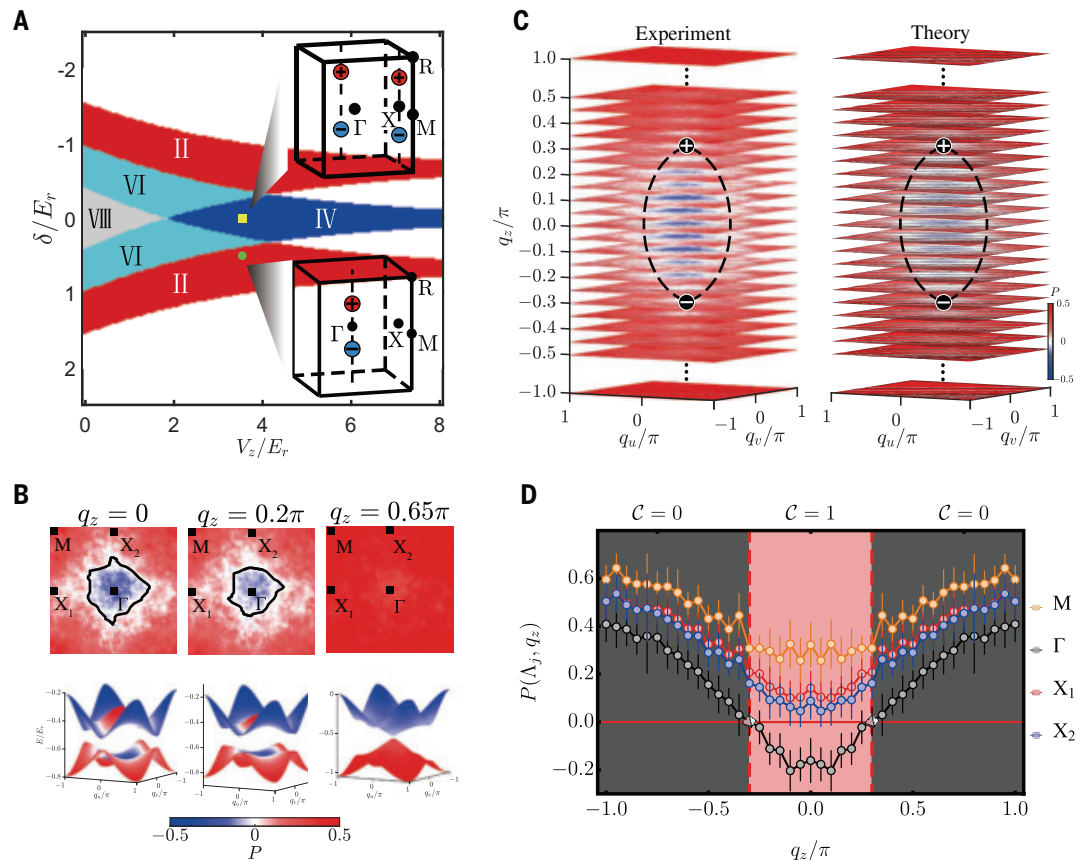
where  $\mathbf{q} = (q_u, q_v, q_z)$  is the dimensionless momentum,  $t_{\text{SO}}$ ,  $t_1$  ( $t_{\text{SO}}$ ) denote the spin-conserved (spin-flipped) hopping coefficients, and  $m_z = \delta/2$ . The spin-dependence of the  $t_{z,1}$  terms is caused by the staggered configuration of Raman potentials and derived from a state-dependent gauge transformation, whereas the  $t_{\text{SO}}$  terms characterize the SO coupling driven by Raman potentials (44). For each fixed  $q_z$ ,  $H_{\text{TB}}$  gives rise to a 2D QAH model in the  $uv$  plane (27, 35, 37, 42), with topology modulated by both  $m_z$  and  $q_z$ . The Weyl points emerge when the 2D QAH layers change topology as  $q_z$  is varied.

We demonstrate the realization of a 3D SO coupling in an optically trapped  $^{87}\text{Rb}$  Bose-Einstein condensate (BEC) with  $2.0 \times 10^5$  atoms in the  $|\uparrow\rangle = |1, -1\rangle$  state. As the 3D Raman lattice beams are adiabatically ramped up in 100 ms, the BEC is loaded into the ground state of Eq. 2. Two probe beams shine along the  $\hat{z}$  and  $\hat{y}$  directions simultaneously after the atoms are freely released for 22 ms. The spin-resolved time-of-flight (TOF) images are taken on CCD-Z and CCD-Y, respectively, as shown in Fig. 1C (CCD, charge-coupled device). The  $|\uparrow\rangle$  clouds are from the diffraction of the 3D optical lattices. On CCD-Z, most of the BEC is at momentum  $(k_x, k_y) = (0, 0)$ , and four small dots are at momenta  $(k_x, k_y) = (\pm k_0, \pm k_0)$ . On CCD-Y, there are two small dots at  $(k_x, k_z) = (0, \pm 2k_0)$  and another set of two at  $(k_x, k_z) = (\pm k_0, 0)$ , the latter of which arise from the overlaps of the four diffractions at  $(k_x = \pm k_0, k_y = \pm k_0, k_z = 0)$ . The  $|\downarrow\rangle$  clouds



**Fig. 2. Phase diagram and observation of the IWSM phase in the equilibrium approach.**

(A) Phase diagram of a Weyl semimetal band with  $V_{2D} = 1.77E_r$  and  $\Omega_0 = 1.02E_r$ . Numbers of Weyl points are indicated by Roman numerals, and the corresponding regions are distinguished by different colors. The green circle and yellow square are experimental points. Insets show 3D Brillouin zones for four Weyl points (upper) and IWSM (lower). Weyl points are labeled by  $\oplus$  or  $\ominus$ . The four high-symmetry points are marked by  $\Gamma(0, 0, 0)$ ,  $M(\pi, \pi, 0)$ ,  $X(0, \pi, 0)$ , and  $R(\pi, \pi, \pi)$ . (B) Three typical spin textures, imaged on CCD-Z. In the experiment,  $V_{2D} = 1.77E_r$ ,  $V_z = 3.54E_r$ , and  $\Omega_0 = 1.02E_r$ . The first Brillouin zone is shifted with  $\Gamma(0, 0)$  in the center. Four high-symmetry momenta ( $M, \Gamma, X_1, X_2$ ) are marked in the spin textures. Black contours indicate the band inversion rings. The corresponding band structures are shown below. (C) Reconstruction of spin textures of different  $q_z$  layers in 3D Bloch momentum space with  $\delta_0 = -0.5E_r$ . Experimental data are shown at left; theoretical calculations are shown at right. Weyl points are marked by  $\oplus$  or  $\ominus$ . Two black dashed lines depict the fusiform of the band inversion surface. (D) Spin polarizations  $P(\Lambda_j, q_z)$  at four high-symmetry momenta versus  $q_z$ . Weyl points are marked by pyramids. Error bars indicate the SD of measured  $P(\Lambda_j, q_z)$ .



are from the Raman couplings. On CCD-Z, they are at  $(k_x, k_y) = (\pm k_0, 0)$  and  $(0, \pm k_0)$ . On CCD-Y, they are at  $(k_x, k_z) = (k_0, \pm k_0), (0, \pm k_0)$ , and  $(-k_0, \pm k_0)$ . The 3D momentum distributions of the BEC (Fig. 1D) confirm the successful realization of a 3D SO coupling.

### Topological phase diagram and Weyl node measurement

We locate Weyl nodes and use carefully prepared thermal atoms to explore the topological phase diagram of the IWSM band. The Weyl node momentum  $\mathbf{q}^W$  is determined via  $|\hbar(\mathbf{q}^W)| = 0$ . Around these points, the linear expansion  $H(\mathbf{q}^W + \delta\mathbf{q}) = 2t_{so}\delta q_u\sigma_x + 2t_{so}\delta q_v\sigma_y + 2t_z\sin q_z^W\delta q_z\sigma_z$  yields the Weyl Hamiltonian around the  $\mathbf{q}^W$  node. Figure 2A is the calculated topological phase diagram of Eq. 2. Regions with different numbers of Weyl nodes, ranging from zero to eight, are indicated by different colors. Notably, there are phases with only two Weyl nodes, corresponding to the IWSM phase. The insets of Fig. 2A show the 3D Brillouin zone with the Weyl nodes marked by positive ( $\oplus$ ) or negative ( $\ominus$ ) chirality. To experimentally determine the positions of Weyl nodes, one can characterize the Chern number of 2D band structures for a given  $q_z$  plane. The Hamiltonian in Eq. 2 de-

lineates a set of 2D QAH bands in  $uv$  planes, stacked along  $q_z$ . The locations of Weyl nodes can be detected by measuring the topological change of 2D QAH bands as a function of  $q_z$  (42).

In the experiment,  $\sim 2.0 \times 10^5$  atoms cooled to  $\sim 150$  nK are adiabatically loaded into the lowest band of the Hamiltonian in Eq. 2. The temperature is chosen such that the entire lowest band is occupied by a sufficient number of atoms, whereas the higher bands are less occupied, to optimize the signal-to-noise ratio (27). After performing a spin-resolved TOF imaging along the  $\hat{z}$  direction, we obtain the 2D momentum distribution ( $q_u$  and  $q_v$ ) of the atoms in  $|\uparrow\rangle$  and  $|\downarrow\rangle$  states on CCD-Z, with  $q_z$  being integrated out. Spin polarization at  $\mathbf{q}$  is calculated as  $P(\mathbf{q}) = [n_{\uparrow}(\mathbf{q}) - n_{\downarrow}(\mathbf{q})]/[n_{\uparrow}(\mathbf{q}) + n_{\downarrow}(\mathbf{q})]$ , with  $n_{\uparrow(\downarrow)}(\mathbf{q})$  denoting the atom number in state  $|\uparrow\rangle$  ( $|\downarrow\rangle$ ) states at  $\mathbf{q}$ . As in (42), the Weyl band has an emergent magnetic group symmetry. As a consequence, for a given Raman detuning  $\delta_0$  in Eq. 2, the 2D spin texture for fixed  $q_z$  is identical to the  $q_z$ -integrated spin texture with proper  $\delta = \delta_0 + \delta'$  observed on CCD-Z. The shifted detuning  $\delta'$  is a function of  $\delta_0$  and  $q_z$ , and in particular,  $\delta' = 0$  for  $q_z = \pi/2$ . Therefore, by

scanning  $\delta'$  (adjusting Raman laser frequencies), we can achieve a series of 2D spin textures that reconstruct the 3D spin distribution of given  $\delta_0$ . This technique is known as virtual slicing imaging (42–44). Figure 2B shows the typical observed 2D spin textures at  $\delta_0 = -0.5E_r$ , where  $q_z = 0, 0.2\pi, 0.65\pi$  are equivalent to  $\delta' = 0.396E_r, 0.315E_r, 0.176E_r$ , respectively. The spin texture for  $q_z = 0, 0.2\pi$  exhibits band inversion ring patterns (45), marked by black contours in Fig. 2B, that correspond to spin polarizations  $P(\mathbf{q}) = 0$  (27, 37, 42). The Chern number for each of these 2D bands with fixed  $q_z$  is determined by the product  $\Theta$  of signs of spin polarizations  $P(\Lambda_j, q_z)$  at four high-symmetry momenta  $\{\Lambda_j\} = \{\Gamma(0, 0), X_1(0, \pi), X_2(\pi, 0), M(\pi, \pi)\}$ —i.e.,  $\Theta(q_z) = \prod_j \text{sgn}(P(\Lambda_j, q_z))$  (27, 46). By scanning the  $q_z$  planes through the entire 3D Brillouin zone, the topology and Weyl points of the 3D Weyl semimetal band can be fully determined.

The stack 2D spin textures in the Bloch momentum space with  $\delta_0 = -0.5E_r$  are shown in Fig. 2C. Only two Weyl nodes are observed, marked as  $\oplus$  and  $\ominus$ , revealing an IWSM regime. The black dashed lines sketch the virtual

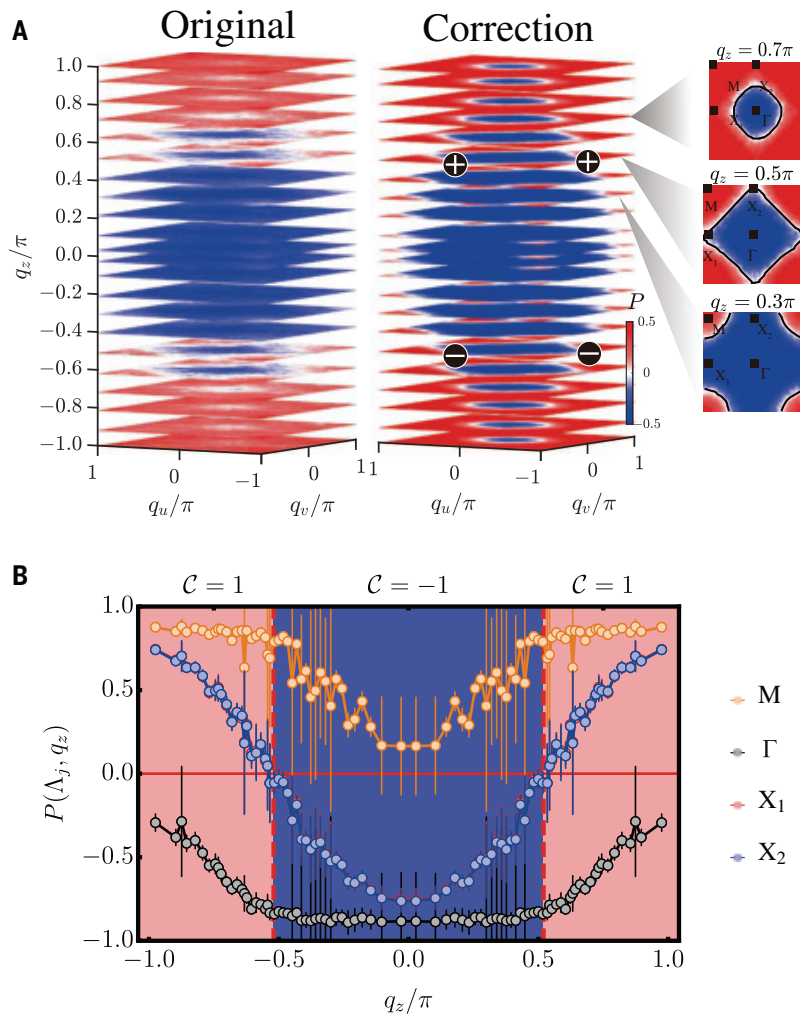


**Fig. 3. Observation of a semimetal band with four Weyl nodes in the equilibrium approach. (A)** Reconstruction of spin textures of different  $q_z$  layers in 3D Bloch momentum space with  $\delta_0 = 0$ . Original experimental data are shown at left; high-band correction data are shown at right. Weyl points are marked by  $\oplus$  or  $\odot$ . Three 2D spin textures are shown to demonstrate changes in topology around four Weyl points. **(B)** Spin polarizations  $P(\Lambda_j, q_z)$  at four high-symmetry momenta versus  $q_z$  with high-band correction. Error bars indicate the SD of measured  $P(\Lambda_j, q_z)$ .

slices of the fusiform band inversion surfaces. For  $q_z \approx 0$ , the spin polarizations are negative near the  $\Gamma$  point  $(0, 0, q_z)$  and positive outside the band inversion ring (Fig. 2B), yielding a Chern number of  $C = 1$  (45, 47). As  $q_z$  goes away from 0, the band inversion rings gradually shrink, and they vanish at Weyl nodes where  $C$  jumps from 1 to 0. When  $q_z$  is close to  $\pm\pi$ , spin polarizations over the entire layer are positive, so  $C = 0$ . From the stack of spin textures in Fig. 2C,  $P(\Lambda_j, q_z)$  are extracted and plotted in Fig. 2D as a function of  $q_z$ .  $\Theta(q_z)$  is positive for  $q_z \sim [-\pi, -0.3\pi]$  and  $[0.3\pi, \pi]$  but is negative for  $q_z \sim [-0.3\pi, 0.3\pi]$ . Hence,  $C$  jumps from 0 to 1 at  $q_z = \pm(0.3 \pm 0.03)\pi$ , indicating the positions of two Weyl points labeled by pyramids.  $P(\Lambda_j, q_z)$  can be affected by the atoms populating higher bands, which would

shift the measured location of the Weyl point (37). After removing the high-band thermal effects, we obtain the revised locations of Weyl points at  $\mathbf{q}^W = (0, 0, \pm(0.54 \pm 0.05)\pi)$ , in agreement with numerical calculations [for details, see (44)].

By varying the detuning term in Eq. 2, we reconstruct the 3D topological spin texture for  $\delta_0 = 0$  using the same protocol. The 3D spin structures for the original data (left) and the high-band correction (right) are presented in Fig. 3A. Three typical 2D spin textures are shown in the insets, with band inversion rings marked. For  $q_z = 0.7\pi$ , the ring encloses the  $\Gamma$  point, indicating  $C = 1$ . For  $q_z = 0.3\pi$ , the ring encloses the M point, indicating  $C = -1$ . For  $q_z = 0.5\pi$ , the ring touches the  $X_1$  and  $X_2$  points, indicating that  $C$  jumps by two across

the plane. The corresponding four Weyl points are located at  $\mathbf{q}^W = (0, \pi, \pm(0.52 \pm 0.07)\pi)$  and  $(\pi, 0, \pm(0.52 \pm 0.07)\pi)$ , which is confirmed by calculating  $P(\Lambda_j, q_z)$  and  $\Theta(q_z)$  (Fig. 3B).

### Measuring the Weyl nodes using quench dynamics

Although capable of revealing the overall topological properties in an intuitive way, the equilibrium approach suffers from the uncertainty of temperature and the high-band effects. Thus, we also apply an alternative method—the non-equilibrium quench dynamics (45, 47–52)—which is more robust in locating the positions of Weyl nodes. Atom clouds at 200 nK are initially prepared in the fully polarized trivial state  $|\uparrow\rangle$ . Raman couplings are effectively excluded, with a large initial detuning  $\delta_i = -200E_r$ . Thereupon,  $\delta$  is suddenly switched in 1  $\mu$ s to  $-0.5E_r$ , which is in the IWSM region. The quench protocol projects the initial state to the eigenstates of the post-quench Hamiltonian, which are superpositions of  $|\uparrow\rangle$  and  $|\downarrow\rangle$  and have different energies. The system evolves under the post-quench Hamiltonian, leading to the spin dynamical oscillations with frequencies governed by the energy differences among the different Bloch bands (47). The CCD-Y is applied to record the time evolution of spin after the quench, together with spin-resolved TOF imaging.

Figure 4A presents the dynamic evolution of the spin polarization  $P(q_x, q_z, t)$  in the Brillouin zone, from 0 to 2 ms (with  $q_y$  being integrated out). We further calculate  $P(q_z, t)$  by integrating out  $q_x$  to emphasize the dynamics along the  $q_z$  direction and plot it on the right side of each panel. For typical values of  $q_z$ ,  $P(q_z, t)$  is plotted as a function of evolution time  $t$  in Fig. 4C. When  $q_z$  is close to 0—e.g.,  $q_z = 0$  and  $\pm 0.3\pi$ — $P(q_z, t)$  exhibits both fast and slow oscillations. In this region, the lowest two s-bands overlap and form a band inversion ring (Fig. 4B). The initial state  $|\uparrow\rangle$  is mainly projected to the two s-bands. The slow oscillations are dominated by the gap opened at the band inversion ring with a typical energy of 0.5 to 1 kHz. When  $q_z$  is close to  $\pm\pi$ , the evolution of  $P(q_z, t)$  is dominated by fast oscillations. In this situation, the lowest two s-bands are separated from each other, and no band inversion ring is formed (Fig. 4B). The initial state is mainly projected to the lowest s- and p-bands rather than the two s-bands, and the oscillation frequency is determined by the gap of the lowest s- and p-bands, with a typical frequency of 4 to 5 kHz. We fit those evolutions with a double-frequency damped oscillator (44) and extract the low-frequency component  $f_{\text{low}}$  as a function of  $q_z$ , as plotted in Fig. 4D. Around  $q_z = -0.64\pi$  and  $q_z = +0.62\pi$ ,  $f_{\text{low}}$  reaches each other, whose underlying physics we explain below.



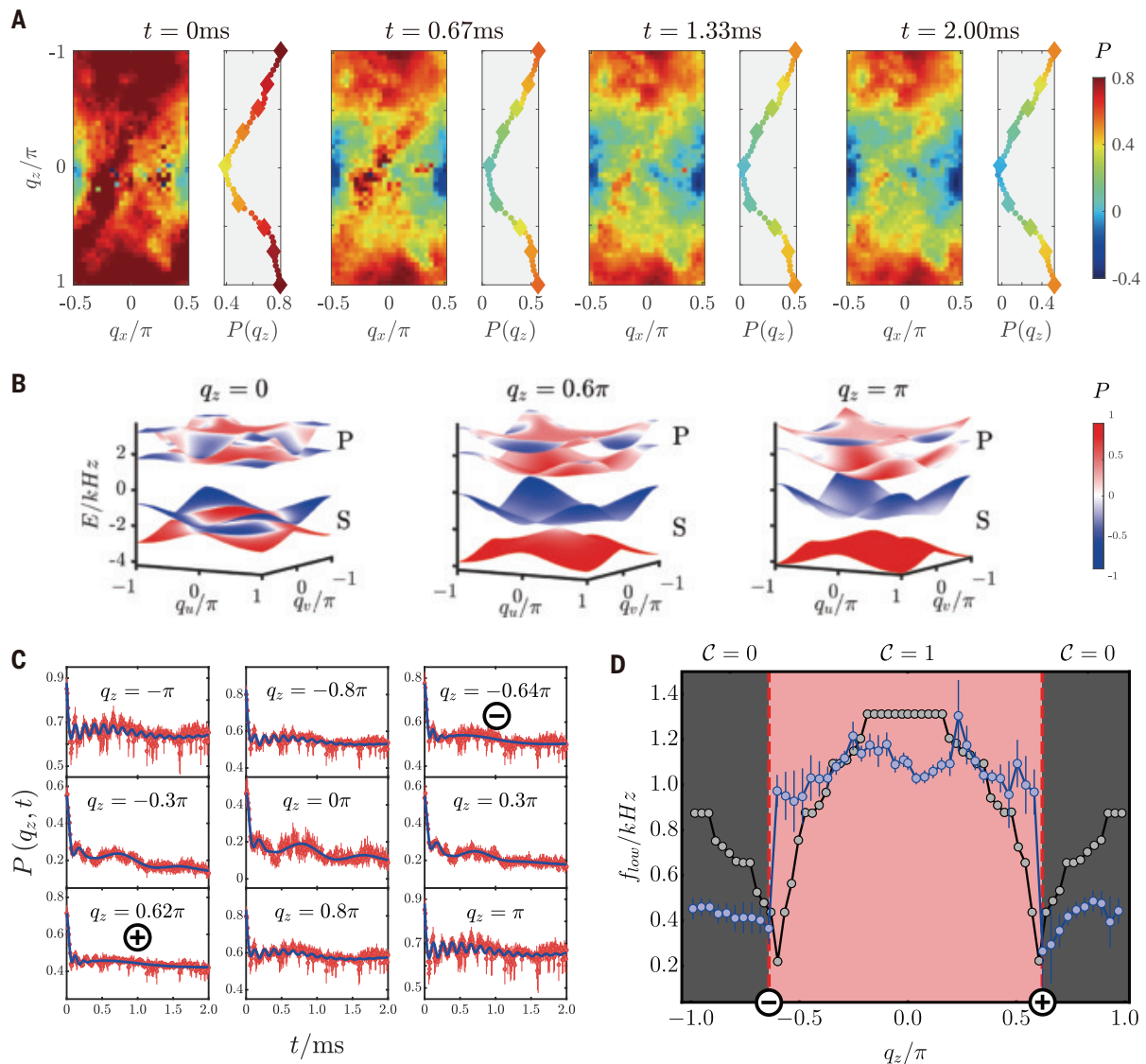


**Fig. 4. Measuring the Weyl nodes with quench dynamics.** (A) Dynamic evolution of spin polarizations in the Brillouin zone, imaged on CCD-Y. In the experiment,  $V_{2D} = 1.77E_r$ ,  $V_z = 3.54E_r$ ,  $\Omega_0 = 1.02E_r$ , and  $\delta_0 = -0.5E_r$ . (B) Band structures with  $q_z = 0$  (topological region),  $q_z = 0.6\pi$  (Weyl node), and  $q_z = \pi$  (topological trivial region) are shown. (C) Typical oscillations of spin polarization  $P(q_z, t)$  for different  $q_z$ . Red circles with error bars are experimental data. Error bars indicate the SD of measured  $P(q_z, t)$ . Blue curves are fits with a double-frequency damped oscillator model. (D) Plot of fitting parameters  $f_{\text{low}}$  versus  $q_z$  in both experimental data (blue circles with error bars) and numerical calculation (gray circles).  $\oplus$  and  $\ominus$  mark the locations of two Weyl points. Error bars indicate the SD of the fitting  $f_{\text{low}}$ .

The critical points  $q_z = (-0.64 \pm 0.08)\pi$  and  $(+0.62 \pm 0.08)\pi$  are identified as positions of the two Weyl nodes, close to the results from the equilibrium approach. In the topological region with  $|q_z| < |q_z^W|$ , the 2D bands of  $|\uparrow\rangle$  and  $|\downarrow\rangle$  are inverted, with band inversion rings in the 2D planes (42). The dynamics is dominated by on-resonance Raman-Rabi oscillations between the two inverted bands (47, 48), corresponding to the low-frequency oscillations with a large amplitude. In the trivial region, the bands of  $|\uparrow\rangle$  and  $|\downarrow\rangle$  are separated; therefore, the on-resonance Raman-Rabi oscillations vanish. Around the Weyl points, the two bands touch each other, and the band inversion ring shrinks to a singular point. The

oscillation behavior in the vicinity of the Weyl nodes is dominated by the gap of the band inversion ring, causing the minima in  $f_{\text{low}}$  (44);  $f_{\text{low}}$  does not reach zero, owing to background noise. The numerical results of low-frequency components, as calculated using the experimental parameters, are also presented in Fig. 4D (44), supporting our observation.

#### Outlook

Realization of the IWSM enables explorations of exotic quantum phenomena. For example, indirect signatures of the chiral anomaly (10, 11) were studied in condensed matter physics by measuring negative magnetoresistance (53). A clean and direct probe of this

phenomenon may be achieved in an IWSM band with high controllability of the ultracold atoms (42). Another notable phenomenon is the phase transition from Weyl to localized phases driven by disorders (54). A far-detuned laser can be used to produce a disorder potential on top of the Weyl system. Alternatively, one can apply an additional lattice that is incommensurate with the current one to realize a quasiperiodic Weyl semimetal. Such quasiperiodic Weyl semimetals can host rich phases (55) and are difficult to study in solids but achievable on the basis of our experimental system.

The present protocol for 3D SO coupling and IWSM bands is generic and can be immediately applied to fermionic systems, where

the various correlated phases can be accessed by tuning strong interactions. In particular, topological superfluidity (56, 57) could be achieved for 3D SO-coupled Fermi gases, where the mean-field theory captures essential physics (13), with higher reliability for 1D or 2D SO-coupled systems.

## REFERENCES AND NOTES

- M. Z. Hasan, S.-Y. Xu, I. Belopolski, S.-M. Huang, *Annu. Rev. Condens. Matter Phys.* **8**, 289–309 (2017).
- N. P. Armitage, E. J. Mele, A. Vishwanath, *Rev. Mod. Phys.* **90**, 015001 (2018).
- X. Wan, A. M. Turner, A. Vishwanath, S. Y. Savrasov, *Phys. Rev. B* **83**, 205101 (2011).
- A. A. Burkov, L. Balents, *Phys. Rev. Lett.* **107**, 127205 (2011).
- B. Q. Lv et al., *Phys. Rev. X* **5**, 031013 (2015).
- S. Y. Xu et al., *Science* **349**, 613–617 (2015).
- H. Weyl, *Proc. Natl. Acad. Sci. U.S.A.* **15**, 323–334 (1929).
- H. Nielsen, M. Ninomiya, *Nucl. Phys. B* **185**, 20–40 (1981).
- D. Zhang et al., *Phys. Rev. Lett.* **122**, 206401 (2019).
- H. Nielsen, M. Ninomiya, *Phys. Lett. B* **130**, 389–396 (1983).
- S. A. Parameswaran, T. Grover, D. A. Abanin, D. A. Pesin, A. Vishwanath, *Phys. Rev. X* **4**, 031035 (2014).
- S.-K. Jian, Y.-F. Jiang, H. Yao, *Phys. Rev. Lett.* **114**, 237001 (2015).
- C. Chan, X.-J. Liu, *Phys. Rev. Lett.* **118**, 207002 (2017).
- A. A. Soluyanov et al., *Nature* **527**, 495–498 (2015).
- L. Huang et al., *Nat. Mater.* **15**, 1155–1160 (2016).
- B. Bradlyn et al., *Science* **353**, aaf5037 (2016).
- B. Q. Lv et al., *Nature* **546**, 627–631 (2017).
- I. Belopolski et al., *Science* **365**, 1278–1281 (2019).
- D. F. Liu et al., *Science* **365**, 1282–1285 (2019).
- N. Morali et al., *Science* **365**, 1286–1291 (2019).
- J.-Z. Ma et al., *Sci. Adv.* **5**, eaaw4718 (2019).
- N. H. Jo et al., *Phys. Rev. B* **101**, 140402 (2020).
- M. A. A. Idelsburger et al., *Phys. Rev. Lett.* **111**, 185301 (2013).
- H. Miyake, G. A. Siviloglou, C. J. Kennedy, W. C. Burton, W. Ketterle, *Phys. Rev. Lett.* **111**, 185302 (2013).
- G. Jotzu et al., *Nature* **515**, 237–240 (2014).
- M. A. Idelsburger et al., *Nat. Phys.* **11**, 162–166 (2015).
- Z. Wu et al., *Science* **354**, 83–88 (2016).
- M. Lohse, C. Schweizer, H. M. Price, O. Zilberberg, I. Bloch, *Nature* **553**, 55–58 (2018).
- B. Song et al., *Sci. Adv.* **4**, eaao4748 (2018).
- X.-J. Liu, M. F. Borunda, X. Liu, J. Sinova, *Phys. Rev. Lett.* **102**, 046402 (2009).
- Y.-J. Lin, K. Jiménez-García, I. B. Spielman, *Nature* **471**, 83–86 (2011).
- J. Y. Zhang et al., *Phys. Rev. Lett.* **109**, 115301 (2012).
- K. Osterloh, M. Baig, L. Santos, P. Zoller, M. Lewenstein, *Phys. Rev. Lett.* **95**, 010403 (2005).
- J. Ruseckas, G. Juzeliūnas, P. Öhberg, M. Fleischhauer, *Phys. Rev. Lett.* **95**, 010404 (2005).
- B. Z. Wang et al., *Phys. Rev. A* **97**, 011605 (2018).
- L. Huang et al., *Nat. Phys.* **12**, 540–544 (2016).
- W. Sun et al., *Phys. Rev. Lett.* **121**, 150401 (2018).
- B. M. Anderson, G. Juzeliūnas, V. M. Galitski, I. B. Spielman, *Phys. Rev. Lett.* **108**, 235301 (2012).
- T. Dubček et al., *Phys. Rev. Lett.* **114**, 225301 (2015).
- Y. Xu, F. Zhang, C. Zhang, *Phys. Rev. Lett.* **115**, 265304 (2015).
- Y.-Q. Wang, X.-J. Liu, *Phys. Rev. A* **94**, 031603 (2016).
- Y.-H. Lu, B.-Z. Wang, X.-J. Liu, *Sci. Bull.* **65**, 2080–2085 (2020).
- B. Song et al., *Nat. Phys.* **15**, 911–916 (2019).
- See supplementary materials.
- L. Zhang, L. Zhang, S. Niu, X.-J. Liu, *Sci. Bull.* **63**, 1385–1391 (2018).
- X. J. Liu, K. T. Law, T. K. Ng, P. A. Lee, *Phys. Rev. Lett.* **111**, 120402 (2013).
- W. Sun et al., *Phys. Rev. Lett.* **121**, 250403 (2018).
- C. R. Yi et al., *Phys. Rev. Lett.* **123**, 190603 (2019).
- M. Tarnowski et al., *Nat. Commun.* **10**, 1728 (2019).
- C. Wang, P. Zhang, X. Chen, J. Yu, H. Zhai, *Phys. Rev. Lett.* **118**, 185701 (2017).
- M. McGinley, N. R. Cooper, *Phys. Rev. Lett.* **121**, 090401 (2018).
- A. Kruckenhauser, J. C. Budich, *Phys. Rev. B* **98**, 195124 (2018).
- H. Huang et al., *Phys. Rev. X* **5**, 031023 (2015).
- S. V. Syzranov, L. Radzihovsky, *Annu. Rev. Condens. Matter Phys.* **9**, 35–58 (2018).
- J. H. Pixley, J. H. Wilson, D. A. Huse, S. Gopalakrishnan, *Phys. Rev. Lett.* **120**, 207604 (2018).
- C. Zhang, S. Tewari, R. M. Lutchyn, S. Das Sarma, *Phys. Rev. Lett.* **101**, 160401 (2008).
- M. Sato, Y. Takahashi, S. Fujimoto, *Phys. Rev. Lett.* **103**, 020401 (2009).
- X. Cheng, Realization of an ideal Weyl semimetal band in a quantum gas with 3D Spin-Orbit coupling, version 1.0, Harvard Dataverse (2021), <https://doi.org/10.7910/DVN/QFSCAQ>.

## ACKNOWLEDGMENTS

We acknowledge insightful discussions with L. Zhang and thank W. Sun and X.-T. Xu for experimental preparation in an early stage of this work. **Funding:** This work was supported by the National Key R&D Program of China (grants 2016YFA0301601 and 2016YFA0301604), the National Natural Science Foundation of China (grants 11825401, 11761161003, 11921005, and 12025406), Anhui Initiative in Quantum Information Technologies (AHY120000), Shanghai Municipal Science and Technology Major Project (grant 2019SHZDZX01), and the Strategic Priority

Research Program of Chinese Academy of Science (grant XDB28000000). **Author contributions:** X.-J.L., S.C., and J.-W.P. conceived the research and designed the experiment. Z.-Y.W., X.-C.C., and S.C. set up the experiment. Z.-Y.W., X.-C.C., J.-Y.Z., and C.-R.Y. performed the measurements. B.-Z.W., Y.-H.L., S.N., Y.D., and X.-J.L. provided the theoretical calculations. All authors contributed to the data analysis and manuscript preparation. **Competing interests:** The authors declare no competing interests. **Data and material availability:** All experimental data and code are available in the Harvard Dataverse (58).

## SUPPLEMENTARY MATERIALS

[science.sciencemag.org/content/372/6539/271/suppl/DC1](https://science.sciencemag.org/content/372/6539/271/suppl/DC1)  
Supplementary Text

Figs. S1 to S7

Tables S1 to S3

References

2 April 2020; accepted 12 March 2021

10.1126/science.abc0105

## REPORTS

## MAGNETISM

# Gapped magnetic ground state in quantum spin liquid candidate $\kappa$ -(BEDT-TTF) $_2$ Cu $_2$ (CN) $_3$

Björn Miksch<sup>1</sup>, Andrej Pustogow<sup>1,2</sup>, Mojtaba Javaheri Rahim<sup>1</sup>, Andrej A. Bardin<sup>3</sup>, Kazushi Kanoda<sup>4</sup>, John A. Schlueter<sup>5,6</sup>, Ralph Hübner<sup>1</sup>, Marc Scheffler<sup>1</sup>, Martin Dressel<sup>1\*</sup>

Geometrical frustration, quantum entanglement, and disorder may prevent long-range ordering of localized spins with strong exchange interactions, resulting in an exotic state of matter.  $\kappa$ -(BEDT-TTF) $_2$ Cu $_2$ (CN) $_3$  is considered the prime candidate for this elusive quantum spin liquid state, but its ground-state properties remain puzzling. We present a multifrequency electron spin resonance (ESR) study down to millikelvin temperatures, revealing a rapid drop of the spin susceptibility at 6 kelvin. This opening of a spin gap, accompanied by structural modifications, is consistent with the formation of a valence bond solid ground state. We identify an impurity contribution to the ESR response that becomes dominant when the intrinsic spins form singlets. Probing the electrons directly manifests the pivotal role of defects for the low-energy properties of quantum spin systems without magnetic order.

**T**he exotic properties of quantum spin liquids (QSL) have continuously drawn interest since Anderson's seminal study half a century ago (1), where he considered spin models that possess an extensive degeneracy of states. At low temperatures, classical spins in magnetically interacting systems usually achieve a long-range periodic arrangement. However, it is widely believed that geometrical frustration may suppress conventional magnetic ordering down to  $T = 0$  K, giving rise to a distinctive, fluctuating, quantum-disordered state (2–4). Organic charge-transfer

salts were the first and most versatile QSL candidates because their microscopic parameters can be easily tuned by chemical means. These salts crystallize in a near-isotropic triangular arrangement of  $S = \frac{1}{2}$  spins on molecular dimers (5) (Fig. 1), in contrast to most inorganic QSL candidates, such as pyrochlore compounds or herbertsmithite, which form tetrahedral or kagome lattices (6, 7), respectively.

For two decades, QSLs have been intensely explored by various magnetic probes, but for most materials, crucial questions remain unanswered: How is magnetic order prevented? What is the ground state? And what is the spin excitation spectrum? For the two-dimensional charge-transfer salts, the importance of disorder became evident only recently (8–12). On the fundamental issue of the existence of a spin gap in  $\kappa$ -(BEDT-TTF) $_2$ Cu $_2$ (CN) $_3$ , however, conflicting conclusions can be drawn from magnetic torque (13), muon spin rotation ( $\mu$ SR) (14), thermal transport (15), specific heat (16),

<sup>1</sup>Physikalisches Institut, Universität Stuttgart, 70569 Stuttgart, Germany. <sup>2</sup>Department of Physics and Astronomy, University of California, Los Angeles, CA 90095, USA. <sup>3</sup>Institute of Problems of Chemical Physics, Russian Academy of Sciences, Chernogolovka, Moscow Region 142432, Russia. <sup>4</sup>Department of Applied Physics, University of Tokyo, Tokyo 113-8656, Japan. <sup>5</sup>Materials Science Division, Argonne National Laboratory, Argonne, IL 60439, USA. <sup>6</sup>National Science Foundation, Alexandria, VA 22314, USA.

\*Corresponding author. Email: [dressel@pi1.physik.uni-stuttgart.de](mailto:dressel@pi1.physik.uni-stuttgart.de)



and nuclear magnetic resonance (NMR) measurements (17). The necessity of studying the range  $T \rightarrow 0$  favors experimental methods that are susceptible to, among other things, impurity spins. Measurements of the bulk susceptibility do not distinguish between its intrinsic and extrinsic components.  $\mu$ SR and NMR spectroscopies are indirect probes, because they record the influence of local magnetism on the spectral and relaxation properties of muons and atomic nuclei, respectively. In contrast, electron spin resonance (ESR) directly probes the magnetic excitation spectrum of the conduction electrons, which allows us to unambiguously identify the intrinsic response and separate it from other contributions. Commonly used commercial instruments do have a very high sensitivity, but they are restricted in frequency and temperature. For that reason, we developed a broadband ultra-low-temperature ESR technique based on coplanar waveguide resonators. The technique can be operated in a dilution refrigerator, increasing the temperature range to the millikelvin regime, and allows measurements not only at a single microwave frequency but also at multiple harmonics of the fundamental frequency of the one-dimensional resonators (18).

In Fig. 2A, we plot the temperature dependence of the spin susceptibility  $\chi_s(T)$ , as derived from the X-band ESR spectra on  $\kappa$ -(BEDT-TTF) $_2$ Cu $_2$ (CN) $_3$  single crystals shown in Fig. 2B. At temperatures above 10 K, the overall behavior can be described by a Heisenberg model on a triangular lattice with strong antiferromagnetic exchange interaction  $J = 250$  K, in agreement with previous estimates (17). However, at  $T^* \approx 6$  K, a rapid drop in  $\chi_s(T)$  is observed; this is at the very same temperature where an anomaly was consistently identified by various methods (15–17, 19–21). Fitting the decay by an activated behavior with functional form  $\chi_s(T) \propto T^{-1} \exp\{-\Delta/T\}$  yields a spin gap of  $\Delta = 12.1$  K, as shown by the green line; details are given in (18). Because the  $g$  value of  $\kappa$ -(BEDT-TTF) $_2$ Cu $_2$ (CN) $_3$  remains unchanged at low temperatures (fig. S2), long-range magnetic order or any well-defined local moments can be ruled out, in accord with previous NMR results that show no splitting in the spectra (17). Thus, our ESR investigations unambiguously identify the anomaly at  $T^*$  as a phase transition to a gapped magnetic ground state.

Because our findings clearly rule out the widely assumed gapless QSL state with itinerant spinons (16, 17), we consider possible scenarios for a spin-gapped ground state on a slightly distorted triangular lattice (Fig. 1B), such as a valence bond solid (VBS), an Amperean pairing instability,  $Z_2$  QSL, or other resonating valence bond phases (2–4, 22, 23). First, we notice that  $\chi_s(T)$  resembles that of other known systems that undergo a contin-

uous transition to a spin-gapped state, for instance the well-known spin-Peierls transitions in organic linear-chain compounds (24), or inorganic CuGeO $_3$  and  $\alpha'$ -NaV $_2$ O $_5$  (25, 26), as elaborated in (18). Similar to these quasi-1D systems,  $\kappa$ -(BEDT-TTF) $_2$ Cu $_2$ (CN) $_3$  exhibits a structural anomaly with anisotropic thermal expansion at the transition (19), corroborating the idea of a broken-symmetry ground state that couples to the lattice. Such a transition occurs when the energy gain by the formation of spin singlets exceeds the energy required for the lattice distortion. Here, the shrinkage of the  $c$  axis below  $T^*$  that is accompanied by pronounced lattice softening (20) suggests that the  $(b \pm c)$  directions are the preferable orientations of the valence bonds (Fig. 1C). Taken together, these experimental signatures are fully consistent with a VBS, a non-magnetic ground state in which neighboring spins of opposite direction form valence bond singlets arranged in a regular fashion—a scenario also discussed for kagome (27) and higher-dimensional QSL candidates (28).

Besides the VBS scenario, a gapped QSL phase could be the result of a topological  $Z_2$  spin liquid found in perfect triangular-lattice dimer models with some analogy to a phase-disordered Bardeen-Cooper-Schrieffer (BCS) superconductor (3, 4, 29). However, the present in-plane anisotropy and potential symmetry breaking at  $T^*$  put tight constraints on a conceivable  $Z_2$  state. Alternatively, it was suggested that an Amperean pairing instability can impose a gap to mobile spinons, with an incommensurate modulation of the amplitude (30), in order to explain the phase transition at  $T^*$  and other low-temperature properties of the title compound. Yet this scenario is rather difficult to reconcile with the vanishing thermal transport (15) and the presence of unscreened orphan spins, discussed below. Precise structural studies through  $T^*$ , by de-

ducing the valence bond arrangement, may prove decisive in distinguishing between the above scenarios.

Having clarified the ground state as a nonmagnetic spin-singlet phase, we next ask: Why did its nature remain unresolved for decades despite much experimental effort? To address this, carefully consider the ESR raw data in Fig. 2B. Below room temperature, the Dysonian absorption at the resonance field  $B_{\text{main}} \approx 337$  mT acquires a Lorentzian shape as the conductivity decreases in accordance with dc transport measurements (31). The line initially broadens when cooled to 40 K, followed by a moderate reduction of the line width  $\Delta B$  at lower temperatures (figs. S2 and S3). Near  $T^*$ , the signal narrows extremely, and the doubly integrated area [corresponding to  $\chi_s(T)$ ] is strongly reduced. Most importantly, a second component with an even smaller  $\Delta B$  appears at  $T^*$ , as illustrated in Fig. 2C. Although just below  $T^*$  the resonance field of the two features is indistinguishable, Fig. 2D shows that the newly emerging component splits off as an additional peak that shifts away from  $B_{\text{main}}$  for  $T < 2.5$  K. We attribute this contribution, whose intensity increases upon cooling (orange symbols in Fig. 2A), to defects, in accord with previous considerations (10–12, 21). The feature actually consists of two or three individual lines with slightly different angle dependence and field variation, consistently observed in all crystals from four different laboratories (figs. S9 and S10); whereas the type of defect is always the same, the density varies from sample to sample. As the defect signals emerge from the main ESR line at  $B_{\text{main}}$ , we conclude that these defect spins arise from molecular dimer sites that remain unpaired below  $T^*$ .

Figure 2E illustrates the low-temperature angle dependence of the ESR lines while the magnetic field is rotated within the  $bc$  plane.

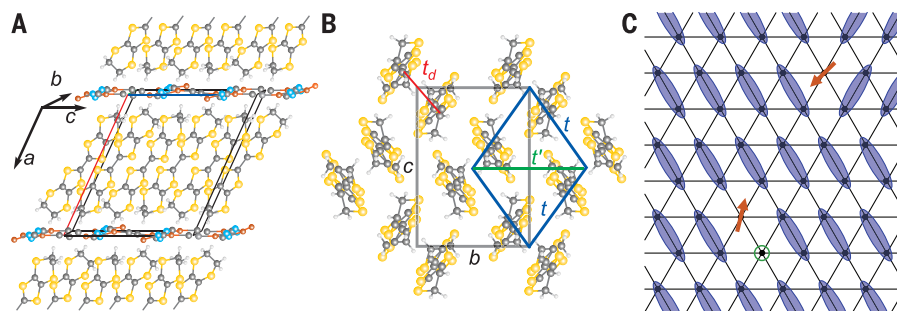


**Fig. 1. Crystal structure of the QSL candidate  $\kappa$ -(BEDT-TTF) $_2$ Cu $_2$ (CN) $_3$ .** (A) Layers of tilted BEDT-TTF dimers in the  $bc$  plane are separated in  $a^*$  direction [ $a^* \perp (bc)$ ] by  $[\text{Cu}_2(\text{CN})_3]_\infty$  anion sheets. The colors represent the different atoms in (A) and (B): gray, carbon; yellow, sulfur; white, hydrogen; blue, nitrogen; and red, copper. (B) The dimers are internally coupled by the transfer integral  $t_d$  and arranged on a slightly distorted triangular lattice. The interdimer transfer integrals  $t$  and  $t'$  define the degree of frustration,  $t'/t \approx 0.83$ . (C) Sketch of a valence bond solid state on an  $S = 1/2$  triangular lattice with spin singlets denoted in blue. Domain walls (top right), topological defects, and monomers are expected in real materials. The orange arrows represent unpaired spins caused by random pinning of local moments; vacancies are represented by a green circle.

The signal at  $B_{\text{main}}$  shifts only by  $10^{-3}$  upon rotation, a change caused by the anisotropy of the  $g$  tensor of the BEDT-TTF molecules owing to spin-orbit interactions. The minor lines, however, exhibit an order of magnitude larger variation and follow a  $(3\cos^2\theta - 1)$  angular dependence, implying that the  $(\text{BEDT-TTF})_2^+$  defect spins are subject to dipole-dipole interaction with a nearby magnetic moment at a distance  $r \approx 6$  to  $7$  Å, as suggested recently (12). We consistently observe similar angle dependences in different crystals (fig. S8), indicating that the defect spins are localized and experience dipolar interaction with a local magnetic moment along a fixed crystallographic direction, specifically ruling out that this local field is caused by regular dimers within the  $bc$  plane. In all samples, however, we detect  $S = \frac{1}{2}$   $\text{Cu}^{2+}$  ions in the anion sheet (fig. S6) (32, 33), which can generate comparable local fields at the organic dimer sites (18). These excess electrons most likely dope the closest  $(\text{BEDT-TTF})_2$  site, creating a vacancy and, hence, an unpaired spin on one of the neighboring dimers (sketched in Fig. 1C). Thus,  $\text{Cu}^{2+}$  impurities may be responsible for the observed defect spins with a  $(3\cos^2\theta - 1)$  ESR signal. Full clarification of the nature and origin of the local magnetic moments remains a desideratum for experiment as well as theory.

The emergent local fields for  $B\parallel a^*$  are of comparable strength to the low-temperature  $^{13}\text{C}$  NMR line width (4.8 mT) (20) and signatures in the  $\mu\text{SR}$  data (14). The distinct anisotropy also explains the angular shift and diverging susceptibility in the magnetic torque observed for low  $T$  and  $B$  (10, 13). To elucidate the relation to the weak-moment antiferromagnetic phase suggested in (14), we performed broadband ESR experiments at different fields down to millikelvin temperatures using superconducting coplanar waveguide resonators as illustrated in Fig. 3A. Figure 3B displays a representative temperature evolution of the ESR absorption of the crystal measured with the fundamental mode at 1.1 GHz upon cooling from 4 K to 25 mK. The defect signal, affected by local moments, separates from  $B_{\text{main}} = 40$  mT at a temperature  $T_{\text{loc}} \approx 1$  K and saturates at lower fields upon cooling; the field dependence of  $T_{\text{loc}}$  is in accord with the suggested phase boundaries (14). Figure 3C illustrates the approximately field-independent offset of the defect signal with respect to  $B_{\text{main}}$  at the base temperature  $T_{\text{base}} = 25$  mK.

What is the origin of the second line in Fig. 3B at  $B_{\text{main}}$ ? Although thermal excitations across the spin gap exceed the defect contributions close to  $T^*$  (Fig. 2), they should not

contribute at  $T_{\text{base}} \approx \Delta/500$ . As sketched in Fig. 1C, there is a possibility of intrinsic valence bond imperfections, for instance through domain walls or other types of broken singlets (10, 11, 23). In the absence of a nearby magnetic moment, the corresponding ESR line remains at  $B_{\text{main}}$ .

There is an obvious advantage of using electron spins to directly probe the magnetic properties of quantum spin liquids. Because the NMR spin-lattice relaxation rate is susceptible to any kind of unpaired spins in the sample, it will be dominated by impurities in the event that a spin gap opens. Indeed, a recent field-dependent NMR study on several  $\kappa$ -type organic QSL compounds suggests that the contribution of the defect spins can dominate over the intrinsic relaxation but is suppressed by fields of order  $B = 10$  T or higher (12). Of course, impurities such as  $\text{Cu}^{2+}$  do not disappear when warming above  $T^*$ , but they are overwhelmed by the large number of intrinsic paramagnetic moments. Whereas high densities of  $\text{Cu}^{2+}$  will dope the system into a metallic state (32), tiny amounts of charged defects embedded in a Mott-insulating matrix are a potential source of electrical polarization, possibly accounting for the controversially discussed relaxor-like dielectric response (31, 34).

The scenario of localized unpaired spins, possibly pinned to  $\text{Cu}^{2+}$ , dispersed in a VBS

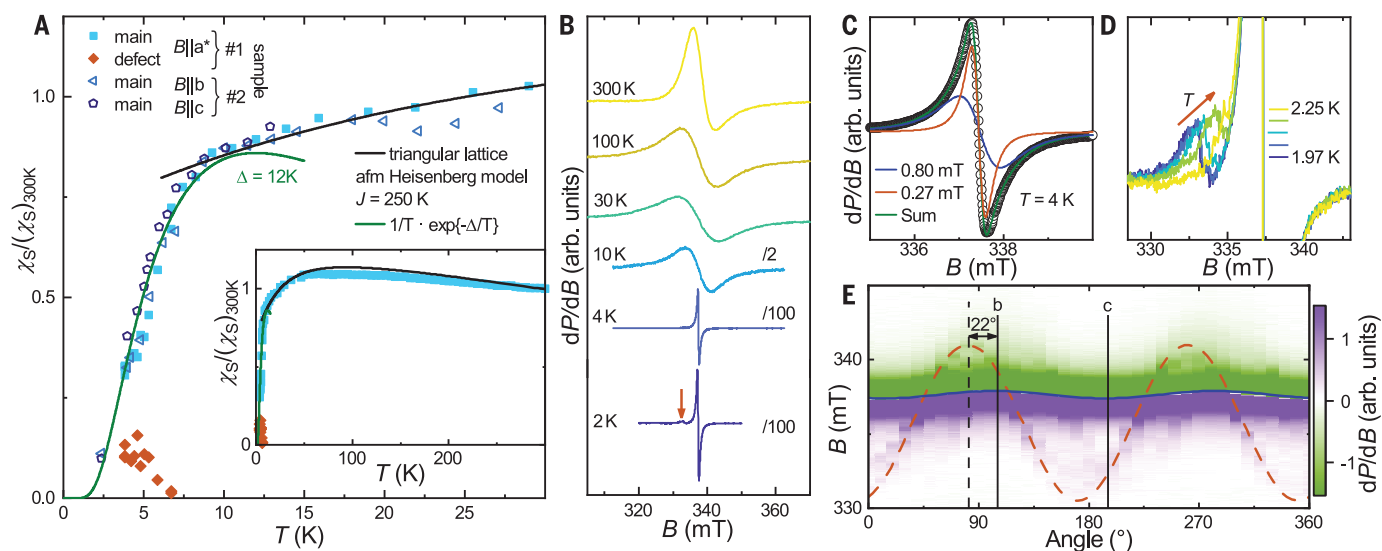


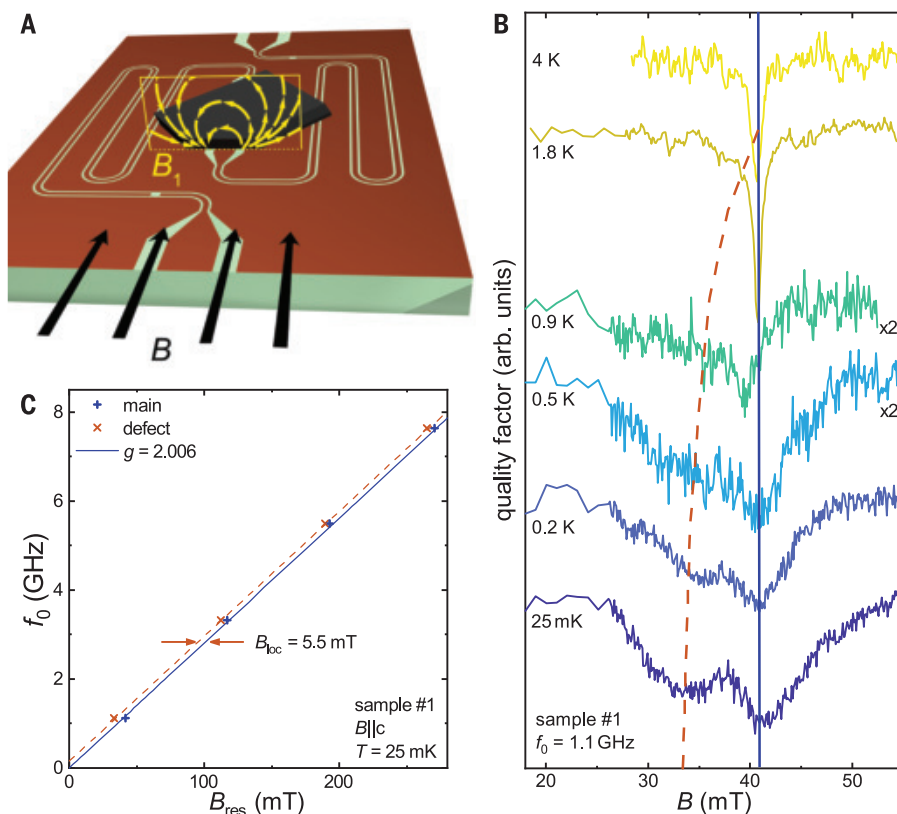
**Fig. 2.** X-band ESR results of  $\kappa$ -(BEDT-TTF) $_2\text{Cu}_2(\text{CN})_3$ . All datasets but one show sample #1; the exception is stated. **(A)** Temperature dependence of the normalized spin susceptibility  $\chi_S$  measured on two samples along different directions. The data shown for  $B\parallel b,c$  are for sample #2. At elevated temperatures,  $\chi_S(T)$  is described by an antiferromagnetic Heisenberg model on a triangular lattice with  $J = 250$  K (black line). Below the anomaly at  $T^* = 6$  K, an exponential decay of the main signal evidences the opening of a spin gap  $\Delta = 12$  K (green line). The orange diamonds correspond to the signal from defect spins, which becomes obvious for  $T < T^*$ . Inset: Susceptibility data up to  $T = 300$  K for  $B\parallel a^*$ . **(B)** Temperature evolution of the X-band spectra with the magnetic field  $B\parallel c$ . The signal at  $T = 10$  K and below is divided by the factors indicated in the figure to account for the increasing peak in

$dP/dB$  as the line sharpens. **(C)** Below  $T^*$ , an additional narrow component appears, requiring a second Lorentzian function to fit the spectra satisfactorily. As an example, the 4 K data are shown with the respective decomposition. **(D)** Upon cooling below 2.5 K, this new signal separates and shifts to lower resonance fields; we attribute the signal to defect spins not involved in the singlet formation. **(E)** Anisotropy of the ESR resonances of  $\kappa$ -(BEDT-TTF) $_2\text{Cu}_2(\text{CN})_3$ . The main signal (solid blue line) is identified by the zero-crossing of  $dP/dB$  from positive (green) to negative (violet) and shows a small angular variation of 0.3 mT when measured within the  $bc$  plane at  $T = 2$  K. In contrast, the signal of the defect spins (dashed orange line) has a huge anisotropy of 10 mT offset from the crystallographic  $c$  direction by an angle of  $22^\circ$  and caused by dipolar interaction to local moments, possibly  $\text{Cu}^{2+}$  (see text).



**Fig. 3. Low-temperature broadband ESR features of  $\kappa$ -(BEDT-TTF) $_2$ Cu $_2$ (CN) $_3$ .**

**(A)** Coplanar waveguide resonator with mounted sample. The direction of the static magnetic field  $B$  is shown in black. The microwave magnetic field  $B_1$  (yellow) is subject to absorption by electron spin resonance within the sample. **(B)**  $B||c$  ESR spectra at 1.1 GHz for different temperatures down to 25 mK. The solid blue line corresponds to the constant main signal  $B_{\text{main}}$ , whereas the dashed orange line indicates the evolution of the local-moment signal. **(C)** Low-temperature peak positions for varying resonance frequencies and fields.



resolves the long-standing controversy of a vanishing  $\kappa/T$  in thermal transport for  $T \rightarrow 0$  despite the gapless excitations concluded from specific heat (11, 15, 16). Recent reexamination of the thermal conductivity suggests that a spin gap also exists in  $\beta'$ -EtMe $_3$ Sb[Pd(dmit) $_2$ ] $_2$  (35). Whereas much larger disorder effects are expected for the inorganic QSL candidate herbertsmithite ZnCu $_3$ (OH) $_6$ Cl $_2$  owing to Cu-Zn antisite exchange on the order of 10% (36), which indeed have been reported (37, 38), Ag $^{2+}$  defects should be absent in  $\kappa$ -(BEDT-TTF) $_2$ Ag $_2$ (CN) $_3$ . Nevertheless, defect spins may prove crucial for the low-temperature magnetic properties of all quantum spin systems that lack magnetic order. There are now few QSL candidates remaining where the opening of a spin gap has not been proven beyond any doubt. The broadband low- $T$  ESR spectroscopy developed here provides a versatile tool to tackle these and related issues.

## REFERENCES AND NOTES

- P. Anderson, *Mater. Res. Bull.* **8**, 153–160 (1973).
- L. Balents, *Nature* **464**, 199–208 (2010).
- L. Savary, L. Balents, *Rep. Prog. Phys.* **80**, 016502 (2017).
- C. Broholm et al., *Science* **367**, eaay0668 (2020).
- B. J. Powell, R. H. McKenzie, *Rep. Prog. Phys.* **74**, 056501 (2011).
- M. J. P. Gingras, P. A. McClarty, *Rep. Prog. Phys.* **77**, 056501 (2014).
- M. R. Norman, *Rev. Mod. Phys.* **88**, 041002 (2016).
- T. Furukawa et al., *Phys. Rev. Lett.* **115**, 077001 (2015).
- Y. Saito, T. Minamitate, A. Kawamoto, N. Matsunaga, K. Nomura, *Phys. Rev. B* **98**, 205141 (2018).
- K. Riedl, R. Valentí, S. M. Winter, *Nat. Commun.* **10**, 2561 (2019).
- H. Kawamura, K. Uematsu, *J. Phys. Condens. Matter* **31**, 504003 (2019).
- A. Pustogov et al., *Phys. Rev. B* **101**, 140401 (2020).
- T. Isono, T. Terashima, K. Miyagawa, K. Kanoda, S. Uji, *Nat. Commun.* **7**, 13494 (2016).
- F. L. Pratt et al., *Nature* **471**, 612–616 (2011).
- M. Yamashita et al., *Nat. Phys.* **5**, 44–47 (2009).
- S. Yamashita et al., *Nat. Phys.* **4**, 459–462 (2008).
- Y. Shimizu, K. Miyagawa, K. Kanoda, M. Maesato, G. Saito, *Phys. Rev. Lett.* **91**, 107001 (2003).
- See supplementary materials.
- R. S. Manna, M. de Souza, A. Brühl, J. A. Schlueter, M. Lang, *Phys. Rev. Lett.* **104**, 016403 (2010).
- M. Poirier, M. de Lafontaine, K. Miyagawa, K. Kanoda, Y. Shimizu, *Phys. Rev. B* **89**, 045138 (2014).
- Y. Shimizu, K. Miyagawa, K. Kanoda, M. Maesato, G. Saito, *Phys. Rev. B* **73**, 140407 (2006).
- Y. Zhou, K. Kanoda, T.-K. Ng, *Rev. Mod. Phys.* **89**, 025003 (2017).
- I. Kimchi, A. Nahum, T. Senthil, *Phys. Rev. X* **8**, 031028 (2018).
- M. Dumm et al., *Phys. Rev. B* **61**, 511–521 (2000).
- M. Hase, I. Terasaki, K. Uchinokura, *Phys. Rev. Lett.* **70**, 3651–3654 (1993).
- M. Isobe, Y. Ueda, *J. Phys. Soc. Jpn.* **65**, 1178–1181 (1996).
- M. R. Norman, N. J. Laurita, D. Hsieh, *Phys. Rev. Res.* **2**, 013055 (2020).
- M. Hermanns, S. Trebst, A. Rosch, *Phys. Rev. Lett.* **115**, 177205 (2015).
- R. Moessner, S. L. Sondhi, *Phys. Rev. Lett.* **86**, 1881–1884 (2001).
- S.-S. Lee, P. A. Lee, T. Senthil, *Phys. Rev. Lett.* **98**, 067006 (2007).
- M. Pinterić et al., *Phys. Rev. B* **90**, 195139 (2014).
- T. Komatsu, N. Matsukawa, T. Inoue, G. Saito, *J. Phys. Soc. Jpn.* **65**, 1340–1354 (1996).
- K. Padmalekha et al., *Physica B Condens. Matter* **460**, 211–213 (2015).
- M. Abdel-Jawad et al., *Phys. Rev. B* **82**, 125119 (2010).
- P. Bourgeois-Hope et al., *Phys. Rev. X* **9**, 041051 (2019).
- D. E. Freedman et al., *J. Am. Chem. Soc.* **132**, 16185–16190 (2010).
- M. Fu, T. Imai, T.-H. Han, Y. S. Lee, *Science* **350**, 655–658 (2015).
- P. Khuntia et al., *Nat. Phys.* **16**, 469–474 (2020).
- B. Miksch et al., Gapped magnetic ground state in quantum spin liquid candidate  $\kappa$ -(BEDT-TTF) $_2$ Cu $_2$ (CN) $_3$ , Version 1, Zenodo (2021); <https://doi.org/10.5281/zenodo.4271607>.

## ACKNOWLEDGMENTS

We thank S. E. Brown, K. Holczer, R. K. Kremer, G. Gorgen Lesseux, A. Tsirlin, and S. M. Winter for fruitful discussions. **Funding:** The work at the University of Stuttgart was supported by the Deutsche Forschungsgemeinschaft (DR228/39-3). A.P. acknowledges support by the Alexander von Humboldt Foundation through the Feodor Lynen Fellowship. K.K. was supported by the Japan Society for the Promotion of Science (grant 18H05225). J.A.S. acknowledges support from the Independent Research and Development program from the NSF while working at the foundation and from the National High Magnetic Field Laboratory (NHMFL) User Collaboration Grants Program (UCGP). **Author contributions:** M.D. conceived of the project. M.S. designed the low-temperature ESR facilities. B.M. and M.J.R. performed the experiments. B.M. and A.P. analyzed and interpreted the results, in perpetual exchange with M.D. A.A.B., K.K., J.A.S., and R.H. were responsible for the crystal growth. B.M., A.P., and M.D. wrote the manuscript, with contributions from the other authors. **Competing interests:** The authors declare that they have no competing financial interests. **Data and materials availability:** All data shown are publicly available on Zenodo (39).

## SUPPLEMENTARY MATERIALS

[science.sciencemag.org/content/372/6539/276/suppl/DC1](https://science.sciencemag.org/content/372/6539/276/suppl/DC1)  
Materials and Methods  
Figs. S1 to S14  
References (40–65)

5 May 2020; accepted 9 March 2021  
10.1126/science.abc6363

## FIRE ECOLOGY

## Carbon loss from boreal forest wildfires offset by increased dominance of deciduous trees

Michelle C. Mack<sup>1,2,3\*</sup>, Xanthe J. Walker<sup>1,2,4</sup>, Jill F. Johnstone<sup>4,5,6</sup>, Heather D. Alexander<sup>3,7</sup>, April M. Melvin<sup>3,8</sup>, Mélanie Jean<sup>4,9</sup>, Samantha N. Miller<sup>1</sup>

In boreal forests, climate warming is shifting the wildfire disturbance regime to more frequent fires that burn more deeply into organic soils, releasing sequestered carbon to the atmosphere. To understand the destabilization of carbon storage, it is necessary to consider these effects in the context of long-term ecological change. In Alaskan boreal forests, we found that shifts in dominant plant species catalyzed by severe fire compensated for greater combustion of soil carbon over decadal time scales. Severe burning of organic soils shifted tree dominance from slow-growing black spruce to fast-growing deciduous broadleaf trees, resulting in a net increase in carbon storage by a factor of 5 over the disturbance cycle. Reduced fire activity in future deciduous-dominated boreal forests could increase the tenure of this carbon on the landscape, thereby mitigating the feedback to climate warming.

The intensification of climate-sensitive disturbances, such as wildfire, can feed back to climate warming by altering net ecosystem carbon balance (NECB), the amount of carbon (C) sequestered or released to the atmosphere over time. Severe disturbance events can lead to loss of organic matter that survived previous events (1), triggering C losses that exceed the potential for reaccumulation during the following disturbance-free interval. Indirect effects of disturbance on C accumulation after fire may also drive NECB (2). Nitrogen (N) lost to the atmosphere during combustion could exacerbate N limitation to primary productivity, making it difficult for plant productivity to recoup combustion-driven C losses during post-disturbance recovery. Severe disturbances can alter the relationship between plant life history traits and habitat characteristics (3), giving rise to alternative successional pathways that affect the rates and patterns of C accumulation (4). Using empirical data to predict the impacts of disturbance on NECB is difficult because of the discrepancy between the time scales of direct and indirect effects on C accumulation. Some disturbances may result in direct effects such as instantaneous C losses, whereas changes to productivity and/or successional trajectory can lead to indirect effects that may lag one to several centuries after the disturbance (2).

The C balance of the boreal biome is of global importance because of the large size of C pools in forests and soils and their vulnerability to warming (5). Current climate-induced changes to boreal fire regimes (6) are expected to alter this biome's historic role as a net C sink relative to the atmosphere (7, 8). Contemporary fires are burning more deeply into organic soils, releasing larger amounts of C (9) and depleting long-term C stores (1). Deeper burning that combusts a larger proportion of organic soil shifts eco-

systems to a negative NECB (a net C source) if C losses are not replaced over the next disturbance-free interval. Understanding whether C accumulation during post-fire recovery compensates for C emissions during fire is essential for determining whether there is a positive feedback between climate warming and fire intensification.

Lightning-ignited wildfire has been a key structuring factor in boreal forests across Alaska and western Canada for most of the Holocene (6, 10). These forests are dominated by conifer stands of black spruce (*Picea mariana*), where stand-replacing fires occur at ~100-year intervals (11). Black spruce release seed from semi-serotinous cones (12), and the successional trajectory of spruce self-replacement is entrained in the first decade after fire (12, 13). In boreal Alaska, larger, more intense, and later season fires have caused deeper burning of the soil organic layer (SOL) (9), exposing suitable seedbeds for the establishment of deciduous tree seedlings such as aspen (*Populus tremuloides*) and birch (*Betula neoalaskana*) (12). Experimental manipulation of burn depth (14), remote sensing of deciduous forest fraction (15), and modeling forecasts (16) indicate that deeper, more severe burning will lead to increasing abundance of mixed and deciduous stands, particularly in moderate to well-drained soils (17). An emergent property of these alternative successional trajectories is a substantial

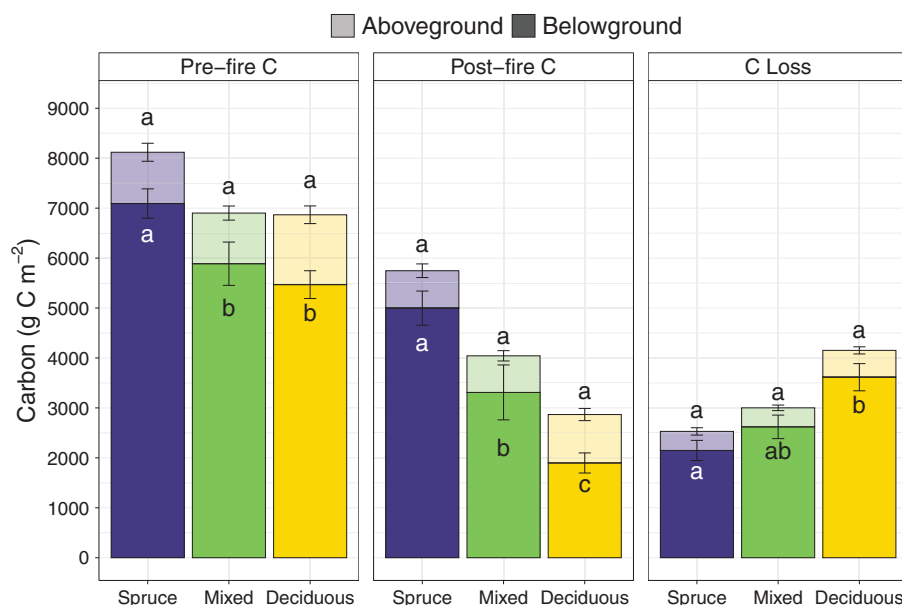


**Fig. 1. Ecosystem carbon pools and wildfire losses across successional trajectories.** Above- and belowground C across three successional trajectories of tree regeneration. In all stands ( $N = 75$ ), black spruce dominated density and biomass prior to fire. Trajectories include stands that returned to spruce dominance (blue;  $n = 21$ ), transitioned to dominance by deciduous broadleaf trees (yellow;  $n = 36$ ), or transitioned to a mixture of black spruce and deciduous tree species (green;  $n = 18$ ). See table S1 for structural classification of successional trajectories, table S3 for associated N pools and C:N ratios, and table S4 for text statistics. Letters represent significant differences ( $P < 0.05$ ) between trajectories within the above- and belowground pools.

<sup>1</sup>Center for Ecosystem Science and Society, Northern Arizona University, Flagstaff, AZ 86001, USA. <sup>2</sup>Department of Biological Sciences, Northern Arizona University, Flagstaff, AZ 86001, USA. <sup>3</sup>Department of Biology, University of Florida, Gainesville, FL 32611, USA. <sup>4</sup>Department of Biology, University of Saskatchewan, Saskatoon, SK S7J 5E2, Canada. <sup>5</sup>Institute of Arctic Biology, University of Alaska, Fairbanks, AK 99700, USA. <sup>6</sup>School of Science, Yukon University, Whitehorse, YT Y1A 5K4, Canada. <sup>7</sup>School of Forestry and Wildlife Sciences, Auburn University, Auburn, AL 36849, USA. <sup>8</sup>National Academies of Science, Engineering and Medicine, Washington, DC 20001, USA. <sup>9</sup>Département de Biologie, Université de Moncton, Moncton, NB E1A 3E9, Canada. \*Corresponding author. Email: michelle.mack@nau.edu



difference in patterns of C accumulation. Spruce stands sequester large amounts of C in a thick SOL but accumulate relatively little biomass aboveground, whereas deciduous stands sequester more biomass aboveground and little in surficial soils (18, 19). It is unknown whether stands that shift from spruce to deciduous trajectories can compensate for C lost in fire.

We examined the consequences of increasing fire severity for the C and N balance of black spruce stands in Interior Alaska, where this stand type covers >50% of the forested landscape (20). We asked whether the impacts of fire severity on successional trajectory, specifically shifts from spruce to deciduous tree dominance, were likely to exacerbate or mitigate the effects of large losses of soil C and N on NECB (21). We combined observations of individual fires with chronosequences of sites of different ages to estimate trajectories of forest recovery and C accumulation that could arise when black spruce forests burn (22).

In 2005, we established a long-term study of multiple burned areas from the 2004 fire year, when the total area burned in Alaska was more than seven times the long-term average (20). We studied 75 forest stands where black spruce was the dominant species prior to fire. Sites were located across a 250,000-km<sup>2</sup> region in Interior Alaska and were selected to cover the range of site conditions (e.g., topo-edaphic position) and fire severities (i.e., proportional combustion of canopy and SOL) (fig. S1). We used estimates of seedling species dominance to determine whether stands returned to black spruce or underwent compositional change to mixed or deciduous tree-dominated trajectories. By 2017, 28% of sites returned to black spruce dominating both relative density and relative biomass (fig. S2). The remaining 72% of sites transitioned to an alternative trajectory: mixed black spruce-deciduous (18 sites) or deciduous-dominated (36 sites). In almost all sites, black spruce density was equal to or greater than pre-fire density (fig. S3), which shows that variation in deciduous density drives initial trajectories. In 37% of stands, deciduous trees were present at low density ( $0.05 \pm 0.02$  trees m<sup>-2</sup>, mean  $\pm$  SEM) prior to fire, but neither their relative and absolute density nor their presence was related to the relative or absolute density of deciduous seedlings after fire (fig. S4), making it unlikely that post-fire deciduous dominance occurred through asexual suckering.

We determined whether post-fire successional trajectories differed in pre-fire and post-fire C and N pools and combustion losses. To project the consequences of these trajectories over longer time scales, we used a chronosequence approach to assemble data from 248 stands that varied in time after fire and tree species dominance (20). We examined C and N pools in biomass, necromass, and SOL across 100 years

of post-fire succession in order to calculate rates of C and N accumulation over time, predict pool sizes at 100 years, and estimate NECB for each trajectory.

Our survey of the 2004 wildfire network showed that sites classified as black spruce in 2017 burned at relatively low severity ( $13 \pm 2$  cm burn depth and  $30 \pm 5\%$  combustion of SOL C). Sites classified as mixed or deciduous trajectory burned similarly in depth ( $13 \pm 2$  and  $15 \pm 2$  cm, respectively) but lost a larger

percent of the SOL C pool than spruce ( $50 \pm 5\%$  and  $65 \pm 4\%$ , respectively; table S2). Sites that transitioned to a deciduous trajectory ranged in landscape position from dry, well-drained hillslopes with thin organic layers to moist valley bottoms with thick organic layers, but on average they had lower pre-fire SOL C pools than stands that returned to spruce (Fig. 1). This pattern is consistent with the idea that drier areas with thinner SOL are predisposed to burn more severely, making these landscape positions

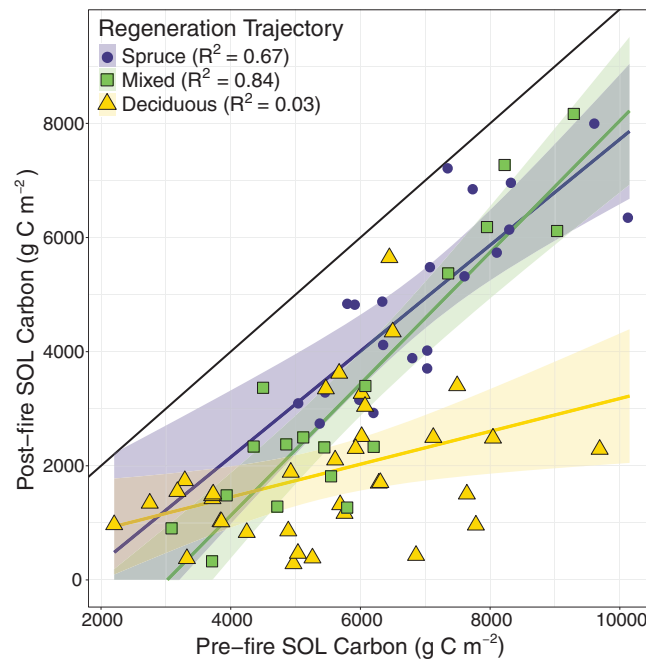


**Fig. 2. Wildfire effects on soil organic layer carbon pools and successional trajectories.**

The relationship between pre- and post-fire SOL C pools was estimated across three successional trajectories of tree regeneration. See Fig. 1 for sample size and table S5 for model results; in the symbol key,  $R^2$  represents marginal  $R^2$  of models fitted for each trajectory separately (table S6). Lines represent model fitted slopes; colored shading denotes 95% confidence intervals.

**Table 1. Net ecosystem carbon and nitrogen balance across successional trajectories.** Mean ( $\pm$ SEM) or estimated ecosystem C and N pools and fluxes across three trajectories of forest regeneration after wildfire. Estimates with different superscript letters indicate significant post hoc differences at  $P < 0.05$ . See table S9 for explanation of ecosystem variables.

Ecosystem variable	Post-fire successional trajectory		
	Spruce	Mixed	Deciduous
C or N pool (g m <sup>-2</sup> ) or flux (g m <sup>-2</sup> year <sup>-1</sup> )			
Pre-fire C pool ( $t_0$ )	8,119 $\pm$ 309 <sup>a</sup>	6,901 $\pm$ 396 <sup>b</sup>	6,867 $\pm$ 297 <sup>b</sup>
Post-fire residual C pool ( $t_1$ )	5,748 $\pm$ 419 <sup>a</sup>	4,452 $\pm$ 522 <sup>b</sup>	3,282 $\pm$ 462 <sup>c</sup>
Net rate of C accumulation	21 $\pm$ 3 <sup>a</sup>	42 $\pm$ 14 <sup>a</sup>	90 $\pm$ 9 <sup>b</sup>
C pool 100 years after fire ( $t_{100}$ )	7,800 $\pm$ 388 <sup>a</sup>	8,622 $\pm$ 1215 <sup>a</sup>	12,284 $\pm$ 766 <sup>b</sup>
Net C pool change ( $t_{100} - t_1$ )	2,052	4,170	9,002
% legacy C ( $t_1/t_{100} \times 100$ )	74	52	27
Net ecosystem C balance ( $t_{100} - t_0$ )	-319	1,721	5,417
Pre-fire N ( $t_0$ )	247 $\pm$ 12 <sup>a</sup>	202 $\pm$ 15 <sup>b</sup>	189 $\pm$ 10 <sup>b</sup>
Post-fire residual N ( $t_1$ )	158 $\pm$ 10 <sup>a</sup>	125 $\pm$ 15 <sup>a</sup>	71 $\pm$ 1 <sup>b</sup>
Net rate of N accumulation	0.5 $\pm$ 0.1 <sup>a</sup>	0.2 $\pm$ 0.5 <sup>a</sup>	1.6 $\pm$ 0.2 <sup>b</sup>
N pool 100 years after fire ( $t_{100}$ )	207 $\pm$ 8 <sup>a</sup>	141 $\pm$ 42 <sup>a</sup>	226 $\pm$ 21 <sup>a</sup>
Net N pool change ( $t_{100} - t_1$ )	49	16	155
% legacy N	76	88	31
Net ecosystem N balance ( $t_{100} - t_0$ )	-40	-61	+37

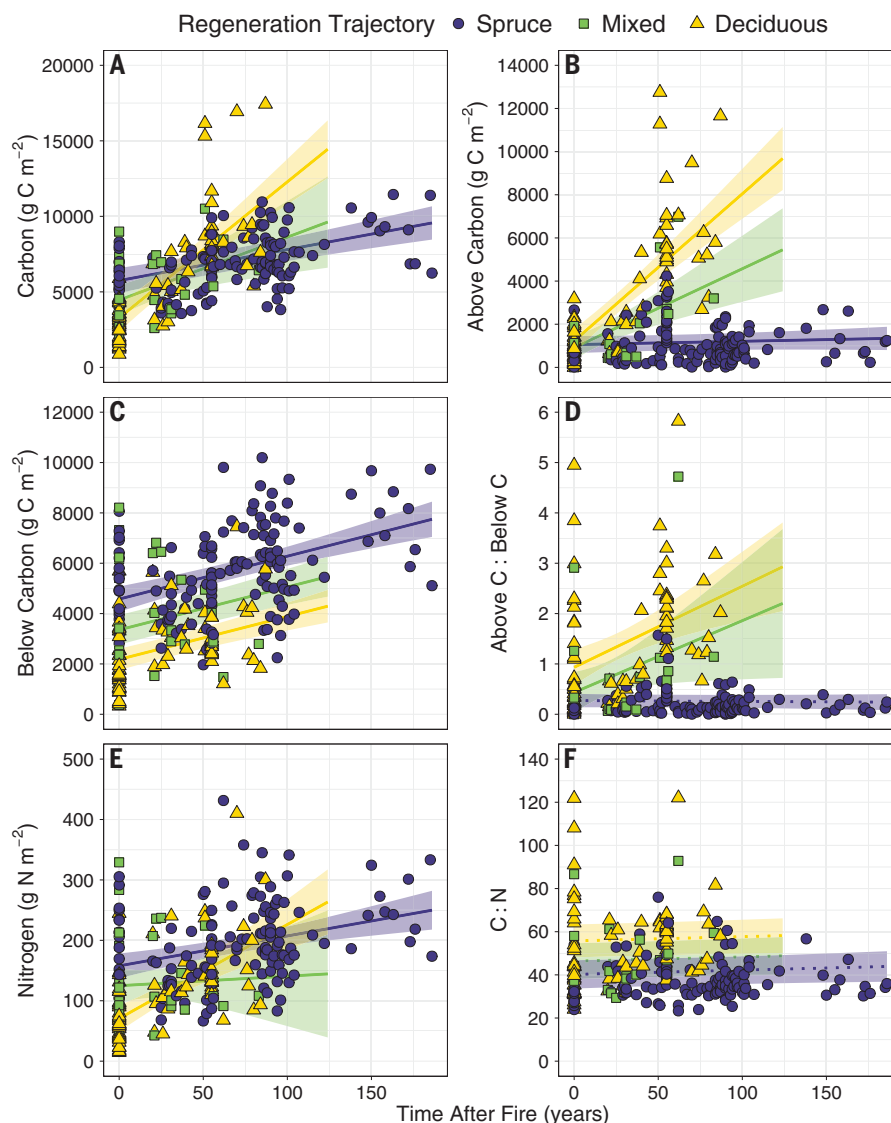


**Fig. 3. Ecosystem recovery across trajectories of forest regeneration after wildfire.** (A to F) Black spruce ( $n = 139$ ), mixed ( $n = 32$ ), and deciduous ( $n = 77$ ) stands that constitute a chronosequence approach to estimating long-term dynamics of ecosystem C pools (A), aboveground C pools (B), belowground C pools (C), ratio of aboveground to belowground C pools (D),

ecosystem N pools (E), and ecosystem C:N ratio (F) over time after fire. See table S7 for results. Solid lines indicate significant slopes; dashed lines indicate slopes not different from zero (table S8). Colored shading denotes 95% confidence intervals. Four high deciduous trajectory data points [(A) and (B)] are discussed in (20).

more vulnerable to fire-driven change in species dominance (13, 23).

Sites that transitioned in dominance had higher C and N losses from fire and carried significantly less C forward into the next successional cycle than did stands that returned to black spruce (Fig. 1 and table S3). Net “carry forward” of C and N pools for the deciduous trajectory was ~30% of pre-fire pools, primarily in the form of coarse woody debris and SOL (Table 1). Spruce self-replacement sites carried forward ~75%, primarily in SOL (Table 1). Across spruce and mixed sites, pre- and post-fire SOL C pools were highly correlated (Fig. 2), showing that pre-fire variation in the SOL was retained post-fire. Across deciduous sites, by contrast, pre- and post-fire C pools were only

weakly related (Fig. 2), hence relatively little pre-fire variation was retained. Pre-fire deciduous tree presence had no effect on C pools or their relationships (fig. S5). Post-fire initial ecosystem C pools for 2004 network trajectories were similar to starting pool size estimates of the independent chronosequence dataset (fig. S6), giving us confidence in linking the two datasets.

Over a 100-year period of post-fire succession, the deciduous trajectory accumulated ecosystem C pools faster than the black spruce trajectory by a factor of 4, reaching  $12,284 \pm 766 \text{ g C m}^{-2}$ , 1.6 times as much C as spruce stands (Fig. 3A and Table 1). Most of the rapid element accumulation on the deciduous trajectory was in aboveground tree biomass (Fig. 3B), not belowground SOL C (Fig. 3C). Im-

mediately after fire, trajectories had similar ratios of aboveground/belowground C pools. Deciduous, but not spruce, trajectories increased aboveground C pools over succession, such that after 100 years, the aboveground/belowground C ratio was higher in deciduous than in spruce trajectories by an order of magnitude (Fig. 3D and Table 1). The deciduous trajectory also accumulated N pools faster than the spruce trajectory by a factor of 3, resulting in no difference in N pools after 100 years (Fig. 3E and Table 1).

In these Alaskan black spruce forests, high-severity burning and a transition from spruce self-replacement to a deciduous-dominated trajectory led to a  $\sim 5000 \text{ g C m}^{-2}$  increase in NECB over the 100-year fire cycle (Table 1). Rapid C accumulation and high C:N ratios



of deciduous stands more than compensated for lower pre-fire C and N pools and higher C and N emissions relative to the spruce replacement trajectory.

Observed increases in NECB and aboveground/belowground C ratios associated with a shift from black spruce to deciduous dominance are consistent with plant-soil-microbial feedbacks that emerge from these contrasting plant functional types (24). Black spruce dominance is characterized by long nutrient residence time in plants and slow C and nutrient turnover in soils, resulting in accumulation of thick organic soils with large C pools. Deciduous stands, by contrast, are characterized by high plant nutrient use efficiency (19). Deciduous litter decomposes rapidly and regenerates nutrients that reinforce high tree growth rates, rapid turnover of organic soil layers, and low soil C storage (18, 19). This litter can also suppress the accumulation of recalcitrant moss, further shifting the balance of accumulating C from belowground to aboveground pools (25).

Similar transitions in aboveground/belowground C ratios have been observed with climate warming and increasing fire severity in other northern ecoregions where rapidly growing species replace slow-growing species, which suggests that this mechanism may have more general application to NECB in these transitional systems. In Canada, increased fire has led to transitions from black spruce to deciduous species (26) or equally rapidly growing pine (27). In Northeastern Eurasia, the monodominant species *Cajander larch* (*Larix cajanderi*) responds to increased fire severity by increasing density and increasing aboveground/belowground C ratios (28), thus mimicking trait changes associated with a shift to faster-growing tree species. In Arctic tundra, deciduous shrub expansion associated with climate warming alone increases aboveground/belowground C ratios (29).

More rapid N accumulation in deciduous trajectories than in mixed or spruce trajectories suggests higher N inputs or lower N losses as drivers of C accumulation. Lower N losses seem unlikely because soils in deciduous stands have higher rates of N mineralization and nitrification (19) and more enriched plant  $^{15}\text{N}$  signatures indicating more N loss (30). If high N inputs are the cause of rapid N accumulation, the source is unlikely to be deposition because inputs to these forests are low ( $<0.1 \text{ kg N ha}^{-1} \text{ year}^{-1}$ ) (31) and similar across trajectories. Moss- or alder-associated  $\text{N}_2$  fixation is also an unlikely cause; deciduous litterfall suppresses moss growth (25), and there was no evidence of increased alder density in deciduous stands relative to spruce stands (18). A plausible driver of rapid N accumulation in deciduous stands is N acquisition from deep soils because deciduous trees have deeper roots than black

spruce (32). Differences in rooting depth could be particularly important when thaw depth increases after fire (33) and exposes N frozen in permafrost (34).

Shifts in C storage from organic soil layers in spruce stands to aboveground biomass in deciduous stands could negate increased NECB if deciduous biomass C has a shorter lifetime on the landscape (35). Burned spruce stands in our study were, on average,  $94 \pm 3.8$  years old at the time of fire, which fits within estimates of fire return interval for western black spruce forests (70 to 130 years) (36). Little is known about the long-term fate of deciduous stands in Alaska, and our study did not include old stands or a second fire cycle for this stand type. Deciduous stands have low flammability, slow fire spread, and low-severity burning (37), which may enable trees to avoid or withstand fire and reduce fire spread on the landscape (38). There is limited empirical evidence of relay succession in this region (39), but where it does occur, deciduous tree mortality and canopy emergence by understory black spruce could drive C accumulation later in succession, revitalizing the plant-soil feedbacks that lead to the formation of a thick SOL (39).

When deciduous-dominated stands do burn, they are likely to regenerate via suckers as well as seed (40). These regeneration traits mean that once alternative deciduous trajectories are in place, they could be resistant to change. Studies of contemporary increases in wildfire disturbance indicate that deciduous trees will dominate the forests of Interior Alaska in this century (16, 41, 42). Longer fire-free intervals, lower fire severity, reduced fire spread on the landscape, and asexual regeneration in deciduous stands support the idea that once initiated, these forests will persist and maintain C pools longer on the landscape—a negative or stabilizing feedback to climate warming.

## REFERENCES AND NOTES

1. X. J. Walker et al., *Nature* **572**, 520–523 (2019).
2. M. Reichstein et al., *Nature* **500**, 287–295 (2013).
3. J. F. Johnstone et al., *Front. Ecol. Environ.* **14**, 369–378 (2016).
4. J. D. Coop et al., *Bioscience* **70**, 659–673 (2020).
5. E. A. G. Schuur, A. D. McGuire, V. Romanovsky, C. Schädler, M. Mack, in *Second State of the Carbon Cycle Report (SOCCR2): A Sustained Assessment Report*, N. Cavallaro et al., Eds. (US Global Change Research Program, Washington, DC, 2018), pp. 428–468.
6. R. Kelly et al., *Proc. Natl. Acad. Sci. U.S.A.* **110**, 13055–13060 (2013).
7. J. T. Randerson et al., *Science* **314**, 1130–1132 (2006).
8. Y. Pan et al., *Science* **333**, 988–993 (2011).
9. M. Turetsky et al., *Nat. Geosci.* **4**, 27–31 (2011).
10. P. E. Higuera, L. B. Brubaker, P. M. Anderson, F. S. Hu, T. A. Brown, *Ecol. Monogr.* **79**, 201–219 (2009).
11. J. F. Johnstone et al., *Can. J. For. Res.* **40**, 1302–1312 (2010).
12. J. F. Johnstone, T. K. N. Hollingsworth, F. S. Chapin III, M. C. Mack, *Glob. Change Biol.* **16**, 1281–1295 (2010).
13. J. F. Johnstone et al., *Ecosphere* **11**, e03129 (2020).
14. J. F. Johnstone, F. S. Chapin III, *Ecosystems* **9**, 14–31 (2006).
15. P. S. A. Beck et al., *Glob. Change Biol.* **17**, 2853–2866 (2011).
16. Z. A. Mekonnen, W. J. Riley, J. T. Randerson, R. F. Grant, B. M. Rogers, *Nat. Plants* **5**, 952–958 (2019).
17. X. J. Walker et al., *Glob. Change Biol.* **24**, 4251–4265 (2018).
18. D. Alexander, M. C. Mack, *Ecosystems* **19**, 98–114 (2016).
19. A. M. Melvin et al., *Ecosystems* **18**, 1472–1488 (2015).

20. See supplementary materials.
21. L. A. Boby, E. A. G. Schuur, M. C. Mack, D. Verbyla, J. F. Johnstone, *Ecol. Appl.* **20**, 1633–1647 (2010).
22. L. R. Walker, D. A. Wardle, R. D. Bardgett, B. D. Clarkon, *J. Ecol.* **98**, 725–736 (2010).
23. X. J. Walker, M. C. Mack, J. F. Johnstone, *Ecosystems* **20**, 1137–1150 (2017).
24. P. M. Vitousek, *Nutrient Cycling and Limitation: Hawaii as a Model System* (Princeton Univ. Press, 2006).
25. M. Jean, J. F. Johnstone, M. C. Mack, *Ecosystems* **23**, 18–33 (2020).
26. N. Lecomte, M. Simard, N. Fenton, Y. Bergeron, *Ecosystems* **9**, 1215–1230 (2006).
27. E. Whitman, M.-A. Parisien, D. K. Thompson, M. D. Flannigan, *Forests* **9**, 151 (2018).
28. H. D. Alexander et al., *Ecosystems* **15**, 1065–1082 (2012).
29. J. DeMarco, M. C. Mack, M. S. Bret-Harte, *Ecosystems* **14**, 804–817 (2011).
30. J. M. Craine et al., *New Phytol.* **183**, 980–992 (2009).
31. J. B. Jones, K. C. Petrone, J. C. Finlay, L. D. Hinzman, W. R. Bolton, *Geophys. Res. Lett.* **32**, L02401 (2005).
32. M. R. Gale, D. F. Grigal, *Can. J. For. Res.* **17**, 829–834 (1987).
33. E. E. Jafarov, V. E. Romanovsky, H. Genet, A. D. McGuire, S. Marchenko, *Environ. Res. Lett.* **8**, 035030 (2013).
34. J. W. Harden et al., *Geophys. Res. Lett.* **39**, L15704 (2012).
35. C. Körner, *Science* **355**, 130–131 (2017).
36. J. Héon, D. Arseneault, M.-A. Parisien, *Proc. Natl. Acad. Sci. U.S.A.* **111**, 13888–13893 (2014).
37. M.-A. Parisien et al., *Ecosystems* **14**, 1141–1155 (2011).
38. J. F. Johnstone, T. S. Rupp, M. Olson, D. Verbyla, *Landsc. Ecol.* **26**, 487–500 (2011).
39. H. D. Alexander, M. C. Mack, *For. Ecol. Manage.* **396**, 35–43 (2017).
40. D. F. Greene et al., *Can. J. For. Res.* **29**, 824–839 (1999).
41. D. H. Mann, T. S. Rupp, M. A. Olson, P. A. Duffy, *Arct. Antarct. Alp. Res.* **44**, 319–331 (2012).
42. W. D. Hansen, R. Fitzsimmons, J. Olnes, A. P. Williams, *J. Ecol.* **109**, 85–98 (2021).
43. M. C. Mack et al., “Estimates of Forest Structure, Successional Trajectory, and Carbon and Nitrogen Pools Across the 2004 Wildfire Network Sites,” ver. 2 (Environmental Data Initiative, 2021).
44. M. C. Mack et al., “A Chronosequence of Biomass and Carbon and Nitrogen Stocks Across Boreal Deciduous, Mixed, and Black Spruce Forests in Interior Alaska,” ver. 2 (Environmental Data Initiative, 2021).

## ACKNOWLEDGMENTS

We thank T. Chapin and T. Hollingsworth for help with initiating the 2004 wildfire site network, T. Schuur and L. Boby for help with combustion methods and soil sampling and processing, and C. Mojica and G. Crummer for help with laboratory analyses. Finally, we thank our dear friend and colleague, J. Reiskind, for inspiring confidence, perseverance, and comradery in us and many other women scientists. **Funding:** Supported by US Department of Defense Strategic Environmental Research and Development Program (grants RC-2754 and RC-2109) and NASA Arctic Boreal Vulnerability Experiment (NNX15AT71A, NNX17AE44G and 80NSSC19M0112) (M.C.M.), by the US Joint Fire Sciences Program (05-1-2-06) (J.F.J.), and by the Bonanza Creek Long-term Ecological Research Program, which is supported by the US NSF (DEB-1636476) and the USDA Forest Service (R/JVA-PNW-01-JV-11261952-231) (M.C.M. and J.F.J.). **Author contributions:** M.C.M. conceived the study. J.F.J. and M.C.M. designed the 2004 wildfire network study and M.C.M. and H.D.A. designed the chronosequence study. M.C.M., J.F.J., H.D.A., A.M.M., X.J.W., and M.J. carried out fieldwork, and S.N.M., A.M.M., and H.D.A. carried out lab work. X.J.W. designed the statistical analyses and figures. M.C.M. wrote the paper and all authors commented on the manuscript. **Competing interests:** The authors declare that they have no competing interests. **Data and materials availability:** All data from this study are archived in the NSF-funded Bonanza Creek Long-Term Ecological Research Data Catalog ([www.lteruaf.edu/data](http://www.lteruaf.edu/data)), which is part of EDI Data Portal (<https://portal.edirepository.org/nis/home.jsp>) (43, 44). Soils, tree cores, and plant materials are archived in the lab of M.C.M.

## SUPPLEMENTARY MATERIALS

science.sciencemag.org/content/372/6539/280/suppl/DC1  
Materials and Methods  
Tables S1 to S11  
Figs. S1 to S6  
References (45–73)

27 October 2020; accepted 8 March 2021  
10.1126/science.abf3903

## PALEONTOLOGY

# Absolute abundance and preservation rate of *Tyrannosaurus rex*

Charles R. Marshall<sup>1,2\*</sup>, Daniel V. Latorre<sup>1,2</sup>, Connor J. Wilson<sup>1,2</sup>, Tanner M. Frank<sup>1,2</sup>, Katherine M. Magoulick<sup>1,2</sup>, Joshua B. Zimmt<sup>1,2</sup>, Ashley W. Poust<sup>1,2,3</sup>

Although much can be deduced from fossils alone, estimating abundance and preservation rates of extinct species requires data from living species. Here, we use the relationship between population density and body mass among living species combined with our substantial knowledge of *Tyrannosaurus rex* to calculate population variables and preservation rates for postjuvenile *T. rex*. We estimate that its abundance at any one time was ~20,000 individuals, that it persisted for ~127,000 generations, and that the total number of *T. rex* that ever lived was ~2.5 billion individuals, with a fossil recovery rate of 1 per ~80 million individuals or 1 per 16,000 individuals where its fossils are most abundant. The uncertainties in these values span more than two orders of magnitude, largely because of the variance in the density–body mass relationship rather than variance in the paleobiological input variables.

**D**espite the famed incompleteness of the fossil record, much can be inferred from fossil material, including cell sizes and thus genome sizes (1); individual longevities (2, 3); and growth and cohort survivorship curves (2, 4, 5). However, quantifying population-level variables such as population density and abundance is made difficult by the incompleteness of the fossil record (6, 7), largely because fossilization rates are unknown, which means that the number of fossils cannot be used to calculate these variables.

Nonetheless, data from living species indicate a strong relationship between population density and body mass (8), which makes it possible to estimate population-level variables. Here, for one of the best understood dinosaurs, *Tyrannosaurus rex* (Fig. 1) (9, 10), we use this relationship to estimate its population density, which we combine (Fig. 2) (11) with our rich knowledge of the species to estimate several population-level variables, including the total number of *T. rex* that ever lived and the species' preservation rate. We assessed the impact of uncertainties in the data used with Monte Carlo simulations (12), but these simulations do not accommodate uncertainties that might stem from the choices made in the design of our approach (12).

Our calculations depend on the ability to estimate the population density ( $\rho$ ) of *T. rex* (Fig. 2). Here, we use Damuth's Law (8, 12, 13) to constrain that density. Derived from living species, Damuth found that  $\rho$  is negatively correlated with a species' body mass ( $M$ ) through a power law (8)

$$\log_{10}(\rho) = \log_{10}(a) - b \times \log_{10}(M) \quad (1)$$

In applying Eq. 1, we used the broadly accepted value of  $b = -3/4$  for the slope (8, 11, 12, 14) [see (11) for  $b = -2/3$ ], which leaves two unknowns: the intercept [ $\log_{10}(a)$ ] and the body mass ( $M$ ).

The intercept [ $\log_{10}(a)$ ] depends on trophic level and physiology. Trophically, *T. rex* was clearly a carnivore, but establishing its physiology has proven challenging (7, 15). Among living species, a slower metabolism is reflected in larger population densities, hence larger values of the intercept. However, ecological differences between species within the same trophic level, regardless of physiology, translate into a large scatter in population densities, independent of the intercept (Fig. 2A). For example, flesh-eating mammals have a 150-fold variation ( $\pm 1.96\sigma$ ) in population density for species of the same body mass (11) (Fig. 2A).

This ecological scatter swamps the uncertainty introduced by the unknown physiology of *T. rex*. Nonetheless, we need an estimate of *T. rex*'s physiology to assign an intercept. There is general agreement that dinosaurs were broadly endothermic (7, 16–21) but that different species had different physiologies

(19–21) with metabolisms equal to or lower than those of living mammals (20, 21). Energetic considerations suggest that dinosaurs were more mesothermic than living mammals (7, 17, 18). For example, the extreme size of saurischian dinosaurs (which include *T. rex*) would be best explained if they had a metabolism similar to that of large varanid lizards such as the Komodo dragon, which uses ~22% as much energy per unit mass as that used by flesh-eating mammals (17). However, dinosaur paleobiologists tend to favor a more energetic physiology (22), so we assumed a physiology midway between that of mammalian carnivores and that of large varanid lizards (11) (Fig. 2A). This translates into population densities 2.1 times as large as the population densities of the average mammalian carnivore and population densities 1/2.1 times the size of population densities of large varanids for the same body mass. By contrast, mammalian herbivores average ~35-fold higher population densities than those of flesh-eating mammals (11), and reptiles have, on average, ~30-fold higher population densities than those of mammals for the same body mass (8). The scatter about the line of best fit noted above (Fig. 2A) means that our analysis encompasses the full range of physiologies proposed for *T. rex*, including physiologies even more energetic than those of the average mammalian carnivore.

For the body mass estimate of *T. rex*, we took into account the fact that Damuth's data included individuals that had not reached maximum size (11). Thus, rather than using the maximum body mass of *T. rex*, we computed the average body mass of postjuvenile individuals (Fig. 1B and Table 1) [see (11) for why we used this cutoff], which we call the ecological body mass. This was estimated by summing, over all postjuvenile age cohorts, the product of the average mass of individuals in each cohort, using a *T. rex* growth curve (2) (Fig. 2C), and the proportion of individuals in that cohort, using available *T. rex* survivorship data (4) (Fig. 2D) (11). This yielded a

**Table 1. Input variable values for calculating *T. rex* population variables and absolute individual preservation rate.** The uncertainty values (bottom row) are the ratios of the 97.5% and 2.5% values, derived from the Monte Carlo simulations.

Values	Intercept, population density $\log_{10}(a)$	Ecological body mass (kg) $M$	Area (million km <sup>2</sup> ) $A$	Temporal range (million years) $T$
2.5% tail	1.80	3700	1.42	1.3
Mean	2.99	5200	2.30	2.4
97.5% tail	4.18	6900	3.18	3.5
Approximate uncertainty	240×*	1.6×†	2.2×	2.7×

\*The uncertainty of the intercept,  $a$ , is equal to  $10^{(97.5\% \text{ tail cutoff} - 2.5\% \text{ tail cutoff})} = 240$ . †Populations density =  $M^b$ . For  $b = -0.75$ , the ratio of the 97.5% tail and 2.5% tail is  $6900/3700 = 1.86$ , which, when raised to the exponent  $b$ , is  $(1.86)^{-0.75} = 1.6$ .

<sup>1</sup>Department of Integrative Biology, University of California, Berkeley, CA, USA. <sup>2</sup>University of California Museum of Paleontology, University of California, Berkeley, CA, USA. <sup>3</sup>San Diego Natural History Museum, San Diego, CA, USA. \*Corresponding author. Email: crmarshall@berkeley.edu



**Fig. 1. Skeletal outline of *T. rex*.** Illustration credit: Danielle Dufault, Royal Ontario Museum.

mean of 5200 kg, ranging from 3700 to 6900 kg ( $\pm 1.96\sigma$ ) (Fig. 2B and Table 1).

Given these values, we estimate that *T. rex*'s population density (Eq. 1) was between 0.00058 and 0.14 postjuvenile individuals/km<sup>2</sup> (with 95% confidence), with a median of 0.0091 individuals/km<sup>2</sup> (Fig. 2E and Table 2). This agrees well with Farlow's (7) estimate of 0.01 individuals/km<sup>2</sup> and is  $\sim 0.16$  times the population density of tigers and  $\sim 0.07$  times the population density of lions (8). The median estimate translates into a population size of 3800 *T. rex* in an area the size of California and just two individuals in an area the size of Washington, DC.

To calculate the standing population size of *T. rex* (Fig. 2G), we multiplied the population density by the estimated geographic area (Fig. 2F) occupied by *T. rex* (eq. S2). For a minimum constraint on the geographic area, we used the convex hull around *T. rex* fossil localities that have yielded published postjuvenile individuals held in public repositories (11). We used this as a minimum constraint given the geographic incompleteness of the fossil and rock records (23). For a maximum constraint, we used the size of the inferred ecological niche for tyrannosaurs in the Late Maastrichtian (11, 24). This is a maximum estimate because it is an extent of occurrence (EOO), whereas Damuth's Law is based on the smaller areas of occupancy (AOOs) (8, 11). Given these con-

straints, the estimated geographic area for *T. rex* is  $2.3 \pm 0.88$  million km<sup>2</sup> ( $\pm 1.96\sigma$ ) (Fig. 2F and Table 1).

Multiplying the plausible population densities by the plausible geographic areas yielded an average population size of 20,000 individuals, with a 95% interval from 1300 to 328,000 individuals (Fig. 2G and Table 2). The lower limit seems too low, given the loose consensus that at least thousands of individuals are needed for long-term persistence (11). Our median estimate of postjuvenile *T. rex* biomass alive at any one time—the population size multiplied by the ecological body mass—is  $1.1 \times 10^5$  tonnes with a 95% interval from  $6.6 \times 10^3$  to  $1.7 \times 10^6$  tonnes.

To estimate the total number of *T. rex* that ever lived, we multiplied the standing population size by the total number of generations that *T. rex* persisted. To estimate the latter, we divided the estimated temporal range of *T. rex* (Fig. 2H) by its generation time (Fig. 2K).

The temporal range of *T. rex* is uncertain because of the poor temporal control on most *T. rex* fossil localities (25) and because there is a substantial dinosaur preservational gap below the oldest *T. rex* fossils (11, 25, 26). Thus, we established minimum and maximum age brackets on its temporal duration (11) from 1.2 to 3.6 million years, which led to a mean estimate of 2.4 million years (Fig. 2H and Table 1).

The generation time was calculated using the proportion of individuals living to age  $x$  years ( $l_x$ ), derived from its cohort survivorship curve (4), and the average number of progeny produced at each age ( $b_x$ ), which requires an estimate of the onset of sexual maturity and its maximum lifetime (eq. S25) (11). This yielded an estimate of  $19.0 \pm 1.2$  years ( $\pm 1.96\sigma$ ) (Table 2 and Fig. 2K) (11). Dividing the longevity by the generation time yielded an estimated persistence for *T. rex* of 127,000 generations, with a 95% interval from 66,000 to 188,000 generations (Fig. 2L and Table 2).

The total number of *T. rex* that ever lived ( $N$ ) (Fig. 2M) was then estimated by multiplying the number of generations that *T. rex* persisted (Fig. 2L) by its standing population size (Fig. 2G). This gave a median of  $2.5 \times 10^9$  individuals, with a 95% interval from  $1.4 \times 10^8$  to  $4.2 \times 10^{10}$  individuals (Fig. 2M and Table 2). The median estimate, although large, is about half of the total number of adult humans currently alive. This translates into a median total postjuvenile biomass for all *T. rex* of  $1.3 \times 10^{10}$  tonnes, with a 95% interval from  $7.5 \times 10^8$  to  $2.2 \times 10^{11}$  tonnes.

With an estimate of the total number of *T. rex* that ever existed and the minimum number of described postjuvenile fossil individuals curated in public repositories (10, 11), which consists of 32 individuals, the minimum median per-individual fossil recovery rate is 1 fossil individual for every 80 million individuals (Fig. 2N and Table 2), with a 95% interval ranging from 1 in every 4.5 million to 1 in every 1.3 billion individuals (Fig. 2N and Table 2). The number of *T. rex* individuals represented in museums and in the hands of private collectors—excluding nondiagnostic elements such as teeth, vertebrae, or phalanges, whether formally described or not—is on the order of 100 individuals, so the current overall fossil recovery rate is approximately three times these values.

However, *T. rex* fossils can only be recovered from places where we have rock of appropriate age deposited in the appropriate environments. Thus, we computed the per-individual fossil

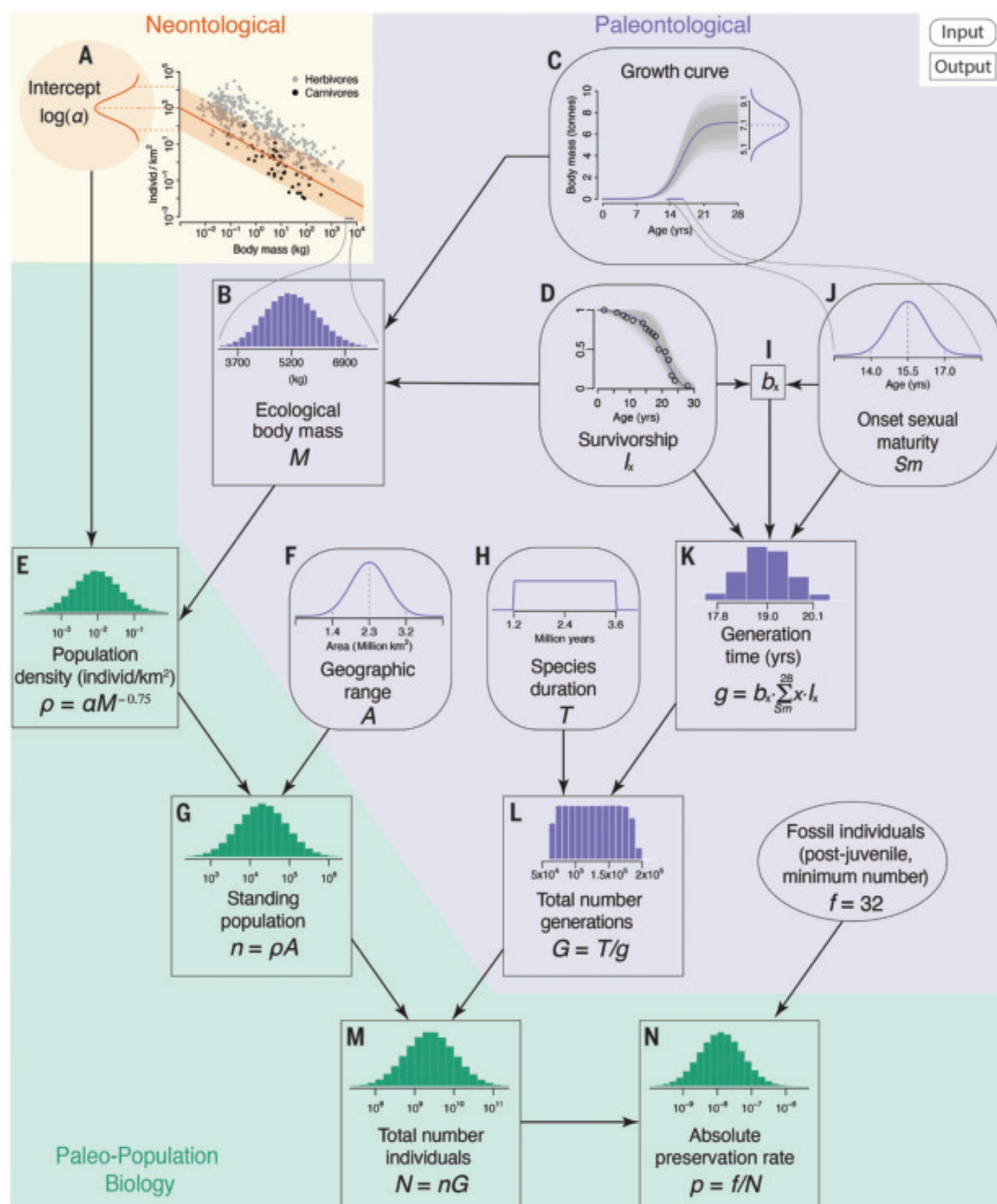
**Table 2. Output variable estimates for *T. rex* population variables and absolute individual preservation rate.** The uncertainty values (bottom row) are the ratios of the 97.5% and 2.5% values, derived from the Monte Carlo simulations. These values are approximate because of rounding errors in the numbers presented in the table.

Values	Population density (individuals/km <sup>2</sup> )	Standing population size	Generation time (years)	Number of generations	Total number of <i>T. rex</i>	Absolute preservation rate	Number of individuals per fossil
	$\rho$	$n$	$g$	$G$	$N$	$p$	$1/p$
2.5% tail	0.00058	1300	17.8	66,000	$1.4 \times 10^8$	$2.2 \times 10^{-7}$	4.5 million
Middle value	0.0091	20,000	19.0	127,000	$2.5 \times 10^9$	$1.3 \times 10^{-8}$	80 million
97.5% tail	0.14	328,000	20.1	188,000	$4.2 \times 10^{10}$	$7.6 \times 10^{-10}$	1.3 billion
Approximate uncertainty	240×	250×	1.1×	2.8×	295×	295×	295×



**Fig. 2. Schematic showing the use of paleontological and neontological data to estimate population variables and the absolute preservation rate for *T. rex*.** The quantitative relationships between the variables (11) are indicated in the insets.

(A) Distribution of intercepts used for the log(population density) versus log(body mass) plot. (B) *T. rex* ecological body mass distribution. (C) Range of growth curves for *T. rex*, given the uncertainty in the maximum body size. (D) Cohort survivorship curves for *T. rex* (5). (E) Inferred *T. rex* population density. (F) Possible geographic ranges for *T. rex*. (G) Inferred *T. rex* population size at any given time. (H) Range of plausible geologic longevities of *T. rex*. (I) Age-specific rates of reproduction,  $b_x$ . (J) Time of onset of sexual maturity ( $S_m$ ). (K) Estimated *T. rex* generation time. (L) Estimated longevity of *T. rex* in generation times. (M) Estimate of total number of *T. rex* that ever lived. (N) Minimum absolute individual preservation rate. Continuous probability distributions were used for the input variables, where the limits shown on the normal distributions represent  $\pm 1.96$  standard deviations. The limits shown for the ecological body mass (B) and generation time (K) also represent  $\pm 1.96$  standard deviations. The output variables are shown as histograms derived from 1 million Monte Carlo simulations (11).



recovery rate for just the geographic range ( $\sim 1000 \text{ km}^2$ ) (27) and duration ( $\sim 1.2$  million years) of the portion of the Hell Creek Formation that has yielded the most *T. rex* fossils. The estimated total number of postjuvenile individuals of *T. rex* that occupied this region during that 1.2 million years is  $\sim 610,000$  (table S6), or about nine at any given time. A decade-long survey (27) yielded fossils from 37 presumed postjuvenile individuals (11), which translates into a median per-individual preservation rate of 1 in 16,000, with a 95% interval ranging from 1 in 1100 to 1 in 260,000 (table S6), ignoring the possibility that fossils might have been washed in from a larger area.

The largest source of uncertainty in our analysis stems from the scatter in the body mass–population density relationship from living species, which is about two orders of magnitude larger than the paleobiological uncertainties (Table 2). Nonetheless, our capacity for inferring population sizes of extinct taxa greatly exceeds what Simpson (6) thought possible more than 75 years ago and Farlow’s (7) pioneering work on the population size of *T. rex* from almost 30 years ago. This capacity has been enabled by the discovery of many more fossils and the ability to establish growth and survivorship curves from age and body mass estimates. Further insights

into the ecology of *T. rex* should reduce the uncertainty in its population density, for example, through the use of paleontological methods for determining whether predator guilds are under- or overrepresented (28). The framework developed here can be applied to any taxon with the appropriate data, or where the data can be developed through the collection of more fossils. It also opens the door for other types of analysis—for example, determining how rare, geographically restricted, or short-lived a species had to be to escape discovery in the fossil record or combining population size estimates with measured rates of morphological evolution to infer

selection coefficients. The range and quantity of data now available for well-sampled and well-studied fossil taxa have the potential to greatly enhance our ecological understanding of extinct species.

## REFERENCES AND NOTES

- C. L. Organ, A. M. Shedlock, A. Meade, M. Pagel, S. V. Edwards, *Nature* **446**, 180–184 (2007).
- G. M. Erickson *et al.*, *Nature* **430**, 772–775 (2004).
- H. N. Woodward, E. A. Freedman Fowler, J. O. Farlow, J. R. Horner, *Paleobiology* **41**, 503–527 (2015).
- G. M. Erickson, P. J. Currie, B. D. Inouye, A. A. Winn, *Science* **313**, 213–217 (2006).
- T. M. Cullen *et al.*, *Proc. R. Soc. B* **287**, 20202258 (2020).
- G. G. Simpson, *Tempo and Mode in Evolution* (Columbia Univ. Press, 1944).
- J. O. Farlow, *Am. J. Sci.* **293**, 167–199 (1993).
- J. Damuth, *Biol. J. Linn. Soc.* **31**, 193–246 (1987).
- S. L. Brusatte *et al.*, *Science* **329**, 1481–1485 (2010).
- T. D. Carr, *PeerJ* **8**, e9192 (2020).
- See the supplementary materials.
- J. Damuth, *Nature* **290**, 699–700 (1981).
- J. Damuth, *Am. Nat.* **169**, 621–631 (2007).
- W. Jetz, C. Carbone, J. Fulford, J. H. Brown, *Science* **306**, 266–268 (2004).
- K. Padian, A. de Ricqlès, *Phil. Trans. R. Soc. B* **375**, 20190147 (2020).
- J. R. Horner, K. Padian, *Proc. R. Soc. Lond. B* **271**, 1875–1880 (2004).
- B. K. McNab, *Proc. Natl. Acad. Sci. U.S.A.* **106**, 12184–12188 (2009).
- J. M. Grady, B. J. Enquist, E. Dettweiler-Robinson, N. A. Wright, F. A. Smith, *Science* **344**, 1268–1272 (2014).
- R. A. Eagle *et al.*, *Nat. Commun.* **6**, 8296 (2015).
- L. Legendre *et al.*, *Zool. Scr.* **42**, 44–53 (2013).
- R. R. Dawson *et al.*, *Sci. Adv.* **6**, eaax9361 (2020).
- R. S. Seymour, S. L. Smith, C. R. White, D. M. Henderson, D. Schwarz-Wings, *Proc. R. Soc. B* **279**, 451–456 (2012).
- S. K. Lyons, P. J. Wagner, in *Conservation Paleobiology: Using the Past to Manage for the Future*, Paleontological Society Short Course, G. P. Dietl, K. W. Flessa, Eds. (The Paleontological Society, 2009), pp. 141–166.
- A. A. Chiarenza *et al.*, *Nat. Commun.* **10**, 1091 (2019).
- D. W. Fowler, *PLOS ONE* **12**, e0188426 (2017).
- D. A. Eberth, S. L. Kamo, *Can. J. Earth Sci.* **57**, 1220–1237 (2019).
- J. R. Horner, M. B. Goodwin, N. Myhrvold, *PLOS ONE* **6**, e16574 (2011).
- G. Rodríguez-Gómez *et al.*, *Palaeogeogr. Palaeoclimatol. Palaeoecol.* **554**, 109805 (2020).
- C. J. Wilson, D. V. Latorre, connorjwilson/Trex-abundance-preservation-2021: Code for “Absolute Abundance and Preservation Rate of ‘Tyrannosaurus rex,’” version v1.0.0, Zenodo (2021); <http://doi.org/10.5281/zenodo.4606800>.

## ACKNOWLEDGMENTS

We thank M. Carrano, A. Chiarenza, T. Cullen, P. Currie, J. Damuth, D. Eberth, D. Evans, W. Getz, M. Goodwin, J. Grady, T. Holtz, J. Horner, P. Leiggi, R. Molnar, K. Padian, R. Rogers, J. Scannella, C. Sprain, G. Wilson, and three anonymous reviewers for their input. **Funding:** This work was partially supported by the Philip Sandford Boone Chair in Paleontology at the University of California, Berkeley. **Author contributions:** C.R.M. conceived of the project and led the analysis and writing. D.V.L., with C.R.M., drafted Fig. 2. D.V.L. and C.J.W. undertook the computations. T.M.F. and J.B.Z. analyzed the stratigraphic range data. K.M.M. undertook the spatial analysis. A.W.P. assembled the *T. rex* ontogenetic data. All authors contributed to the development and writing of the paper. **Competing interests:** The authors declare no competing interests. **Data and materials availability:** All data are available in the main text or the supplementary materials. The code (written by D.V.L. and C.J.W.) for performing the Monte Carlo simulations can be found on Zenodo (29).

## SUPPLEMENTARY MATERIALS

[science.sciencemag.org/content/372/6539/284/suppl/DC1](https://science.sciencemag.org/content/372/6539/284/suppl/DC1)  
Materials and Methods  
Tables S1 to S6  
References (30–60)

15 May 2020; accepted 16 March 2021  
10.1126/science.abc8300

## OCEAN MICROBIOLOGY

# Metagenomic analysis reveals global-scale patterns of ocean nutrient limitation

Lucas J. Ustick<sup>1†</sup>, Alyse A. Larkin<sup>2†</sup>, Catherine A. Garcia<sup>2</sup>, Nathan S. Garcia<sup>2</sup>, Melissa L. Brock<sup>1</sup>, Jenna A. Lee<sup>2</sup>, Nicola A. Wiseman<sup>2</sup>, J. Keith Moore<sup>2</sup>, Adam C. Martiny<sup>1,2\*</sup>

Nutrient supply regulates the activity of phytoplankton, but the global biogeography of nutrient limitation and co-limitation is poorly understood. *Prochlorococcus* adapt to local environments by gene gains and losses, and we used genomic changes as an indicator of adaptation to nutrient stress. We collected metagenomes from all major ocean regions as part of the Global Ocean Ship-based Hydrographic Investigations Program (Bio-GO-SHIP) and quantified shifts in genes involved in nitrogen, phosphorus, and iron assimilation. We found regional transitions in stress type and severity as well as widespread co-stress. *Prochlorococcus* stress genes, bottle experiments, and Earth system model predictions were correlated. We propose that the biogeography of multnutrient stress is stoichiometrically linked by controls on nitrogen fixation. Our omics-based description of phytoplankton resource use provides a nuanced and highly resolved description of nutrient stress in the global ocean.

The supply of nutrients to the surface ocean exerts a fundamental control on phytoplankton growth (1) that may be further exacerbated by future climate-driven stratification (2). However, there is currently large uncertainty about the global patterns of nutrient stress and the possibility of limitation by multiple nutrients (3). For example, studies have independently proposed N, P, or Fe limitation for phytoplankton growing in the North Atlantic Ocean (4–6). Thus, the role and interactions of each nutrient in regulating phytoplankton growth is still unknown for large parts of the ocean.

Experimental nutrient additions and biogeochemical models are important tools for quantifying ocean nutrient stress (7). Nutrient additions have demonstrated Fe limitation in upwelling regions, but it has been difficult to identify the limiting nutrient in many other places. Multiple elements are often required to stimulate growth (8), leading to a proposal of widespread co-limitation (7). However, nutrients are commonly present simultaneously at low concentrations, making it challenging to distinguish between co-limitation and the quick exhaustion of nonlimiting nutrients (9). Bottle experiments can also introduce artifacts and are labor intensive, leading to large regional gaps in coverage (e.g., most of the Indian Ocean) (7). Ocean biogeochemical models predict large-scale patterns of nutrient limitation. However, the degree of nutrient stress and the boundaries between major nutrient-limitation regimes are sensitive to uncertain descriptions of uptake and growth as well as external

nutrient inputs (10). Thus, there are methodological and conceptual challenges associated with quantifying the biogeography of ocean nutrient stress.

*Prochlorococcus*, the most abundant phytoplankton in oligotrophic regions (11), can adapt to low-nutrient conditions through gene gains and losses. The fast growth and large population size of *Prochlorococcus* results in a close association between genome content and local nutritional conditions (12). All *Prochlorococcus* genomes include the *pstABCS* genes for direct assimilation of available inorganic phosphate (12, 13). However, cells gain the capacity for regulation (e.g., *phoBR*) and assimilation of specific P-containing compounds when inorganic P is depleted. They also detoxify the accidental uptake of arsenate with *arsR/acr3* (14). Under high P depletion and stress, cells can broadly assimilate dissolved organic P (DOP) using the alkaline phosphatases *phoA* and *phoX* (15, 16). A similar phylogenomic hierarchy of adaptation is seen for N and Fe acquisition and stress. *Prochlorococcus* cells progressively gain the capacity for ammonia, urea, nitrite, and nitrate uptake with increasing N stress driven by energetic costs of converting oxidized N compounds into glutamine (17, 18). *Prochlorococcus* cells carry genes for increasing uptake by siderophores and additional transporters under medium Fe stress (19) and have lost many Fe-containing proteins under severe Fe stress in high-nutrient, low-chlorophyll (HNLC) zones (20). Thus, genomic content of cells in a region reflects the experienced physiological nutrient stress and the biochemical trade-offs in overcoming the severity of nutrient stress by loss of function or investments in acquisition (21). Thus, we propose using the genome content of *Prochlorococcus* populations as a global-scale biosensor for ocean phytoplankton nutrient stress.

<sup>1</sup>Department of Ecology and Evolutionary Biology, University of California Irvine, Irvine, CA 92697, USA. <sup>2</sup>Department of Earth System Science, University of California Irvine, Irvine, CA 92697, USA.

\*Corresponding author. Email: [amartiny@uci.edu](mailto:amartiny@uci.edu)

†These authors contributed equally to this work.

We collected surface metagenomes from the Atlantic, Pacific, and Indian Oceans to quantify the global genome content of *Prochlorococcus* and inferred nutrient stress (table S1 and data S1). A total of 909 samples were newly collected as part of the Global Ocean Ship-based Hydrographic Investigations Program (Bio-GO-SHIP) (22) and supplemented with 228 from Tara Oceans (<https://oceans.taraexpeditions.org/>) and GEOTRACES (<https://www.geotraces.org/>). We recruited sequences to known *Prochlorococcus* strains, recorded the frequency of established nutrient acquisition genes, and normalized to *Prochlorococcus* single-copy core genes. On the basis of prior biochemical knowledge and as verified by phylogenomics (and without reference to their spatial distribution), we a priori classified genetic adaptations for overcoming a nutrient stress type and severity ( $\Omega$ ) (Table 1 and data S2). Although the classification of adaptations into high, medium, and low stress partially masks the complex biochemical tradeoffs and phylogenomic trait hierarchy of nutrient use, these groupings allow us to quantify the geographic variation of nutrient stress environments in the global surface ocean.

An ordination of nutrient genes demonstrated a continuum of stress type and severity (Fig. 1A and fig. S1). The first principal component (28% variance) was parallel to the occurrence of medium- and high-N-stress indicator genes, suggesting that the largest cluster of samples was linked to N stress. The second principal component (20% variance) separated Fe and P stress genes, and the vectors for Fe and P stress genes pointed in nearly opposite directions ( $0.9\pi$  angular difference). There was also a spread within the N cluster related to N substrate (fig. S2). The vectors for populations with only ammonia and urea assimilation genes had nearly the same angle but were separated by  $0.33\pi$  from populations containing nitrite + nitrate or cyanate genes (fig. S1). We propose that these samples were associated with medium versus high N stress. Several low-light strains of *Prochlorococcus* can use nitrite but not nitrate with a dedicated transporter *focA*. The *focA* and *narB* vectors were nearly in opposite directions (separated by  $0.88\pi$ ), suggesting a distinct ecological niche for nitrite assimilation (cooler waters with deeper mixing; figs. S1 and S2). Samples associated with elevated medium- and high-P-stress genes were predominantly from the North Atlantic Ocean and Mediterranean Sea, where high P stress has been proposed (6) (Fig. 1B). Samples associated with the high-Fe-stress genotype were mostly from the HNLC regions. However, selection for medium-stress genes occurred in many samples, suggesting widespread adaptation to Fe stress. We identified sample clusters between the N and Fe as well as the N and P gene vectors indicating frequent co-stress. By

contrast, Fe and P stress genes showed low correlation (fig. S3) and there were rare co-occurrences of Fe-P stress genes. In sum, the ordination of *Prochlorococcus* genes could identify samples with genes linked to single-nutrient stress or co-stress.

*Prochlorococcus* genome content confirmed known biogeographic patterns but also revealed several previously unrecognized regions of nutrient (co-)stress (Fig. 1B). We observed genotypes adapted to (i) widespread N stress in oligotrophic regions; (ii) P stress in the North Atlantic Ocean, Mediterranean Sea, and Red Sea; and (iii) Fe stress in the equatorial Pacific Ocean. We found additional smaller regions of P stress adaptation in the western South Atlantic Ocean and the North Indian Ocean. Other regions with Fe stress adaptation included the eastern South Pacific Subtropical Gyre, temperate regions in the North and South Atlantic Ocean, and the Arabian Sea. Our data suggested that co-stress was widespread but mostly included N as one of the elements.

*Prochlorococcus* stress genes demonstrated subtle transitions between nutrient stress type and severity in the Atlantic Ocean (Fig. 2 and figs. S4 to S7 and S13). Samples from three independent ocean transects detected a transition between elevated  $\Omega_{Fe}$  and  $\Omega_P$  moving from north to south around  $40^\circ$  to  $50^\circ N$  (figs. S4 to S7). Subtle Fe stress north of the Gulf Stream has been observed in past physiological analyses of phytoplankton (23). Genes for DOP utilization and associated  $\Omega_{P,high} > 1$  were observed in the North Atlantic subtropical gyre between  $\sim 40^\circ N$  and the Intertropical Convergence Zone (ITCZ) but peaked near  $30^\circ N$  (figs. S4 to S7). An exception was a smaller region of elevated  $\Omega_{Fe,med}$  in the Canary Current, where upwelling likely relieved macronutrient stress. In the central-eastern gyre core, we detected  $\Omega_{N,high} > 1$ , suggesting adaptation to N-P co-limitation. Some samples from the western gyre showed an unusual combination of co-occurring Fe-P

stress genes. A clear meridional shift between P stress and other nutrients at the ITCZ has been suggested (24). In support,  $\Omega_{P,high}$  and  $\Omega_{P,med}$  were substantially lower in the South Atlantic Ocean ( $\Omega_{P,high} = -0.5$  to  $0.5$ ,  $\Omega_{P,med} = -0.5$  to  $1$ ) and constrained to a small western gyre region. By contrast, genotypes in the eastern South Atlantic Ocean indicated adaptation to medium Fe stress ( $\Omega_{Fe,med} = 1$  to  $1.5$ ). This is consistent with recent bottle experiments (8) as well as a negative east-west gradient in P concentration (25).  $\Omega_{N,high}$  was positive in the central part of the South Atlantic subtropical gyre ( $\Omega_{N,high} = 0.5$  to  $1$ ), indicating strong N stress in the region (figs. S4 to S7). In parallel to the north,  $\Omega_{Fe,med}$  rose near the subtropical front toward the Southern Ocean. Distinct nutritional regimes are thus present across the Atlantic Ocean.

The Pacific Ocean also showed clear transitions in stress type and severity. We detected a sharply bounded region in the eastern equatorial Pacific Ocean with  $\Omega_{Fe,high} > 1$  (figs. S8, S9, and S13). There was also a surrounding zone with elevated  $\Omega_{Fe,med}$ , revealing a wider impact of upwelling on Fe stress than indicated by macronutrient concentrations (figs. S8 and S9). To the north of the HNLC region,  $\Omega_{Fe,med}$  was eventually replaced with elevated  $\Omega_{N,high}$  ( $\Omega_{N,high} = 0.5$ ,  $\Omega_{Fe,med} = 0$ ) and some P stress genes near Station ALOHA (<http://aco.sds.soest.hawaii.edu/ALOHA/>).  $\Omega_{Fe,med}$  was  $> 1$  in most of the southeastern Pacific Ocean, which is consistent with Fe stress seen in bottle incubations and photophysiology studies (26, 27). There was additional elevated  $\Omega_{N,high}$  in the South Pacific Ocean gyre core surrounded by a wider zone with high  $\Omega_{N,med}$  (fig. S9). In the western South Pacific Ocean, we mainly detected adaptation to N stress ( $\Omega_{N,high} = 0.5$  to  $1.5$ ,  $\Omega_{N,med} = 0.5$  to  $1$ ) (fig. S10). However, there were slight increases in  $\Omega_P$  toward the western edge of the gyre ( $\Omega_{P,high} = 0$  to  $0.5$ ,  $\Omega_{P,med} = 0$  to  $0.2$ ) (fig. S10). This zonal shift toward increasing P stress was consistent

Table 1. *Prochlorococcus* genes associated with nutrient stress type and severity.

$\Omega_{type,severity}$	Function	Marker genes	Reference(s)
$\Omega_{Fe,high}$	Loss of Fe-containing proteins	HLIII-IV core genes	(20)
$\Omega_{Fe,medium}$	Fe uptake (transporters)	<i>cirA</i> , <i>expD</i> , <i>febB</i> , <i>fepB/C</i> , <i>tolQ</i> , <i>tonB</i>	(19)
$\Omega_{P,high}$	Alkaline phosphatase	<i>phoA</i> , <i>phoX</i>	(12, 15)
$\Omega_{P,medium}$	P starvation regulation, arsenate toxicity, specific DOP assimilation	<i>arsR</i> , <i>acr3</i> , <i>chrA</i> , <i>gap1</i> , <i>mfs</i> , <i>phoB/E/R</i> , <i>ptrA</i> , <i>PMM707</i> , <i>PMM721</i> , <i>unkP1-5</i>	(12–14)
$\Omega_{N,high}$	Nitrite and nitrate assimilation and uptake	<i>focA</i> , <i>moaA-E</i> , <i>moeA</i> , <i>napA</i> , <i>narB</i> , <i>nirA</i>	(17)
$\Omega_{N,medium}$	Urea and cyanate utilization	<i>cynA/S</i> , <i>tauE</i> , <i>ureA-G</i> , <i>urtA</i> , <i>unkN1-2</i>	(17, 18)



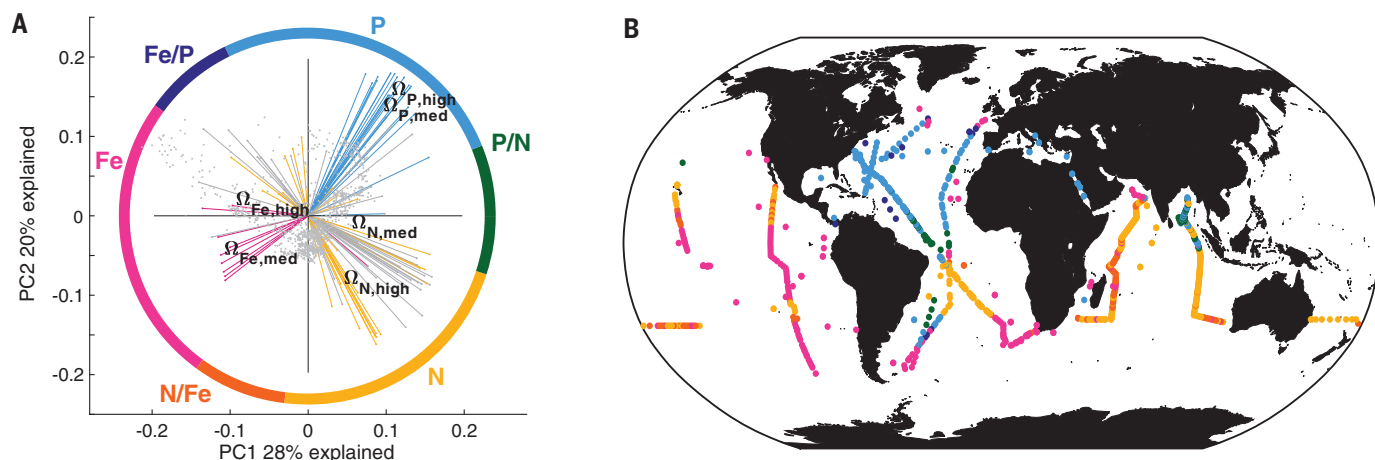


**Fig. 1. Variation in nutrient stress genes among *Prochlorococcus* populations.** (A) Principal component analysis of stress genes across all metagenome samples (gray dots,  $n = 1137$ ). Vectors for stress genes ( $z_i$ ) and composite metrics ( $\Omega_z$ ) are overlaid and colored according to nutrient type: red, Fe; blue, P; yellow, N; and gray, low stress. The outer ring represents angular separation and the boundaries at which samples are categorized by nutrient stress type (table S2). (B) Global biogeography of nutrient stress type defined by the angular separation in (A).

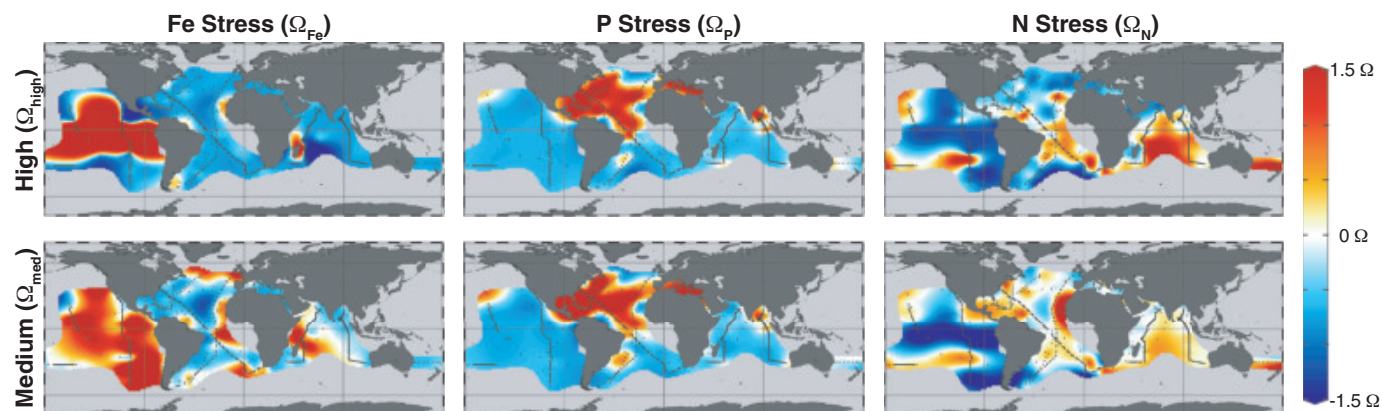


**Fig. 2. Global biogeography of *Prochlorococcus* nutrient stress type and severity.** On the basis of their biochemical role, genes were categorized by nutrient stress “type” and “severity” and combined into a composite metric ( $\Omega_z$ ) (Table 1). Background coloring is based on an interpolation between sampling points shown in dark gray.

with the low P concentrations in the southwestern Pacific Ocean (25). We lacked samples from large regions of the Pacific Ocean (including the northwest), illustrating the substantial effort required to cover the entire Pacific basin.

We previously had a limited understanding of nutrient stress in the Indian Ocean (7, 28), but two recent Global Ocean Ship-based Hydrographic Investigations Program (GO-SHIP; <https://www.go-ship.org/>) expeditions greatly improved metagenomics coverage. Most of the Indian Ocean had elevated  $\Omega_{N,high}$  and  $\Omega_{N,med}$  (figs. S11 to S13), with the highest values seen in the Southern Indian Ocean gyre. N stress genes decreased north of the equator and were lowest in the Arabian Sea upwelling region (figs. S11 and S13). We detected a region with elevated  $\Omega_{P,high}$  on the northeastern side

of the Indian Ocean associated with several fronts from the equator to the Bay of Bengal (fig. S12). There were also indications of some P stress adaptation associated with the south-flowing Leeuwin and Agulhas currents. Samples from GO-SHIP I07N (fig. S11) ( $\Omega_{Fe,high} = 0.5$ ,  $\Omega_{Fe,med} = 1$  to 2) and Tara Ocean (fig. S13) ( $\Omega_{Fe,high} = 3$ ,  $\Omega_{Fe,med} = 1$ ) both demonstrated high  $\Omega_{Fe}$  in a small upwelling region near 10°S on the western side of the basin. This zone of high  $\Omega_{Fe}$  is supported by satellite and model studies (29). There was also widespread elevated  $\Omega_{Fe,med}$  in most of South Indian Ocean gyre and in a few samples in the Arabian Sea (30). Overall, our metagenomics assessment greatly expands our understanding of nutrient stress across the Indian Ocean basin.

We speculate that the global-scale biogeography of *Prochlorococcus* multinutrient adap-

tation is stoichiometrically linked by N fixation. *Prochlorococcus* can use nutrients at a stoichiometric ratio substantially above the vertically supplied N:P (31). This leads to a default state of residual phosphate and corresponding N limitation in oligotrophic regions unless additional N is supplied by diazotrophs (32). As reflected in the relative ordination positions in Fig. 1A, cells appear to become adapted to simultaneous N-Fe co-stress if the external Fe supply and diazotroph activity are low. Moving counterclockwise in Fig. 1A, populations are mainly N stressed at an intermediate Fe supply, and then ultimately P stressed at high Fe supply and N fixation rates (33). The Atlantic meridional shift in nutrient stress emerges from these stoichiometric interactions (34). We saw signs of the same connections in the zonal shifts from elevated  $\Omega_{Fe,med}$

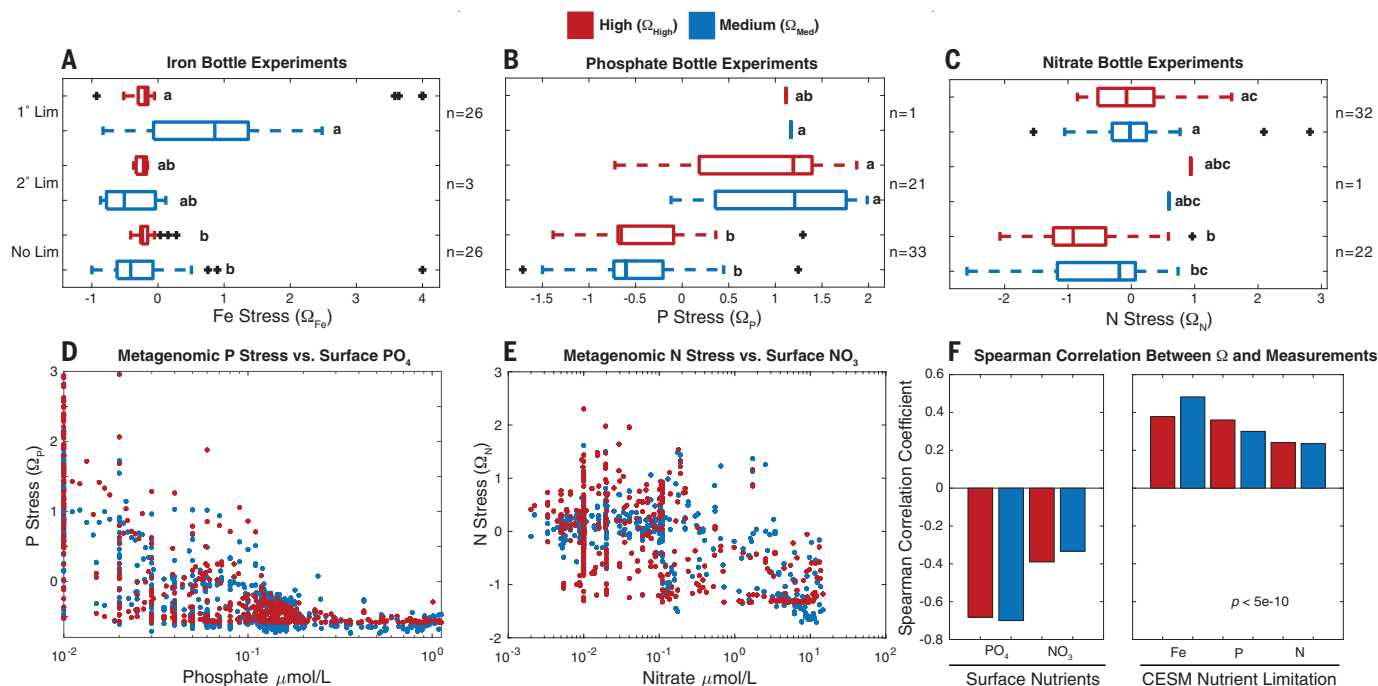


**Fig. 3. Comparison between the *Prochlorococcus* biosensor and established approaches to characterizing nutrient stress.** (A) Comparison between Fe addition experiments and genomic Fe stress ( $\Omega_{Fe}$ ) ( $n = 55$ ). (B) Comparison between P addition experiments and genomic P stress ( $\Omega_P$ ) ( $n = 55$ ).

(C) Comparison between N addition experiments and genomic N stress ( $\Omega_N$ ) ( $n = 55$ ). Small letters in (A) to (C) represent a Tukey post hoc comparison.

(D) Comparison between surface phosphate concentrations and  $\Omega_P$  ( $n = 658$ ).

(E) Comparison between surface nitrate concentrations and  $\Omega_N$  ( $n = 802$ ).

(F) Summary of Spearman correlations between established approaches and genomic stress ( $\Omega$ ). All correlations are significant ( $p < 5 \times 10^{-10}$ ). Data are colored by stress level across all figures (red, high-stress  $\Omega_{High}$ ; blue, medium-stress  $\Omega_{Med}$ ).

in the southeastern Atlantic and Pacific Oceans toward elevated  $\Omega_{P,med}$  and  $\Omega_{P,high}$  in the southwestern Atlantic and Pacific Oceans. Cellular resource demand results in adaptation to high Fe stress in the upwelling zone in the equatorial Pacific Ocean (35). As the water flows outward, cells experience and adapt to first medium Fe/N, and then high N stress and even some P stress near Station Aloha as the vertical Fe:P supply ratio increases. These meridional and zonal shifts in adaptation to nutrient stress mirror a recent synthesis of surface phosphate concentrations (25). An exception was the North Indian Ocean and Bay of Bengal, where we detected a region of high  $\Omega_P$  without a clear connection to N fixation (36). We detected samples with Fe-P co-stress in the western North Atlantic Ocean. Because Fe and P stress are commonly opposite (Fig. 1A), this co-stress may be linked to the lateral advection of low-P water from the central Atlantic Ocean (37). Despite the exceptions, our omics-based approach supports an emergent stoichiometric connection of oceanic multnutrient stress.

We saw a significant correspondence between *Prochlorococcus* stress genes and nutrient addition experiments, Earth system model predictions, and the depletion of surface nutrient concentrations (Fig. 3). There was a signif-

icant increase in the frequency of *Prochlorococcus* stress genes from no limitation, to co-limitation (2°), and then to primary (1°) limitation using bottle experiments (Fig. 3, A to C) (7). However, there was no distinction between medium and high stress and bottle experiments.

There were also significant negative correlations between  $\Omega_P$  and  $\Omega_N$  and surface phosphate or nitrate concentrations, respectively (Fig. 3, D to F). At high phosphate concentrations,  $\Omega_P$  was depressed, but a wide range in  $\Omega_P$  appeared at low phosphate concentrations (Fig. 3D). There was also a significant correlation between  $\Omega_N$  and nitrate concentrations, but again with a considerable spread (Fig. 3E). This pattern suggested a large spread in stress among *Prochlorococcus* populations at low nutrient concentration that could be driven by stoichiometric interactions with other nutrients or shifts in the supply rate of nutrients to the surface ocean. We saw a limited difference between  $\Omega_{Med}$  and  $\Omega_{High}$  and the respective nutrient concentration. Thus, the metagenomic approach can delineate stress even when nutrients are severely depleted.

There was a broad agreement between  $\Omega$  and simulated nutrient stress in an Earth system model [CESMv2\_BEC (38)] (Fig. 3F and fig. S14). The strongest overlap in Fe stress was observed in the eastern equatorial Pacific Ocean. How-

ever,  $\Omega_{Fe}$  suggested additional adaptation to Fe stress in the eastern Pacific Ocean, the southeastern Atlantic Ocean, and the south-central Indian Ocean (fig. S14), all regions where the biogeochemical model predicted N stress. This is at least partially a CESMv2\_BEC bias, because both satellite and other model data support severe Fe stress in the Indian Ocean region (29), and recent incubation experiments found some Fe stress in the southeastern Atlantic Ocean (3). CESMv2\_BEC and  $\Omega_P$  agreed on P stress in the western North Atlantic Ocean, but  $\Omega_P$  suggested adaptation to P stress in the wider subtropical North Atlantic Ocean. Both efforts detected a smaller P stress region in the southwestern Atlantic Ocean. However, CESMv2\_BEC did not show any P stress in the northern Indian Ocean. There was broad agreement between CESMv2\_BEC and  $\Omega_N$  throughout most of the Pacific and Atlantic Oceans. However,  $\Omega_N$  suggested stronger N stress adaptation in the Indian Ocean than captured in CESMv2\_BEC. With the exception of the little-studied Indian Ocean, there was broad agreement in the regional patterns of nutrient stress between an Earth system model and our omics-based metric.

There are several important caveats to consider. First, genomic variations can reflect both the demand for nutrients as well as the

availability of different nutrient species. Cyanobacteria up-regulate the acquisition of oxidized N sources at a low ammonia supply and have no dedicated sensory proteins for the concentration of urea or nitrate (39). In addition, the genome organization of N acquisition supports sequential acquisition of ammonia, urea, nitrite, and nitrate genes (fig. S15) (40). For example, as illustrated by our eastern Pacific Ocean transect, there was strong upwelling and divergent flow of nitrate centered on 5°S (fig. S16). At the upwelling core with high nitrate, *Prochlorococcus* solely contained genes for ammonia uptake and thus likely relies on recycled ammonia, followed by urea at the gyre transition (~15°S), and then nitrate assimilation within the gyre (~30°S). Moreover, there was an inverse relationship between surface nitrate concentrations and nitrate reductase in *Prochlorococcus*. Thus, the genome regulation, genome organization, and biogeography of *Prochlorococcus* nutrient acquisition genes suggest a first-order relationship with cellular resource demands and environmental gradients in nutrient availability, and thus an experienced stressful supply. However, it appears unlikely that cells would retain these genes without access to the associated resources being supplied by community recycling (e.g., through nitrification). Second, we categorized a priori each gene into three levels of stress severity based on their biochemical role, phylogenomics, and regulation to avoid “circularity” in our quantification of nutrient stress. However, the biogeographic patterns suggest that nitrite assimilation occurs in regions with deep mixing and likely lower N stress, whereas cyanate utilization genes covary closely with high N stress. Furthermore, medium- and high-phosphate-stress genes generally co-occur, suggesting a limited resolution of regional P stress. Thus, some genes could be reclassified or added to the classification system (e.g., assimilation of organic N sources) (41) in future analyses to refine the approach. A third caveat is that our study is based on the assessment of nutrient stress adaptation in a single organism. *Prochlorococcus* is the smallest and most abundant phytoplankton in most nutrient-limited marine ecosystems between 40°N and 40°S (11). However, *Prochlorococcus* is not abundant or even present in many coastal or high-latitude environments, restricting the geographical reach of the technique. Furthermore, coexisting taxa could show divergent nutrient stress profiles because of physiological differences (21, 31, 42). However, *Prochlorococcus* generally has the highest nutrient uptake affinity and is least likely to experience cellular nutrient stress (43). We also found a significant correspondence between our stress metric and three established approaches, implying that we captured the general community physiological state in the regions analyzed. A fourth

caveat is the use of genomic changes to assess the underlying physiological state: A genome-based approach will work in populations with rapid adaptation to local conditions, but transcriptomic or proteomic approaches may work better in ecosystems with longer generation times. However, these approaches are more labor intensive and affected by strong diurnal expression changes. Thus, omics-based assessments of nutrient stress should be carefully calibrated to the biological behavior of the targeted ecosystem.

Connecting omics-based microbiome studies and biogeochemically important processes is a widespread convergence challenge, and links have been elusive and mainly correlation based (44). Our stress metric builds upon 30 years of studies of *Prochlorococcus* physiology and adaptation to different nutrient regimes and allows for a mechanistic description of resource utilization. It is also a semiquantitative, cost-effective, and standardized way of assessing nutrient stress and does not require labor-intensive incubation experiments. Finally, our method can provide a sensitive description of phytoplankton stress and identify nutrient stress severity for multiple elements simultaneously (9). Thus, our findings demonstrate how we can harness omics-based information to develop a nuanced and high-resolution understanding of global biogeochemistry.

## REFERENCES AND NOTES

1. T. Tyrrell, *Nature* **400**, 525–531 (1999).
2. L. Bopp et al., *Biogeosciences* **10**, 6225–6245 (2013).
3. T. J. Browning et al., *Nature* **551**, 242–246 (2017).
4. J. H. Martin, S. E. Fitzwater, R. Michael Gordon, C. N. Hunter, S. J. Tanner, *Deep. Res. Part II* **40**, 115–134 (1993).
5. M. Davey et al., *Limnol. Oceanogr.* **53**, 1722–1733 (2008).
6. J. W. Ammerman, R. R. Hood, D. A. Case, J. B. Cotner, *Eos* **84**, 165–170 (2003).
7. C. M. Moore et al., *Nat. Geosci.* **6**, 701–710 (2013).
8. T. J. Browning et al., *Nat. Commun.* **8**, 15465 (2017).
9. E. A. Davidson, R. W. Howarth, *Nature* **449**, 1000–1001 (2007).
10. A. Krishnamurthy, J. K. Moore, N. Mahowald, C. Luo, C. S. Zender, *J. Geophys. Res.* **115**, G01006 (2010).
11. F. Partensky, L. Garczarek, *Ann. Rev. Mar. Sci.* **2**, 305–331 (2010).
12. A. C. Martiny, M. L. Coleman, S. W. Chisholm, *Proc. Natl. Acad. Sci. U.S.A.* **103**, 12552–12557 (2006).
13. D. J. Scanlan, N. J. West, *FEMS Microbiol. Ecol.* **40**, 1–12 (2002).
14. J. K. Saunders, G. Rocap, *ISME J.* **10**, 197–209 (2016).
15. S. Kathuria, A. C. Martiny, *Environ. Microbiol.* **13**, 74–83 (2011).
16. L. R. Moore, M. Ostrowski, D. J. Scanlan, K. Feren, T. Sweetsir, *Aquat. Microb. Ecol.* **39**, 257–269 (2005).
17. A. Herrero, A. M. Muro-Pastor, E. Flores, *J. Bacteriol.* **183**, 411–425 (2001).
18. A. C. Tolonen et al., *Mol. Syst. Biol.* **2**, 53 (2006).
19. R. R. Malmstrom et al., *ISME J.* **7**, 184–198 (2013).
20. D. B. Rusch, A. C. Martiny, C. L. Dupont, A. L. Halpern, J. C. Venter, *Proc. Natl. Acad. Sci. U.S.A.* **107**, 16184–16189 (2010).
21. C. A. Garcia et al., *Philos. Trans. R. Soc. Lond. B Biol. Sci.* **375**, 20190254 (2020).
22. A. A. Larkin et al., bioRxiv 285056 [Preprint]. 8 September 2020. <https://doi.org/10.1101/2020.09.06.285056>
23. M. C. Nielsdóttir, C. M. Moore, R. Sanders, D. J. Hinz, E. P. Achterberg, *Global Biogeochem. Cycles* **23**, GB3001 (2009).

24. R. L. Mather et al., *Nat. Geosci.* **1**, 439–443 (2008).
25. A. C. Martiny et al., *Sci. Adv.* **5**, eaax0341 (2019).
26. S. Bonnet et al., *Biogeosciences* **5**, 215–225 (2008).
27. M. J. Behrenfeld, Z. S. Kolber, *Science* **283**, 840–843 (1999).
28. B. S. Twining et al., *Deep. Res. Part II Top. Stud. Oceanogr.* **166**, 125–140 (2019).
29. M. J. Behrenfeld et al., *Biogeosciences* **6**, 779–794 (2009).
30. S. W. A. Naqvi et al., *Biogeosciences* **7**, 2091–2100 (2010).
31. A. R. Moreno, A. C. Martiny, *Ann. Rev. Mar. Sci.* **10**, 43–69 (2018).
32. M. M. Mills, K. R. Arrigo, *Nat. Geosci.* **3**, 412–416 (2010).
33. J. Wu, W. Sunda, E. A. Boyle, D. M. Karl, *Science* **289**, 759–762 (2000).
34. B. A. Ward, S. Dutkiewicz, C. M. Moore, M. J. Follows, *Limnol. Oceanogr.* **58**, 2059–2075 (2013).
35. M. A. Saito et al., *Science* **345**, 1173–1177 (2014).
36. C. R. Löscher, W. Mohr, H. W. Bange, D. E. Canfield, *Biogeosciences* **17**, 851–864 (2020).
37. M. W. Lomas et al., *Biogeosciences* **7**, 695–710 (2010).
38. J. K. Moore, S. C. Doney, K. Lindsay, *Global Biogeochem. Cycles* **18**, GB4028 (2004).
39. G. Rocap et al., *Nature* **424**, 1042–1047 (2003).
40. A. C. Martiny, S. Kathuria, P. M. Berube, *Proc. Natl. Acad. Sci. U.S.A.* **106**, 10787–10792 (2009).
41. M. V. Zubkov, B. M. Fuchs, G. A. Tarran, P. H. Burkil, R. Amann, *Appl. Environ. Microbiol.* **69**, 1299–1304 (2003).
42. H. Alexander, B. D. Jenkins, T. A. Ryneerson, S. T. Dyhrman, *Proc. Natl. Acad. Sci. U.S.A.* **112**, E2182–E2190 (2015).
43. M. W. Lomas, J. A. Bonachela, S. A. Levin, A. C. Martiny, *Proc. Natl. Acad. Sci. U.S.A.* **111**, 17540–17545 (2014).
44. J. D. Rocca et al., *ISME J.* **9**, 1693–1699 (2015).

## ACKNOWLEDGMENTS

We thank the chief scientists L. Barbaro, B. Carter, M. Lomas, R. Sonnerup, G. Tarran, and D. Volkov and the coordinators of GO-SHIP (L. Tally and G. Johnson) and the Atlantic Meridional Transect (AMT; A. Rees) for supporting the collection of metagenomic data. **Funding:** This work was supported by the National Science Foundation (OCE-1046297, 1559002, 1848576, and 1948842 to A.C.M. and 1658392 to J.K.M.), a National Aeronautics and Space Administration Earth and Space Science Fellowship (NESSF16R to C.A.G.), the National Institutes of Health (T32AI141346 to L.J.U.), and the DOE BER Earth System Modeling Program (DE-SC0016539 to J.K.M.). A.M.T. is funded by the UK Natural Environment Research Council through its National Capability Long-term Single Centre Science Programme, Climate Linked Atlantic Sector Science (NE/R015953/1). This study contributes to the international Integrated Marine Biosphere Research (IMBeR) project (AMT contribution #358). **Author contributions:** L.J.U., A.A.L., and A.C.M. designed the study and wrote the manuscript with input from all authors. A.A.L., C.A.G., N.S.G., and J.A.L. collected samples. A.A.L., C.A.G., M.L.B., and J.A.L. sequenced metagenomes. L.J.U. analyzed the data. N.A.W. and J.K.M. produced CESM BEC model outputs. A.C.M. supervised the study. **Competing interests:** The authors declare no competing interests. **Data and materials availability:** All data are available in the main text or the supplementary materials. Raw metagenomic reads are available through the National Center for Biotechnology Information Sequence Read Archive (BioProject ID PRJNA656268). Metadata are available through <http://cchdo.ucsd.edu> and BCO-DMO (project 2178). A complete description of all Bio-GO-SHIP metagenomes and associated metadata are available (22).

## SUPPLEMENTARY MATERIALS

[science.sciencemag.org/content/372/6539/287/suppl/DC1](https://science.sciencemag.org/content/372/6539/287/suppl/DC1)  
Materials and Methods  
Figs. S1 to S16  
Tables S1 to S3  
References (45–61)  
Databases S1 and S2  
MDAR Reproducibility Checklist

10 September 2020; accepted 1 March 2021  
10.1126/science.abe6301



## SIGNAL TRANSDUCTION

## Decoupling transcription factor expression and activity enables dimmer switch gene regulation

C. Ricci-Tam<sup>1†</sup>, I. Ben-Zion<sup>1†</sup>, J. Wang<sup>2†</sup>, J. Palme<sup>1</sup>, A. Li<sup>1</sup>, Y. Savir<sup>3</sup>, M. Springer<sup>1\*</sup>

Gene-regulatory networks achieve complex mappings of inputs to outputs through mechanisms that are poorly understood. We found that in the galactose-responsive pathway in *Saccharomyces cerevisiae*, the decision to activate the transcription of genes encoding pathway components is controlled independently from the expression level, resulting in behavior resembling that of a mechanical dimmer switch. This was not a direct result of chromatin regulation or combinatorial control at galactose-responsive promoters; rather, this behavior was achieved by hierarchical regulation of the expression and activity of a single transcription factor. Hierarchical regulation is ubiquitous, and thus dimmer switch regulation is likely a key feature of many biological systems. Dimmer switch gene regulation may allow cells to fine-tune their responses to multi-input environments on both physiological and evolutionary time scales.

To respond appropriately to varying circumstances, cells use transcriptional programs to integrate multiple inputs from their environment and determine the appropriate output. The yeast galactose-responsive (GAL) pathway, which controls the decision to metabolize galactose in the presence of other sugars, is a model system for multi-input responses (1, 2). We found that the output of this pathway has two independently controlled features: (i) the fraction of cells that express genes in the pathway and (ii) their level of expression. We set out to determine the molecular mechanism underlying this behavior.

The decision to express GAL genes is triggered by galactose but inhibited by glucose, a sugar that is easier to metabolize. The two features of this response are a switch-like decision to activate the pathway and a rheostat-like (i.e., graded) control of the expression level (Fig. 1 and fig. S1). We measured the steady-state GAL response in 77 different combinations of glucose and galactose using a yellow fluorescent protein (YFP) fused to the promoter of GalIp, the first enzyme in the GAL pathway (Fig. 1A, figs. S1 and S3, and materials and methods) (3). The fraction of cells that activate the pathway (ON fraction, defined by comparing the YFP signal with an uninduced reference sample) was a one-dimensional switch-like function of the ratio of the galactose:glucose concentrations in the medium (1) (Fig. 1, B and J, and fig. S1, C and E). However, we found that when most of the cells were activated, the mean expression level of cells in the ON subpopulation (ON expression level) depended solely on the glucose concentration (Fig. 1, C and K;

fig. S1, D and F; and materials and methods). This behavior is analogous to that of a mechanical dimmer switch often used for home lights. The galactose:glucose ratio, like the on-off light switch, determines whether cells turn on the pathway. The glucose concentration, like a dimmer knob or rheostat, controls the expression level of ON cells. Inside a narrow region near where the ON fraction is transitioning from mostly off to mostly on, the ON expression level is well described by the product of the glucose dependence of ON expression level and the ratiometric dependence of the ON fraction (supplementary text and fig. S2, F to K).

We found that the switch and rheostat were controlled by separate genetic elements (Fig. 1 and fig. S2). We measured the steady-state GAL response of mutant yeast strains lacking key GAL pathway regulators (*gal80Δ*, *mig1Δ*, and *mig1Δgal80Δ*) in the same 77 combinations of glucose and galactose (fig. S2, A to E, and fig. S3). The *gal80Δ* ON fraction was always 100% independently of the concentrations of glucose and galactose (Fig. 1, D and J), whereas the *gal80Δ* rheostat was normal; the ON expression level responded to glucose concentration similarly to wild-type cells (Fig. 1, C, E, and K). By contrast, the *mig1Δ* strain had a normal switch, where the ON fraction responded to the galactose:glucose ratio similarly to wild-type cells (Fig. 1, F and J, and supplementary text), but its rheostat was always at its maximum outside the switch threshold region regardless of glucose concentration (Fig. 1, G and K, and fig. S2J). Thus, Gal80p is necessary for the switch and Mig1p is necessary for the rheostat. Consistent with this, the *mig1Δgal80Δ* strain was constitutively ON at its maximal level (Fig. 1, H to K) regardless of glucose or galactose concentration.

The first mechanism that we considered for the switch-and-rheostat response was a “chromatin-decoupled regulation” model in-

spired by pioneer factors (4) and observations in the yeast phosphate pathway (5). This model proposes that the switch is controlled by Gal4p-mediated chromatin remodeling and the rheostat by Mig1p-mediated transcriptional regulation (6) in fully accessible *GAL1* promoters (fig. S4A). To test this idea, we measured chromatin accessibility and gene expression in many glucose and galactose combinations with a modified version of the assay for transposase-accessible chromatin sequencing (ATAC-seq) (7, 8) (figs. S4 and S8 and materials and methods). Consistent with the model, the chromatin accessibility of the OFF subpopulation was almost identical to that of maximally repressed wild-type cells (Fig. 2A and fig. S4, D to F). However, whereas the model predicts that all ON cells have fully accessible chromatin, we found a graded range of chromatin accessibility at the *GAL1* promoter that correlated with GAL reporter expression (Fig. 2A and fig. S4, H to K).

The chromatin-decoupled regulation model also failed to explain the behavior of the rheostat-only *gal80Δ* strain, which showed a range of glucose-dependent chromatin accessibility (Fig. 2A, bottom right) despite always having an ON fraction close to 1. Furthermore, the switch-only *mig1Δ* strain's chromatin was either fully open or fully closed (Fig. 2A, top right), indicating that not only the switch but also the rheostat modulates chromatin accessibility. We created a doxycycline-titratable Mig1p strain to test this hypothesis (*mig1Δgal80Δ* TetO7pr-MIG1 *GAL1pr*-YFP; SLYM03 in table S1, also see the materials and methods). Increasing Mig1p expression by increasing doxycycline lowered both the expression of *GAL1pr*-YFP (fig. S4L) and the chromatin accessibility in a sugar-independent manner. The relationship between chromatin accessibility and transcription was the same as that of a wild-type strain (Fig. 2A). These data show that chromatin accessibility is not the primary mediator of decoupling between the switch and the rheostat (fig. S4A).

Our observation of a Mig1p-dependent correlation between chromatin accessibility and expression level conflicts with a report that nucleosome and Mig1p binding are mutually exclusive at the *GAL1pr* (6). To resolve this, we deleted the Mig1p-binding sites in the *GAL1pr*-YFP reporter (fig. S5A) and measured the response to varying combinations of glucose and galactose concentrations. Unexpectedly, the phenotype of the *GAL1pr<sup>mig1bsΔ</sup>* reporter strain was nearly identical to that of the wild type (Fig. 2, B and C, and fig. S5C) despite the fact that the Mig1p-binding sites were highly conserved and presumed to be functionally important (9). This indicated that the direct effect of Mig1p at *GAL1pr* has a relatively minor contribution to the steady-state *GAL1* expression level. Therefore, the Mig1p rheostat must regulate *GAL1* upstream of the *GAL1* promoter.

<sup>1</sup>Department of Systems Biology, Harvard Medical School, Boston, MA, USA. <sup>2</sup>Department of Chemical Engineering, University of Washington, Seattle, WA, USA. <sup>3</sup>Department of Physiology, Biophysics, and Systems Biology, Technion, Haifa, Israel.

\*Corresponding author. Email: Michael\_Springer@hms.harvard.edu

†These authors contributed equally to this work.

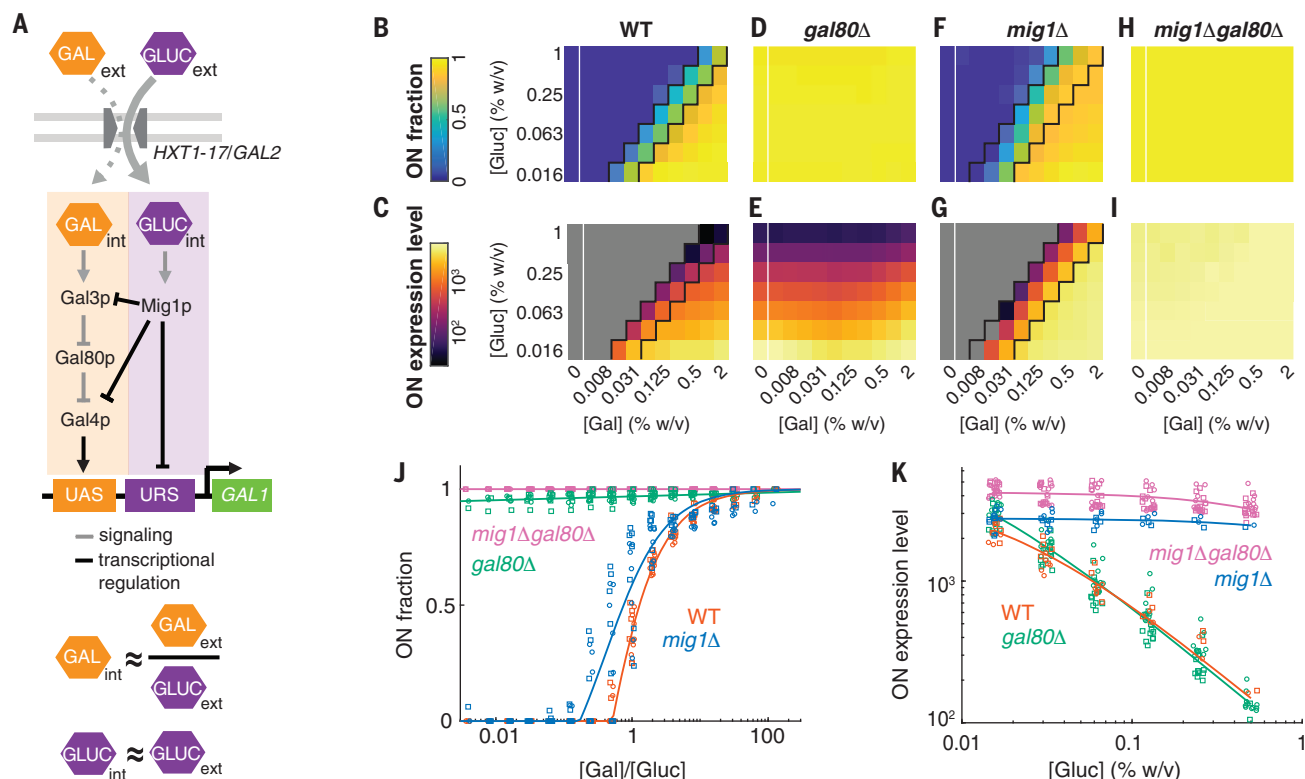


**Fig. 1. Switch-like activation and rheostat-like control of expression level are genetically decoupled in the yeast GAL pathway.** (A) Schematic of the yeast GAL pathway, including the hypothesized competitive transport mechanism (1) by which the internal galactose level is a function of the ratio of external concentrations of the sugars, leading the GAL branch of the pathway (orange) to be responsive to the galactose:glucose ratio. (B to I) ON fraction and ON expression level heatmaps of the wild-type, *mig1Δ*, *gal80Δ*, and *mig1Δgal80Δ* strains in a glucose-galactose double gradient (two biological replicates are shown for each strain and glucose-galactose combination). Black lines delimit the

region of ON fraction threshold (range of galactose:glucose ratios where  $0.2 < \text{ON fraction} < 0.8$ ). (J) Plot of the ON fraction versus galactose:glucose ratio for the wild-type, *mig1Δ*, *gal80Δ*, and *mig1Δgal80Δ* strains for experiments in (B) to (I). Scatterplot X-values are randomly jittered for visualization purposes. Deletion of *GAL80* eliminates the switch. (K) Plot of ON expression level in the ON region (ON fraction  $> 0.8$ ) versus the glucose concentration for the wild-type, *mig1Δ*, *gal80Δ*, and *mig1Δgal80Δ* strains for experiments in (B) to (I). Scatterplot X-values are randomly jittered for visualization purposes. Deletion of *MIG1* eliminates the rheostat. See fit parameters in table S4.

In addition to regulating *GAL1* expression, Mig1p also inhibits *GAL4* expression (10, 11) (Fig. 1A), and changing Gal4p concentrations can affect the GAL response (12, 13). We therefore investigated whether modulation of *GAL4* expression might be involved in the rheostat. Deleting the Mig1p-binding site in the *GAL4* promoter (fig. S5B) was sufficient to phenocopy the *mig1Δ* strain (Fig. 2, B and C, and fig. S5D), suggesting that glucose control of Gal4p levels is achieved solely through the regulation of Gal4p abundance. Supporting this hypothesis, YFP reporters for other Gal4p-regulated promoters, including two synthetic promoters, responded to glucose in the same way as *GAL1*, even if the promoter did not contain a Mig1p-binding site (fig. S5, H to M). As further support for this hypothesis, when we introduced a transcriptional reporter for *GAL4* expression (*GAL4pr-mScarlet-I*) into the wild-type and mutant backgrounds, we found similar glucose-dependent titration of *GAL4* expression level in the wild-type and *gal80Δ* backgrounds, which is in contrast to the elevated and less variable

*GAL4* expression for the *GAL4pr<sup>mig1bsΔ</sup>* and *mig1Δ* backgrounds. (Fig. 2D and fig. S6, A and B). To directly test whether Gal4p abundance regulates *GAL1* expression and thus mediates the Mig1p rheostat, we built a strain with a doxycycline-titratable mScarlet-I-Gal4p fusion (14) (*gal4Δ TetO7pr-mScarlet-I-GAL4 GAL1pr-YFP*; SLYM08 in table S1; also see the materials and methods) (fig. S6, C and D). By measuring fluorescence from both mScarlet-I-Gal4p and *GAL1pr-YFP*, we observed a direct correlation between the fluorescence of red fluorescent protein (RFP) and YFP in the ON subpopulation (Fig. 2E and fig. S6, E to H), confirming that the GAL pathway responds to Gal4p abundance (see also fig. S5, N and O).

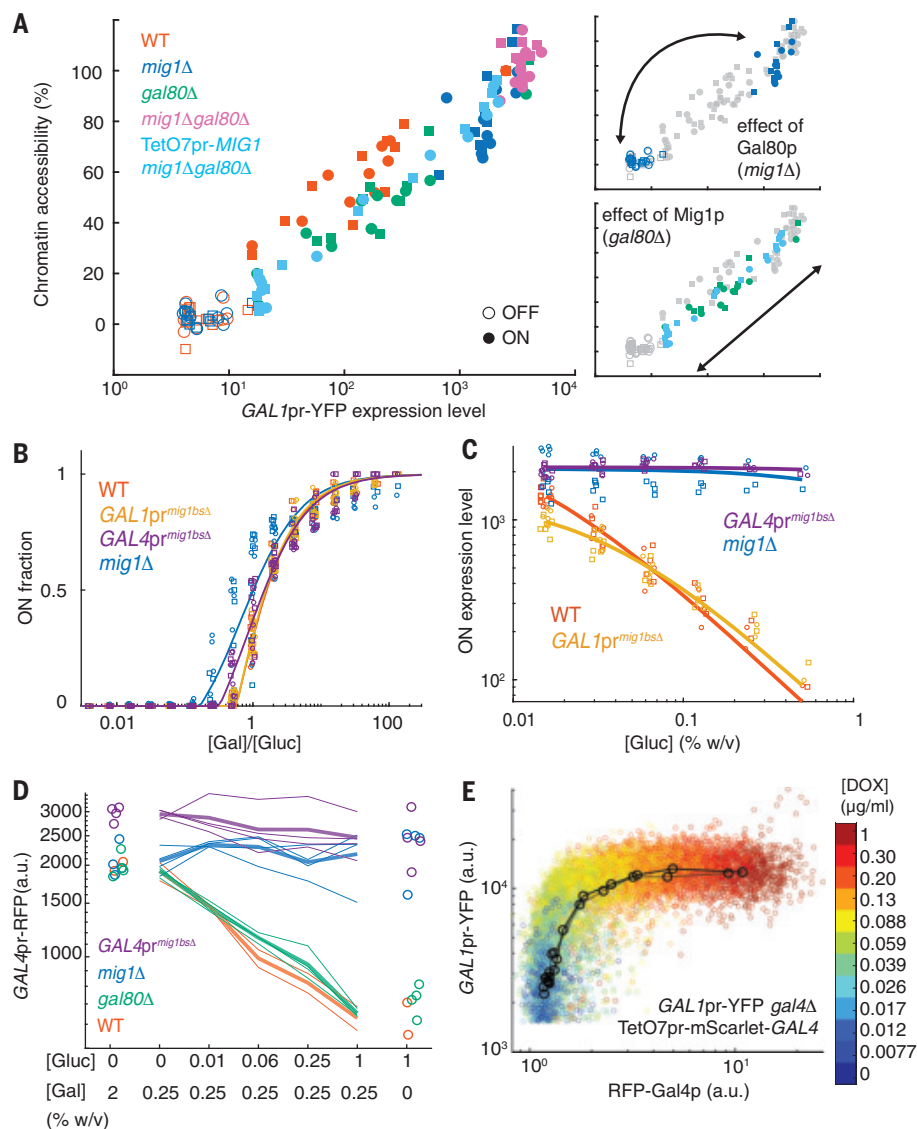
Our results support a “hierarchically decoupled regulation” model in which the abundance and activity of a single transcription factor, Gal4p, are regulated independently (Fig. 3). In this model, transcriptional regulation of Gal4p abundance by the upstream transcription factor Mig1p mediates the response to glucose, whereas protein binding of

Gal80p to Gal4p (15, 16) regulates Gal4p activity in response to the galactose:glucose ratio. Unlike our initial chromatin-decoupled regulation model (fig. S4A), a single transcription factor, Gal4p, controlled both the switch and the rheostat at the final step of the pathway. In both models, decoupling was achieved by regulation working through two distinct mechanisms; this is reminiscent of other cases, such as the frequency versus amplitude modulation of the Msn2p-Msn4p stress responses in yeast (17). Our model is agnostic to mechanistic details of how Gal4p activates downstream GAL promoters and is thus compatible with recent observations that different Gal4p-binding sites have different functional roles (18).

What physiological function could be served by decoupling the on-off switch of pathway activation from the expression level of the pathway? When faced with mixtures of sugars, yeast first use glucose, then less-preferred carbon sources (19), a phenomenon called diauxic growth (20). Yeast prepare by expressing GAL genes before glucose is depleted; the earlier a

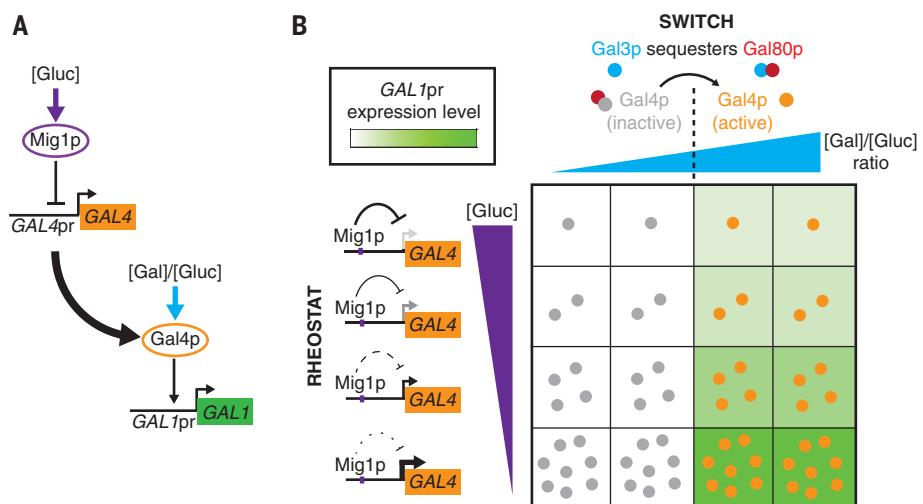
**Fig. 2. Decoupling occurs through regulation of the Gal4p transcription factor rather than directly at the *GAL1* promoter through chromatin.**

(A) Scatterplot of YFP expression level (x-axis) versus the percentage chromatin accessibility (y-axis) at the *GAL1* promoter across all samples from wild-type, *mig1Δ*, *gal80Δ*, *mig1Δgal80Δ*, and TetO7pr-MIG1 *mig1Δgal80Δ* strain backgrounds. Data plotted include two biological replicates (circles indicate replicate 1, squares indicate replicate 2) for each strain and glucose-galactose and doxycycline condition. (B and C) ON fraction as a function of the galactose:glucose ratio (B) and ON expression level as a function of glucose concentration (C) in a glucose-galactose double gradient assay (two biological replicates) across the wild-type, *mig1Δ*, *GAL1pr<sup>mig1bsΔ</sup>*, and *GAL4pr<sup>mig1bsΔ</sup>* strains. Scatterplot X-values are randomly jittered for visualization purposes. See pairwise comparisons from (B) in fig. S5, E to G. (D) Plot of *GAL4pr*-mScarlet expression versus sugar concentration in a glucose titration series across the wild-type, *mig1Δ*, *gal80Δ*, and *GAL4pr<sup>mig1bsΔ</sup>* strains. Thin lines represent individual biological replicate data (two replicates for wild-type and four replicates for all other strains), and thick lines represent the average across replicate measurements. Scatterplot X-values are randomly jittered for visualization purposes. (E) RFP versus YFP fluorescence in a *gal4Δ* TetO7pr-mScarlet-GAL4 *GAL1pr*-YFP strain from microscopy of a doxycycline (DOX) titration series (see fig. S6D for a flow cytometry YFP versus DOX plot). Scatter represents single-cell measurements, with colors corresponding to discrete DOX concentrations; black circles are the average YFP and RFP values at each given DOX concentration (two biological replicates).



**Fig. 3. Mechanistic model: switch-and-rheostat works through decoupled regulation of Gal4p activity and abundance.**

(A) Switch-and-rheostat regulation in the GAL pathway is achieved through a hierarchical design. In response to glucose, the rheostat works through Mig1p transcriptional regulation of *GAL4*, where the activity of Gal4p is then regulated in response to the galactose:glucose ratio. (B) Molecular mechanism of the independent control of Gal4p abundance and activity. Internal galactose concentrations (which depend on the external ratio of glucose:galactose) controls the activity of Gal3p (x-axis). Gal80p sequesters Gal4p; active Gal3p sequesters Gal80p. Thus, when the active Gal3p concentration exceeds the total Gal80p concentration, Gal4p will convert sharply in the galactose:glucose ratio space from inactive (gray circles) to active (orange circles). However, the total amount of active Gal4p controls the amount of transcriptional output from the *GAL1* promoter (green shading). Glucose controls Mig1p activity, thereby setting the total level of Gal4p (y-axis). Thus, glucose controls the level of Gal1p by controlling the total level of Gal4p and thereby the amount of active Gal4p.





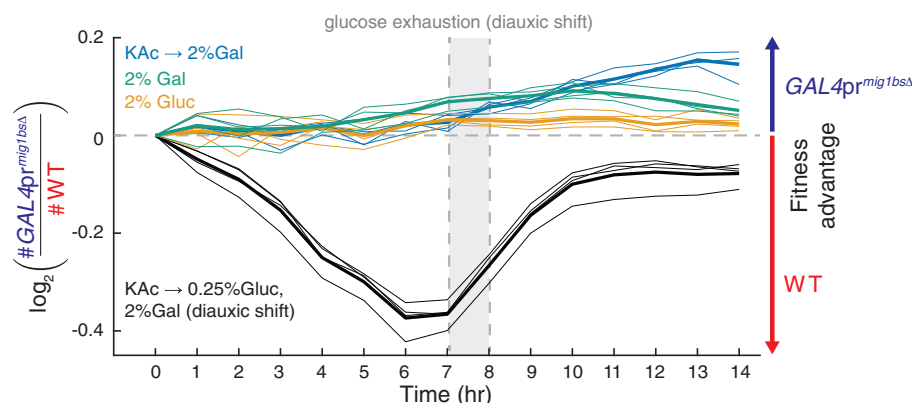


**Fig. 4. Physiological benefit of switch-and-rheostat design.** Log<sub>2</sub> ratio of *GAL4pr<sup>mig1bsΔ</sup>* cell counts over wild-type cell counts versus time during diauxic growth (black, four biological replicate cocultures), an “instantaneous” shift to pure galactose (blue, four biological replicate cocultures), steady-state growth on 2% glucose (yellow, four biological replicate cocultures), or steady-state

growth on 2% galactose (green, four biological replicate cocultures). Thick lines are the average of the four measurements (thin lines). A positive value on the y-axis indicates that *GAL4pr<sup>mig1bsΔ</sup>* has a net fitness advantage since the initial time point, and a negative value indicates that the wild type has a net fitness advantage since the initial time point.

strain expresses GAL genes, the higher the fitness advantage it has once glucose is depleted. However, preparation comes at a fitness cost in the period before the glucose runs out (21). One possible function of the decoupled switch-and-rheostat design is to allow early activation of the pathway but with a reduced cost.

To test this, we set up a competition between a wild-type strain and a rheostat-lacking *GAL4pr<sup>mig1bsΔ</sup>* strain during diauxic growth conditions (fig. S7A). *GAL4pr*-YFP expression quickly reached its maximum in the *GAL4pr<sup>mig1bsΔ</sup>* strain but was delayed in a wild-type strain until glucose was depleted (fig. S7, B and D). During this time ( $t = 0$  to 7 hours), the wild-type strain had a fitness advantage over the *GAL4pr<sup>mig1bsΔ</sup>* strain (Fig. 4 and materials and methods), presumably due to the saving of resources required to maximally activate the GAL pathway (21, 22). After glucose was exhausted (fig. S7B), expression of GAL genes increased in the wild-type strain (fig. S7D). During this period ( $t = 7$  to 10 hours), the *GAL4pr<sup>mig1bsΔ</sup>* strain had a competitive advantage (Fig. 4) that lasted until the wild-type strain also reached maximal expression of GAL genes (21). However, this temporary benefit for the *GAL4pr<sup>mig1bsΔ</sup>* strain was insufficient to offset the initial cost of over-expressing GAL genes (Fig. 4). The observed fitness differences were not due to differences in growth on glucose or galactose alone (Fig. 4 and fig. S7, F and G). In addition, the fitness advantage of the wild-type strain was absent when both strains were switched directly to galactose (Fig. 4 and fig. S7E). We conclude that the Mig1p rheostat reduces the fitness cost of preactivating GAL genes during the gradual depletion of glucose.

Decoupled control is a useful property because it allows response features to be in-

dependently controlled physiologically and evolutionarily (23–25). Decoupling has often been proposed to involve independent transcription factor-binding sites on promoters and to be aided by chromatin (5). We show here that the same result can be accomplished by hierarchical regulation of the abundance and activity of a transcription factor. Because regulation of this kind is common, it is likely that decoupling of responses is also achieved by this mechanism in other systems (26, 27).

#### REFERENCES AND NOTES

- R. Escalante-Chong *et al.*, *Proc. Natl. Acad. Sci. U.S.A.* **112**, 1636–1641 (2015).
- O. S. Venturelli, H. El-Samad, R. M. Murray, *Proc. Natl. Acad. Sci. U.S.A.* **109**, E3324–E3333 (2012).
- P. J. Bhat, *Galactose Regulon of Yeast: From Genetics to Systems Biology* (Springer, 2008).
- K. S. Zaret, J. S. Carroll, *Genes Dev.* **25**, 2227–2241 (2011).
- F. H. Lam, D. J. Steger, E. K. O’Shea, *Nature* **453**, 246–250 (2008).
- E. Frolova, M. Johnston, J. Majors, *Nucleic Acids Res.* **27**, 1350–1358 (1999).
- J. D. Buenostro, B. Wu, H. Y. Chang, W. J. Greenleaf, *Curr. Protoc. Mol. Biol.*, (2021).
- A. N. Schep *et al.*, *Genome Res.* **25**, 1757–1770 (2015).
- M. Kellis, N. Patterson, M. Endrizzi, B. Birren, E. S. Lander, *Nature* **423**, 241–254 (2003).
- M. Johnston, J. S. Flick, T. Pexton, *Mol. Cell. Biol.* **14**, 3834–3841 (1994).
- P. A. Silver, L. P. Keegan, M. Ptashine, *Proc. Natl. Acad. Sci. U.S.A.* **81**, 5951–5955 (1984).
- D. W. Griggs, M. Johnston, *Proc. Natl. Acad. Sci. U.S.A.* **88**, 8597–8601 (1991).
- M. Acar, B. F. Pando, F. H. Arnold, M. B. Elowitz, A. van Oudenaarden, *Science* **329**, 1656–1660 (2010).
- D. S. Bindels *et al.*, *Nat. Methods* **14**, 53–56 (2017).
- O. Egrizov *et al.*, *Mol. Cell. Biol.* **33**, 3667–3674 (2013).
- F. Jiang, B. R. Frey, M. L. Evans, J. C. Friel, J. E. Hopper, *Mol. Cell. Biol.* **29**, 5604–5610 (2009).
- Z. AkhavanAghdam, J. Sinha, O. P. Tabbaa, N. Hao, *eLife* **5**, 684 (2016).
- G. L. Elison, Y. Xue, R. Song, M. Acar, *Cell Rep.* **25**, 737–748.e4 (2018).
- J. M. Gancedo, *Microbiol. Mol. Biol. Rev.* **62**, 334–361 (1998).

- L. Galdieri, S. Mehrotra, S. Yu, A. Vancura, *OMICS* **14**, 629–638 (2010).
- J. Wang *et al.*, *PLOS Biol.* **13**, e1002041 (2015).
- G. I. Lang, A. W. Murray, D. Botstein, *Proc. Natl. Acad. Sci. U.S.A.* **106**, 5755–5760 (2009).
- H. Mengistu, J. Huizinga, J.-B. Mouret, J. Clune, *PLOS Comput. Biol.* **12**, e1004829 (2016).
- H. Yu, M. Gerstein, *Proc. Natl. Acad. Sci. U.S.A.* **103**, 14724–14731 (2006).
- D. M. Lorenz, A. Jeng, M. W. Deem, *Phys. Life Rev.* **8**, 129–160 (2011).
- S. S. Shen-Orr, R. Milo, S. Mangan, U. Alon, *Nat. Genet.* **31**, 64–68 (2002).
- R. Milo *et al.*, *Science* **298**, 824–827 (2002).
- Data for: C. Ricci-Tam *et al.*, Decoupling transcription factor expression and activity enables dimmer-switch gene regulation. Dryad (2021); <https://doi.org/10.5061/dryad.70xwdbt3>.

#### ACKNOWLEDGMENTS

We thank R. Ward, D. Davidi, R. Milo, and A. Klein for critical feedback on the manuscript; P. Nanda for help with image analysis; S. Boswell, S. Schink, H.-Y. Jhuang, N. Johnson, and members of the Springer laboratory for helpful discussions; the HMS Systems Biology FACS Facility for technical support; and S. Javadi and Stratigim for flow cytometry assistance. **Funding:** This work was supported by an NIH grant (R01-GM120122-03 to M.S.), a National Science Foundation Graduate Research Fellowship (DGE1144152 to C.R.-T.), and a National Science Foundation grant (1349248 to M.S.). **Author contributions:** C.R.-T., I.B.-Z., J.W., J.P., A.L., Y.S., and M.S. designed the experiments. C.R.-T., I.B.-Z., J.W., J.P., and A.L. performed the experiments and analyzed the results. C.R.-T., I.B.-Z., J.W., and M.S. wrote the manuscript. All authors read and approved the final manuscript. **Competing interests:** The authors declare no competing interests. **Data and materials availability:** All datasets generated and analyzed for this study are available for download from Dryad (28). All custom code used is also available for download from Dryad (28) and GitHub (<https://github.com/springerlab/Flow-Cytometry-Toolkit>).

#### SUPPLEMENTARY MATERIALS

[science.sciencemag.org/content/372/6539/292/suppl/DC1](https://science.sciencemag.org/content/372/6539/292/suppl/DC1)  
Materials and Methods  
Supplementary Text  
Figs. S1 to S8  
Tables S1 to S4  
References (29–36)  
MDAR Reproducibility Checklist

3 January 2020; accepted 5 March 2021  
10.1126/science.aba7582

## MEMBRANES

## Ion-capture electrodialysis using multifunctional adsorptive membranes

Adam A. Uliana<sup>1,2</sup>, Ngoc T. Bui<sup>2,3,†</sup>, Jovan Kamcev<sup>4,‡</sup>, Mercedes K. Taylor<sup>2,4,5</sup>,  
Jeffrey J. Urban<sup>2,3</sup>, Jeffrey R. Long<sup>1,2,4,\*</sup>

Technologies that can efficiently purify nontraditional water sources are needed to meet rising global demand for clean water. Water treatment plants typically require a series of costly separation units to achieve desalination and the removal of toxic trace contaminants such as heavy metals and boron. We report a series of robust, selective, and tunable adsorptive membranes that feature porous aromatic framework nanoparticles embedded within ion exchange polymers and demonstrate their use in an efficient, one-step separation strategy termed ion-capture electrodialysis. This process uses electrodialysis configurations with adsorptive membranes to simultaneously desalinate complex water sources and capture diverse target solutes with negligible capture of competing ions. Our methods are applicable to the development of efficient and selective multifunctional separations that use adsorptive membranes.

**E**scalating demand for water in agriculture, energy, industry, and municipal sectors, coupled with limited natural freshwater, necessitates the rapid development of technologies that will enable access to clean water from alternative sources (1). Nontraditional water sources, such as wastewater, brackish water, or seawater, could provide abundant water globally, but these complex solutions contain high salt concentrations and trace toxic ions (such as heavy metals and oxyanions), which vary by location and type of water source (2–4). At the same time, nontraditional water sources often contain high-value ions (for example, uranyl in seawater and precious metals and nutrients in wastewater), but current technologies lack the efficiency and selectivity needed for their cost-effective extraction (5, 6). Electrodialysis, membrane capacitive deionization, and reverse osmosis are among the most common membrane-based technologies used for removing ions from water (2, 4). However, these approaches are incapable of selectively isolating individual solutes, and toxic ions are instead returned to the environment with the concentrated brine solutions (2). Accordingly, developing membrane technologies with substantially improved selectivity for either water desalination or the recovery of individual ions

or molecules from water is considered one of the most important objectives in the separations industry (3–5, 7, 8).

Adsorptive membranes are an emerging class of materials that have been shown to exhibit improved performance in numerous separations when compared with conventional

membranes, including for water purification (4, 9–13). However, improvements are needed in the capacities, selectivities, and regenerabilities achievable with these materials to enable their wide-scale use, which is also currently hindered by the limited structural and chemical tunability of most adsorptive membranes (4). We therefore sought to develop a highly modular adsorptive membrane platform for use in multifunctional water-purification applications, which is based on the incorporation of porous aromatic frameworks (PAFs) into ion exchange membranes. Built of organic nodes and aromatic linkers, PAFs have high-porosity diamondoid structures with pore morphologies and chemical affinities that can be tuned through the choice of node and linker (Fig. 1, A and B) (14, 15). Densely functionalized PAFs exhibit among the highest selectivities, capacities, and uptake kinetics for the capture of  $\text{Hg}^{2+}$  (16),  $\text{Nd}^{3+}$  (17),  $\text{Cu}^{2+}$  (18),  $\text{Pb}^{2+}$  (19),  $\text{UO}_2^{2+}$  (20, 21),  $\text{B(OH)}_3$  (22),  $\text{Fe}^{3+}$  (23), and  $\text{AuCl}_4^-$  (24) from water. In contrast to typical inorganic or hybrid adsorbent fillers, such as metal-organic frameworks (25), PAFs also have extraordinary hydrothermal stability (15) and chemical compositions that should facilitate incorporation into polymer membranes. However, there are

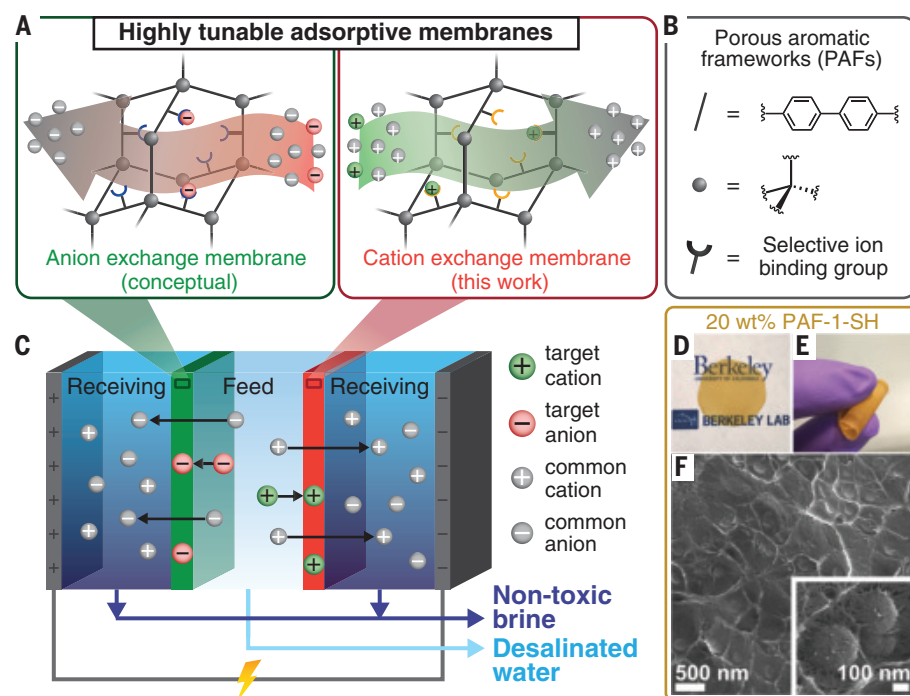


**Fig. 1. Design of composite membranes and application in ion-capture electrodialysis (IC-ED).** (A and B) Tunable composite membranes were prepared by embedding PAFs with selective ion binding sites into cation exchange polymer matrices. (C) We demonstrate the use of these adsorptive membranes in an electrodialysis-based process for the selective capture of target cations (right-hand side) from water and simultaneous desalination. Water splitting occurs at both electrodes to maintain electroneutrality. (D and E) PAF-embedded membranes are defect-free and exhibit optical transparency and high flexibility. (F) Cross-sectional scanning electron micrographs (expanded view in inset) revealed high PAF dispersibility and strong, favorable interactions between the PAF and polymer matrix.

<sup>1</sup>Department of Chemical and Biomolecular Engineering, University of California, Berkeley, CA 94720, USA. <sup>2</sup>Materials Sciences Division, Lawrence Berkeley National Laboratory, Berkeley, CA 94720, USA. <sup>3</sup>The Molecular Foundry, Lawrence Berkeley National Laboratory, Berkeley, CA 94720, USA. <sup>4</sup>Department of Chemistry, University of California, Berkeley, CA 94720, USA. <sup>5</sup>Center for Integrated Nanotechnologies, Sandia National Laboratories, Albuquerque, NM 87185, USA.

\*Corresponding author. Email: jrlong@berkeley.edu  
†Present address: School of Chemical, Biological, and Materials Engineering and School of Civil Engineering and Environmental Science, University of Oklahoma, Norman, OK 73019, USA.  
‡Present address: Department of Chemical Engineering, and Macromolecular Science and Engineering, University of Michigan, Ann Arbor, MI 48109, USA.

only few examples of PAF-incorporated membranes in the literature, with applications limited to antiaging gas-separation membranes, fiber membranes, pervaporation membranes, and thin-film layers (15, 26).

We present a class of adsorptive membranes featuring ion-selective PAF nanoparticles blended into ion exchange membranes. Target ions ( $\text{Hg}^{2+}$ ,  $\text{Cu}^{2+}$ , and  $\text{Fe}^{3+}$ ) in feedwater solutions are selectively captured by these adsorbent-embedded membranes, whereas competing ions (such as  $\text{Na}^+$  and  $\text{Cl}^-$ ) permeate freely (Fig. 1C). This process allows for desalination and detoxification of water, recovery of toxic or high-value target ions, and generation of nontoxic brine streams in an efficient one-step process. This proof-of-concept report focuses on the selective capture of various cationic and neutral species, but the concept can be extended to construct more complex separation schemes for simultaneous capture of target cations and anions.

Model adsorptive membranes were prepared with up to 20 wt % (44 vol %) of the  $\text{Hg}^{2+}$ -selective PAF-1-SH (16) embedded in a sulfonated polysulfone (sPSF) cation exchange matrix (60% sulfonation) (figs. S1, S6, and S7). Loadings were confirmed with thermogravimetric analysis, helium pycnometry, and  $\text{N}_2$  gas adsorption measurements (figs. S8 and S17 and table S2). All the films exhibit substantial optical transparency, which is indicative of high PAF dispersity (Fig. 1D and fig. S2). The films are also highly flexible and can be contorted without damage (Fig. 1E and fig. S3). Dynamic light scattering and scanning electron microscopy (SEM) characterization of PAF samples before membrane incorporation revealed the presence of spherical particles with typical diameters of  $\sim 200$  nm (figs. S15 and S16). Cross-sectional SEM images of 20 wt % PAF-1-SH membranes revealed that these particles are uniformly dispersed without agglomerations, defects, or sieve-in-a-cage morphologies (Fig. 1F and fig. S18). The uniform and robust nature of the composite membranes can be ascribed to favorable van der Waals interactions between the framework and polymer,  $\pi$ - $\pi$  stacking, and polymer filling of the PAF mesopores (26).

Conventional charged membranes are subject to an ion permeability-selectivity trade-off, in which swelling resulting from water uptake decreases selectivity but enlarges free-volume pathways, thereby increasing permeability (27). By contrast, our composite membranes exhibit enhanced water uptake in tandem with diminished swelling, which is due to the presence of a highly porous filler that is capable of cross-linking interactions with the parent polymer (Fig. 2A). These interfacial interactions can be seen in cross-sectional SEM images (Fig. 1F, inset) and are reflected in an increase in the membrane glass transition temperature ( $T_g$ )

with increasing PAF loading (Fig. 2B). The dimensional and chemical stabilities of neat and PAF-embedded sPSF membranes were further probed by dissolution studies, in which each membrane was reimmersed in casting solvents, 12 M HCl, or 12 M NaOH for 24 hours. Neat sPSF membrane samples redissolved in various casting solvents, as expected, but the abundant cross-linking interactions in membranes loaded with 20 wt % PAF-1-SH rendered them fully or partially insoluble in each solvent (fig. S20). Similarly, whereas neat sPSF membranes with ultrahigh charge densities become water soluble owing to excessive water uptake (figs. S6, S7, and S21), incorporation of 20 wt % PAF-1-SH into these highly charged matrices yields freestanding membranes that exhibit minimal swelling even after 1 year of water immersion (fig. S21 and section 2.1 of the supplementary materials).

Batch adsorption experiments revealed that up to 93% of the  $\text{Hg}^{2+}$  adsorption sites in bulk PAF-1-SH (fig. S23) remain accessible upon incorporation of 20 wt % of the framework into a sPSF membrane (Fig. 2C and table S6). A comparison of the kinetics data for the bulk framework (fig. S26) with that obtained for the neat sPSF and 20 wt % PAF-1-SH membranes (fig. S27) suggests that adsorption in the composite membrane is rate-limited by transport

through the sPSF matrix. Bulk PAF-1-SH exhibits a high affinity for  $\text{Hg}^{2+}$  over a number of competing ions and exceptional  $\text{Hg}^{2+}$  selectivity when exposed to environmental water samples (fig. S28). This selectivity stems from optimal soft acid-soft base interactions between  $\text{Hg}^{2+}$  and the thiol groups in PAF-1-SH (16) and is preserved in the 20 wt % PAF-1-SH-loaded membrane (Fig. 2D). The membrane exhibits excellent stability to adsorption-desorption cycling, with only an 8% loss in  $\text{Hg}^{2+}$  capacity over the course of 10 cycles, and the  $\text{Hg}^{2+}$  capacity remains approximately constant after three cycles.

Composite membranes with 20 wt % PAF-1-SH were evaluated for  $\text{Hg}^{2+}$ -capture electrodialysis of synthetic groundwater, brackish water, and industrial wastewater samples with 5 parts per million (ppm) added  $\text{Hg}^{2+}$  (Fig. 3, A to C). These complex feedwater sources were chosen for their diversity in salinity levels, dissolved ions, and pH values (tables S4 and S5). For these proof-of-concept experiments, we used a custom-made, two-compartment cell with the membrane separating the feed from the receiving solution (figs. S30 to S32). Notably, the  $\text{Hg}^{2+}$  concentration in the feed solution was selectively reduced below levels detectable with inductively coupled plasma optical emission spectrometry (ICP-OES), and no  $\text{Hg}^{2+}$

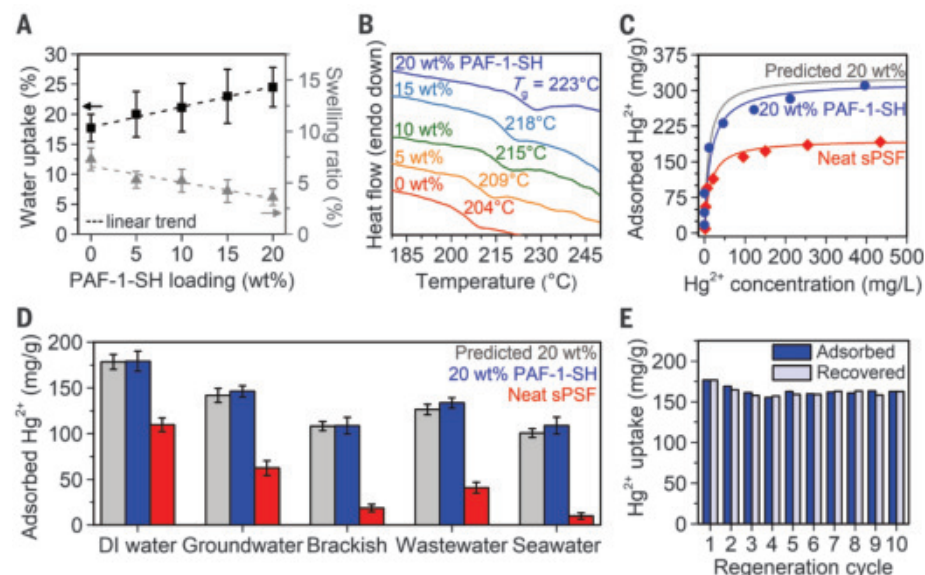


**Fig. 2. Properties of PAF-embedded ion exchange membranes.** (A and B) Composite membranes exhibit increasing water uptake, swelling resistance, and glass transition temperature ( $T_g$ ) with increasing PAF-1-SH loading. (C) Comparison of equilibrium  $\text{Hg}^{2+}$  uptake in neat sPSF and sPSF with 20 wt % PAF-1-SH. Solid lines represent fits with a Langmuir model. Mercury ion uptake in the composite membrane closely approaches the predicted saturation uptake (329 mg/g), assuming all binding sites in the PAF particles are accessible. (D) Equilibrium uptake of  $\text{Hg}^{2+}$  in neat sPSF and sPSF with 20 wt % PAF-1-SH exposed to deionized (DI) water and various synthetic water samples with 100 ppm added  $\text{Hg}^{2+}$ . (E) Mercury ion uptake in 20 wt % PAF-1-SH membranes as a function of cycle number. Minimal decrease in  $\text{Hg}^{2+}$  uptake occurs over 10 cycles. The initial  $\text{Hg}^{2+}$  concentration was 100 ppm for each cycle, and all  $\text{Hg}^{2+}$  captured in each cycle was recovered by using HCl and  $\text{NaNO}_3$ . Error bars denote  $\pm 1$  SD around the mean from at least three separate measurements.



was detected in the receiving solution, indicating the complete capture of  $\text{Hg}^{2+}$  during treatment of each water sample. Meanwhile, all competing cations ( $\text{Na}^+$ ,  $\text{K}^+$ ,  $\text{Mg}^{2+}$ ,  $\text{Ca}^{2+}$ ,  $\text{Ba}^{2+}$ ,  $\text{Mn}^{2+}$ ,  $\text{Fe}^{3+}$ ,  $\text{Ni}^{2+}$ ,  $\text{Cu}^{2+}$ ,  $\text{Zn}^{2+}$ ,  $\text{Cd}^{2+}$ , and  $\text{Pb}^{2+}$ ) were successfully transported into the receiving solution, resulting in >97 to 99% feed desalination (Fig. 3, A to C, insets). Negligible quantities of each competing ion were captured by the membrane (figs. S37 to S43). These selective, multifunctional performances were also maintained upon integrating the PAF-1-SH membranes into a practical stack electro-dialysis device (figs. S54 to S57 and section 1.9 of the supplementary materials). By contrast, no appreciable  $\text{Hg}^{2+}$  was captured when using neat sPSF membranes (figs. S34 to S36 and S58).

Breakthrough experiments further revealed the outstanding  $\text{Hg}^{2+}$  ion-capture efficiency of the adsorptive membranes in an ion-capture electrodialysis (IC-ED) process. Both 10 and 20 wt % PAF-1-SH membranes achieved 96% of their theoretical capacities before  $\text{Hg}^{2+}$  was first detected in the receiving solution (Fig. 3D and section 1.10 of the supplementary materials). By contrast,  $\text{Hg}^{2+}$  immediately permeated through a neat sPSF membrane (Fig. 3D, inset). Furthermore, the breakthrough time in the case of the 20 wt % PAF-1-SH membrane was approximately double that achieved with the 10 wt % membrane. Because of this high attainable efficiency, 1 kg of 20 wt % PAF-1-SH membrane material may treat up to 34,500 liters of water contaminated with 5 ppm  $\text{Hg}^{2+}$

before regeneration is required (table S8), according to simplified upper-bound calculations (section 2.3 of the supplementary materials).

To test the generalizability of the IC-ED approach for the capture of diverse target ions, we also fabricated sPSF membranes embedded with particles of PAF-1-SMe (thioether) or PAF-1-ET (ether-thioether), which are selective for  $\text{Cu}^{2+}$  (18) and  $\text{Fe}^{3+}$  (23), respectively (section 1.1 of the supplementary materials). Notably, the resulting composite membranes are optically transparent (fig. S4), flexible (fig. S5), and dispersible (figs. S16 and S19) while also exhibiting polymer matrix compatibility (fig. S19 and table S3). Composite membranes containing 20 wt % of PAF-1-SMe or PAF-1-ET were tested in our IC-ED setup for the capture of  $\text{Cu}^{2+}$  or  $\text{Fe}^{3+}$  from feed solutions containing 6 ppm  $\text{Cu}^{2+}$  or 2.3 ppm  $\text{Fe}^{3+}$ , respectively, in 0.1 M HEPES buffer. The target ion concentration in each feed solution was reduced by the membranes to levels below detection with ICP-OES with no permeation into the receiving solution, and the membranes simultaneously achieved >96 to 99% desalination of their feeds (Fig. 4, A and B). As expected, negligible target ion capture was obtained when using neat sPSF membranes (figs. S47 and S48).

The fundamental insights from our IC-ED analyses can be applied more broadly to create other multifunctional membrane separation processes. For example, composite membranes prepared by incorporating PAF-1-NMDG (N-methyl-D-glucamine) (22) nanoparticles in sPSF (figs. S1, S4, and S5) were found to be highly selective for  $\text{B}(\text{OH})_3$  capture in solute-capture diffusion dialysis (SC-DD) (fig. S33). In this process, concentration gradients, rather than electric potential gradients, drive solute transport across the membrane. Membranes containing 20 wt % PAF-1-NMDG selectively captured  $\text{B}(\text{OH})_3$ , reducing levels of the solute in the feed solution below levels detectable by ICP-OES, without any measured permeation into the receiving solution (Fig. 4C). By contrast, no appreciable  $\text{B}(\text{OH})_3$  was captured by a neat sPSF membrane (Fig. 4C, inset). Notably, 20 wt % PAF-1-SH composite membranes also exhibited selective  $\text{Hg}^{2+}$  capture when used in our SC-DD setup (fig. S52). These results suggest that an array of efficient, multifunctional processes, such as IC-ED and SC-DD, can be developed through modification of traditional membrane processes (for example, for gas separations or fuel cells), regardless of the transport driving force.

We have described a general approach for the fabrication of robust, tunable adsorptive membranes through incorporation of PAF nanoparticles into ion exchange membranes. Implementation of these membranes in IC-ED and SC-DD processes enables exceptionally selective capture of target solutes [in this work,  $\text{Hg}^{2+}$ ,  $\text{Cu}^{2+}$ ,  $\text{Fe}^{3+}$ , and  $\text{B}(\text{OH})_3$ ] and simultaneous

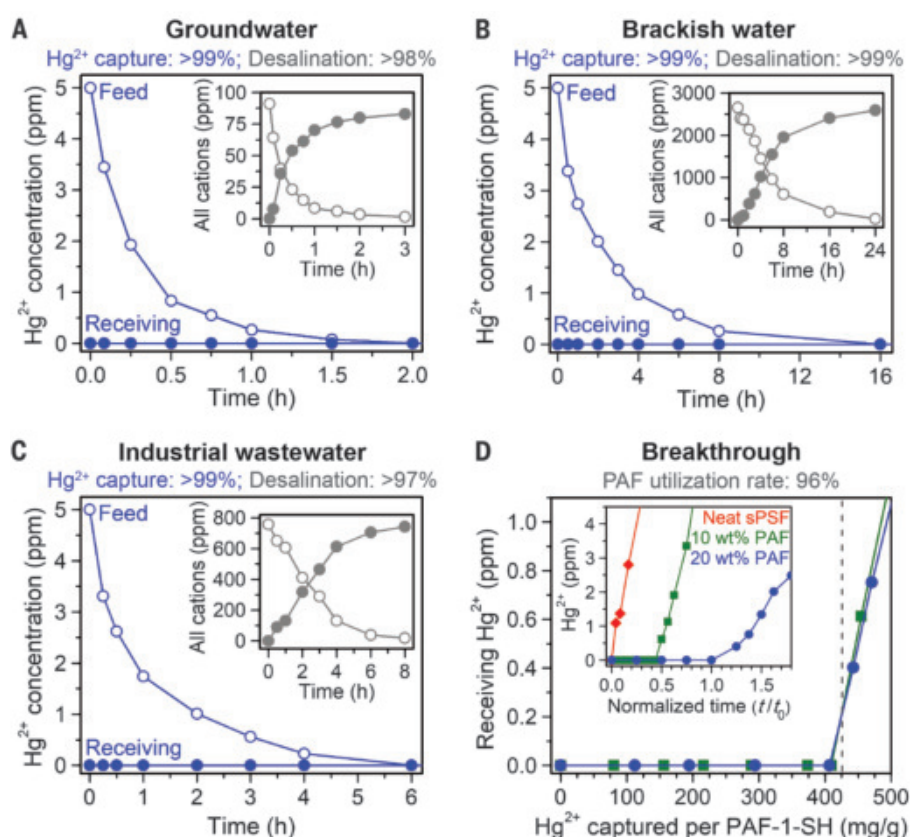


**Fig. 3. IC-ED of diverse water sources.** (A to C) Results from IC-ED of synthetic (A) groundwater, (B) brackish water, and (C) industrial wastewater containing 5 ppm  $\text{Hg}^{2+}$  by using 20 wt % PAF-1-SH in sPSF (applied voltage,  $-4$  V versus  $\text{Ag}/\text{AgCl}$ ). All  $\text{Hg}^{2+}$  was selectively captured from the feeds (open circles) without detectable permeation into the receiving solutions (solid circles). (Insets) All other cations were transported across the membranes to desalinate the feeds. The long duration of the IC-ED tests is an artifact of the experimental setup rather than the materials or IC-ED method (section 2.2 of the supplementary materials). (D) Breakthrough data for IC-ED using sPSF embedded with 10 or 20 wt % PAF-1-SH. Receiving  $\text{Hg}^{2+}$  concentrations are plotted against the amount of  $\text{Hg}^{2+}$  captured at different time intervals (in milligrams per gram of PAF-1-SH in each composite membrane). The predicted capacity (gray dotted line) corresponds to the  $\text{Hg}^{2+}$  uptake achieved by using PAF-1-SH powder under analogous testing conditions (section 1.10 of the supplementary materials). (Inset) Concentration of  $\text{Hg}^{2+}$  in the receiving solutions for IC-ED processes using neat sPSF (diamonds) and sPSF with 10 wt % PAF-1-SH (squares) and 20 wt % PAF-1-SH (circles), plotted versus time  $t$  normalized by the breakthrough time for the 20 wt % PAF-1-SH composite membrane,  $t_0$ . Mean values determined from two replicate experiments are shown. Initial feed, 100 ppm  $\text{Hg}^{2+}$  in 0.1 M  $\text{NaNO}_3$ ; applied voltage,  $-2$  V versus  $\text{Ag}/\text{AgCl}$ .

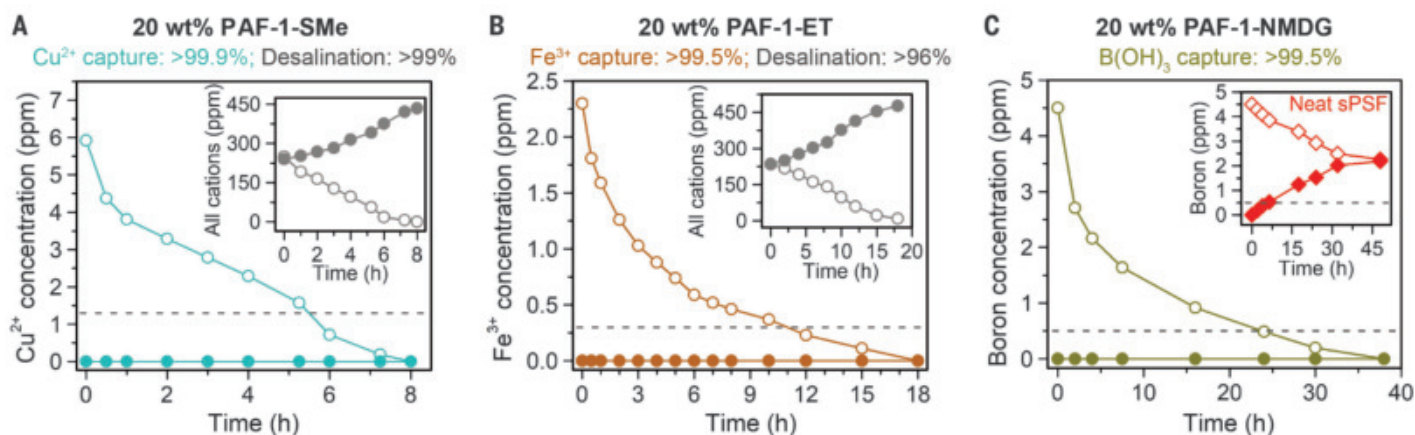


**Fig. 4. Tuning membranes to selectively recover various target solutes.**

(A and B)  $\text{Cu}^{2+}$  (A) and  $\text{Fe}^{3+}$ -capture (B) electro dialysis (applied voltages,  $-2$  and  $-1.5$  V versus Ag/AgCl, respectively) using composite membranes with 20 wt % PAF-1-SMe and PAF-1-ET in sPSF, respectively. HEPES buffer (0.1 M) was used as the source water in each solution to supply competing ions and maintain constant pH. The insets show the successful transport of all competing cations across the membrane to desalinate the feed. (C)  $\text{B(OH)}_3$ -capture diffusion dialysis of groundwater containing 4.5 ppm boron using

composite membranes with 20 wt % PAF-1-NMDG in sPSF (no applied voltage). The inset shows results by using neat sPSF membranes for comparison. Open and solid symbols denote feed and receiving concentrations, respectively. Each plot point represents the mean value determined from two replicate experiments. Gray dotted lines indicate recommended maximum contaminant limits imposed by the US Environmental Protection Agency (EPA) for  $\text{Cu}^{2+}$  (29), the EPA and World Health Organization for  $\text{Fe}^{3+}$  (29, 30), and agricultural restrictions for sensitive crops for  $\text{B(OH)}_3$  (31).

desalination of diverse source waters. The high efficiency of this one-step process contrasts starkly with conventional intensive water treatment methodologies, which require multiple steps to achieve similar results (further comparisons are in section 2.5 of the supplementary materials) (28). The technology should be suitable more broadly for use with diverse adsorptive membranes and in the purification of complex water streams at various scales, such as in isolated regions that lack the necessary infrastructure for the treatment of contaminated groundwater or in desalination plants situated near nuclear waste sites for the treatment of wastewater polluted with radionuclides. To achieve these more complex separations, we envision the design of membranes featuring specialized combinations of embedded adsorbents, including nanoparticles of various hybrid and inorganic materials.

## REFERENCES AND NOTES

- M. M. Mekonnen, A. Y. Hoekstra, *Sci. Adv.* **2**, e1500323 (2016).
- M. A. Shannon *et al.*, *Nature* **452**, 301–310 (2008).
- J. R. Werber, C. O. Osuji, M. Elimelech, *Nat. Rev. Mater.* **1**, 16018 (2016).
- M. R. Landsman *et al.*, *Annu. Rev. Chem. Biomol. Eng.* **11**, 559–585 (2020).
- D. S. Sholl, R. P. Lively, *Nature* **532**, 435–437 (2016).
- W. W. Li, H. Q. Yu, B. E. Rittmann, *Nature* **528**, 29–31 (2015).
- H. B. Park, J. Kamcev, L. M. Robeson, M. Elimelech, B. D. Freeman, *Science* **356**, eaab0530 (2017).
- J. R. Werber, A. Deshmukh, M. Elimelech, *Environ. Sci. Technol. Lett.* **3**, 112–120 (2016).
- S. Bolisetty, R. Mezzenga, *Nat. Nanotechnol.* **11**, 365–371 (2016).
- Y. Zhang *et al.*, *ACS Cent. Sci.* **4**, 1697–1707 (2018).
- K. V. Petrov, L. Paltrinieri, L. Poltorak, L. C. P. M. de Smet, E. J. R. Sudhölter, *Chem. Commun.* **56**, 5046–5049 (2020).

- S. Chaudhury, O. Nir, *Ind. Eng. Chem. Res.* **59**, 10595–10605 (2020).
- J. E. Bachman, Z. P. Smith, T. Li, T. Xu, J. R. Long, *Nat. Mater.* **15**, 845–849 (2016).
- T. Ben *et al.*, *Angew. Chem. Int. Ed.* **48**, 9457–9460 (2009).
- Y. Tian, G. Zhu, *Chem. Rev.* **120**, 8934–8986 (2020).
- B. Li, Y. Zhang, D. Ma, Z. Shi, S. Ma, *Nat. Commun.* **5**, 5537 (2014).
- S. Demir *et al.*, *ACS Cent. Sci.* **2**, 253–265 (2016).
- S. Lee *et al.*, *J. Am. Chem. Soc.* **138**, 7603–7609 (2016).
- Y. J. Yang *et al.*, *J. Mater. Chem. A* **6**, 5202–5207 (2018).
- Y. Yuan *et al.*, *Adv. Mater.* **30**, e1706507 (2018).
- B. Li *et al.*, *ACS Appl. Mater. Interfaces* **9**, 12511–12517 (2017).
- J. Kamcev *et al.*, *Adv. Mater.* **31**, e1808027 (2019).
- S. Lee *et al.*, *Chem. Sci.* **10**, 6651–6660 (2019).
- T. Ma *et al.*, *ACS Appl. Mater. Interfaces* **12**, 30474–30482 (2020).
- X. Li *et al.*, *Chem. Soc. Rev.* **46**, 7124–7144 (2017).
- S. J. D. Smith *et al.*, *Acc. Chem. Res.* **53**, 1381–1388 (2020).
- H. Fan, N. Y. Yip, *J. Membr. Sci.* **573**, 668–681 (2019).
- M. Elimelech, W. A. Phillip, *Science* **333**, 712–717 (2011).
- U.S. Environmental Protection Agency (EPA), “2018 edition of the drinking water standards and health advisories” (US EPA, 2018).
- World Health Organization, “Guidelines for drinking-water quality, 4th edition, incorporating the 1st addendum” (WHO, 2017).
- E. Güler, C. Kaya, N. Kabay, M. Arda, *Desalination* **356**, 85–93 (2015).

## ACKNOWLEDGMENTS

We thank H. Furukawa for analysis of pore size distributions, T. Xu for assistance with dynamic light scattering measurements, N. P. Balsara for potentiostat use, J. Breen for fabrication of electro dialysis cells, D. J. Miller for assistance with water contact angle measurements, E. Kreimer and the Microanalytical Facility for microbalance use and assistance with elemental analyses and ICP-OES measurements, R. Kostecki and E. Velasquez for helpful discussions, and K. R. Meihaus for editorial assistance. **Funding:** The synthesis and characterization of materials and membranes were supported by the Center for Gas Separations, an Energy Frontier Research Center supported by the US Department of Energy (DOE), Office of Science, Office of Basic Energy Sciences

(award DE-SC0001015), and the electro dialysis measurements were supported by the US DOE, Office of Science, Office of Basic Energy Sciences (award number DE-SC0019992). Preliminary experiments were also supported by the Molecular Foundry and the Laboratory Directed Research and Development (LDRD) Program of the US DOE (contract no. DE-AC02-05CH11231) for Lawrence Berkeley National Laboratory. We thank the US National Science Foundation for providing graduate fellowship support for A.A.U. and M.K.T. We gratefully acknowledge the support of the Center for Integrated Nanotechnologies, an Office of Science User Facility operated for the US DOE Office of Science. Sandia National Laboratories is a multimission laboratory managed and operated by National Technology and Engineering Solutions of Sandia, LLC, a wholly owned subsidiary of Honeywell International, Inc., for the US DOE's National Nuclear Security Administration (contract no. DE-NA-0003525). The views expressed in the article do not necessarily represent the views of the US DOE or the US government. **Author contributions:** A.A.U., J.J.U., and J.R.L. formulated the project with valuable input from N.T.B., J.K., and M.K.T.; A.A.U. synthesized the PAFs and membranes with assistance from J.K. and M.K.T.; A.A.U. performed and analyzed all material characterizations. A.A.U. collected and analyzed the adsorption data. A.A.U. and N.T.B. designed the electro dialysis cells. A.A.U. collected and analyzed the electro dialysis and diffusion dialysis data. N.T.B. performed and analyzed preliminary electro dialysis experiments and preliminary microscopy characterizations. A.A.U. and J.R.L. wrote the manuscript, and all authors contributed to revising the manuscript. **Competing interests:** The University of California, Berkeley, has applied for a patent (US application no. 63/079,457) on some of the technology discussed here, on which A.A.U., N.T.B., J.J.U., and J.R.L. are listed as coinventors, as well as an additional patent (US application no. 63/118,322) on some of the materials discussed here, on which A.A.U. and J.R.L. are listed as coinventors. **Data and materials availability:** All data are available in the manuscript or the supplementary materials.

## SUPPLEMENTARY MATERIALS

science.sciencemag.org/content/372/6539/296/suppl/DC1  
 Materials and Methods  
 Supplementary Text  
 Figs. S1 to S59  
 Tables S1 to S8  
 References (32–71)

8 November 2020; accepted 15 March 2021  
 10.1126/science.abf5991



## PALEONTOLOGY

# Punctuated ecological equilibrium in mammal communities over evolutionary time scales

Fernando Blanco<sup>1\*</sup>, Joaquín Calatayud<sup>2</sup>, David M. Martín-Perea<sup>3,4,5</sup>, M. Soledad Domingo<sup>6</sup>, Iris Menéndez<sup>4,7</sup>, Johannes Müller<sup>1</sup>, Manuel Hernández Fernández<sup>4,7</sup>, Juan L. Cantalapiedra<sup>8</sup>

The study of deep-time ecological dynamics has the ability to inform conservation decisions by anticipating the behavior of ecosystems millions of years into the future. Using network analysis and an exceptional fossil dataset spanning the past 21 million years, we show that mammalian ecological assemblages undergo long periods of functional stasis, notwithstanding high taxonomic volatility due to dispersal, speciation, and extinction. Higher functional richness and diversity promoted the persistence of functional faunas despite species extinction risk being indistinguishable among these different faunas. These findings, and the large mismatch between functional and taxonomic successions, indicate that although safeguarding functional diversity may or may not minimize species losses, it would certainly enhance the persistence of ecosystem functioning in the face of future disturbances.

In the context of the current biodiversity crisis, conservation efforts can be directed to safeguarding interactions and processes within ecosystems (ecosystem functioning), including those that are—and will be—beneficial to people (ecosystem services) (1, 2). This notion departs from taxon-based approaches and rather focuses on phenotypic features of species, with an emphasis on functional traits—those traits that condense multiple aspects of a species' ecological role (3). The conviction is that conserving a higher phenotypic diversity should help to stabilize ecosystems in the face of disturbances (the “insurance effect”) (4), increasing the persistence of ecosystem functioning and ensuring yet-unknown future benefits to humanity (5). Even so, current conservation decisions will have consequences on the evolutionary future of life that we cannot fully understand by investigating ongoing habitat perturbations (6, 7).

Only by looking into the past can we ask fundamental questions regarding the persistence of ecosystem functioning over evolutionary time and guide long-term future conservation actions (1). How long does ecosystem func-

tional structure typically endure, and how much of this functioning is tied to the wax and wane of taxonomic faunas over millions of years? Ecological assessments of faunas have a long tradition in paleobiology (8–10). However, to answer such questions, rather than conducting a functional assessment of chronofaunas (taxonomy-defined temporal faunas), we need to assess the duration of FFs (functional faunas) independently from taxonomy (1), exclusively on the basis of functional coherence of communities. If temporal associations of ecosystems with similar functional structures (that is, similar FFs) are found to weather the succession of taxonomic faunas, this would further endorse prioritizing the conservation of ecosystem functioning.

We turned to the fossil record, adopting a taxon-free perspective that enabled us to evaluate ecological dynamics over evolutionary time (1). Investigating deep-time patterns in ecological assembly at the community level demands a high-resolution fossil record (11). Our study draws on a new dataset of the exceptional and well-resolved fossil record of large Iberian mammals spanning the past 21 million years (Myr), including 167 fossil and two extant communities with an average resolution of around 0.1 Myr and an estimated 0.8 probability that a 1-Myr-duration taxon is sampled (supplementary materials and data file S1) (12, 13). Our dataset contains a total of 396 mammalian species, for which we compiled information on three fundamental functional traits: body size, diet, and locomotion (table S1 and data file S1). Species were assigned to functional entities (FEs), which are distinct combinations of these three traits (14). We used a community detection algorithm (CDA), borrowed from network theory, to reveal both the functional and taxonomic structure of mammalian communities (supplementary materials). Network-based CDA identifies clusters of communities with similar functional or tax-

onomic structures (modules) defined by the presence of functional entities or taxa (species), respectively. Shifts in past ecological community structure were assessed by the emergence of new associations of functional entities over time and compared with shifts in taxonomic structure (presence of taxa). Our CDA ignores the age of communities, and it is only later that we evaluated the tempo of module succession by plotting the sites within each module against their age (Fig. 1 and supplementary materials).

We used several analysis configurations. We first selected localities with representatives of the orders Proboscidea, Carnivora, Perissodactyla, and Artiodactyla because these were frequent constituents of Neogene-Quaternary ecosystems (Fig. 1A). Second, we selected only exceptional localities (11): those sites whose richness values were above the 75th percentile of sites with similar age (figs. S1 to S3). Last, we analyzed the data aggregated into 0.5-Myr temporal bins, which reflect regional trends (an extended methodological explanation is provided in the supplementary materials) (figs. S1 to S3). The results from the first configuration are shown in Fig. 1.

A common pattern emerges from all approaches: Ecosystem functional composition shows longer persistence than taxonomic composition (Fig. 1). Both functional and taxonomic faunas follow a virtually irreversible temporal succession, but taxonomic modules are replaced every 0.9 Myr on average, whereas functional modules have a mean span of 2.8 Myr. A randomization analysis indicates that such organization reflects a genuine ecological signal ( $P = 0.01$ ) (fig. S4) and does not simply arise because FEs are an aggregation of taxa. Furthermore, taxonomic modules at the generic level [a taxonomic aggregation of taxa (15)] show a labile pattern similar to the species-level network (figs. S2 and S3). Sensitivity analyses show that our approach is robust toward reasonable error in functional categorizations (supplementary materials and fig. S5), stochasticity inherent to the detection of modules, and the choice of community detection algorithms (supplementary materials and tables S2 and S3).

We identified three periods with marked functional stability corresponding with three long-lasting and robust modules: earlier Middle Miocene (FF1), later Middle Miocene to earlier Late Miocene (FF2), and later Late Miocene to present (FF3), with durations of 2.58, 4.66, and 9.37 Myr, respectively (summing 80% of the analyzed interval) (Fig. 1). An exploration of the transitional intervals between FFs demonstrates that ecological reassembly was fast, lacking communities with intermediate functional configurations (Fig. 1A, fig. S6, and supplementary materials). Altogether, our procedure reveals gradual changes in taxonomic assembly that contrast with the punctuated

<sup>1</sup>Museum für Naturkunde, Leibniz-Institut für Evolutions- und Biodiversitätsforschung, an der Humboldt-Universität zu Berlin, Invalidenstrasse 43, 10115 Berlin, Germany. <sup>2</sup>Departamento de Biología, Geología, Física y Química Inorgánica, Universidad Rey Juan Carlos, Calle Tulipán s/n, 28933 Móstoles, Spain.

<sup>3</sup>Museo Nacional de Ciencias Naturales-Consejo Superior de Investigaciones Científicas (CSIC), Calle José Gutiérrez Abascal 2, 28006 Madrid, Spain. <sup>4</sup>Departamento de Geodinámica, Estratigrafía y Paleontología, Universidad Complutense de Madrid, C/ José Antonio Nováis 12, 28040 Madrid, Spain.

<sup>5</sup>Instituto de Evolución Humana en África IDEA, Calle Covarrubias 26, 28010 Madrid, Spain. <sup>6</sup>Departamento de Didáctica de las Ciencias Experimentales, Ciencias Sociales y Matemáticas, Universidad Complutense de Madrid (UCM), C/Rector Royo Villanova s/n, 28040 Madrid, Spain.

<sup>7</sup>Departamento de Cambio Medioambiental, Instituto de Geociencias (UCM, CSIC), C/ Severo Ochoa 7, 28040 Madrid, Spain. <sup>8</sup>Departamento de Ciencias de la Vida, GloCEE Global Change Ecology and Evolution Research Group, Universidad de Alcalá, Plaza de San Diego s/n, 28801 Alcalá de Henares, Spain.

\*Corresponding author. Email: fblancosegovia@gmail.com, fernando.blanco@mfn.berlin



stasis shown by the functional faunas, revealing an emergent property of ecosystem functioning observable only over broad time scales (Fig. 1).

The contrasting timing of change in ecosystem functioning compared with taxonomic turnover became even more evident when we examined the regional diversification and dis-

persal patterns through time (Fig. 1C, fig. S7, and supplementary materials). Overall, species-level volatility in Iberian Neogene-Quaternary faunas has been severe (average speciation and immigration rate =  $1.40 \text{ Myr}^{-1}$ ; average regional extinction rate =  $1.17 \text{ Myr}^{-1}$ ), ensuring a continuous replacement of the Iberian species pool over the past 21 Myr, as captured through

network analysis (Fig. 1B). Nevertheless, only major faunal events were able to push the system toward a new state, around 14 and 9 Myr ago (Ma), triggering fast reassembly of ecological guilds into new functional faunas.

The onset of the FF2 around 14 Ma seems related to profound reconfiguration of biogeographic and climatic settings. There is

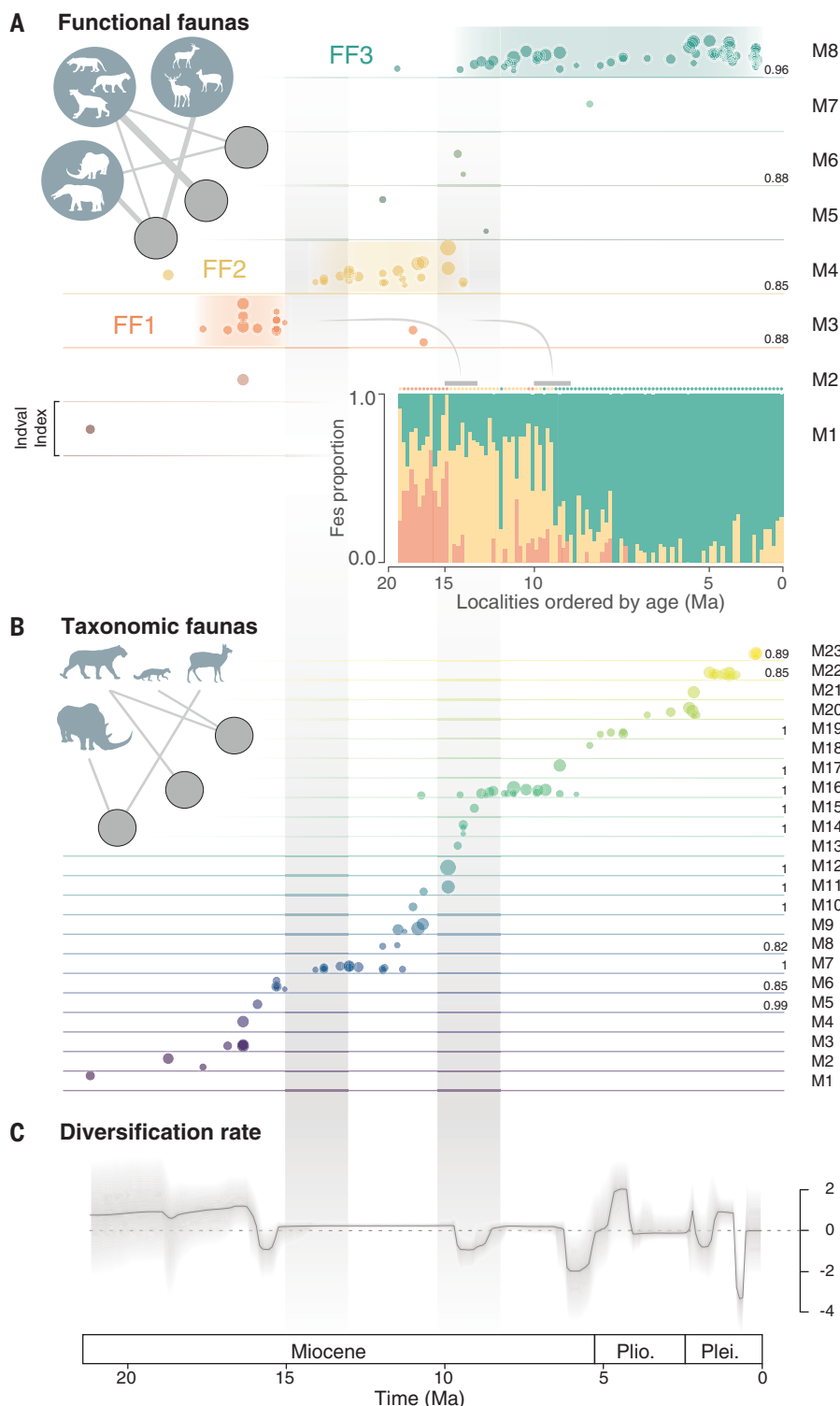


**Fig. 1. Temporal trends of Iberian mammal communities over the past 21 Myr.** (A and B) Localities colored by modules (M) are plotted against time. Dots indicate communities (localities), and each dot's size is proportional to the species richness of that community. (A) Modules derived from the functional network analysis show the succession of FFs. The height of the points reflects relevance within the module (IndVal index) (supplementary materials). Numbers above the module lines indicate the module robustness as the probability of being found in different runs of the community detection algorithm (only values above 0.8 are shown) (supplementary materials). (A) Color-shaded areas indicate the three long-lasting FFs. Vertical gray bars indicate the transitions between FF1 to FF2 and FF2 to FF3. (Inset) The proportion of functional entities belonging to the three main FFs in each locality (dots). (B) Modules based on species composition represent the taxonomic succession. (C) Changes in taxonomic composition are represented by the net diversification rate over time. Shaded regions indicate the 95% confidence interval. Plio., Pliocene; Plei., Pleistocene. [Silhouettes are from PhyloPic ([www.phylopic.org](http://www.phylopic.org)).]

evidence of a higher resemblance of Iberian taxonomic faunas with Eurasian faunas by this age (16). Regional isotopic data depict a sustained trend toward a prevalence of more forested, less arid habitats in the Iberian Peninsula (16), which is consistent with the observed enrichment of communities with browsing herbivores of all sizes (fig. S8). The FF2-FF3 transition (around 9 Ma) seems triggered by an intensification of hydric seasonality and the associated spread of grassland habitats (16). In fact, this second major reassembly pulse replaced the browser-rich faunas of the later Middle Miocene and earlier Late Miocene with ecosystems that packed a broad variety of mixed-feeders (feed both through browsing and on grass) (fig. S8) (17).

The context of both functional transitions suggests an important role of abiotic changes (climate and climate-driven biogeographic context) on the system shifts. However, a trait-dependent extinction model (18) did not find an overall effect of particular traits or their combinations (FEs) on extinction across different time bins. The influence of such abiotic factors was not expressed through trait-mediated local extirpation. Instead, these analyses show that during functional transitions, characteristic species (those species with at least 60% of their occurrences in localities of one of the three FFs) of the outgoing functional fauna

showed significantly higher extinction risk than that of the incoming fauna (Fig. 2A and fig. S9). Thus, the extinction of species during severe ecological shifts seems to be determined by their attachment to a collapsing functional system rather than their particular functional traits (19).

Altogether, these findings portray a system in which species gains and losses are governed by their restriction to functional scaffolds defined by ecological interactions. These interactions should limit the inclusion of new functional strategies into established ecosystems (20), constraining both the evolution (21) and the immigration of species belonging to other FEs (22). Major disturbances forced the system into new ecological states, rendering the disassembly of the prevailing functional fauna and the assembly of a new functional scaffold (Fig. 1).

Not all major faunal events caused a reorganization of ecosystem functioning. During the past 8 Myr, the most recent functional fauna (FF3) survived three severe extinction events (Fig. 1C): the Messinian salinity crisis (6 to 5 Ma), the beginning of the Plio-Pleistocene glaciations (~2.5 Ma), and the Early-Middle Pleistocene transition (~0.8 Ma) (fig. S7). Thus, FF3 is not only the most enduring but also the most resistant functional fauna of the studied time interval. Overall, the Neogene-

Quaternary Iberian functional systems have increased in duration and persistence.

Why do functional faunas increase in persistence during the analysis interval? The above-mentioned trait-dependent extinction model shows no evidence of lower extinction risk in species associated with more persistent FFs, suggesting that persistence of each functional fauna draws from emergent properties of the system and not from the persistence of the constituent species. Linear models show that communities in successive functional faunas increased their functional diversity ( $F_{div}$ , as the Shannon index) (tables S4 to S6), which is mostly driven by an increase in functional richness ( $F_{ric}$ ) (tables S7 to S9) rather than by functional evenness (tables S10 to S12). FF2 and FF3 show increases in  $F_{ric}$  and  $F_{div}$  with respect to FF1 (Fig. 2B and tables S4 to S9). A higher  $F_{ric}$  associated with more persistent functional faunas agrees with the idea that biodiversity enhances ecosystem resilience (4, 23). Differential persistence in FF2 and FF3 may be further explained by environmental conditions that operated during their onset. Whereas FF2 originated during milder climatic conditions, the inception of FF3 took place during an episode of increased aridity in the region (24). Such conditions brought an entourage of arid-adapted immigrants from Eurasia and Africa (16, 25). Their ecological assemblage, forged by strong abiotic forces from FF3's inception, would have coped with the milder conditions of the latest Iberian Miocene first (16) and, subsequently, with the increasing seasonality and glacial regimes in Pliocene and Pleistocene times.

Our analyses of the fossil record set out key differences in the mode that taxonomic and functional assemblages wax and wane over evolutionary time scales. The marked decoupling between taxonomic and ecological turnover further demonstrates the value of functional and trait-based procedures when assessing the magnitude and consequences of environmental disturbances in paleobiological studies. Moreover, because the collapse of FFs seems to be the main force pulling species out of the system, investigation of preterit turnover episodes should look beyond trait selection in extinction events and also account for the integration of species into particular FFs during ecological dismantling.

Our study provides a deep-time dimension to the functional perspective in conservation (2): Actions carried out to ensure ecosystem functioning will tend to endure longer than actions oriented toward protecting taxonomic structure. We found that higher  $F_{div}$  enhances the persistence of ecosystem functioning, yielding a long-term version of the temporal insurance (4, 23). However, the vague connection between taxonomic and ecological assembly yields a cautionary reading. Because species in

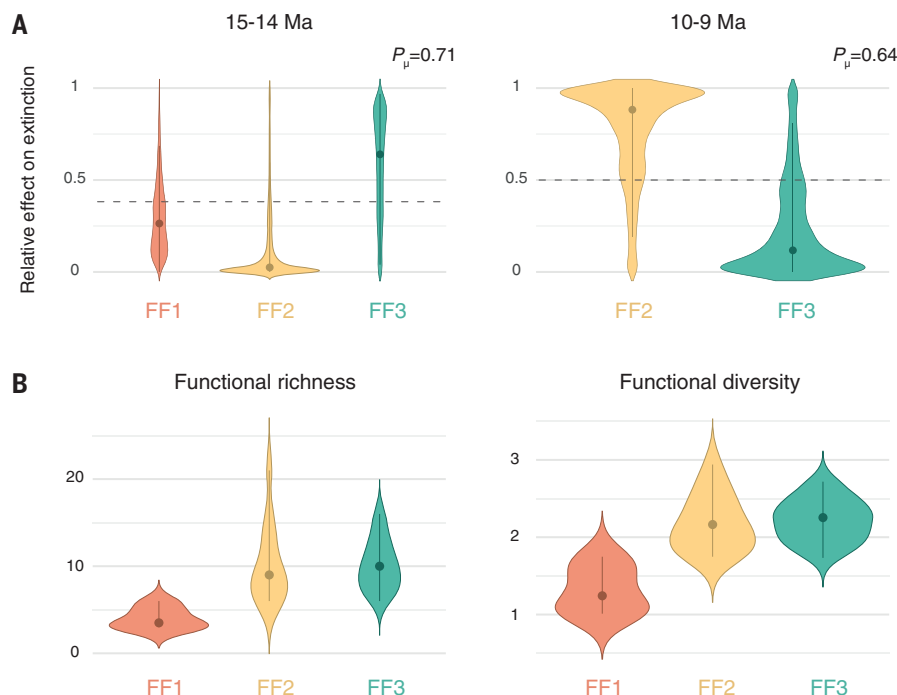


**Fig. 2. Differential extinction risk during functional transitions and functional richness and diversity among the three main functional faunas.** (A) Violin plots indicate the differential extinction risk of species associated with the FFs during the two major transitions (15 to 14 Ma and 10 to 9 Ma).  $P_{\mu}$  is the probability of the trait affecting extinction risk. The horizontal dashed lines indicate the expected effect if the trait had no effect. (B) Functional richness and functional diversity of the FFs (supplementary materials). Colors are as in Fig. 1.

high- $F_{\text{div}}$  faunas do not show lower extinction risk, betting on higher- $F_{\text{div}}$  systems would not necessarily minimize species loss in the long term. If the past is useful to illuminate the future, our paleobiological perspective further emphasizes the gap between conservation policies that minimize extinctions and those that target ecosystem functioning and its benefits to people (26).

## REFERENCES AND NOTES

1. A. D. Barnosky *et al.*, *Science* **355**, eaah4787 (2017).
2. C. M. Tucker *et al.*, *Biol. Rev. Camb. Philos. Soc.* **94**, 1740–1760 (2019).
3. F. Mazel *et al.*, *Nat. Commun.* **9**, 2888 (2018).
4. M. Loreau, C. de Mazancourt, *Ecol. Lett.* **16** (suppl. 1), 106–115 (2013).
5. S. Díaz *et al.*, *Science* **359**, 270–272 (2018).
6. F. Aubree *et al.*, *Ecol. Lett.* **23**, 1263–1275 (2020).
7. J. L. Cantalapiedra *et al.*, *Proc. Biol. Sci.* **286**, 20182896 (2019).
8. R. K. Bambach, J. B. Bennington, *Evolutionary Paleobiology* (Univ. of Chicago Press, 1996), pp. 123–160.
9. B. Figueirido, P. Palmqvist, J. A. Pérez-Claros, C. M. Janis, *Proc. Natl. Acad. Sci. U.S.A.* **116**, 12698–12703 (2019).
10. J. A. Dunne, C. C. Labandeira, R. J. Williams, *Proc. Biol. Sci.* **281**, 20133280 (2014).
11. R. A. Close *et al.*, *Nat. Ecol. Evol.* **3**, 590–597 (2019).
12. F. Blanco *et al.*, R. Scripts Blanco *et al.* 2021. Figshare (2021); doi:10.6084/m9.figshare.13516253.
13. F. Blanco *et al.*, Occurrence data Blanco *et al.* 2021. Figshare (2021); doi:10.6084/m9.figshare.13332755.
14. D. Mouillot *et al.*, *Proc. Natl. Acad. Sci. U.S.A.* **111**, 13757–13762 (2014).
15. G. G. Simpson, *The Major Features of Evolution* (Columbia Univ. Press, 1953).
16. J. L. Cantalapiedra, M. S. Domingo, L. Domingo, *Sci. Rep.* **8**, 13413 (2018).
17. M. S. Domingo, C. Badgley, B. Azanza, D. DeMiguel, M. T. Alberdi, *Paleobiology* **40**, 197–221 (2014).
18. C. Pimiento *et al.*, *Proc. Biol. Sci.* **287**, 20201162 (2020).
19. P. D. Roopnarine, K. D. Angielczyk, *Biol. Lett.* **8**, 147–150 (2012).
20. G. E. Hutchinson, *Am. Nat.* **93**, 145–159 (1959).
21. P. J. Morris, L. C. Ivany, K. M. Schopf, C. E. Brett, *Proc. Natl. Acad. Sci. U.S.A.* **92**, 11269–11273 (1995).
22. T. A. Kennedy *et al.*, *Nature* **417**, 636–638 (2002).
23. S. Yachi, M. Loreau, *Proc. Natl. Acad. Sci. U.S.A.* **96**, 1463–1468 (1999).
24. L. Domingo *et al.*, *PLOS ONE* **8**, e63739 (2013).
25. M. Fortelius *et al.*, *Palaeogeogr. Palaeoclimatol. Palaeoecol.* **238**, 219–227 (2006).
26. A. Purvis, *Nat. Ecol. Evol.* **4**, 768–769 (2020).

## ACKNOWLEDGMENTS

We thank J. Morales, M. Ríos, O. Sanisidro, and A. Valenciano for their insights on functional traits; D. Silvestro for technical assistance; and N. Baird, F. Bibi, M. Fabbri, P. Medina-García, I. A. Lazagabaster, G. Navalón, M. A. Rodríguez, and two anonymous reviewers for their valuable comments and advice. We acknowledge

the effort of all the people working in Iberian fossil sites over the decades that made this study possible. **Funding:** F.B. was funded by Deutsche Forschungsgemeinschaft (LO 2368/1-1). D.M.M.-P. was funded by an FPI predoctoral grant BES-2016-079560 from the Spanish Government associated with project CGL2015-6833-P and PGC2018-094122-B-I00. I.M. was funded by a predoctoral grant from the Complutense University of Madrid (CT27/16-CT28/16). J.L.C. was funded by the Talent Attraction Program of the Madrid Government and the Universidad de Alcalá (2017-T1/AMB5298). D.M.M.-P., I.M., M.H.F., and M.S.D. acknowledge the project PGC2018-094955-A-I00 granted by the Spanish Ministerio de Ciencia, Innovación y Universidades. **Author contributions:** F.B., J.L.C., and J.M. conceptualized the research. F.B., D.M.M.-P., I.M., M.S.D., and M.H.F. gathered the data. F.B., J.C., and J.L.C. designed and performed the analysis. F.B., J.C., and J.L.C. wrote the paper with input from all authors. **Competing interests:** The authors declare no competing interests. **Data and materials availability:** All data and code are available at (12, 13).

## SUPPLEMENTARY MATERIALS

science.sciencemag.org/content/372/6539/300/suppl/DC1  
Materials and Methods  
Figs. S1 to S10  
Tables S1 to S12  
References (27–52)  
Data File S1

25 June 2020; accepted 23 February 2021  
10.1126/science.abd5110





### SARS-CoV-2 RT-PCR Kits

Bio-Rad Laboratories' Reliance SARS-CoV-2/FluA/FluB RT-PCR and Reliance SARS-CoV-2 RT-PCR Assay Kits have been granted emergency use authorization by the U.S. Food and Drug Administration. The multitarget Reliance SARS-CoV-2/FluA/FluB RT-PCR Assay Kit

simultaneously detects and differentiates SARS-CoV-2 (the virus associated with COVID-19), influenza A, and influenza B in a single, multiplex reaction. The highly sensitive respiratory pathogen panel is intended for use with nasopharyngeal swabs and anterior nasal swabs. Bio-Rad's Reliance SARS-CoV-2 RT-PCR Assay Kit is a multiplex test that targets two separate regions in the nucleocapsid gene (N1 and N2 regions) to ensure greater sensitivity and tolerance to potential mutations that may occur within the viral genome over time in the detection of SARS-CoV-2. Both assay kits contain the company's standard and negative molecular controls and are validated to run on the CFX Opus 96, CFX96 Touch, and CFX96 Dx qPCR Systems, and for higher-throughput testing, can be run on the CFX Opus 384 and CFX384 Touch Systems; they are also validated to run on qPCR systems offered by other manufacturers.

#### Bio-Rad Laboratories

For info: 800-424-6723

[www.bio-rad.com](http://www.bio-rad.com)

### Animal-Free Enzymes for In Vitro Tissue Dissociation

AMS Biotechnology (AMSBIO), in association with Nordmark Biochemicals (NB), is now offering animal-free Collagenase and Neutral Protease enzymes isolated from *Clostridium histolyticum*, for in vitro tissue dissociation that delivers high yields of viable cells. They are produced under good manufacturing practice guidelines using a plant-based production process that guarantees no risk of cross-contamination with animal-derived materials. These top-quality enzymes can be used on a wide range of cell/tissue types and are supported with specific protocols available based on each application. Our highly consistent, superior Collagenase and Neutral Protease are essential tissue-dissociation enzymes for tissue-engineering and regenerative-medicine applications. The high level of quality control involved in the production of these enzymes provides reliable lot-to-lot consistency with accurate analysis of proteolytic enzyme activities. AMSBIO also offers research-grade Collagenase and Neutral Protease enzymes. As each application requires different digestion conditions, this large range of Collagenase NB products offers optimal digestion conditions for a wide variety of tissue types.

#### AMS Biotechnology

For info: 617-945-5033

[www.amsbio.com/collagenase-nb-and-neutral-protease](http://www.amsbio.com/collagenase-nb-and-neutral-protease)

### Borosilicate Glass Microplates

Made from ultrapure-grade borosilicate glass, Porvair Sciences' Krystal Glass Bottom microplates with Schott D 263 M technology are precision manufactured for high optical performance in high-resolution microscopy applications, such as charge-coupled device imaging and laser-detection applications. Krystal Glass Bottom plates combine the advantageous optical properties of glass, low background, and low birefringence with the versatility of a microplate. The latest Krystal microplate is available in two different thicknesses—50  $\mu\text{m}$  and 175  $\mu\text{m}$ —and in addition, a high-performance version D 263 M/1.5-H plate with a thickness tolerance of  $\pm 5 \mu\text{m}$  is available for high-sensitivity applications. Precisely manufactured to SBS/ANSI microplate dimensions, the affordable Krystal Glass Bottom design is fully compatible with all

commercially available plate readers, robotic sample processors, and automated liquid-handling systems. The complete Krystal range of glass bottom microplates is available either in tissue-culture treated format to optimize cell growth, or without surface modification.

#### Porvair Sciences

For info: 800-552-3696

[www.microplates.com/krystal-clear-bottom-opaque-sides](http://www.microplates.com/krystal-clear-bottom-opaque-sides)

### Flow Chemistry Mixer

The Uniqsis range of glass static mixer (GSM)/chip reactor blocks produces an efficient, turbulent mixed reagent stream for flow chemistry reactions that is not diffusion dependent. Now available in sizes from 270  $\mu\text{L}$  to 20 mL, our recently expanded range of GSM chips can be used to perform reactions from  $-80^\circ\text{C}$  to over  $150^\circ\text{C}$ . GSM chips up to 2 mL can be operated up to 40 bar and are available in two-channel or three-channel inlet configurations. Larger GSM chips of 10 mL and 20 mL have a premixing channel followed by a residence domain and can operate up to 10 bar. Uniqsis GSM chips are precision machined from inert borosilicate glass to withstand a wide temperature range and can be conveniently attached to a FlowSyn column heater module, Cold Coil module, or Polar Bear Plus cryogenic reactor module.

#### Uniqsis

For info: +44-(0)-845-864-7747

[www.uniqsis.com/paProductsDetail.aspx?ID=ACC\\_CHIP](http://www.uniqsis.com/paProductsDetail.aspx?ID=ACC_CHIP)

### Small-Scale Photoreactor

The DrySyn Illumin8 from Asynt allows users to run up to eight parallel photochemical reactions at a time in precision borosilicate tubes of up to 6 mL in volume. The unit mounts on a standard magnetic hotplate stirrer, enabling powerful agitation and heating (up to  $80^\circ\text{C}$ ). Convenient connectors on top of the unit allow for an inert atmosphere or vacuum to be applied to each reaction tube. Compact in size, the DrySyn Illumin8 features a ring of eight high-power ultraviolet (365 nm) or blue (450 nm) light-emitting diodes (LEDs) with safety interlocks to ensure light-tight photochemical reactions. With each LED positioned close to a corresponding reaction tube, the unit efficiently delivers an even photon flux to each reaction, enhancing the consistency of your photochemical reactions. The DrySyn Illumin8 is simple to set up, flexible in operation, and easy to use, with just one on/off switch.

#### Asynt

For info: +44-(0)-1638-781709

[www.asynt.com/product/illumin8-parallel-photoreactor](http://www.asynt.com/product/illumin8-parallel-photoreactor)

### SARS-CoV-2 B.1.351 (S. African Variant) Spike Protein Mutants

As potentially more transmissible variants of SARS-CoV-2 emerge, understanding how mutations in the spike protein impact SARS-CoV-2 behavior is critical. With the pPACK-SPIKE B.1.351 RBD Mutations Lentivector Packaging Mix, you can safely characterize the SARS-CoV-2 spike protein, which has three key receptor-binding domain mutations found in the emerging South African lineage B.1.351 (also known as 501Y.V2)—K417N, E484K, N501Y—making it an ideal reagent for vaccine and antiviral drug discovery projects. You can conduct a range of SARS-CoV-2 studies under biosafety level 2 conditions, including neutralization assays and studies of virus interactions with host surface proteins, as well as the development of vaccines and therapeutics. For added convenience we also offer pPACK-BALD, an envelope protein-free lentivector packaging mix that can be used as a negative control for any pPACK-SPIKE study or to create lentivirus particles pseudotyped with the envelope protein of your choice.

#### System Biosciences

For info: 888-266-5066

[systembio.com](http://systembio.com)

Electronically submit your new product description or product literature information! Go to [www.sciencemag.org/about/new-products-section](http://www.sciencemag.org/about/new-products-section) for more information.

Newly offered instrumentation, apparatus, and laboratory materials of interest to researchers in all disciplines in academic, industrial, and governmental organizations are featured in this space. Emphasis is given to purpose, chief characteristics, and availability of products and materials. Endorsement by *Science* or AAAS of any products or materials mentioned is not implied. Additional information may be obtained from the manufacturer or supplier.



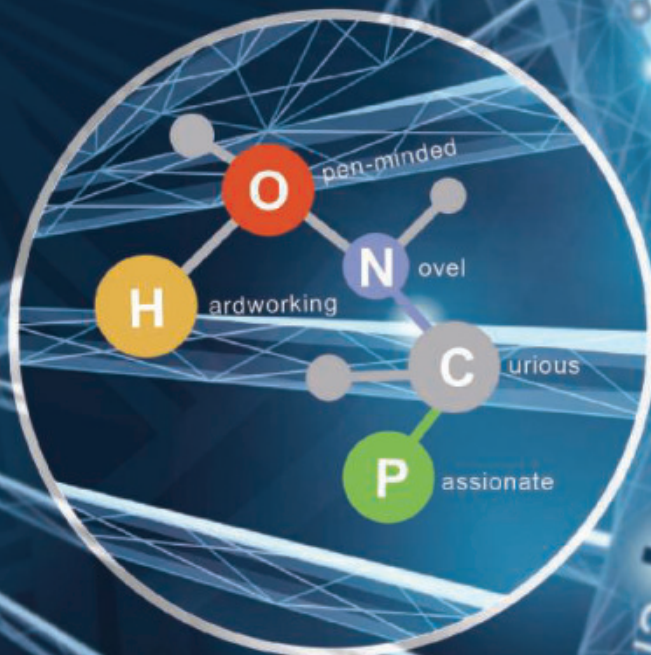
## JOIN US

Free your imagination and open up a new world.  
Find out more at

<http://en.ustc.edu.cn>

# USTC

University of Science  
and Technology of China,  
with the DNA of innovation, offering  
unlimited space for the unique talents and great  
minds, rising to be a world leader  
in fundamental science and breakthrough  
technology.



# Who's the top employer for 2020?

*Science Careers'* annual survey reveals the top companies in biotech & pharma voted on by *Science* readers.

Read the article and employer profiles at [sciencecareers.org/topemployers](https://sciencecareers.org/topemployers)



## Science 2020 TOP EMPLOYER





# 4th Hideyo Noguchi Africa Prize

## Calling for Nominations

The Prize, to be awarded by the Government of Japan on the occasion of 2022 Tokyo International Conference on African Development (TICAD 8), carries ideals and aspirations of a Japanese microbiologist Dr. Hideyo NOGUCHI (1876-1928) who fell victim to yellow fever in Africa during his research of the disease. It aims to honor individuals with outstanding achievements in the fields of medical research and medical services to combat infectious and other diseases in Africa, thus contributing to the health and welfare of the Africans. The challenges caused by Covid-19 is test for humanity and reaffirm the importance of the Prize that aspires “to improve the health and welfare of the African people and all humankind.”

### ■ Medical Research

- Basic medical research
- Clinical medical research
- Research in all fields of life science closely related to medicine

### ■ Medical Services

- Field-level medical/public health activities to combat diseases and advance public health

Please access at: <https://www.cao.go.jp/noguchisho/english/index.html>

<https://www.jsps.go.jp/english/e-noguchiafrica/index.html>

**DEADLINE: August 20th, 2021**

**Laureates for the Hideyo Noguchi Africa Prize**



**2008**  
**Dr. Brian Greenwood**  
(Medical Research)



**2008**  
**Prof. Miriam Were**  
(Medical Services)



**2013**  
**Dr. Peter Piot**  
(Medical Research)



**2013**  
**Dr. Alex G. Coutinho**  
(Medical Services)



**2019**  
**Dr. Jean-Jacques Muyembe-Tamfum**  
(Medical Research)



**2019**  
**Dr. Francis Gervase Omaswa**  
(Medical Services)



## TEXAS POSTDOCTORAL FELLOW POSITIONS AVAILABLE

Two postdoctoral fellow positions are available in the laboratory of Dr. Shao-Cong Sun in the Department of Immunology at **The University of Texas MD Anderson Cancer Center**. Selected candidates will participate in innovative projects studying the molecular basis of T cell activation, metabolic reprogramming, and exhaustion using mouse models of antitumor immunity and autoimmune diseases. The Sun lab also studies the signaling network in innate immune cells that regulate inflammation and T cell functions. For more information, please refer to our recent publications:

- Gu M et al (2021), NF-κB-inducing kinase maintains T cell metabolic fitness in antitumor immunity. *Nature Immunology*, 22(2):193-204.
- Zhu et al (2020), TBKBP1 and TBK1 form a growth factor signaling axis mediating immunosuppression and tumorigenesis. *Nature Cell Biology* 21(12):1604-1614.
- Zhou X et al (2019), The deubiquitinase Otub1 controls the activation of CD8+ T cells and NK cells by regulating IL-15-mediated priming. *Nature Immunology* 20(7):879-889.
- Jie Z et al (2018), NIK signaling axis regulates dendritic cell function in intestinal immunity and homeostasis. *Nature Immunology* 19(11):1224-1235.

The Sun laboratory has a long history of success in research and postdoctoral training. Candidates should have a solid background in immunology, with hands-on experience in flow cytometry, molecular techniques, and mouse models of anti-tumor immunity and/or autoimmune diseases. To apply, send your CV and the names of three references to [ssun@mdanderson.org](mailto:ssun@mdanderson.org).

*It is the policy of The University of Texas MD Anderson Cancer Center to provide equal employment opportunity without regard to race, color, religion, age, national origin, sex, gender, sexual orientation, gender identity/expression, disability, protected veteran status, genetic information, or any other basis protected by institutional policy or by federal, state or local laws unless such distinction is required by law.*

## OPPORTUNITIES IN CHINA



### Faculty Positions in School of Life and Health Sciences The Chinese University of Hong Kong, Shenzhen

The Chinese University of Hong Kong, Shenzhen (CUHK-Shenzhen) invites applications for full-time faculty positions in Life and Health Sciences at ranks of professors/associate professors/assistant professors. Qualified candidates must have an earned doctoral degree in life sciences, postdoctoral training and research and teaching experiences. Applicants for professor and associate professor positions should have an established research program, teaching experience and an excellent publication record. Lecturer and Senior Lecturer positions are also available for candidates with teaching experience in life sciences. Applicants in the following disciplines are preferred.

**Bioinformatics.** The ideal candidates should demonstrate research interests and teaching potentials in bioinformatics and related fields including data mining, machine learning and mathematical modeling focusing on biological sciences.

**Biomedical Engineering.** Jointly developed by the School of Life and Health Sciences (LHS) and School of Science and Engineering (SSE), this program is recruiting faculty members with teaching and research interests in biomechanics, tissue engineering, biomaterials, regenerative medicine, biomedical imaging, nanomedicine, biosensors and bio-robotics, and systems and synthetic biology.

**Pharmaceutical Science.** The applicants are expected to teach and conduct research in pharmaceuticals, medicinal chemistry, pharmaceutical analysis, pharmacokinetics, pharmacogenomics, biologics and immunotherapy, and pharmacy administration.

Established in 2014, CUHK-Shenzhen is a research-intensive university that inherits the fine academic traditions of The Chinese University of Hong Kong. The University adopts a tenure-track system for Assistant Professors and above. English is the main language for classroom teaching, and graduates receive degrees of The Chinese University of Hong Kong. Please visit [lhs.cuhk.edu.cn](http://lhs.cuhk.edu.cn) for additional descriptions of the program. Interested applicants should submit their curriculum vitae, teaching statements and research descriptions to: <http://academicrecruit.cuhk.edu.cn/lhs>. Applications will be reviewed on a rolling basis until the positions are filled.

# ScienceCareers

FROM THE JOURNAL SCIENCE  AAAS

## Confused about your next career move?



**Download Free Career  
Advice Booklets!**

[ScienceCareers.org/booklets](http://ScienceCareers.org/booklets)



## myIDP:

A career plan customized  
for you, by you.



For your career in science, there's only one Science

### Features in myIDP include:

- Exercises to help you examine your skills, interests, and values.
- A list of 20 scientific career paths with a prediction of which ones best fit your skills and interests.
- A tool for setting strategic goals for the coming year, with optional reminders to keep you on track.
- Articles and resources to guide you through the process.
- Options to save materials online and print them for further review and discussion.
- Ability to select which portion of your IDP you wish to share with advisors, mentors, or others.
- A certificate of completion for users that finish myIDP.



Visit the website and start  
planning today!  
[myIDP.sciencecareers.org](https://myIDP.sciencecareers.org)

Science  
Careers  
MAAS

In partnership with:



BURROUGHS  
WELLCOME  
FUND



UNIVERSITÉ  
DE GENÈVE

The Faculty of Medicine of the University of Geneva  
is seeking to fill a position of:

## FULL OR ASSOCIATE PROFESSOR IN PSYCHIATRIC NEUROSCIENCE

### CHARGE:

This is a full time position in psychiatric neurosciences to conduct basic research relevant to clinical psychiatry. The candidate is expected to be involved in teaching in the field of basic neurosciences and psychiatry where appropriate, as well as in the supervision of academic master's and doctoral theses.

He/she is also expected to take on management and organizational tasks at the Department of Psychiatry and at the Faculty level.

He/she will have to demonstrate an ability to establish links with partner hospital services and research groups as part of a transversal mission.

### REQUIREMENTS:

MD-PhD or PhD degree (or equivalent degree).

Experience in direction of research and skills for teaching.

Good knowledge of French and training in psychiatry would be an advantage.

Publications in leading peer-reviewed journals.

### ENVIRONMENT:

The successful candidate will be member of the Department of Psychiatry and affiliated member of the Department of Basic Neurosciences. Furthermore, he/she will be part of the Synapsy network (<https://nccr-synapsy.ch>).

### STARTING DATE:

January 1st, 2022 or according to agreement.

Mandatory online registration before **May 25th, 2021** at:  
<http://www.unige.ch/academ>

Additional information may be obtained from:  
[sylvia.deraemy@unige.ch](mailto:sylvia.deraemy@unige.ch)

*The University is an equal opportunities employer and  
particularly welcomes applications from women*



By Suhas Eswarappa Prameela

## Finding my online voice

It was a beautiful August day, and I was on a socially distanced hike with friends along the Appalachian Trail. But instead of enjoying the scenery, I was distracted by my phone. It kept buzzing in my pocket as hundreds of Twitter notifications flooded in. I had been on Twitter for about a year, mainly tweeting about science. I enjoyed it, but none of my tweets ever got much traction—until that day. I was excited—and nervous. Was I ready to be Twitter famous?

I had spent much of the previous day wrestling with data files prepared by a junior co-worker, first using the version they named “final” only to find that the actual values I needed were in a file named “final2.” After I sorted it out, I sent a quick—hopefully polite and constructive—email saying that we needed to do a better job naming our shared files. Late that night, I was awoken by a notification on my phone: My colleague had emailed with an apology and assurance that they would do better in the future. Unable to go back to sleep, I decided to tweet a brief comment about the importance of properly naming research files, hoping that some of my few dozen followers would benefit. To my astonishment, it was retweeted by a high-profile academic account, and it had blown up by morning.

Before that point, my tweets had been limited to sharing research results, without adding any personal perspective. I was hesitant to share my thoughts or experiences, thinking no one would care—or, worse, that colleagues and potential future employers might misinterpret them. After all, who was I to offer advice? I’m just a Ph.D. student doing my best; I didn’t know whether I was doing anything right myself!

But seeing people from across academia retweeting me and agreeing with my point shifted my mindset. Maybe I do have something to offer.

Since then, I have been regularly tweeting about my experiences as a Ph.D. student, including navigating authorship conflicts, maintaining work-life balance, mentoring undergraduate students, giving presentations, writing, and more. Some tweets inspire a lot of responses, others fewer. Regardless, I’ve found that I enjoy offering my perspective. I am not an expert on academic life, but I’ve learned that I don’t need to pretend to be. Sharing my experiences is still useful and rewarding.



**“I am not an expert on academic life, but ... sharing my experiences is still useful and rewarding.”**

I recently posted about the personal statement component of graduate school applications. I recalled struggling with this when I first applied to Ph.D. programs, as an international student with no scientist family members to advise me. I searched the internet for advice and crafted my application as well as I could, but my statement mostly ticked off items from my CV. I didn’t get into most of the places where I applied. One school invited me to a master’s program, though, and I enrolled. When I applied for Ph.D. programs again a few years later, my experience in academia and my mentor’s advice led me to take a different approach to the personal statement. I focused on the ideas I wished to pursue, and wrote about how my background and the school I was applying to were a good fit. This time, most programs offered me a spot. I thought others might benefit from the insight I had gained, so I posted a series of tweets.

Many students reached out, thanking me and asking follow-up questions. One first-generation student in Nigeria—someone I would never have connected with were I not active on Twitter—asked me whether I had time to provide feedback about their statement, which I was honored to do. The student also mentioned how they benefited from my posts and the discussions they spurred, which reinforced my motivation to keep at it.

Although I sometimes feel uncomfortable and vulnerable sharing my experiences on a massive global platform, I’ve found that it is well worth it. I’ve learned that we are all stronger if we authentically share and connect with one another. ■

Suhas Eswarappa Prameela is a Ph.D. student at Johns Hopkins University in Baltimore, Maryland. Send your career story to [SciCareerEditor@aaas.org](mailto:SciCareerEditor@aaas.org).

CALL FOR PAPERS



# Plant Phenomics

 OPEN ACCESS

*Plant Phenomics* is a Science Partner Journal published in affiliation with the State Key Laboratory of Crop Genetics & Germplasm Enhancement, Nanjing Agricultural University (NAU) and distributed by the American Association for the Advancement of Science (AAAS). *Plant Phenomics* publishes novel research that advances both in field and indoor plant phenotyping, with focus on data acquisition systems, data management, data interpretation into structural or functional traits, integration into process based or machine learning based models, and connects phenomics to applications and other research domains.

**Submit your research to *Plant Phenomics* today!**

Learn more: [spj.sciencemag.org/plantphenomics](https://spj.sciencemag.org/plantphenomics)

The Science Partner Journals (SPJ) program was established by the American Association for the Advancement of Science (AAAS), the non-profit publisher of the *Science* family of journals. The SPJ program features high-quality, online-only, Open-Access publications produced in collaboration with international research institutions, foundations, funders, and societies. Through these collaborations, AAAS furthers its mission to communicate science broadly and for the benefit of all people by providing top-tier international research organizations with the technology, visibility, and publishing expertise that AAAS is uniquely positioned to offer as the world's largest general science membership society.

Learn more at [spj.sciencemag.org](https://spj.sciencemag.org)



@SPJournals



@SPJournals

ARTICLE PROCESSING CHARGES WAIVED UNTIL 2022



## Pushing the Boundaries of Knowledge

As AAAS's first multidisciplinary, open access journal, *Science Advances* publishes research that reflects the selectivity of high impact, innovative research you expect from the *Science* family of journals, published in an open access format to serve a vast and growing global audience. Check out the latest findings or learn how to submit your research: [ScienceAdvances.org](https://www.scienceadvances.org)

Science  
Advances  
AAAS

---

**GOLD OPEN ACCESS, DIGITAL, AND FREE TO ALL READERS**

---